8-2013

Novel Ceria-Zirconia-Yttria Mesostructures: Synthesis, Characterization, Diffusional Studies and the Effects of Morphology on their Properties

Alma Cordova morales
Clemson University, mcordov@clemson.edu

NOVEL CERIA-ZIRCONIA-YTTRIA MESOSTRUCTURES: SYNTHESIS, CHARACTERIZATION, DIFFUSIONAL STUDIES & THE EFFECTS OF MORPHOLOGY ON THEIR PROPERTIES

A Dissertation
Presented to
the Graduate School of
Clemson University

In Partial Fulfillment
of the Requirements for the Degree
Doctor of Philosophy
Chemical Engineering

---

by
Alma Iris Cordova Morales
August 2013

Accepted by:
Dr. David A. Bruce, Committee Chair
Dr. Douglas Hirt
Dr. Scott Husson
Dr. Shiou-Jyh Hwu

ABSTRACT

Ceria-zirconia-yttria (CZY) mixed oxides are used as catalyst supports for three-way catalysts for automotive exhaust emission control and in solid oxide fuel cells. By improving the morphology of CZY mesopores it is possible to reduce the sintering of supported noble metals and enhance overall catalyst lifetime and performance. However, limited studies have been published on the synthetic control of the morphology of CZY materials and the effects that CZY pore geometry has on catalyst operation.

To create optimized CZY catalyst supports, novel mesoporous CZY oxides were synthesized via classical sol-gel and evaporation induced self-assembly (EISA) methods, obtaining mesostructures that exhibited excellent physical and diffusional properties. This dissertation provides a detailed analysis of the factors and mechanisms that promote the creation of ordered mesoporous CZY structures via classical sol-gel and EISA approaches.

Classical sol-gel methods are reaction-limited syntheses in which, for the case of CZY materials, the formation of polyoxides occurs rapidly as a result of the availability of water and hydrolyzing agents in the initial solution, yielding disordered oxide mesostructures. Alternatively, EISA is a diffusion-limited process, where the rate of oxide forming reactions is limited by the slow diffusion of water into the initial ethanolic-metal salts solution. The slow loss of ethanol by evaporation enables the condensation-polymerization of metal oxy-hydroxide species to coincide with the ordering of these oligomers around the self-organized polymer template. Thus, for the templated synthesis

of mesoporous CZY materials, it is the rate of metal oxide condensation that determines the nature of the resulting oxide structure.

The choice of templating technique used during CZY synthesis heavily influenced post-calcination morphologies and pore sizes, but to-date no relationships between pore morphology and catalyst performance for CZY materials was presented. For this reason, the diffusion of n-hexane in mesoporous CZY supports synthesized using a variety of templates and synthesis techniques was studied by the Zero Length Column (ZLC) method obtaining each material diffusion coefficients.

Data from the ZLC method proved to be valuable in developing an understanding of the effects of pore morphology on intraparticle diffusion phenomena. The CZY oxides diffusivity values provide means of comparison of diffusional aspects that can significantly impact catalyst performance during the treatment of exhaust gases formed by combustion engines. A higher diffusivity value is expected to bring catalytic advantages for the oxide support.

DEDICATION

This is for you son. You have taught me how to be happy even in the most imperfect circumstances.

ACKNOWLEDGMENTS

First of all, I would like to thank God for giving me life and wisdom to fulfill this achievement. Todo lo puedo en Cristo que me fortalece.

I would like to specially acknowledge my advisor, Dr. David Bruce, whose expertise, guidance, enthusiasm, patience and humor added considerably to my graduate experience.

I also would like to thank my very good friends and fellow researchers at Clemson for their assistance, helpful discussions and friendship; they have taught me so much and have been an example of excellence and professionalism. I specifically thank Prince Anyaba and Ha Nguyen, whose expertise, skills and assistance was indispensable as I carried out this work.

Special thanks to the EM Facility staff for their assistance with imaging needs throughout my research, especially Haijun Qian.

Thanks to my dissertation committee members, for thoroughly reading this work and constructive comments and suggestions: Dr. Douglas Hirt; Dr. Scott Husson, and Dr. Shiou-Jyh Hwu.

Thanks to Dr. Bob Lippert and the Graduate School International Ambassadors Program. This program is the reason I decided to pursue a PhD and come to Clemson.

I specially acknowledge Dr. Paul Fanson and Dr. Kimber Stamm for all their useful suggestions and comments and also to Toyota Motor Engineering & Manufacturing North America for providing the funds for this project.

I lovingly thank my parents for their support and encouragement; they have been my biggest support over the years and for that and many other reasons I owe them my eternal gratitude

I need to mention my family in Clemson, the Woolbrights; they have been a Christian inspiration and an example to follow. I could not have finished my PhD without their help and understanding in all aspects of my life.

For all the love, all the adventures and incredible happy moments, your tender heart has shown me what love and forgiveness is and I cannot thank God enough for the opportunity to have you in my life. This is what God had destined for me and is just the beginning of a lifetime story.

I would like to thank a very special person, this journey would not have been the same without you and I thank God for the day you came into my life and opened my heart to so many beautiful experiences, you have aged me prematurely but have filled me with joy and unselfish love, my reason to succeed, my son Alex. Te amo little oso.

TABLE OF CONTENTS

Page

Table of Contents (Continued)

Page

Table of Contents (Continued)

Page

LIST OF TABLES

Table Page

List of Tables (Continued)

Table Page

List of Tables (Continued)

Table Page

LIST OF FIGURES

List of Figures (Continued)

Figure Page

List of Figures (Continued)

Figure Page

List of Figures (Continued)

Figure Page

List of Figures (Continued)

Figure Page

List of Figures (Continued)

Figure Page

CHAPTER ONE

INTRODUCTION

During the last forty years, increasing environmental regulations for gas pollutants from automobiles have created the necessity for practical and cost-effective ways to treat exhaust gases. Catalytic converters have been developed for this purpose, but their relatively high cost and negative impact on engine power have meant that ever since the development of the first generation of catalytic converters there has been an ongoing research effort to improve converter efficiency and lower costs.

The heart of a modern catalytic converter is a ceramic honeycomb or metallic foil structure that contains the catalytically active noble metals that actually perform the chemistry needed to convert pollutants in the engine exhaust into less harmful gases. These catalysts, which often contain expensive precious metals such as Pt, Pd, and Rh, are often referred to as three-way catalysts because they convert three unique classes of pollutants into less harmful species. Specifically, three-way catalysts are designed to oxidize unburnt hydrocarbons (HCs) and carbon monoxide (CO), yielding carbon dioxide (CO2) and water (H2O), while simultaneously reducing nitrogen oxides (NOx) into nitrogen (N2) and oxygen (O2). It has been well established that for all conversions to occur, the engine's operation should be performed at the exhaust gases stoichiometric point, where oxygen is neither insufficient nor in excess so oxidation and reduction processes can occur by alternating between oxygen lean and rich conditions. However, the inevitable time-lag in the system to adjust the air/fuel ratio (A/F) can decrease the conversion rate of the exhaust gases. This problem has been solved by the use of catalyst

supports with oxygen storage capacities (OSC), which are able to accept oxygen under fuel lean conditions (combustion with an excess of air) and donate oxygen under fuel rich conditions (combustion with a fuel to air ratio greater than the stoichiometric ratio (~14.6:1) needed for combustion).

Ceria is the usual catalyst support material used for oxygen storage and release purposes as it has a high OSC compared to other transition metal oxides and the activation barrier for the removal of oxygen from the ceria lattice is relatively low. However, a pure ceria support is unsatisfactory as it exhibits thermal and mechanical fragileness. To overcome the poor physical properties of ceria, catalyst researchers have created mixed oxide supports that combine this OSC material with other metal oxides that display enhanced mechanical properties over a broad temperature range.

Zirconia and yttria oxides were found to be the best options to provide these enhanced mechanical properties. Due to these characteristics, ceria-zirconia-yttria mixed oxides have been proven to be optimal catalyst supports for three way catalysts, and a solid solution or wash coat of these materials on rigid ceramic or metal monoliths now constitutes the catalyst support used for most vehicle exhaust treatment applications.

The purpose of this work is to develop improved mesoporous ceria-zirconia-yttria (CZY) catalyst supports to further enhance the efficiency and longevity of automotive catalytic converters. Besides their oxygen storage capacity and thermal and mechanical stability, these mixed oxide materials can be designed to maintain the dispersion and enhance the activity of three-way catalysts used in automobile emissions control,

minimizing the quantities of noble metals needed to achieve the required level of performance and thereby reducing costs for the automobile industry.

In addition to catalytic converters, mesoporous ceria, zirconia and yttria oxides are used in solid oxide fuel cell, catalysis, electronic and sensor applications. The improvement of these materials has faced many challenges but continues to be of great importance as they remain in high demand for numerous costly applications.

Since the successful synthesis of silica based mesoporous materials by researchers at Mobil in 1991, mesoporous materials have been extensively studied, and significant effort has been put toward the development of novel templating strategies and advanced synthesis techniques. The synthesis procedures developed for silica based materials were later extended to non-silica based materials with great difficulty, as their fabrication proved to be more challenging than expected. Ceria, zirconia and yttria oxides have not been an exception, as numerous articles have chronicled difficulties encountered with the synthesis of single component and mixed mesoporous oxides of these metals. Of particular difficulty, has been the synthesis of ordered CZY mesostructures, which have been hypothesized to be advantageous for reducing noble metal sintering and enhancing reactant and product diffusion rates through the material.

The synthesis of high surface area mesoporous CZY oxides has been previously investigated by this research group using organic surfactants, activated carbon, resins and polymers as templates. Numerous chemical and structural characterization methods were

used to critically evaluate the effectiveness of these various templating strategies for synthesizing ordered CZY mesostructures.

The emphasis of this unique work is on advanced synthesis strategies that yield improvements to the morphology and physical properties of CZY mixed oxides as well as the use of advanced characterization techniques that are capable of evaluating the diffusional enhancements gained by the formation of ordered mesoporous structures. Specifically, this work examines mesoporous CZY materials prepared via classical synthesis techniques as well as a novel synthesis approach capable of producing the elusive, ordered mesostructures that so many research groups have tried to synthesize.

CZY materials were characterized by a variety of techniques that include Brunauer-Emmer-Teller (BET) surface area, Barret-Joyner-Halenda (BJH) average pore size, scanning transmission electron microscopy (STEM), small and wide angle X-ray diffraction, inductively coupled plasma atomic emission spectroscopy (ICP-AES), as well as other physical characterization techniques. Finally, transient diffusional studies using hexane as the probe molecule were used to quantify the diffusion properties of several CZY mesostructures having a range of pore types, with some exhibiting an ordered pore morphology.

The first chapters of this thesis deal with the synthesis and characterization of mesoporous CZY oxides, starting with the classical sol-gel synthesis approach for materials with high surface area, large pore volume, uniform pore size distribution, uniform oxide incorporation, among other improved characteristics. Later efforts focus

on the development of ordered and reproducible mesostructures that are prepared by the evaporation induced self-assembly (EISA) method using block copolymers as structure directing agents (templates).

The final chapters of this work are focused on the diffusional properties of CZY materials synthesized by sol-gel and EISA techniques, where the materials were prepared using either endo-templates (block copolymers, surfactants, and dendrimers) or exo-templates (resins and activated carbon). The diffusion of gases inside pores of different geometries and sizes leads to an understanding of the advantages of some catalyst supports over others.

These experiments focused on the measurement of diffusion in CZY oxides to find if a specific pore morphology and/or size is optimal for the conversion of gaseous exhaust pollutants. This work evaluates not only the physical characteristics of the synthesized CZY materials, but also the real diffusion behavior of gases inside the pores of these supports. This type of synthesis and characterization information will help guide the design of future mesoporous CZY catalyst supports for exhaust gas treatment as well as other sensor and reaction applications.

CHAPTER TWO

BACKGROUND INFORMATION AND FUNDAMENTALS

The objective of this dissertation is to synthesize and characterize improved ceria-zirconia-yttria catalyst supports for three-way catalysts, which are commonly used in catalytic converters. To further enhance the reader's ability to understand the material presented in the following chapters, I have provided a brief overview of the important concepts that will be used throughout this dissertation.

Mesoporous materials

Mesoporous materials are any material containing pores between 2 and 50 nm in diameter. Often they possess many highly useful features, namely, high surface area, uniform pore size distribution, large pore volume and enhanced thermal stability. These properties makes them ideal for a considerable number of applications in catalysis,[1-4] adsorption,[5, 6] biomolecular separation,[7, 8] and drug delivery[9, 10]. The successful synthesis of the mesoporous silica-based highly ordered MCM-41 materials[11] in the early 1990s started intensive research in this area with an initial focus on siliceous materials. The synthesis techniques created for silica-based materials were later extended to non-silica based materials in an effort to expand both their molecular diversity and the range of possible applications.

Mesoporous transition metal oxides have been investigated increasingly as their varied chemistry and redox properties make them useful for many innovative purposes. Within metal oxides, ceria, zirconia and yttria have been of particular interest as a result of a number of catalytic and electronic applications[12,26,28-29], among which, their use as

catalyst supports in catalytic converters is arguably their largest use.

Properties and Applications of Ceria, Zirconia and Yttria Oxides

Ceria

Cerium oxide (CeO_2), also known as ceria, is a pale yellow powder with a melting point of 2400 °C. Pure stoichiometric CeO_2 exhibits a calcium fluoride (fluorite) type of structure with space group *Fm3m* over the whole temperature range from room temperature to its melting point. Further, it can tolerate a considerable level of reduction without undergoing any phase change.[12]

Thousands of articles in the last twenty years have been dedicated to ceria and ceria-based materials, in part due to its oxygen storage capacity, which is based on its unique ability to undergo reversible redox transitions from cerium (III) to cerium (IV) and vice versa. Practical applications of this material include high temperature ceramics, catalysis, and solid oxide fuel cells.[13] Despite the significant amount of work on ceria and ceria-based materials, its particular capability to store and release oxygen will likely ensure to keep research in the area proliferating.

Zirconia

Zircon has been known as a gem from ancient times. The name of the metal, zirconium, comes from the Arabic *Zargon* (golden in colour), which in turn comes from the two Persian words *Zar* (Gold) and *Gun* (Colour). Zirconia, the metal dioxide (ZrO_2), was identified as such in 1789 by the German chemist Martin Heinrich Klaproth. It is the reaction product obtained after heating some gems, and was used for a long time blended

with rare earth oxides as pigment for ceramics.[14] Zirconia is a white crystalline oxide whose most naturally occurring form is the mineral baddeleyite, which has a monoclinic crystalline structure. It is usually produced by calcining zirconium compounds exploiting its thermal stability. It is relatively unreactive chemically and one of the most studied ceramic materials.[15]

Zirconia is a well-known polymorph that occurs in three forms: monoclinic (M), cubic (C) and tetragonal (T). Pure zirconia is monoclinic at room temperature. This phase is stable up to 1170 °C. Above this temperature, it transforms into a tetragonal and then into a cubic phase at 2370 °C.[15]

High temperature ionic conductivity makes zirconia ceramics suitable as solid electrolytes in fuel cells and oxygen sensors. Good chemical and dimensional stability, mechanical strength and toughness, coupled with a Young's modulus comparable to stainless steel alloys was the origin of interest in using zirconia as a ceramic biomaterial.[14]

Zirconia has been widely studied for numerous applications including: medicine, catalysis, fuel cell electrolytes, electro-optical materials, damage-resistant optical coatings and gate dielectrics.[16-25]

Low-quality zirconia is used as an abrasive in huge quantities, whereas tough, wear resistant, refractory zirconia ceramics are used to manufacture parts operating in aggressive environments, like extrusion dies, valves and port liners for combustion engines, low-corrosion thermal-shock resistant refractory liners, or valve parts in

foundries. For example, zirconia blades are used to cut Kevlar, magnetic tapes and cigarette filters because of their reduced wear.

Yttria

Yttrium oxide (Y_2O_3), also known as yttria, is a white solid oxide used in material science and inorganic chemistry. It has a cubic crystalline structure and a melting point of 2425 °C.

Yttria, together with alumina (Al_2O_3), are the two most important sesquioxides within the general class of refractory ceramics.[26] Yttria has been widely used in catalysis, solid-state laser applications, sintering aids in the processing of ceramic materials, substrates for semi-conducting films, optical windows, components for rare-earth doped lasers, and high temperature ceramics. Yttria is well known for enhancing the mechanical stability of high temperature ceramics.[27] A small addition of Y_2O_3 influences both the properties and the microstructures of Al_2O_3, the so-called yttrium effect; and it has a beneficial effect of increasing the adhesion oxide scales in all Al-containing metals. Many of the unique properties of yttria and yttria-related materials depend critically on the defect structures and their concentrations, and on the formation of intermediate phases.[26]

Ceria-Zirconia-Yttria (CZY) mixed oxides

Combinations of CZY oxides have found extensive use. For instance, yttria-stabilized zirconia (YSZ) has been widely used for thermal barrier, jewelry, and solid oxide fuel cell applications.

Zirconia is routinely blended with other oxides like yttria, ceria and magnesium oxide to stabilize its cubic and/or tetragonal phases so that cracks due to phase transitions and stress induced by cooling from high temperatures can be reduced or eliminated. This (yttria) stabilized form of zirconia not only resists phase changes but has also been shown to have enhanced thermal, mechanical and electrical properties.[15]

Ceria-zirconia-yttria (CZY) mixed oxides are most often used for applications including solid oxide fuel cells[28-31] and as catalyst supports for three-way catalysts (TWC) that are used for automotive exhaust emission control.[32-34] This last application has been the motivation and is the focus of this dissertation and will be discussed in greater detail in the next section of this chapter.

Catalytic Converters

Catalytic converters are emissions control devices that convert toxic fuel combustion byproducts in the vehicle's exhaust to less harmful species. If not converted to less harmful species, these pollutants would significantly contribute to the production of acid rain and smog.

Catalytic converters were introduced around 1975 to comply with increasing environmental regulations on air quality and emissions. The Clean Air Act in the United States (passed in 1970) was the first law that sought to control vehicle emissions, setting the requirements at 0.41 g/mile for hydrocarbons (non-methane organic gases or NMOG), 13.4 g/mile for carbon monoxide and 0.4 g/mile for nitrogen oxides (current standards are 0.075 g NMOG/mile, 3.4 g CO/mile and 0.2 g NO_x/mile).[35, 36] Since then, catalytic converters have evolved considerably to increase effectiveness, to fulfill the

worldwide need to reduce pollution created by the exhaust systems of internal combustion engines, and to reduce the economic burden created by them.

Main pollutants from the vehicle's engine are nitrogen oxides (NOx), carbon monoxide (CO) and unburnt hydrocarbons (HC, also known as non-methane organic gases or NMOG) produced by incomplete combustion of the air/fuel (A/F) mixture in the engine. These have a huge impact on air quality; for example, studies in the U.S have shown that approximately 10 percent of vehicles are responsible for 50 percent of the CO emissions. [35]

The three main reactions taking place in a catalytic converter are:

i. $2CO + O_2 \rightarrow 2CO_2$

ii. $2C_xH_y + (2x+y/2)O_2 \rightarrow 2xCO_2 + yH_2O$

iii. $2NO_x \rightarrow N_2 + xO_2$

This device simultaneously converts the HCs, CO and NOx present in automotive exhaust to H_2O, CO_2 and N_2. The first two listed reactions are oxidation processes (i) and are favored by an excess of oxygen in the exhaust (lean fuel conditions), while the last reaction is a reduction process (iii) that operates more effectively under rich fuel (fuel rich conditions). Because of the competing requirements of these three reactions, the air to fuel ratio (A/F, mass basis) has to be carefully controlled to operate close to the stoichiometric point (A/F of 14.7, as set by the US-EPA for gasoline burning engines). At this point, oxygen is neither insufficient nor in excess, and the conversion rate of pollutants to more inert products is optimized.

Components

The catalytic converter for a vehicle exhaust system is comprised of three main parts: a ceramic or metallic support, a single or double washcoat and the catalytic layer containing the noble metal catalyst.

All modern catalytic converter supports are ceramic or metallic honeycomb structures, similar to that shown in Figure 2.1. This linear channel design maximizes the surface area containing catalysts per volume of support and reduces the overall pressure drop across the converter. The ceramic component is formed of extruded cordierite ($2MgO\text{-}2Al_2O_3\text{-}5SiO_2$), which is optimal for catalytic converter applications because its relatively low thermal expansion imparts greater thermal shock resistance.[37] Cordierite is catalytically inert and also refractory, which allows it to operate at high temperatures.

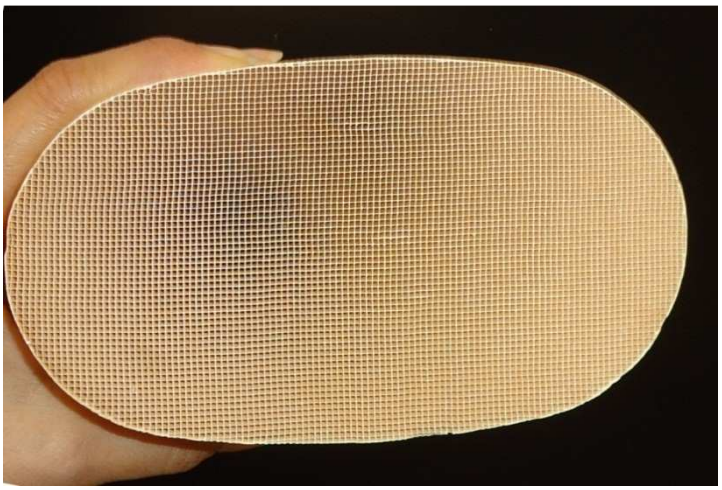

Figure 2.1. Ceramic honeycomb catalytic converter structure.

The second main component is the washcoat. It usually consists of stabilized gamma alumina or a mixture of silica and alumina, and it is about 5-15% of the converter weight with a surface are of 100-200 m^2/g. The washcoat helps enhance reactions (often

containing Lewis and Brönsted acid sites), improves durability and is designed for minimal diffusion resistance so gases readily reach the catalytically active sites.[35] The washcoat layer forms a rough, irregular surface, which effectively increases the surface area of the low surface area cordierite support providing more sites for active precious metals.

The third and most important part of the catalytic converter is the top coat of precious metals. This catalytic layer often contains noble metals and a catalyst support that helps enhance the activity of the former and prevents noble metal sintering. This mixture of precious metals and catalytically active supports is incorporated into the washcoat that is later deposited on the monolithic substrate.

The most common noble metals used in the automotive industry are platinum (Pt), palladium (Pd), rhodium (Rh) and ruthenium (Ru). They are impregnated into the highly porous alumina washcoat and usually become effective at temperatures above 140 °C. A catalytic converter usually contains about 2-3 grams of noble metals. They comprise between 0.1 to 0.15 wt% of the catalytic converter.[35]

Most catalytic converters use platinum, palladium and rhodium to catalyze both oxidation and reduction reaction processes inside the catalytic converter. Platinum and palladium promote the oxidation reactions, whereas rhodium promotes the reduction of NOx. These catalysts are commonly known as “three-way catalysts” or TWC because they simultaneously work on the three main reactions (i, ii, iii) that clean gaseous pollutants in the catalytic converter.

Oxygen sensors are used in the exhaust gas stream to monitor the air to fuel ratio. These devices send signals to the fuel injection system and air manifold in the engine to control the A/F within a narrow band close to stoichiometry.[38] The system alternates between slightly fuel rich and fuel lean conditions to perform both reduction and oxidation processes, respectively.

During fuel lean conditions, there is sufficient oxygen to combust all CO and HCs in the cylinder of the engine, which optimizes fuel efficiency. However, under these conditions greater amounts of NOx species are produced, but the excess oxygen in the exhaust stream makes it more difficult to reduce these species. In contrast, during fuel rich conditions the reduced levels of oxygen in the engine causes incomplete combustion and the production of more CO and HCs. This is the reason optimal balance is reached near the stoichiometric point.

However, there is an inevitable time lag in the system as it adjusts the A/F ratio, which can decrease the conversion rate of unwanted pollutants in the exhaust. This rate also declines during acceleration/deceleration when the A/F ratio varies greatly. In order to maintain conversion efficiencies in the catalytic converter and avoid unacceptable levels of contaminants, it was necessary to engineer a way to reversibly store and release oxygen when exhaust oxygen levels were not optimal for the conversion of pollutants. Specifically, over the range of exhaust temperatures, the converter catalyst should release oxygen during fuel rich conditions and store oxygen during fuel lean conditions. Materials with high oxygen-storage capacity (e.g., ceria) were incorporated as catalyst supports for this purpose.

Catalysts supports usually consist of ceria-zirconia or CZY mixed oxides. Besides their high oxygen storage capacity (OSC), they also provide thermal stability, higher surface area and help maintain noble metal dispersion. The following section provides a more detailed discussion of these phenomena and their importance.

Finally, the coated ceramic monoliths are surrounded by an expanding mat that insulates and protects the monoliths. The entire structure is encased by a stainless steel housing that provides corrosion and oxidation resistance. This encased structure is the one that can be seen when looking under a vehicle. Figure 2.2 shows each component of the catalytic converter as a visual aid for this section.

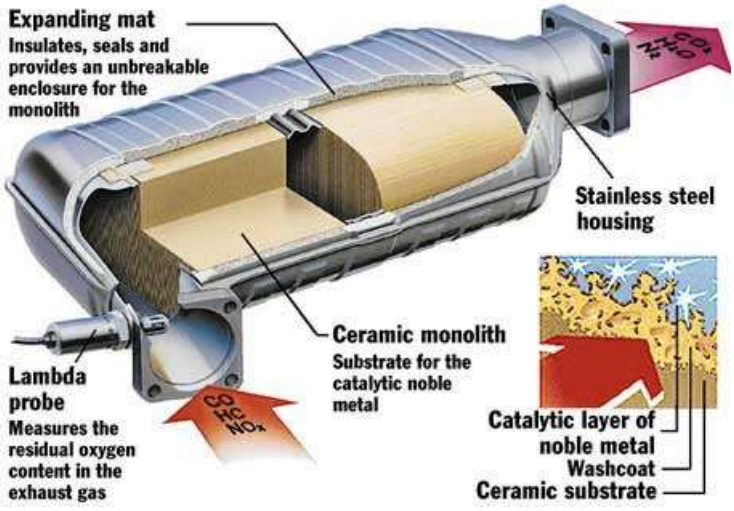

Figure 2.2. Typical catalytic converter used in gasoline engines. Copyright © 2013 Hearst Communications, Inc.

Ceria, Zirconia and Yttria in Emissions Control

Catalytic supports are vital to the correct functioning, efficiency, and longevity of three-way catalysts. Modern catalytic converters generally use transition metal oxide combinations, namely, ceria-zirconia or ceria-zirconia-yttria as catalysts supports.

Ceria is a vital component in TWC for mobile emissions control. It helps stabilize the alumina washcoat, prevents the diffusion of noble metals into the washcoat and inhibits noble metal deactivation by preventing them from being held in high oxidation states.[13]. It also promotes noble metal dispersion and provides thermal stability to catalyst supports.[40] However, its most important property for this application is its capacity to store and release oxygen by switching between stable Ce^{3+} and Ce^{4+} states.

Ceria's oxygen storage capacity (OSC) has proven to be crucial in controlling the ratio of oxidants and reductants in the exhaust allowing the simultaneous oxidation of CO and hydrocarbons and the reduction of nitrous oxides.[41] However, the exhaust conditions decrease the OSC of ceria. For example, the effectiveness of ceria as a catalyst is reduced at elevated temperatures due to sintering and loss of surface area.[13] The loss of OSC has been hypothesized to be due to a decrease in the interfacial contact between ceria and the precious metals since it is accompanied by an increase in ceria crystallite size.

The broad use of ceria in automotive pollution control catalysts quickly lead to it becoming the largest application of rare earth oxides.[42] Its inclusion in automotive three-way catalysts has transitioned away from alumina-supported ceria to high surface area, thermally stable, preformed ceria rich powders. [43] Modern ceria powders are usually a mix of oxide components, especially transition metal oxide mixture containing zirconia, which helps prevent the aforementioned sintering and degradation problems.

The use of ceria catalyst supports with enhanced thermal stability was driven by the so-called close coupled catalyst (CCC) for cold start engine emissions. These catalysts experience temperatures up to 1373 K, which required an extremely high thermal

resistance.[42] This is crucial in determining ceria promoting effects because as soon as sintering of ceria occurs, due to thermal degradation, both oxygen storage capacity (OSC) and metal-support interactions appear inhibited.

Zirconia helps stabilize OSC properties of ceria preventing degradation with time in the automotive exhaust high-temperature environment. Jen et al.[44] showed that pure ceria has poor surface area stability compared to solid solutions of ceria and zirconia (CZ), and that it retains little useful OSC after being aged at temperature above 1050 °C.

Additionally, zirconia promotes the formation of more structurally active ceria sites and imparts added thermal stability to supported ceria catalysts. [45] The enhanced stability of the CZ samples appear to result primarily from structural modification of the ceria in contact with the zirconia. Putna et al.[41] demonstrated that ceria films on zirconia are more reducible and have a higher activity towards promotion of the ceria-mediated oxidation of CO on supported metals than do ceria films on alumina. Their studies demonstrated that, following high-temperature calcination, CZ model catalysts show higher activities toward promotion of the ceria-mediated mechanism than ceria only samples.

As a result of the aforementioned facts, ceria-zirconia mixed oxides have been used openly for TWC applications. Yet, solid solutions with zirconia higher than 20% resulted in homogeneity problems. The addition of yttrium as a third cation showed improved homogeneous solid solutions over the whole range from ceria 100% to 0% mol. The CZY mixed oxides synthesized were evaluated for OSC before and after thermal aging and showed great improvement compared to other ceria based oxides. Combinations like

$Ce_{0.60}Zr_{0.30}Y_{0.10}$ oxide and $Ce_{0.40}Zr_{0.45}Y_{0.15}$ showed almost no decrease in OSC at 500 °C after thermal aging at temperatures of 800, 900 or 1000 °C.[46]

Studies of palladium supported on CZY oxides[47] provided further evidence of performance improvement by the use of CZY supports under fuel fluctuating conditions. Furthermore, some research groups, including ours, believe that ordered mesoporous CZY structures provide additional advantages for TWC applications than CZY mesostructures with no long-range organization or limited mesoporosity. Ordered mesoporous supports overcome the size and morphological constraints of microporous or disordered mesoporous materials, facilitating the mass transport of bulky, partially-combusted hydrocarbon molecules. Their intrinsic high surface area allows a high concentration of active sites per mass of material. Additionally, these active sites are highly dispersed and spatially uniform.

Compared to other support materials, ordered mesopores have the advantage of reduce sintering of catalysts by stabilizing larger metal particles, because they cannot grow to sizes larger than the pore size unless they move to the external surface of the particle.[48] Further, the synthesis of ordered CZY structures will not only enhance catalytic performance by increasing the oxygen storage properties of the support it will also improve the dispersion of noble metals (reducing metal sintering) and thereby improving catalyst longevity.

The advanced synthesis and characterization of improved CZY mesostructures is the ultimate goal of this work. These enhancements will bring advantages to the morphology and physical properties of CZY mixed oxides. Additionally, characterization techniques

that are capable of evaluating the diffusional improvements gained by the formation of ordered mesoporous structures will be developed.

LITERATURE REVIEW

As established previously, the focus of this work is to develop advanced synthesis strategies that result in improvements to the physical properties and morphology of ceria-zirconia-yttria catalysts supports for three-way catalysts in catalytic converters. Different characterization techniques to evaluate physical properties are used including diffusional properties evaluation techniques to assess the enhancements gained by the formation of ordered mesostructures.

Therefore, before proceeding to discuss the work depicted in this dissertation it is important to review previously published studies in the field. I am going to start by discussing synthesis strategies for silica-based mesoporous materials and continue with non-silica based mesoporous materials. The second part of this review will focus on diffusion studies for porous materials from traditional techniques to the Zero-Length Column (ZLC) chromatographic technique. This latter technique will be discussed in detail as it was widely used to characterize the diffusional properties of the materials prepared during this study.

Synthesis of mesoporous materials

In general, most mesoporous oxides synthesis strategies involve the use of a structure directing agent (SDA) or template and reactive oxide precursors to create an oxide network with a homogeneous mesostructure. The template (often an organic moiety) can be removed from the oxide pores post synthesis via extraction or more often by calcination (heating in air or inert atmosphere at temperatures above 300 °C). Templating pathways provide a high degree of control over structural and textural properties.

Copious literature explains a diverse array of synthesis strategies for mesoporous materials. The most cost effective approaches to create pores of certain sizes involves the use of different SDAs that can be classified as exo and endo-templates[49]. Endo-templating refers to the process in which templates are occluded in the growing solid and leave a pore system after their removal.[49] Examples are surfactants, block copolymers and dendrimers.[29, 30, 50-53, 53-55] Exo-templating refers to synthesizing a connected material within the pores and along the exterior of a rigid porous solid that acts as a scaffold (or negative mold) for the newly assembled material. After removal of the scaffold, a high surface area porous solid remains.[49] Examples of hard or exo-templates are activated carbons[56, 57] and polymeric resins[58]. Exotemplates are usually cheaper and a simpler way to create highly porous silica and non-silica based oxides, but the resulting structures tend to have very limited long range order. Both endotemplating and exotemplating approaches are depicted in Figure 2.3.

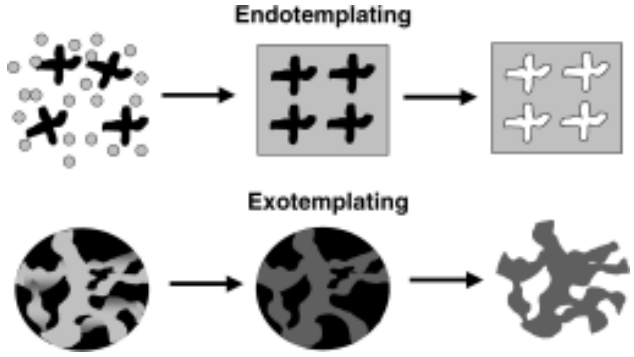

Figure 2.3. Schematic drawing of the endotemplating and exotemplating approach to synthesize porous and high-surface-area materials. For endotemplating, the templating species are occluded in the forming solid, for exotemplating, a rigid porous solid is infiltrated with the precursor for another solid. Endotemplates as well as exotemplates are removed from the composite to yield the porous or high-surface-area material. Reprinted with permission from ref [49]. Copyright © 1999–2013 John Wiley & Sons, Inc.

For flexible or endo-templates that often self-organize in solution, sol-gel, evaporation-induced self-assembly (EISA), and templating methods have been found to work effectively. The sol-gel procedure is the most common. It consists of a series of steps during which an oxide structure is formed from an initial solution (or gel) containing template and metal oxide precursors dissolved in polar solvents like water or alcohols. At moderate temperatures (25 – 200 °C), water and to a greater extent dissolved Brönsted bases catalyze the hydrolysis and condensation of the oxide precursors to form three dimension oxide networks that phase separate from the solution when they reach an appropriate size. These reactions routinely require three days for complete precipitation of the oxide product. The solid oxide is then removed via filtration or centrifugation from the solution, dried, and later calcined to remove any residual organic template trapped within the oxide pore structure. The result is a porous oxide framework with high surface area and other advantageous properties.

For rigid template materials, such as activated carbon and amine based resins, a simple adsorption and calcination process is all that is required. The metal precursors are dissolved in solution using a polar solvent (a slurry is also acceptable for some oxide precurors). The solution is mixed with the dried exo-template, where it readily adsorbs into the template pores. The final oxide-template slurry is dried and calcined, yielding a mesoporous structure that is the reverse mold of the original template.

Since a variety of templates and techniques can be used to prepare mesoporous materials, the resulting oxide frameworks exhibit a range of pore sizes, arrangements and geometries.

Synthesis of silica-based mesoporous materials

The breakthrough findings of Mobil researchers in the 1990s led to the discovery and development of a family of materials known as M41S. M41S materials are mesoporous silicates with regularly spaced nanometer-sized pores synthesized by using liquid crystals to cast the silica shapes.[59] The original MCM-41 synthesis was carried out in water under alkaline conditions with a liquid-crystalline self-assembled surfactant molecule as template.[60] For this case, the formation of the organic-inorganic composites is based on electrostatic interactions between the positively-charged surfactants and the negatively charged silicate species.[61]

This synthesis pathway opened a wide variety of synthesis approaches for the development of new mesoporous materials. Many of the techniques developed for these materials are sol-gel approaches. The sol-gel process is a wet-chemical technique widely used in the fields of material science and ceramic engineering primarily for the fabrication of materials (typically metal oxides) starting from a colloidal solution (*sol*) that acts as the precursor for an integrated network (or *gel*) of either discrete particles or network polymers.

Silica-based porous materials have been investigated extensively and remain the most studied family of mesoporous structures. Initially, most efforts were focused on silica-based materials because many research groups active in this field had their origins in zeolite chemistry and thus, were very familiar with the chemistry of silicon and aluminum.[62] Furthermore, other compositions, which are typically less stable, are more

difficult to synthesize as compared to silica and aluminosilicates. However, a much wider range of applications can be found for non-siliceous mesoporous materials.

Synthesis of non-siliceous mesoporous materials

The synthesis techniques developed for mesoporous siliceous materials were later extended to non-siliceous materials, adjusting as necessary for differences in the chemistry of the new compounds. However, the synthesis of non-siliceous mesoporous materials presented a number of difficulties vastly different than the phenomena seen with silica-based materials.[62] For instance, siliceous materials have amorphous walls that provide stability to the mesostructures. In contrast, most non-silica based porous materials have crystalline walls that make their structures more prone to collapse at high temperatures. This can be explained by the curvature necessary to form the mesopores in the mesostructure being more compatible with amorphous wall structures. Similarly, condensed frameworks formed with non-siliceous materials are not as strongly bonded as the frameworks for siliceous materials, collapsing easily as the template is removed.

For the case of transition metal oxide mesostructures (especially CZY materials), their redox properties often make them unstable. For example, the reduction and reoxidation processes that take place during calcination can cause the collapse of the oxide pore structure. Additionally, faster hydrolysis and condensation reaction rates for most transition metal precursors do not provide sufficient time for oxide intermediates and template to polymerize and assemble in an ordered mesostructure, which leads to a loss of morphological control and the formation of condensed oxide structures.

Therefore, it is crucial to surpass these limitations in order to create mesoporous non-siliceous materials with structural integrity.

Synthesis of ceria, zirconia and yttria mesoporous materials

Since CZY mesostructures are the focus of this thesis, this section will review previous work and concepts of special importance for the creation of ceria, zirconia and yttria mesoporous materials. Additional attention is given to creating ordered mesoporous structures for these components. A more detailed tabulated review of different synthesis techniques and conditions for the synthesis of ceria, zirconia and yttria mesostructures is shown in Appendix A.

Traditional sol-gel and exotemplating approaches

Numerous complications, similar to the aforementioned, have been reported for the synthesis of stable mesoporous ceria, zirconia and yttria.[13, 63-71] Classical sol-gel synthesis approaches have been largely ineffective at producing ordered mesoporous structures containing these metals. For the case of pure ceria, Lyons et al.[13] reported the synthesis of ordered ceria using cerium acetate as the inorganic framework precursor. However, TEM images of the resulting material showed the presence of both ordered and disordered mesostructures within the same sample.

For the case of mesoporous zirconia structures, Chen et al.[34, 72] and Yuan et al.[73] reported the synthesis of mesoporous zirconia by a classical sol-gel route using zirconium propoxide. Despite the resulting materials displaying a relatively homogeneous mesostructure, analysis via TEM showed no evidence of an ordered arrangement of

pores. Similarly, Blin et al.[69] and Rezaei et al.[68] reported the sol-gel synthesis of mesoporous zirconia using zirconyl chloride and zirconyl nitrate, respectively, but both materials failed to exhibit the presence of an ordered array of mesopores.

Highly ordered porous zirconium oxide-sulfate and zirconium oxo-phosphate materials were prepared by Ciesla et al.[74], yet they were unsuccessful at preparing ordered mesoporous pure zirconia. In this study, the presence of sulfate and phosphate groups helped to inhibit zirconia crystallization, thus, enabling sufficient time for the amorphous zirconia oligomers to assemble into ordered hexagonal arrangements. When the crystallization inhibitors were removed (pure zirconia case), the zirconia precursors rapidly condensed into disordered oxide structures.

Challenges increase when the objective is to create ordered mesoporous mixed oxides of ceria, zirconia and yttria like ceria-zirconia (CZ) or yttria stabilized zirconia (YSZ).[30, 40, 64, 75-83] For instance, Feng et al.[82] reported the synthesis of mesoporous ceria-zirconia-yttria and zirconia-yttria using metal nitrates as oxide precursors, instead of costly alkoxides, and cetyltrimethylammonium bromide (CTAB) as the structure directing agent, but the resulting oxides showed no long range order. In a similar effort, Terribile et al.[83] used both cerium and zirconyl chlorides as precursors and CTAB as the template, but they were also unsuccessful in creating ordered CZ mesostructures.

In a more successful study, Zhao et al.[84] prepared three-dimensionally ordered macroporous (3-DOM) yttria-stabilized zirconia (YSZ) via an aqueous organic gel method, using the interstitial spaces between polystyrene spheres assembled on glass substrates as the structure directing agent. However, this study was never expanded to

include the synthesis of ordered mesoporous materials. Mesoporous ceria-zirconia was also obtained by Desphande and Niederberger[85] using nitrate precursor salts and a nanocasting approach with polymeric beads as the structure directing agent, but again, no ordered oxide structure was formed.

Even though numerous articles reported a variety of synthesis approaches for silica and non-silica based mesoporous materials including the individual ceria, zirconia and yttria oxides, limited publications have reported methodologies for preparing mesoporous CZY materials using all three oxide materials. Prior work at Clemson University[86] showed the synthesis of CZY mixed oxides with good physical properties (e.g., high surface area, homogeneous oxide incorporation, crystalline uniformity, and thermal stability) by sol-gel and exotemplating approaches. For these studies, metal nitrate precursors and a variety of templates (e.g., CTAB, amine functionalized dendrimers, porous activated carbons, etc.) were used, but the resulting CZY materials did not exhibit any long range order.

Evaporation-induced self-assembly

Traditional sol-gel methods have been unsuccessful in creating either single or mixed ceria, zirconia and yttria oxides with an ordered mesostructure. More recently, studies abandoning classical sol-gel methods have successfully shown that ordered mesoporous zirconia and related materials can be prepared using the evaporation induced self-assembly (EISA) process.[87, 88]

Self-assembly refers to the spontaneous organization of materials through non-covalent interactions with no external intermediation.[88] With the EISA process, the self-

assembly of oxide precursors is driven by the evaporation of solvent molecules from a metal precursor containing organic solvent solution and the absorption of a hydrolyzing agent (water) from the vapor phase. As the hydrolyzing agent (water) slowly enters the organic metal-rich phase, metal oxide oligomers form, diffuse, and assemble around template materials included in the starting organic phase mixture. Following a further loss of organic solvent and the addition of sufficient water, a final inorganic oxide phase is formed around the template, often yielding a thin film exhibiting a long-range mesoporous architecture.

Successful attempts to prepare ordered mesoporous transition metal oxides have also been reported for the EISA technique. For instance, Hung et al.[79, 80] reported the synthesis of ordered yttria-zirconia mesoporous structures using chloride precursors for zirconia and yttria along with evaporation induced self-assembly (EISA) synthesis at 40° C for 3 days controlling the relative humidity at 40%. Similarly, Yuan et al.[75, 76] reported the successful synthesis of ordered zirconia based functional materials by EISA.

EISA methods were also combined with a novel type of amphiphilic block copolymer template by Brezesinski et al.[64] to yield mesostructured thin films of ceria, zirconia and ceria-zirconia mixed oxides having highly crystalline pore walls and ordered arrays of mesopores. Despite these developments, EISA has to-date not been used to synthesize a highly-ordered porous oxide containing a homogeneous mixture of ceria, zirconia, and yttria oxides.

Since it has been hypothesized that an ordered mesoporous CZY arrangement has advantages when it comes to catalytic performance, EISA was used in this thesis as a way to synthesize these ordered materials with interesting results as shown in Chapter 4.

Diffusion studies for porous materials

The measurement of diffusion parameters in porous solids is very important in catalysis. Specifically, its importance becomes more relevant when studying mass transfer restrictions in heterogeneous catalysts that usually employ materials with specific porosity. In general, catalyst and catalyst supports are considered to have certain simplified geometries which are in some cases very far from reality, therefore an empirical approach is necessary to understand gas behavior inside these materials and explain how overall particle morphology effects catalytic material.

For the specific case of diffusion studies for CZY mesoporous catalyst support materials with different pore geometries and arrangements, this experimental work can help explain which CZY oxide synthesis technique is better for a specified catalytic converter application. For example, supports with higher diffusion capabilities are hypothesized to be advantageous as they allow faster and easier contact between reactants and the catalyst.

Basics of gas diffusion in porous materials (from Bruce[89])

The application of porous solids as adsorbents, catalysts and membranes has sparked an increase in research efforts focused on understanding the diffusion of molecules through these materials. This is of primary importance in analyzing the factors limiting their performance.

One of the most basic and important concepts is *Fick's law*. Fick recognized similarities between Fourier's Law of thermal conduction and diffusion phenomena. He defined the diffusion coefficient and showed that mass flux in a stagnant system equaled

the product of this coefficient and the concentration gradient for the species undergoing diffusion. The molar form of Fick's Law is:

$$J_i^* = -\mathcal{D}_{ij} C_T \frac{dx_i}{dz} = -\mathcal{D}_{ij} \frac{dC_i}{dz} \qquad \text{(2-i)}$$

Equation 2-i states that the molar flux of species *i* in the z-direction relative to the molar average system velocity (J_i^*) equals the negative of the diffusion coefficient ($\mathcal{D}_{ij}$) times the product of the total concentration of the system and the mole fraction (x_i) gradient for species *i* in the z-direction.

Diffusion in small pores was studied by Martin Knudsen.[90] Using concepts from the kinetic theory of gases, he showed that gases flowing in small diameter tubes have diffusion coefficients that are independent of pressure and vary linearly with the tube diameter and average molecular velocity of the diffusing gas:

$$\mathcal{D}_{K,A} = \frac{d_{pore}}{3}\left(u_A^*\right) \qquad \text{(2-ii)}$$

where $\mathcal{D}_{K,A}$ is the gas diffusivity in the tube (m^2/s), d_{pore} is the average tube/pore diameter (m), and u_A^* is the average molecular (or molar) velocity for component *A* (m/s).

For porous materials, there are three basic modes of gas diffusion as consequent of their Knudsen number ($N_{Kn} = \frac{\lambda}{d_{pore}}$, where λ is the mean free path length for the gas and d_{pore} is the pore diameter): *Fickian diffusion*, *Knudsen diffusion* and *combined Fickian-Knudsen diffusion*.

Fickian diffusion refers to the diffusion behavior observed when the normal mean free path length of the gas (λ) is smaller than the diameter of the pore so gas-gas

collisions are more probable. On the other hand, Knudsen diffusion refers to diffusion behavior observed when a gas molecule diffuses through a pore or tube whose diameter is smaller than λ for the gas. In this case, the probability of gas-wall collisions is of similar magnitude or greater than the probability of gas-gas collisions. These frequent collisions with the tube wall tend to decrease the rate of molecular transport through the tube or pore. These behaviors are depicted in Figure 2.4.

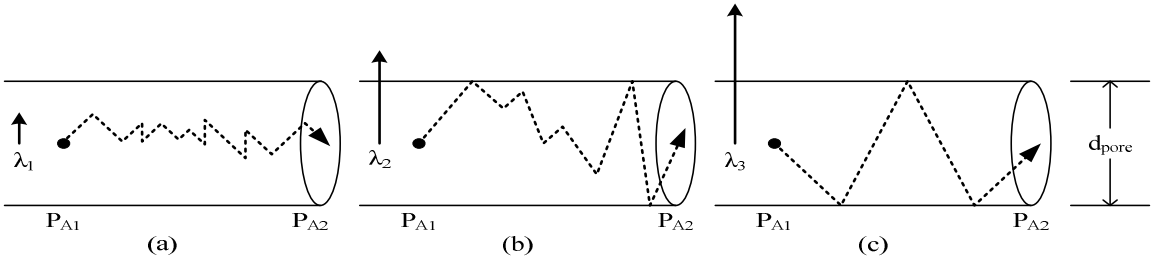

Figure 2.4. Modes of gas diffusion: (a) Fickian, $N_{Kn} < 1$; (b) combined Fickian and Knudsen, $N_{Kn} \approx 1$; and (c) Knudsen, $N_{Kn} >> 1$

In general, Knudsen diffusion is only important in materials having pore diameters from 1 – 50 nm (as is the case with mesoporous materials) and a Knudsen number (N_{Kn}) that is much greater than one. Additionally, from the kinetic theory of gases, the mean free path of a gas molecule can be calculated using the equation:

$$\lambda_A = \frac{\kappa_B T}{2^{1/2} \pi \sigma_A^2 P} \qquad \text{(2-iii)}$$

where κ_B is Boltzmann's constant, T is temperature (K), P is pressure (atm), and σ_A is the molecular diameter of gas molecule *A*.

For the case of mesoporous materials, equimolar counter diffusion (flux of A = flux of B in the opposite direction, $N_A = -N_B$) is occurring in each pore during the transition

from one gas to another in the feed stream. The pore diffusion for gases in these materials is best described by Knudsen diffusion:

$$\mathcal{D}_{K,A} = \frac{d_{pore}}{3}\left(\frac{8RT}{\pi \mathcal{M}_A}\right)^{1/2} = 48.50 \cdot d_{pore}\left(\frac{T}{\mathcal{M}_A}\right)^{1/2} \qquad \text{(2-iv)}$$

where $\mathcal{D}_{K,A}$ is the gas diffusivity in the pore (m^2/s), d_{pore} is the average pore diameter (m), T is absolute temperature (K), and $\mathcal{M}_A$ is the molecular weight of gas A (g/mol).

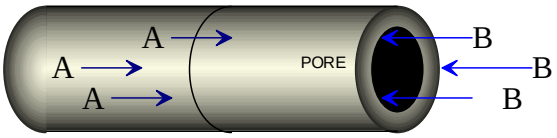

Figure 2.5. Equimolar counter-diffusion of gases A and B in a cylindrical pore.

These basic concepts are of great importance in the evaluation of diffusion in porous solids and will be used throughout this dissertation.

Techniques to study gas diffusion in porous media

The diffusion measuring techniques for porous solids may be classified as equilibrium techniques and non-equilibrium techniques[91] with respect to the thermodynamic regime and as microscopic and macroscopic with respect to the relevant diffusion paths.

Macroscopic diffusion techniques refer to measurements where the diffusion paths traversed by the molecules of interest during the experiment are typically much larger than the individual crystallites. Macroscopic measurements are further sub-divided in to steady-state and unsteady-state experiments. Steady-state macroscopic techniques directly study the diffusion rates of molecules through a sample. In contrast, unsteady-

state experiments measure concentration as a function of time at a given point. Some advantages of macroscopic techniques include less expensive techniques, lower cost measuring devices and less cumbersome procedures.

On the other hand, microscopic techniques refer to measuring techniques capable of monitoring molecular displacements or the evolution of molecular concentration profiles over physical dimensions smaller than the crystallite diameters. An example is pulsed field gradient nuclear magnetic resonance (PFG-NMR), which have often yielded diffusion rates vastly different than those values previously measured using macroscopic methods.[91] These inconsistencies question the reliability of macroscopic methods since they reflected kinetic limitations due to heat transfer, external film resistances, bed effects and surface barriers.[92] However, numerous researchers have concluded that macroscopic measurements can be reliable if all considerations of the earlier difficulties are ensured.

Table 2.1 shows an extended summary of the most common diffusion measuring techniques for porous solids showing advantages and disadvantages for each technique.[91-101]

Table 2.1**.** Comparison Chart of Diffusion Techniques for Porous Solids

TECHNIQUE	ADVANTAGES	DISADVANTAGES
Classical steady state techniques	✓Relatively easy to use	✓Necessity to monitor composition of the two outlet streams (analytical instruments are required) ✓Necessity of equal pressure in both compartments of diffusion cell ✓Ignores dead end pores because it measures diffusion *through* the pellet ✓Cannot be readily adapted to temperatures much exceeding ambient ✓Difficulties for certain types of materials, for which it is difficult to prepare a sample of suitable thickness. ✓Diffusion coefficients are not always accurate due to kinetic limitations.
Classical unsteady state techniques	✓Do not need to wait any time before doing measurements ✓Relatively easy to set up	✓Interchange time is usually too short to obtain accurate results ✓Diffusion coefficients are not always accurate due to kinetic limitations. ✓Not easily applied to some systems (especially low molecular weight gases). ✓This method is unable to distinguish between different types of molecules. ✓Some techniques like the TAP method require high vacuum or a very careful pressure control (piezometric method)
Time Lag Method	✓Simple experiment ✓Mathematical treatment of data is straightforward ✓Transport parameters can be directly obtained from experimental data ✓Great flexibility, favorable for a wide range of applications	✓Diffusion coefficients are not always accurate due to kinetic limitations. ✓Requires careful construction of the membrane in order for it to yield consistent data ✓Strict vacuum is required for the experiment.

Table 2.1 cont.

Frequency response technique	✓All the necessary diffusion and adsorption data are obtained in the frequency-response experiments ✓It is not necessary to assume adsorption-desorption equilibrium	✓Complicated test method ✓Involved procedures to interpret the data
Methods based on Gas Chromatography: IGC and RF-IGC	✓Possible to use in experimental conditions such as high temperatures ✓Can be used without any perturbation of the system. ✓Versatile tool for the characterization of porous materials properties ✓True surface analysis method ✓Provide great variety of information offering means for a lot of adsorption and catalytic studies. (Even more information in the case of RF-IGC) ✓RF-IGC accounts for mass transfer and desorption phenomena and is not influenced by the carrier gas flow and it has not to account the sorption effect as well ✓RF-IGC makes possible to study in detail the mechanism of a heterogeneous surface reaction. ✓RF-IGC accounts not only the adsorbate-adsorbent interaction, but also the adsorbate-adsorbate interaction.	✓IGC measurements have been performed as pulse measurements which only provide desorption information ✓IGC high concentration pulse measurements can be difficult in some cases due to kinetic problems.
NMR Techniques	✓No concentration gradients or labeling of the diffusing species are required ✓PFR NMR method is able to record the mean length of the diffusion paths of the adsorbed molecules ✓Versatile for both macroscopic and microscopic observation ✓Noninvasive technique ✓Can be used as an efficient tool for determining tortuosity factors ✓Direct measurement of the coefficients of intracrystalline and intraparticle diffusion ✓PFR-NMR information available for mesoporous materials	✓The application of PFG NMR is subject to a number of prerequisites which prohibit its application as a routine technique to any arbitrary system

Table 2.1 cont.

Quasi-elastic neutron scattering	✓Higher sensitivity towards small molecular displacements ✓Length scale of measurement extended to several nanometers	✓Complicated ✓Specialized research facility is required to do the experiment. ✓Expensive resource, usually this is the technique of last resort.
Interference Microscopy	✓Capable of monitoring transient intracrystalline concentration profiles ✓Resolution of micrometers and seconds	✓Does not allow a distinction between the various components involved in chemical reactions
IR Spectroscopy and IR Microscopy	✓Allows a distinction between the various components involved in chemical reactions. ✓Transient intracrystalline concentration profiles can be monitored.	
Isotopic Labeling	✓Potential to separate the contributions of diffusion and adsorption ✓The majority of apparent diffusivities obtained with this method are in the same order as transport diffusivities obtained from uptake and chromatography measurements.	✓Apparent diffusivities are obtained
Positron Emission Profiling (PEP) and Tracer-Exchange PEP	✓Due to the high penetrating power of the gamma rays, in situ measurements can be performed on ordinary laboratory-scale reactors at normal reaction conditions ✓One has the possibility of only labeling one component in a mixture, thus making it possible to study only this component or doing a multicomponent analysis. ✓The advantage of using tracer-exchange experiments over using transient experiments is that one is assured that the entire experiment is performed under steady-state conditions so that true self diffusion constants are measured. ✓Can be used at elevated temperatures	✓Experimentally complex

Among macroscopic approaches, a method called Zero-Length Column (ZLC) has proven to be quite successful at measuring diffusivities in microporous and mesoporous materials, while taking into consideration the difficulties mentioned earlier. It minimizes the effects of axial dispersion, heat transfer and external mass transfer resistance on the pore diffusion kinetics. The following section provides a brief overview of the ZLC method, which was used to determine gas diffusivity values for several CZY mesoporous oxide structures synthesized by our group. These materials are analyzed and compared in Chapter 6 of this thesis.

ZLC Method: Background and Theory

Eic and Ruthven[102] developed the ZLC technique in 1988 to directly measure transport diffusivities in porous adsorbent particles. The method has been widely used during the last two decades to study diffusion in microporous to macroporous systems for a wide variety of gases and even liquids. It was originally developed as a simple and versatile way of measuring intracrystalline or intraparticle diffusion in zeolite based adsorbents.[103]

The technique is relatively simple and consists of following the desorption of a gas through a previously equilibrated sample. The adsorbate concentration is very low and the carrier flow rate during desorption is sufficiently high to enable the measurement of kinetic behavior instead of equilibrium behavior. A very small quantity of sample contained between two sintered discs is used to eliminate mass and heat transfer effects. This last characteristic is the reason for the name zero-length column as the sample cell has almost no height. The relevant parameters are extracted using the long-time

asymptote of the desorption curve[102], a short-time approximate method[104], or an intermediate time analysis technique[105-107].

The basic aspects and advantages of this technique are shown in Table 2.2.

Table 2.2. Basics of the Zero-Length Column Method

Basics	**Advantage**
Develop a desorption curve for a previously equilibrated sample to obtain a curve of fractional desorption versus time	Simple set up
Use large or small crystals, low adsorbate concentrations and very small adsorbent sample amount as well as high carrier gas flow rate during desorption	Eliminate intrusion of extraneous heat and mass transfer resistances
Conditions are normally adjusted so as to work within the Henry's Law region	Not a restriction
Use long, short or intermediate-time analysis techniques to get diffusivities.	Proven effective for diffusion in mesoporous materials

A tabulated review of the literature published for ZLC systems for micro and mesoporous materials is shown in Appendix B.

Experimental set-up

A general schematic of the ZLC apparatus used in this thesis is shown below. Additional details and schematics for the system are shown and discussed in Chapter 6. Pictures of the complete Clemson ZLC system, as set up by our group for this method, is presented in Appendix C.

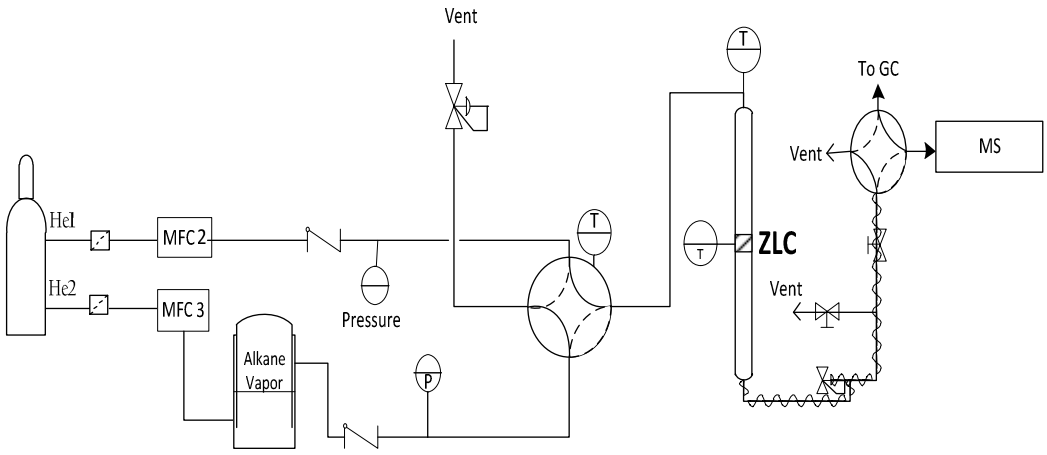

Figure 2.6. Schematic of ZLC apparatus. Additional apparatus images are shown in Appendix C and Chapter 6.

The ZLC experiments consist of 6 basic steps:

i. 1-5 mg of sample (catalyst) are loaded between two sintered discs inside the diffusion chamber. Small quantities prevent heat and mass transfer effects.

ii. Samples are activated/dried overnight at high temperatures (> 200 °C).

iii. The sorbate used is adjusted and maintained at low concentrations in the carrier gas stream. This maintains the experiments in the linear region of the adsorption isotherm or Henry's law region.

iv. The samples are equilibrated with the diluted sorbate for at least 1-2 hours.

v. Desorption is performed using a pure carrier gas at a high flow rate to minimize mass and heat resistances on the sample surface.

vi. Desorption curves are analyzed using the appropriate method.

Data Analysis

Response curves are normalized with respect to the initial concentration; therefore, calibration of the detector is not required. The following equation is used to normalize the response:

$$\frac{c(t)}{c_0} = \frac{\sigma(t) - \sigma_{\text{inf}}}{\sigma_0 - \sigma_{\text{inf}}} \qquad \text{(v)}$$

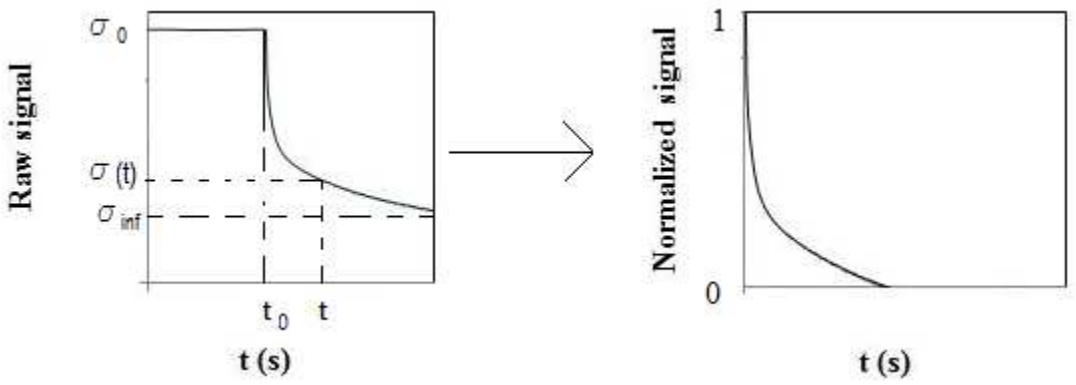

Figure 2.7. Qualitative Raw ZLC response and its corresponding normalized response curve.

The normalized response curves are analyzed using a mathematical model derived from the fluid-phase mass balance in radial coordinates for the sample material and the mass transfer equation through spherical particles (due to model assumptions described below, adsorbent particles are assumed to be spherical).

Mathematical Model

The basics of the ZLC model are derived from Fick's second law of diffusion, which describes the mass balance through the solid phase via diffusion. Mass transfer also

occurs via the constant flow through the reactor bed.[108] The main equations for the system are shown below.

Fluid phase mass balance

$$V_S \frac{dq}{dt} + V_f \frac{dc}{dt} + F \cdot c(t) = 0 \qquad \text{(2-vi)}$$

Solid phase mass balance

$$\frac{dq}{dt} = D\left(\frac{\partial^2 q}{\partial r^2} + \frac{2}{r}\frac{\partial q}{\partial r}\right) \qquad \text{(2-vii)}$$

where V_s is the volume of the solid phase, q is the concentration of the adsorbed-phase, F the fluid flow rate, c is the concentration of sorbates in the fluid-phase, D the effective diffusion constant and r the radial coordinate.

Both mass balance equations (2-vi) and (2-vii) need to be solved simultaneously using the initial and boundary conditions below. A detailed derivation can be found in Appendix D.

Initial conditions

$$q(r,0) = q_o = Kc_0; c(0) = c_0$$

Boundary conditions

$$\left(\frac{\partial q}{\partial r}\right)_{r=0} = 0; q(R,t) = Kc(t)$$

where K is the Henry's law constant.

For convenience I present the basic outline of the mathematical approach as described by Qiao and Bhatia.[109] The model is based on four assumptions:

- The fluid phase accumulation term in the particles is small compared to that in the adsorbed phase. Therefore, it is neglected in the fluid phase mass balance.
- The adsorbent particles are spherical, and adsorption equilibrium is attained at the particle surface, while satisfying Henry's law.
- The flow rate of the carrier gas stream is sufficiently high, so as to eliminate the intrusion of heat and external mass transfer resistances.
- The temperature of the adsorption column is considered to be constant.

Using the assumptions mentioned, the adsorptive mass balance equation in the fluid phase and the adsorptive mass balance for a spherical adsorbent particle are solved using their respective initial and boundary conditions. This system yields the solution:

$$\frac{C}{C_o} = 2L \sum_{n=1}^{\infty} \frac{\exp\left(-\frac{\beta_n{}^2 Dt}{R^2}\right)}{\beta_n^2 + L(L-1)} \tag{2-viii}$$

where *c* is the gas-phase concentration of adsorbate, *D* is the intra-particle diffusivity, *t* is time, *R* is the particle radius and *L* is a dimensionless factor. The β or eigenvalues are given by the roots:

$$\beta_n cot\beta_n + L = 1 \tag{2-ix}$$

with

$$L = \frac{1}{3} \frac{F}{KV_s} \frac{R^2}{D} \tag{2-x}$$

and

$$V_s = \frac{m_s}{\rho_s} = \frac{m_s}{\rho(1-\varepsilon_p)} \tag{2-xi}$$

where F is the gas volumetric flow rate, V_s is the volume of the solid phase, ρ is the pore wall density, ρ_s is the particle density and ε_p is the particle porosity.

Equations viii - xi are used to fit the experimental desorption curves using two different methods to obtain the best fitting parameters for D/R^2 and L. The implementation of these techniques will be shown in Chapter 6.

Applications to mesoporous materials

In the last 10 years, mesoporous materials diffusion properties have been studied by different groups using the ZLC method.[107-112] Qiao and Bathia[109, 110] have studied the diffusion of linear paraffins in MCM-41 finding diffusivities using a non-linear square method that uses the full-time range desorption curve. Similarly, Gobin[108] found the diffusion behavior of different gases in SBA-16 materials finding pore diffusivities around $1x10^{-9}$ cm^2/s. Similar work for systems of mesoporous materials and different gases were done by Huang et al.[111], Malekian et al.[107], Mejonge et al.[112], among others.

Limited studies have been published on the effect of CZY pore morphology in catalysts operation. The ZLC method can be useful in measuring diffusion effects related to pore morphology.

Summary

This chapter has presented a detailed overview of the concepts, fundamentals and previous work in the area of mesoporous materials, CZY applications, synthesis of silica and non-silica based mesoporous materials and diffusion in porous solids. These concepts will be of importance throughout the dissertation.

References

(1) Bhaumik, A.; Tatsumi, T. *J. Catal.* 2000, *189*, 31-39.

(2) Aprile, C.; Abad, A.; Garcia, H.; Corma, A. J. *J. Mater. Chem.* 2005, *15*, 4408-4413.

(3) Fujiwara, M.; Terashima, S.; Endo, Y.; Shiokawa, K.; Ohue, H. *Chem. Comm.* 2006, , 4635-4637.

(4) Chandra, D.; Laha, S. C.; Bhaumik, A. *Appl. Catal. , A: Gen.* 2008, *342*, 29-34.

(5) Yoshitake, H.; Yokoi, T.; Tatsumi, T. *Chem. Mater.* 2003, *15*, 1713-1721.

(6) Gierszal, K. P.; Jaroniec, M. *J. Phys. Chem. C* 2007, *111*, 9742-9748.

(7) Sathe, T. R.; Agrawal, A.; Nie, S. *Anal. Chem.* 2006, *78*, 5627-5632.

(8) Fan, R.; Huh, S.; Yan, R.; Arnold, J.; Yang, P. *Nat. Mater.* 2008, *7*, 303-307.

(9) Vallet-Regı, M. *Chem. Eur. J.* 2006, *12*, 5634-5643.

(10) Yang, P.; Quan, Z.; Li, C.; Lian, H.; Huang, S.; Lin J. *Microporous Mesoporous Mater.* 2008, *116*, 524-531.

(11) Beck, J. S.; Vartuli, J. C.; Roth, W. J.; Leonowicz, M. E.; Kresge, C. T.; Schmitt, K. D.; Chu, C. T. W.; Olson, D. H.; Sheppard, E. W.; McCullen, S. B.; Higgins, J. B.; Schlenker, J. L. *J Amer Chem Soc* 1992, *114*, 10834-10843.

(12) Mogensen, M.; Sammes, N. M.; Tompsett, G. A. *Solid State Ionics* 2000, *129*, 63-94.

(13) Lyons, D. M.; Ryan, K. M.; Morris, M. A. *J. Mater. Chem.* 2002, *12*, 1207-1212.

(14) Piconi, C.; Maccauro, D. *Biomaterials* 1999, *20*, 1-25.

(15) Nielsen, R. In *Zirconium and Zirconium Compounds;* Ullmann's Encyclopedia of Industrial Chemistry; Wiley-VCH Verlag GmbH & Co. KGaA: 2000; .

(16) Jaenicke, S.; Chuah, G.; Raju, V.; Nie, V. *Cat Surv Asia* 2008, , 153-169.

(17) Yuan, Q.; Li, L.; Lu, S.; Duan, H.; Li, Z.; Zhu, Y.; Yan, C. *J Phys. Chem. C* 2009, *113*, 4117-4124.

(18) Badwall, S. P. S. *Appl. Phys. A: Mater. Sci. Process* 1990, *50*, 449.

(19) Garvie, R. C.; Hannik, R. H.; Pascoe, R. T. *Nature* 1975, *258*, 703.

(20) Murase, Y.; Kato, E. *J. Am. Ceram. Soc.* 1982, *66*, 196.

(21) Phillips, J. M. *J. Appl. Phys.* 1996, *79*, 1829.

(22) Leon, C.; Lucia; M.L.; Santamaria, A. *J. Phys. Chem. B* 1997, *55*, 882.

(23) Masour, N.; Mansour, K.; Stryland, E. W. E.; Soileau, M. J. *J. Appl. Phys.* 1990, *67*.

(24) Wilk, G. D.; Wallca, R. M.; Anthony, J. M. *J. Appl. Phys.* 2001, *89*, 5243.

(25) Affanasev, V. V.; Houssa, M.; Stesmans, A.; Heyns, M. M. *Appl. Phys. Lett.* 2001, *78*, 3073.

(26) Xu, Y.; Gu, Z.; Ching, W. Y. *Phys. Rev. B* 1997, *56*, 14993-15000.

(27) Micheli, A. L.; Dungan, D. F.; Mantese, J. V. *J Am Ceram Soc* 1992, *75*, 709-711.

(28) Mamak, M.; Coombs, N.; Ozin, G. *J. Am. Chem. Soc.* 2000, *122*, 8932-8939.

(29) Mamak, M.; Coombs, N.; Ozin, G. *Adv Mater* 2000, *12*, 198-202.

(30) Chen, F.; Liu, M. *J. Mater. Chem.* 2000, *10*, 2603-2605.

(31) Wang, Y.; Yin, L.; Palchik, Y.; Hacohen, Y.; Kotypin, A.; Gedaken, A. *Langmuir* 2001, *17*, 4131-4133.

(32) He, H.; Dai, H.; Ng, K.; Wong, W.; Au, T. *J. Catal.* 2002, *206*, 1-13.

(33) Ho, C.; Yu, Y.; Wang, X.; Lai, S. Y.; Qui, Y. F. *J. Mater. Chem.* 2005, *15*, 2193-2201.

(34) Chen, L. F.; Gonzalez, J. A.; Wang, L. E.; Norena, A.; Toledo, S.; Castillo, M.; Moran-Pineda, M. *Appl. Surf. Sci* 2005, *243*, 319-328.

(35) Sideris, M. In *Methods for Monitoring and Diagnosing the Efficiency of Catalytic Converters: A Patent-oriented Survey;* Elsevier Science: 1998; , pp 447.

(36) United States Environmental Protection Agency Emissions Standards Reference Guide. http://www.epa.gov/otaq/standards/light-duty/ld-cff.htm (accessed 06/20, 2013).

(37) Lachman, I.; Bagley, R.; Lewis, R. Ceramic Bulletin 1981, 60, 202-205.

(38) Sugiura, M. Catalysis Surveys from Asia 2003, 7, 77-87.

(39) Motavalli, J. The 20-Year Fight to Get the Lead Out. Why didn't cars have smog-killing catalytic converters in 1955? http://www.thedailygreen.com/living-green/blogs/cars-transportation/lead-gasoline-catalytic-converters-pollution-461219 (accessed 05/17, 2013).

(40) Deshpande, A. S.; Pinna, N.; Beato, P.; Antonietti, M.; Niederberger, M. Chemistry of Materials 2004, *16*, 2599-2604.

(41) Putna, E. S.; Bunluesin, T.; Fan, X. L.; Gorte, R. J.; Vohs, J. M.; Lakis, R. E.; Egami, T. *Catalysis Today* 1999, *50*, 343-352.

(42) Kašpar, J.; Fornasiero, P.; Graziani, M. *Catalysis Today* 1999, *50*, 285-298.

(43) Nunan, J. G.; Robota, H. J.; Cohn, M. J.; Bradley, S. A. *Journal of Catalysis* 1992, *133*, 309-324.

(44) Jen, H. -.; Graham, G. W.; Chun, W.; McCabe, R. W.; Cuif, J. -.; Deutsch, S. E.; Touret, O. *Catalysis Today* 1999, *50*, 309-328.

(45) Ohata, T.; Tsuchitani, K.; Kitaguchi, S. European Patent Patent EP0337809, 1989.

(46) Tanaka, H.; Yamamoto, M. *SAE Technical Papers* 1996, .

(47) Yamamoto, M.; Tanaka, H. *SAE Technical Papers* 1998, *1353*, 1.

(48) Taguchi, A.; Schüth, F. *Microporous and Mesoporous Materials* 2005, *77*, 1-45.

(49) Schuth, F. *Angew. Chem. Int. Ed.* 2003, *42*, 3604-3622.

(50) Pavasupree, S.; Suzuki, Y.; Pivsa-Art, S.; Yoshikawa, S. *Ceram. Int.* 2005, *31*, 959-963.

(51) Chen, L. F.; González, G.; Wang, J. A.; Noreña, L. E.; Toledo, A.; Castillo, S.; Morán-Pineda, M. *Appl. Surf. Sci.* 2005, *243*, 319-328.

(52) Chen, H.; Gu, J.; Shi, J.; Liu, Z.; Gao, J.; Ruan, M.; Yan, D. *Adv Mater* 2005, *17*, 2010-2014.

(53) Crepaldi, E. L.; Soler-Illia, G. J.; Bouchara, A.; Grosso, D.; Durand, D.; Sanchez, C. *Angew. Chem. Int. Ed.* 2003, *42*, 347-351.

(54) Larsen, G.; Lotero, E.; Marquez, M. *J. Mater. Res.* 2000, *15*, 1842-1842-1848.

(55) Knowles, J. A.; Hudson, M. J. *J. Chem. Soc. , Chem. Commun.* 1995, *20*, 2083-2084.

(56) Schwickardi, M.; Johann, T.; Schmidt, W.; Schuth, F. *Chem. Mater.* 2002, *14*, 3913-3919.

(57) Schwickardi, M.; Spliethoff, B.; Schmidt, W.; Schuth, F. *Z. Phys. Chem.* 2005, *219*, 939-948.

(58) Xu, L.; Shi, Z.; Feng, Y. *Microporous and Mesoporous Materials* 2007, *98*, 303-308.

(59) He, X.; Antonelli, D. *Angew. Chem. Int. Ed.* 2002, *41*, 214-214-229.

(60) Kresge, C. T.; Leonowicz, M. E.; Roth, W. J.; Vartuli, J. C.; Beck, J. S. *Nature* 1992, *359*, 710-712.

(61) Ciesla, U.; Schüth, F. *Microporous and Mesoporous Materials* 1999, *27*, 131-149.

(62) Schuth, F. *Chem. Mater.* 2001, *13*, 3184-3195.

(63) Brezesinski, T.; Smarsly, B.; Groenewolt, M.; Antonietti, M.; Grosso, D.; Boissière, C.; Sanchez, C. *N e w J . C h e m .* 2005, *Volume 156*, 243-248.

(64) Brezesinski, T.; Antonietti, M.; Groenewolt, M.; Pinna, N.; Smarsly, B. *New J. Chem.* 2005, *29*, 237-242.

(65) Li, X.; Chen, F.; Lu, X.; Ni, C.; Chen, Z. *Journal of rare earths* 2009, *27*, 943-947.

(66) Yang, P.; Zhao, D.; Margolese, D. I.; Chmelka, B. F.; Stucky, G. *Chem. Mater.* 1999, *11*, 2813-2826.

(67) Larsen, G.; Lotero, E.; Nabity, M.; Petkovic, L.; Shobe, D. *Journal of Catalysis* 1996, *164*, 246-248.

(68) Rezaei, M.; Alavi, S.; Sahebdelfar, S.; Xinmei, L.; Yan, Z. *J Mater Sci* 2007, *42*, 7086-7092.

(69) Blin, J. L.; Flamant, R.; Su, B. L. *International Journal of Inorganic Materials* 2001, *3*, 959-959-972.

(70) Kim, A.; Bruinsma, P.; Chen, Y.; Wang, L.; Liu, J. *Chem. Commun.* 1997, , 161-161-162.

(71) Ni, C.; Li, X.; Chen, Z.; Li, H. H.; Jia, X.; Shah, I.; Xiao, J. Q. *Microporous and Mesoporous Materials* 2008, *115*, 247-252.

(72) Chen, H.; Yan, J.; Ye, Z.; Zhang, L.; Gao, J.; Shi, J.; Yan, D. *J Mater Sci* 2009, *44*, 6531-6531-6537.

(73) Yuan, Z.; Vantomme, A.; Léonard, A.; Su, B. *Chem. Commun.* 2003, , 1558-1559.

(74) Ciesla, U.; Froba, M.; Stucky, G.; Schuth, F. *Chemistry of Materials* 1999, *11*, 227-234.

(75) Yuan, Q.; Li, L.; Lu, S.; Duan, H.; Li, Z.; Zhu, Y.; Yan, C. *The Journal of Physical Chemistry C* 2009, *113*, 4117-4124.

(76) Yuan, Q.; Liu, Q.; Song, W.; Feng, W.; Pu, W.; Sun, L.; Zhang, W.; Yan, C. *J. Am. Chem. Soc.* 2007, *129*, 6698-6699.

(77) Li, H.; Zhang, L.; Dai, H.; He, H. *Inorg. Chem.* 2009, *48*, 4421-4434.

(78) Teng, M.; Luo, L.; Yang, X. *Microporous and Mesoporous Materials* 2009, *119*, 158-164.

(79) Hung, M.; Fung, K.; Hung, D.; Hon, M. *Journal of the European Ceramic Society* 2008, *28*, 1161-1161-1167.

(80) Hung, M.; Hung, D.; Fung, K.; Hon, M. *Materials Letters* 2008, *62*, 1147-1147-1150.

(81) Hung, M.; Hung, D.; Fung, K.; Hon, M. *Journal of the European Ceramic Society* 2006, *26*, 2627-2632.

(82) Feng, R.; Yang, X.; Ji, W.; Aua, C. *Materials Chemistry and Physics* 2008, *107*, 132-132-136.

(83) Terribile, D.; Trovarellia, A.; Llorcab, J.; Leitenburga, C.; Dolcetti, G. *Catalysis Today* 1998, *43*, 79-88.

(84) Zhao, J. P.; Li, Y.; Xin, W. H.; Li, X. *Journal of Solid State Chemistry* 2008, *181*, 239-244.

(85) Deshpande, A.; Niederberger, M. *Microporous and Mesoporous Materials* 2007, *101*, 413-418.

(86) Anyaba, P. N. Novel techniques for the synthesis of three-way catalytic converter support materials, Clemson University, 2009.

(87) Grosso, D.; Cagnol, F.; Soler-Illia, G. J. d. A. A.; Crepaldi, E. L.; Amenitsch, H.; Brunet-Bruneau, A.; Bourgeois, A.; Sanchez, C. *Adv. Functional Mater.* 2004, *14*, 309-322.

(88) Brinker, C. J.; Lu, Y.; Sellinger, A.; Fan, H. *Adv Mater* 1999, *11*, 579-585.

(89) Bruce, D. A. *Mass Transfer Material Class ChE 403. Clemson University* 2011.

(90) Knudsen, M. *Annalen der Physik* 1909, *28*, 75-130.

(91) Kärger, J.; Vasenkov, S. *Microporous and Mesoporous Materials* 2005, *85*, 195-206.

(92) Brandani, S. *Diffusion Fundamentals* 2007, *6*, 4.1-4.10.

(93) Katsanos, N. A.; Thede, R.; Roubani-Kalantzopoulou, F. *Journal of Chromatography A* 1998, *795*, 133-184.

(94) Reyes, S. C.; Sinfelt, J. H.; DeMartin, G. J. *J. Phys. Chem. B* 2000, , 5750-104, 5750-5761.

(95) Villet, R.; Wilhelm, R. *Industrial & Engineering Chemistry* 1961, *53*, 837-840.

(96) Deisler, P. F.; Wilhelm, R. H. *Industrial & Engineering Chemistry* 1953, *45*, 1219-1227.

(97) Stallmach, F.; Gräser, A.; Kärger, J.; Krause, C.; Jeschke, M.; Oberhagemann, U.; Spange, S. *Microporous and Mesoporous Materials* 2001, *44-45*, 745-753.

(98) Rutherford, W.; Do, D. *Adsoption* 1997, *3*, 283-283-312.

(99) Bowen, T. C.; Wyss, J. C.; Noble, R. D.; Falconer, J. L. *Microporous and Mesoporous Materials* 2004, *71*, 199-210.

(100) Karaiskakis, G.; Gavril, D. *Journal of Chromatography A* 2004, *1037*, 147-189.

(101) Satterfield, C. In *Mass Transfer in Heterogeneous Catalysis;* M.I.T. Press: Cambridge, Massachusetts, 1970; , pp 267 pp.

(102) Eic, M.; Ruthven, D. M. *Zeolites* 1988, *8*, 40-45.

(103) Ruthven, D.; Brandani, S. *Recent Advances in Gas Separation by Microporous Ceramic Membranes* 2000, *6*, 187-.

(104) Hufton, J. R.; Ruthven, D. M. *Ind Eng Chem Res* 1993, *32*, 2379-2386.

(105) Brandani, S.; Ruthven, D. *Adsorption* 1996, *2*, 133-143.

(106) Vidoni, A. Adsorption and diffusion of light hydrocarbons in DDR zeolite, The University of Maine, Maine, 2011.

(107) Malekian, A.; Vinh-Thang, H.; Huang, Q.; EiC, M.; Kaliaguine, S. *Ind Eng Chem Res* 2007, *46*, 5067-5073.

(108) Gobin, O. SBA 16 Materials: synthesis, diffusion and sorption properties, Laval University, Quebec, Canada, 2006.

(109) Qiao, S. Z.; Bhatia, S. K. *Microporous and Mesoporous Materials* 2005, *86*, 112-123.

(110) Qiao, S. Z.; Bhatia, S. K. *Ind Eng Chem Res* 2005, *44*, 6477-6484.

(111) Huang, Q.; Eic, M.; Xiao, H.; Kaliaguine, S. *Adsorption* 2010, *16*, 531-539.

(112) Menjoge, A. R.; Huang, Q.; Nohair, B.; Eic, M.; Shen, W.; Che, R.; Kaliaguine, S.; Vasenkov, S. *J. Phys. Chem. C* 2010, *114*, 16298-16308.

CHAPTER THREE

BLOCK COPOLYMER (BC) TEMPLATE ROUTE FOR THE SYNTHESIS OF CZY MATERIALS: EFFECT OF TYPE OF BC AND BC CONCENTRATION ON CZY PHYSICAL PROPERTIES

Introduction

The synthesis of mesoporous materials has been an area of significant relevance in the last decade. Since the discovery of the ordered mesoporous MCM-41[1] family of oxide materials, a series of novel mesoporous oxides have been synthesized starting with silica based mesostructures but quickly extending to other types of oxides. These mesoporous materials have high surface areas and large pore sizes, which makes them optimal supports for a variety of catalytic systems[2, 3] as reviewed in the last chapter.

Mesoscopic order is imparted typically by cooperative self-assembly of the inorganic and surfactant species interacting across their hydrophilic-hydrophobic interfaces. The inorganic species are then cross-linked to form dense, continuous metal oxide networks.[4] A great deal of effort has been devoted to control the morphology of these mesoporous materials. A variety of factors, such as type of precursors, solvent, temperature, aging, drying, stirring rates, template type, solution pH, and ratio of template to precursor have been investigated in detail.[5-12]

Despite the large number of studies examining synthesis parameter effects on final physical properties and morphology of mesoporous materials, it remains crucial to examine in detail the role of the template and template to precursor ratio on the final product. In this regard, limited work has been done on CZY mesoporous oxides. As

reviewed in the Chapter 2, CZY mesoporous oxides are of great importance in various fields. For this particular case, their application as catalyst supports for three-way catalysts in catalytic converters is our focus.

In the past, our group[13] has conducted successful efforts to synthesize CZY oxides with mesoporous structures using different templates. Block copolymers (BC), and in particular Pluronic P123, have proven to be some of the best templates for synthesizing mesoporous CZY materials as compared to other hard and soft templates like surfactants, porous carbons and resins.

Block copolymers are polymers that contain two or more homo-oligomer subunits that are covalently bonded together. For example, Pluronic P123 is a triblock copolymer of poly(ethylene) oxide and poly(propylene oxide) PEO-PPO-PEO [$((EO)_{20}(PO)_{70}(EO)_{20}$] This polymer is a "triblock copolymer" because it contains three different chemical blocks. It is also possible to make diblocks, tetrablocks, multiblocks, etc. Poly(ethylene oxide)-poly(propylene oxide)-poly(ethylene oxide) PEO-PPO-PEO block copolymers (available commercially as Pluronics or Polaxamers) are a very promising class of BCs for both material science and pharmaceutical applications.[14]

Block copolymers are interesting because they can "microphase separate" to form periodic nanostructures. Microphase separation is a situation similar to that of oil and water. Oil and water are immiscible - they phase separate. Due to incompatibility between the blocks, block copolymers undergo a similar phase separation. Because the blocks are covalently bonded to each other, they cannot demix macroscopically as water and oil. Thus, with "microphase separation", the blocks form nanometer-sized structures.

The microstructures resulting from the self-assembly of P123 block copolymer vary from micelles in solution to various types of liquid crystalline phases such as cubic, 3D-hexagonal, 2D-hexagonal and lamellar when the concentration of the polymer is increased.[14]

Depending on the relative lengths of each block, several block copolymer morphologies can be obtained as seen in Figure 3.1. By using blocks of dissimilar length, a hexagonally-packed-cylinder geometry can be obtained. Blocks of similar length tend to form layers (often called lamellae in the technical literature). Between the cylindrical and lamellar phase is the gyroid phase. The nanoscale structures created from block copolymers could potentially be used for creating devices for use in computer memory, nanoscale-templating and nanoscale separations.[15] This capacity to form nanostructures makes them highly useful in creating mesoporous materials with certain mesoscale arrangements of pores.

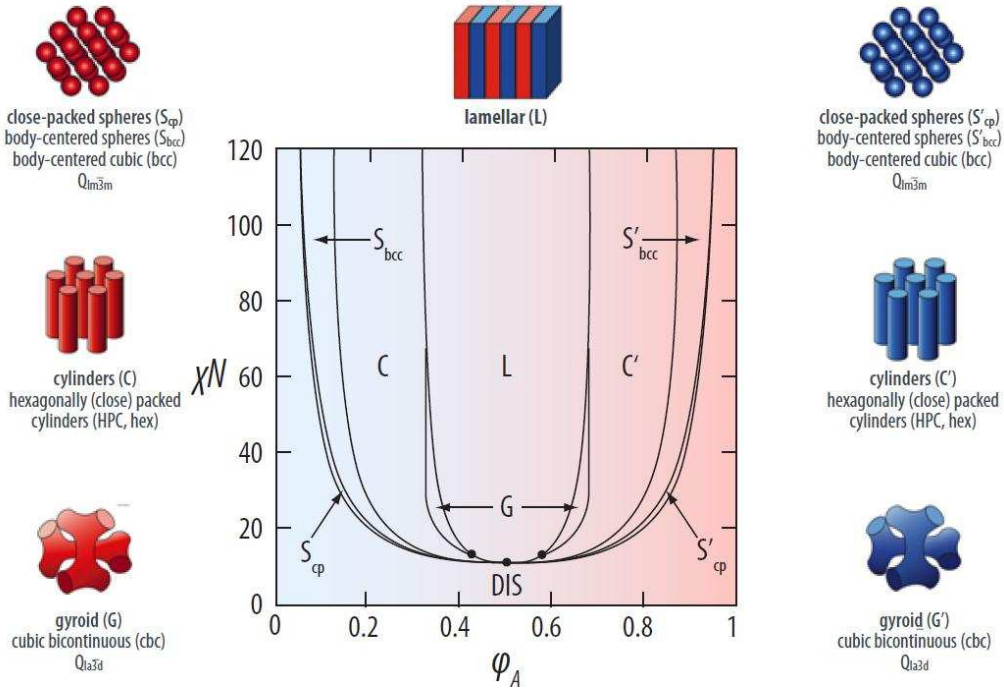

Figure 3.1.Theoretical AB diblock copolymer phase diagram (χN is the segment-segment interaction parameter and φ_A is the volume fraction of component A). Reprinted with permission from ref[16]. Copyright © Holger Frauenrath, 2000–2013.

Given their inherent ability to self-assemble, Pluronics, such as P123 and F127, have been used as templating agents for the design of highly organized oxide materials by sol-gel chemistry.[1, 17] The detailed review of BC templated mesoporous oxides by Soller-Illia[18] illustrates the great possibilities of this templating route, but stresses how the physical, chemical and processing parameters must be thoroughly controlled to reproducibly obtain mesoporous materials. Studies by Lelong et al.[19] on MCM-41 materials showed the effect of surfactant concentration on the morphology and texture of MCM-41 materials. They found that both, the external organization and internal pore structure, are governed by the silicate:surfactant ratio.

Similar work for silica monoliths[4] showed that the degree of microphase separation and the resulting mesostructure of bulk samples depended strongly upon the BC concentration, with higher concentrations producing higher degrees of order. However, it is well-known that silica structures have a very different chemistry than transition metal oxides.[20, 21] Thus far, a limited amount of work has been conducted on the BC templating of transition metal oxides mesostructures.[22-29] Still to the best of my knowledge, only CTAB templated synthesis of CZY materials has been reported.[30]

This work deals with the synthesis of mesoporous CZY materials using different block copolymers (BC) and different BC concentrations and its effects on physical properties and pore morphology of CZY oxides. This work is important because BCs are one of the most effective and versatile templates for the synthesis of mesoporous oxide materials, and yet their use as templates for the synthesis of mesoporous CZY materials has not been reported. The first section of this chapter deals with the effects of changing the P123 BC concentration for the synthesis of CZY mixed oxides and the second part deals with the effects of changing the type of BC.

I. Effect of P123 Block Copolymer Template Concentration on the Properties of Sol-Gel Synthesized Mesoporous CZY Mixed Oxides

This section focuses on the effects of changing the composition of the Pluronic template during the synthesis of the CZY supports since previously these supports have only been synthesized using the same starting compositions via sol-gel synthesis.[13] This variable might be able to positively affect a range of physical properties, such as surface area, average pore size, and ordering of the porous network among others.

Experimental

Materials

Pluronic® P-123 (M_{av} = 5800, PEO_{20} $PPO_{70}PEO_{20}$), zirconyl nitrate hydrate ($ZrO(NO_3)_2 \cdot H_2O$) and yttrium nitrate hexahydrate ($Y(NO_3)_3 \cdot 6H_2O$) were purchased from Sigma-Aldrich. Cerium nitrate hexahydrate ($Ce(NO_3)_3 \cdot 6H_2O$) from Alfa Aesar. Ammonium hydroxide (NH_4OH), hydrogen peroxide (H_2O_2, 30% solution) and 1-Propanol were obtained from Fisher. All chemicals were used as received without further purification.

Synthesis

In a typical synthesis, 4 g of zirconyl nitrate, 0.7 g of yttrium nitrate and 8.3 g of cerium nitrate were dissolved in 80 ml of distilled water. The proportions were chosen by Toyota Motor Engineering as the optimal combination for their interests. Later, 1 ml of hydrogen peroxide was added to the solution to transform Ce(III) to Ce(IV), causing a color change to the solution. Various amounts of Pluronic P123 were dissolved in 40-200 ml of an aqueous ethanol solution (50% vol). The two solutions were combined with

vigorous stirring, and then ammonium hydroxide was added as a precipitating agent for the metal oxides. The resulting solution was aged for 1 day at 100 °C in a closed PFA Teflon vessel. The aging time and temperature were decided based on reported conditions for similar systems. The precipitate was washed and filtered to eliminate impurities and nitrate salts remaining in the product. It was finally dried at 100 °C for 1 day and calcined (using a heating rate of 1 °C/min) at 600 °C for 4 hours. Figure 3.2 depicts the general synthesis procedure described above.

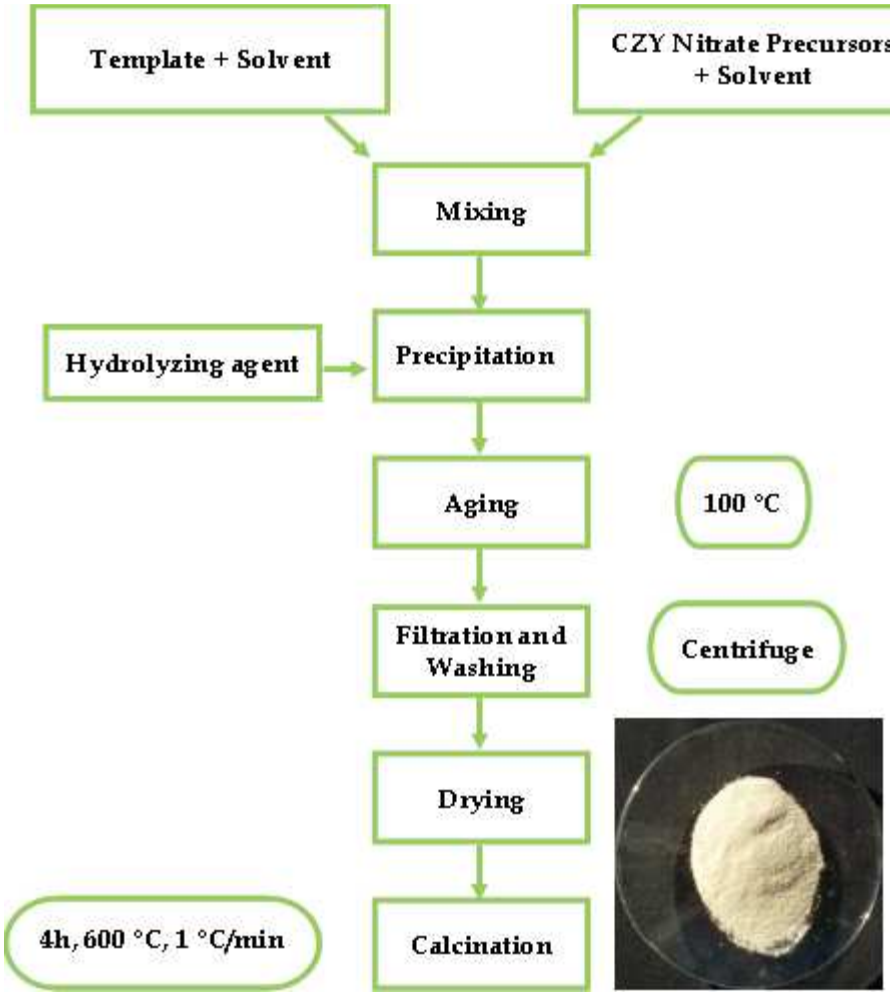

Figure 3.2. Schematic procedure for the synthesis of CZY mesoporous oxides and picture of final product.

All samples were prepared using the same procedure above but the molar ratio of P123 was varied such that starting molar ratios were xP123 : $1Y_1O_{1.5}$: $9ZrO_2$: $10CeO_2$ where x = 0.1, 0.5, 1.0, 2.0, 3.0, 6.0, 8.0 or 10.0.

Tables 3.1 and 3.2 below show typical compositions for the synthesis for CZY materials using different (block-copolymer):(precursor) ratios.

Table 3.1 Typical composition of P123 templated CZY mixed oxides using a molar ratio of 0.1 for the block copolymer.

	Oxide Molar Ratio	**Scaled Salt Wt (g)**
$ZrO(NO_3)_2{\cdot}H_2O$ (ZrO_2)	9	4.000
$Y(NO_3)_3{\cdot}6H_2O$ ($Y_1O_{1.5}$)	1	0.736
$Ce(NO_3)_3{\cdot}6H_2O$ (CeO_2)	10	8.346
NH_4OH		2.021
P123		1.115
H_2O_2		1 ml
Water		100ml
Propan-1-ol		25ml

Table 3.2. Typical composition of P123 templated CZY mixed oxides using a molar ratio of 10 for the block copolymer.

	Oxide Molar Ratio	**Scaled Salt Wt (g)**
$ZrO(NO_3)_2{\cdot}H_2O$ (ZrO_2)	9	4.000
$Y(NO_3)_3{\cdot}6H_2O$ ($Y_1O_{1.5}$)	1	0.736
$Ce(NO_3)_3{\cdot}6H_2O$ (CeO_2)	10	8.346
NH_4OH		2.021
P123		111.481
H_2O_2		0.327
Water		280ml
Propan-1-ol		100ml

Characterization

Nitrogen adsorption and desorption isotherms at 77 K were measured using a Micromeritics ASAP 2020 system after the samples were outgassed under vacuum at 473 K overnight. The sorption data were analyzed using the Barret-Joyner-Halenda (BJH) model to obtain the pore size distribution and with the Brunauer-Emmet-Teller (BET) model for surface area.

The phase characterization was performed by powder X-ray diffraction (PXRD) using a Scintag XDS Model 2000 diffractometer with Cu K α radiation (λ = 1.5406 Å) and Ni filter, operated at 30 kV and 20 mA. Similarly, small-angle X-ray diffraction (SAXRD) patterns were obtained using a Rigaku Ultima IV X-ray diffractometer with Cu K α radiation (λ = 1.5406 Å) and Ni filter, operated at 40 kV and 44 mA.

A Horiba Jobin Yvon ULTIMA 2 inductively couple plasma atomic emission spectrometer (ICP-AES) was used to determine elemental compositions. To dissolve the samples, 0.1 g of calcined CZY oxides were mixed in a PFA vessel with 0.5 g of ammonium sulfate ($(NH_4)_2SO_4$), 10 ml of concentrated sulfuric acid (H_2SO_4) and 30 ml of distilled water. The sample dissolution was carried out in a CEM Mars 5 Microwave Accelerated Reaction System with microwave power range between 0 to 100% with options of 300, 600 and 1200 W. The microwave digestion protocol consisted of 5 stages: 1 hour hold time for each 230, 200, 180, 130 and 120 °C digestion temperatures, each stage immediately followed by the next. All stages were performed at 600 W and 100% power.

Transmission Electron Microscopy (TEM) and Scanning Electron Microscopy (SEM) studies were carried out on a TEM-Hitachi H7600 and on a STEM-Hitachi HD 2000 electron microscope operating at 120 and 200 kV, respectively, to determine the morphology of the samples. Energy-dispersive X-ray (EDX) spectra were taken on an Oxford INCA Energy 200 Energy Dispersive X-ray spectrometer (EDS) connected to the HD200 electron microscope to determine localized compositions.

Thermogravimetric analysis (TGA) and differential scanning calorimetry (DSC) were carried out using a SDT Q600 Simultaneous DSC/TGA Analyzer.

Results and Discussion

Table 3.3 summarizes the data for BET surface area and BJH average pore sizes for the different CZY materials synthesized with different P123 compositions. The corresponding nitrogen adsorption-desorption isotherms and the corresponding BJH pore size distribution plots for some of the oxide materials listed in the table are shown in Figure 3.3. Additional isotherms and pore size distribution plots for the other compositions are not shown since their shape is very similar to that shown in Figure 3.3.

Table 3.3. Comparative chart of P123 composition effects on CZY materials [Pluronic® P-123 (Sigma-Aldrich, $PEO_{20}PPO_{70}PEO_{20}$)]

Molar ratio P123	**Weight % P123****	**BET surface area (m^2/g)***	**BJH pore diameter (nm)***
0.1	7.9	92	5.2
0.5	29.9	90	6.2
1	46.0	96	6.2
2	63.0	103	18.4***
3	71.9	123	15
6	83.6	137	14.9

8	86.7	146	16.0
10	89.5	165	17.9

* The error margin for the surface area is ±5 m^2/g and ±0.5 nm for the pore diameter.
**Weight percentages are based on the weight of the nitrate salts and the template only.
*** This value is off the trend and is probably due to some measurement error.

The BET surface area for the synthesized CZY materials increases from 92 to 165 m^2g^{-1} as the concentration of P123 increases and the BJH average pore diameter increases as well from 5.2 to 17.9 nm. I believe the pore diameter data for the sample prepared with a P123 molar ratio of 2.0 is an error and should be ignored. The higher concentrations of block copolymer in the synthesis sol-gel generally lead to an increase in the average pore size and surface area of the calcined oxide products. This is partially due to the as synthesized oxides containing a proportionately greater amount of template as the template concentration is increased, which upon calcination lead to a final oxide product that is more open and porous. In general, these data show that the pore diameter can be tuned by varying the concentration of the surfactant as shown in previous studies.[18]

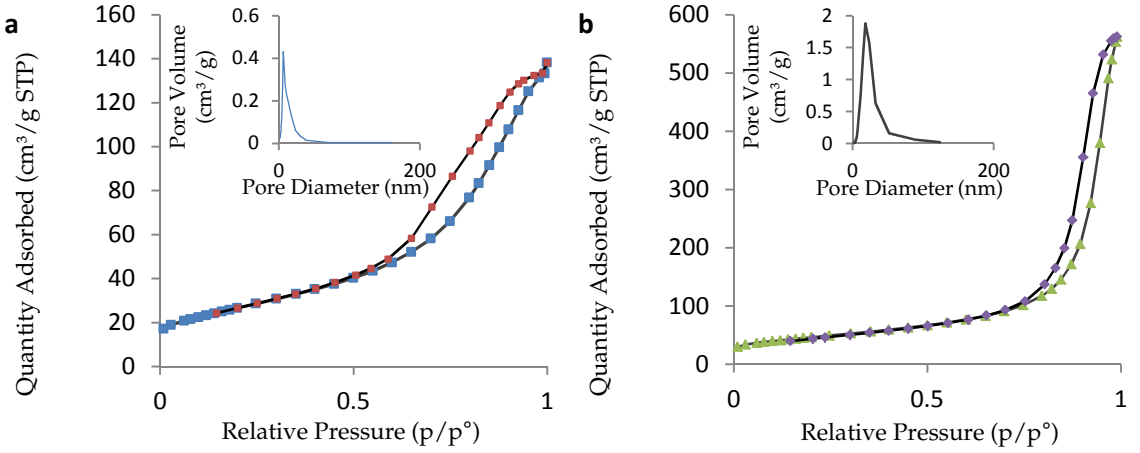

Figure 3.3.. N_2 adsorption-desorption isotherms and BJH pore size distribution plot (inset) for P123 templated CZY at (a) 1.0 and (b) 10.0 P123 molar ratio.

In the nitrogen adsorption isotherms (Figure 3.3), the hysteresis loops of the samples resemble that of a typical type-IV isotherm, indicating the presence of mesopores. As shown, the pore size distribution plots (Figure 3.3, inset) are unimodal.

Powder X-ray diffraction patterns for calcined CZY materials are shown in Figure 3.4 and Figure 3.5. The wide-angle XRD patterns (Figure 3.4) show well-resolved broad peaks similar to the pattern of pure ceria indicating the samples have the same cubic structure of ceria. This is not surprising as it has been previously shown that transition metal oxides tend to have crystalline structures,[31] contrary to the amorphous structures of silica-based oxides.

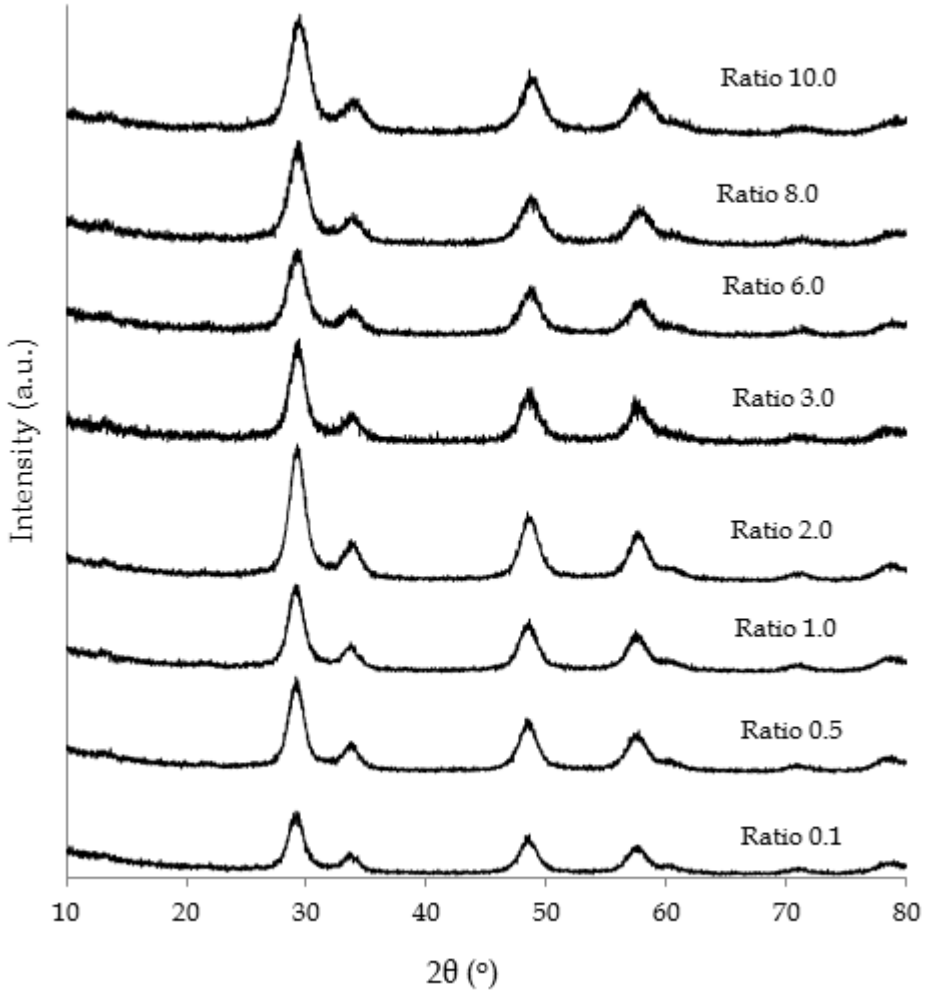

Figure 3.4. Wide-angle powder X-ray diffractogram for synthesized CZY mixed oxides at different block copolymer P123 ratios.

The line broadening in the XRD pattern indicates that the powder consists of nanocrystallites. Further, the absence of peak twinning in the spectra suggests no phase segregation occurred. One interesting observation is that template concentration during synthesis does not play a role in the resulting phase structure of the crystalline regions of the samples since all patterns are basically the same over all studied P123 concentrations,

which means that all samples have uniform crystalline structures over the full range of sol-gel template concentrations studied.

Table 3.4. Comparative chart of crystallite dimensions for the different P123 templated CZY oxides calculated using the Scherrer equation on the diffraction peaks.

Molar ratio P123	Mean Crystallite Dimension (nm)
0.1	5.6
0.5	5.4
1	5.3
2	5.2
3	5.5
6	4.8
8	4.4
10	4.3

* The error margin for the crystallite dimension is ±0.5 nm.

As shown in Table 3.4, the corresponding primary crystal size was between 4.3 and 5.6 nm as calculated by applying the Scherrer equation on the first peak of the XRD pattern. The size of the crystallites has a general tendency to decrease as the concentration of the template was increased. This result agrees quite well with the tendency observed with the BET surface area of the materials to increase as more template is present during synthesis. Thus, for P123 templated CZY systems, increased template concentrations lead to smaller but more numerous CZY crystallites condensing to form larger particles, which leads to a more jagged pore wall and higher overall surface areas.

Small angle XRD patterns (Figure 3.5) did not reveal any low angle peaks, indicating that the porous network in the mesostructures lacked long range ordered mesoporosity despite the use of differing concentrations of block copolymer during the CZY synthesis.

Previous synthesis studies of mesostructures with similar metal oxide components were also unable to form ordered mesoporous structures using sol-gel synthesis techniques.[31]

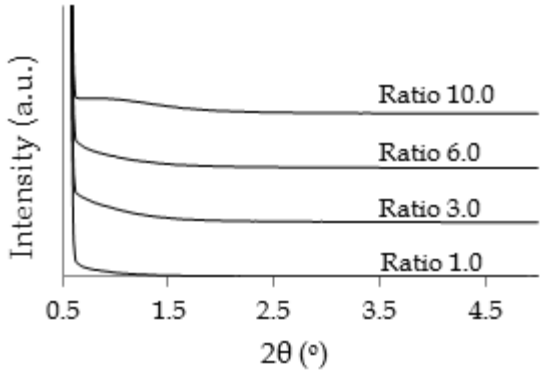

Figure 3.5.. Small-angle powder X-ray diffractogram for synthesized CZY mixed oxides at different block copolymer P123 ratios.

Elemental composition studies using ICP-AES were carried out in order to determine if the proportions of oxides incorporated during synthesis (theoretical amount) were unchanged after calcination, because prior studies[32-34] have shown that catalytic converter performance can be significantly enhanced using specific ratios of ceria, zirconia, and yttria oxides as catalyst supports. The results are shown in Table 3.5.

Table 3.5. Elemental compositions for the different P123 templated CZY oxides after calcination.

Sample	**ZrO_2 (mol %)[g]**	**$YO_{1.5}$ (mol %)[g]**	**CeO_2 (mol %)[g]**
Theoretical Amount	45.00	5.00	50.00
P123 R0.1	46.43	5.07	48.50
P123 R1.0	46.13	4.99	48.88
P123 R3.0	47.10	4.93	47.98
P123 R10.0	53.60	4.32	42.09

g. The error margin for the elemental composition is ±2.0 mol%

Elemental analysis for all samples, except for the sample having a P123 molar ratio of 10.0 (most concentrated in P123), show that the measured oxide composition is within the margin of error of the theoretical composition indicating that all oxides are well incorporated into the final mesoporous structure in the proportions used during synthesis. However, there is a slight decrease of ceria and yttria content as BC concentration increases and an increase in zirconia content. The decrease in ceria might reduce the oxygen storage capacity of the synthesized material but for this case the reduction is not significant enough to cause an effect on the OSC properties of the support.

One of the most important steps for the synthesis of mesoporous networks is the formation of micelles in which the oxides will be deposited during synthesis[35]. Since previous efforts by my research group failed to produce mesostructured CZY materials with ordered pores, it was concluded that the lack of ordering of the mesopores could have resulted from the P123 template not being present at concentrations above its critical micellization concentration (cmc), the copolymer concentration at which micelles start forming.[36] Thus, increasing Pluronic concentrations during the synthesis of these mesostructures might increase the likelihood that the template would reach its cmc of $8x10^{-4}$ mol/L for P123 and form ordered oxide structures. To check if mesopores ordering was improved, TEM and SEM images were collected for CZY oxide samples prepared using differing concentrations of template.

The TEM and SEM images of some of the calcined CZY samples are shown in Figure 3.6. The existence of mesopores is clearly observed but the mesopores are not highly ordered. The size and crystalline nature of the observed samples is in good

agreement with the XRD results, the crystallites have sizes from approximately 2 to 11 nm and they seem to decrease in size as the ratio of template increases.

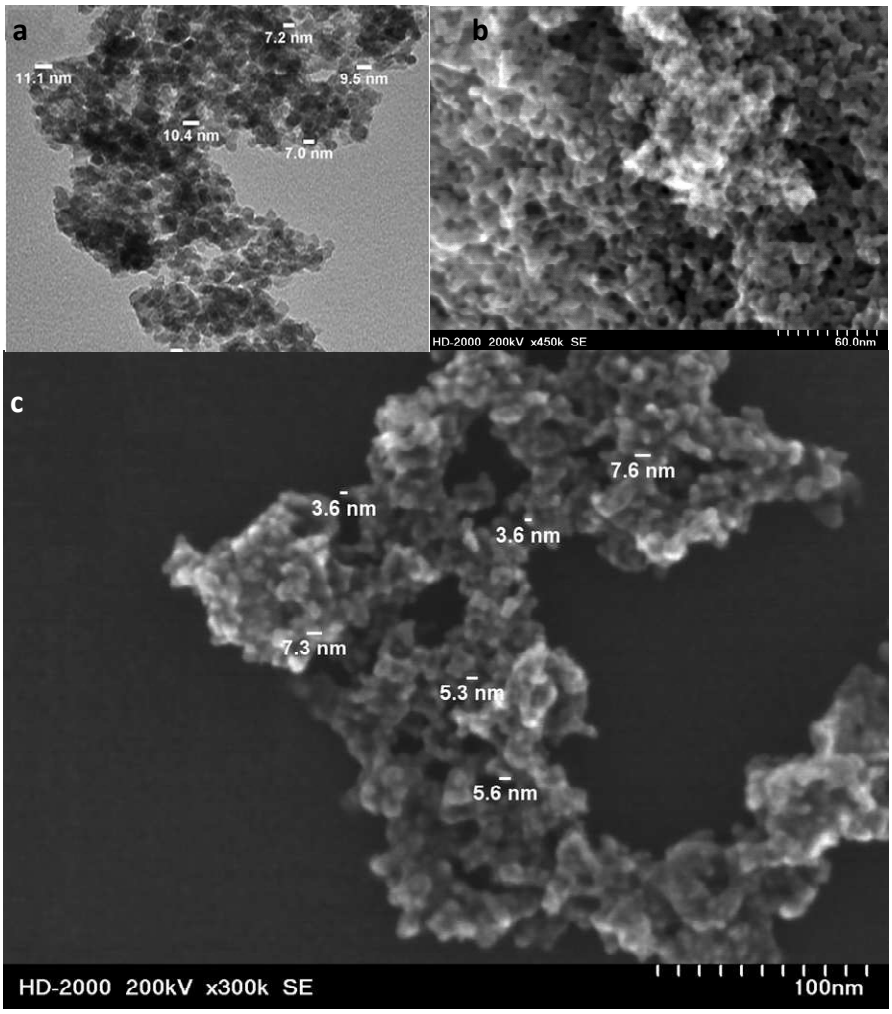

Figure 3.6. (a) TEM and (b-c) SEM images of calcined CZY samples at different P123 template molar ratios: a) ratio of 1, b) ratio of 3, and c) ratio of 10.

The TEM images are similar for all samples, despite them being prepared at the different template concentrations. Specifically, all samples look like an agglomeration of nanosized particles with no particular order, which differs from the honeycomb morphology of MCM-41 and SBA-15 silica materials prepared using the same template.

This last observation is confirmed by the SAXRD patterns, as they do not show any low angle diffraction peaks that are attributable to the spacing between ordered pores.

This result suggests that no ordered assembly process is occurring during the synthesis process yielding random arrangements of CZY oxides with mesopores resulting from the voids between the oxides generated by the Pluronic template removal. The lack of periodicity in the arrangement of pores might be caused by the instant precipitation of oxides, preventing the micelles to reach their cmc and self-assemble into secondary structures before the oxides are formed.

The block copolymer template route for mesoporous oxides is expected to yield ordered arrangements of pores as a result of self-assembly processes that occur for these templates under the ideal circumstances. The expected process is explained by Soler-Illia et al.[18] and is shown in Figure 3.7. However the lack of an ordered consolidated CZY mesostructure for this case indicates that the self-assembly process might not have taken place. This can be a result of insufficient time for the Pluronic template to microphase separate or to the collapse of the mesostructure during calcination caused by the fragile crystalline mesostructure of CZY oxides. Further analysis of these circumstances for sol-gel processes will be shown in the next chapter of this thesis.

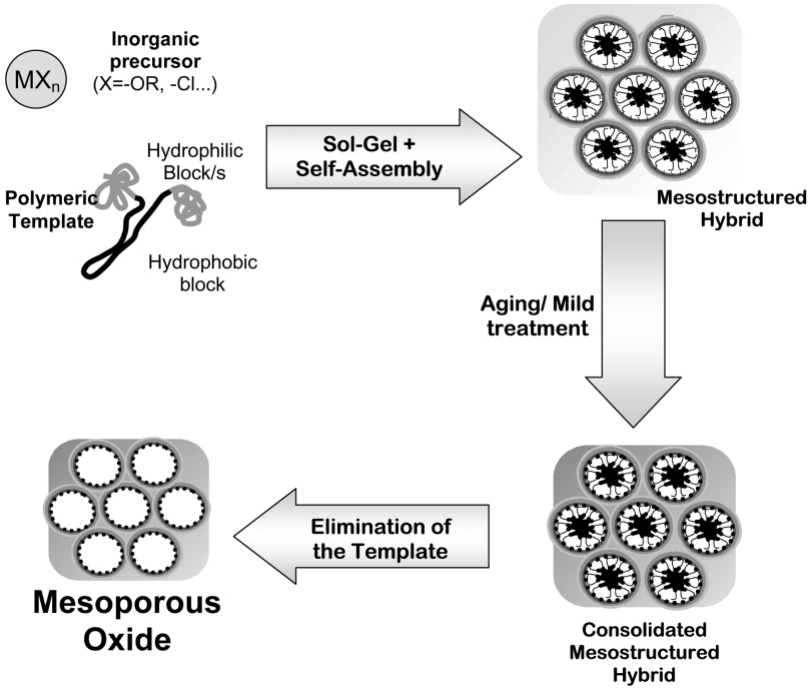

Figure 3.7. Schematic view of the steps leading from a solution to a mesoporous oxide network. Reprinted with permission from ref[18]. Copyright © Elsevier Limited.

The energy dispersive X-ray (EDX) results (see Appendix E) indicated that the measured molar ratios of oxides are similar to the initial proportions of the oxides adopted during synthesis, supporting the results from the ICP-AES analysis. The distribution of oxides on the surface is also uniform indicating no phase segregation as well.

The DSC and TGA curves of the synthesized CZY materials at different template concentrations are shown in Figure 3.8. Two different calcination protocols were compared in order to decide which heating rate for calcination would be efficient with respect to heating times but also heat sufficiently slow so as to prevent the thermal collapse of the pores. For CZY materials, their high thermal stability suggest that thermal

collapse could only occur if the P123 template underwent rapid thermal oxidation, generating extremely high local temperatures sufficient to melt local oxide framework. The heating rates compared in the experiments were 1 and 20 °C/min. For the equipment used, the downward peaks indicate endothermic (evaporation) processes while the upward peaks indicate exothermic (combustion) processes.

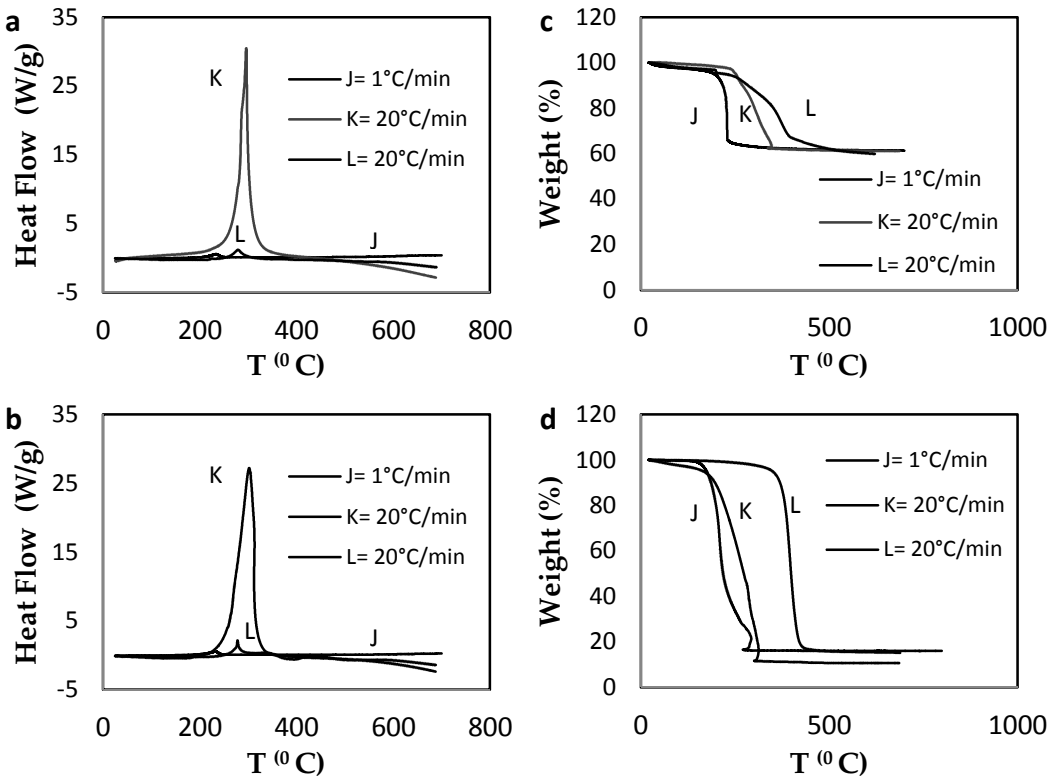

Figure 3.8. DSC and TGA profiles of the CZY materials at (a) 0.5 (b) 1.0 (c) 3.0 and (d) 10.0 molar ratio calcined from room temperature to 600 °C. J and K burned in air and L in nitrogen.

The DSC plots show that the samples calcined at a heating rate of 20 °C/min have noticeably higher exotherms than the samples calcined at 1 °C/min, suggesting that samples heated at the higher rate experience significantly higher local temperatures. The most significant exotherms were recorded between 200 and 400 °C and come from the

burning of the template. It is also possible to observe a shift in the temperature at which the exothermic process occurs at the different heating rates (see Table 3.6). If samples are calcined slowly, the exotherm arising from template oxidation occurs at temperatures 50 to 160 °C lower than if the sample were calcined at 20 °C/min since high heating rates do not allow enough time for the uniform and stable burning of the template causing the peak to appear later.

Table 3.6. Comparison of temperatures at which exothermic peaks have highest point and the difference of their appearance at the different heating rates and template molar ratios.

Template molar ratio	**Exothermic peak (°C)[a]**		**Difference (°C)**
	1 °C/min	**20 °C/min**	
0.5	233	291±4	58±4
1	232	300±3	68±3
3	274±4	338	64±4
10	260±28	351±40	91±68

a. The margin of error related to equipment is ± 8 °C.

Table 3.6 also shows that higher template concentrations lead to the exotherm associated with template removal/oxidation being shifted to higher temperatures when the samples are calcined at the same heating rate. This observation indicates that in order to avoid the appearance of hot spots in the samples, which might contribute to localized melting of the oxide and subsequent loss of structure, CZY mesoporous materials containing organic templates must be calcined at low heating rates. Also, the upper allowable heating rate is directly related to the level of template in the as synthesized sample, with higher template loadings requiring lower heating rates.

TGA curves (Figure 3.8) show some of the same phenomena that was shown by the DSC analysis. For example it is observed that samples calcined at higher heating rates

have greater weight loss at higher temperatures due to the less uniformity of the burning process. The removal of physically adsorbed water does not appear in the TGA plot indicating the samples were well dried at the beginning of the measurements. Complete removal of the Pluronic template is observed at around 400 °C in the TGA plot.

Table 3.7. Comparison of template weight percent loss during calcination and the quantities of template incorporated during synthesis.

Template molar ratio	**Weight % P123 (synthesis)[a]**	**Weight % loss during calcination[b]**
0.5	30	18±4
1	46	20±6
3	72	37±4
10	89	80±9

a. The margin of error for the synthesis is ±1% weight.
b. The margin of error related to equipment is ±2% weight.

Table 3.7 shows the difference between the quantity of template incorporated during synthesis and the quantity of template lost during calcination. These data provide an estimate of how much template was incorporated into the as synthesized oxide structure following filtration and washing processes. It is observed that for the lower molar ratios the relative quantity of template lost during synthesis is about a half of the quantity of template incorporated in the starting sol-gel. For the highest concentration of template (P123 molar ratio of 10.0), a greater percentage of the template seems to be incorporated into the as synthesized oxide sample. This might show that the ticker the solution (higher BC concentration), the better it remains after being washed and filtrated.

Conclusions

Mesoporous CZY supports were synthesized from inorganic salts using different concentrations of block copolymer templates via sol-gel techniques. Higher surface areas and larger pore volumes were observed in samples where the template concentration was increased. These results confirm that it is possible to tune the pore diameter of CZY mesostructures by changing the (template):(oxide precursors) ratio.

Despite showing uniform crystalline structures at all sol-gel template concentrations, none of the mesostructures were well ordered, suggesting that template concentration alone does not control the periodicity of the structure. This might be due to insufficient time for the micelles to organize into mesostructures and/or to the collapse of any mesostructure formed due to the fragile crystalline walls of CZY mixed oxides. The reasons behind this phenomenon will be analyzed in depth in the next chapter.

The relative proportions of the various oxide components were maintained throughout the synthesis and calcination processes, except for supports made with extremely high block copolymer concentrations. It was also shown that using a low heating rate and maintaining appropriate template concentrations might lessen the probability of collapse of the mesostructure during calcination. The loss of structure during calcination was attributed to the formation of hot spots that are generated by the rapid oxidation of organic template. This deleterious effect is compounded by the use high heating rates and high organic template loadings.

II. Effect of Different Pluronic Block Copolymer Templates on the Properties of Sol-Gel Synthesized Mesoporous CZY Mixed Oxides

Block copolymers have become a widely used template to create mesoporous networks with different oxides for a wide variety of applications.[18] Our research group has previously worked with Pluronic P123, as it is one of the most widely used block copolymers for templating purposes.[13]

To expand upon previous studies with P123 templates, I tried other block copolymers, such as Pluronic P65 and Pluronic F127, which could serve as templates for the synthesis of mesoporous oxide materials. The other Pluronics considered have the same poly(ethylene oxide)-poly(propylene oxide)-poly(ethylene oxide) (PEO-PPO-PEO) structure. They feature shorter hydrophobic chains and larger hydrophilic chains, respectively. Significantly different molecular weight is also shown among the three.

Experimental

Materials

Pluronic® F127 (M_{av} = 12600, $PEO_{106}PPO_{70}PEO_{106}$) and Pluronic® P65 ($M_{av}$ = 3400, $PEO_{20}PPO_{30}PEO_{20}$) were obtained from BASF. Pluronic® P-123 (M_{av} = 5800, $PEO_{20}PPO_{70}PEO_{20}$), zirconyl nitrate hydrate ($ZrO(NO_3)_2.H_2O$) and yttrium nitrate hexahydrate ($Y(NO_3)_3.6H_2O$) were purchased from Sigma-Aldrich. Cerium nitrate hexahydrate ($Ce(NO_3)_3.6H_2O$) from Alfa Aesar and ammonium hydroxide (NH_4OH), hydrogen peroxide (H_2O_2) and 1-Propanol were obtained from Fisher. All chemicals were used as received without further purification.

Synthesis

All samples were prepared using the procedure discussed in the previous section of this chapter, except that the molar ratio of Pluronics was varied such that the starting molar ratios were xP123 / yP65 / zF127 : 9 ZrO_2: 1 $Y_1O_{1.5}$: 10 CeO_2, where x = 1 for P123; y = 1, 2, 3 for P65 and z = 0.5, 1, 2 for F127. Tables 3.8-10 show typical compositions for the synthesis for CZY materials.

Table 3.8. Typical composition of P123 templated CZY mixed oxides using a molar ratio of 1 for the block copolymer.

	Oxide Molar Ratio	**Scaled Salt Wt (g)**
$ZrO(NO_3)_2.H_2O$ (ZrO_2)	9	4.000
$Y(NO_3)_3.6H_2O$ ($Y_1O_{1.5}$)	1	0.736
$Ce(NO_3)_3.6H_2O$ (CeO_2)	10	8.346
NH_4OH		2.021
P123		11.148
H_2O_2		1 ml
Water		160 ml
Propan-1-ol		25 ml

Table 3.9. Typical composition of P65 templated CZY mixed oxides using a molar ratio of 1 for the block copolymer.

	Oxide Molar Ratio	**Scaled Salt Wt (g)**
$ZrO(NO_3)_2.H_2O$ (ZrO_2)	9	4.000
$Y(NO_3)_3.6H_2O$ ($Y_1O_{1.5}$)	1	0.736
$Ce(NO_3)_3.6H_2O$ (CeO_2)	10	8.346
NH_4OH		2.021
P65		6.535
H_2O_2		0.327
Water		100 ml
Propan-1-ol		25 ml

Table 3.10. Typical composition of F127 templated CZY mixed oxides using a molar ratio of 1 for the block copolymer.

	Oxide Molar Ratio	Scaled Salt Wt (g)
$ZrO(NO_3)_2.H_2O$ (ZrO_2)	9	4.000
$Y(NO_3)_3.6H_2O$ ($Y_1O_{1.5}$)	1	0.736
$Ce(NO_3)_3.6H_2O$ (CeO_2)	10	8.346
NH_4OH	30	2.021
F127	1	24.218
H_2O_2		0.327
Water		100 ml
Propan-1-ol		25 ml

Characterization

All characterization methods and techniques were identical to those used in previous section of this chapter.

Results and Discussion

Figure 3.9 shows the nitrogen adsorption-desorption isotherms and the corresponding BJH pore size distribution plots for CZY supports synthesized with Pluronic P123, P65 and F127 at an equal molar ratio of template to oxides (i.e., a molar ratio of 1.0). All of the Pluronic templates have the same polymer constituents but the sizes of the oligomer subunits or blocks are different for each case. The templates consist of block copolymers of ethylene oxide (EO) and propylene oxide (PO), where the two ends of the linear PO chain are covalently bounded to two separate EO oligomers (EO_n-PO_m-EO_n). Pluronic P123 (n=20, m=70) was the initial block copolymer tested, while later testing examined the use of Pluronic P65 (n=20, m=30), which has a shorter hydrophobic chain, and Pluronic F127 (n=106, m=70), which has a longer hydrophilic chain. Table 3.11 shows

BET surface area and BJH average pore sizes for the corresponding calcined CZY oxide materials.

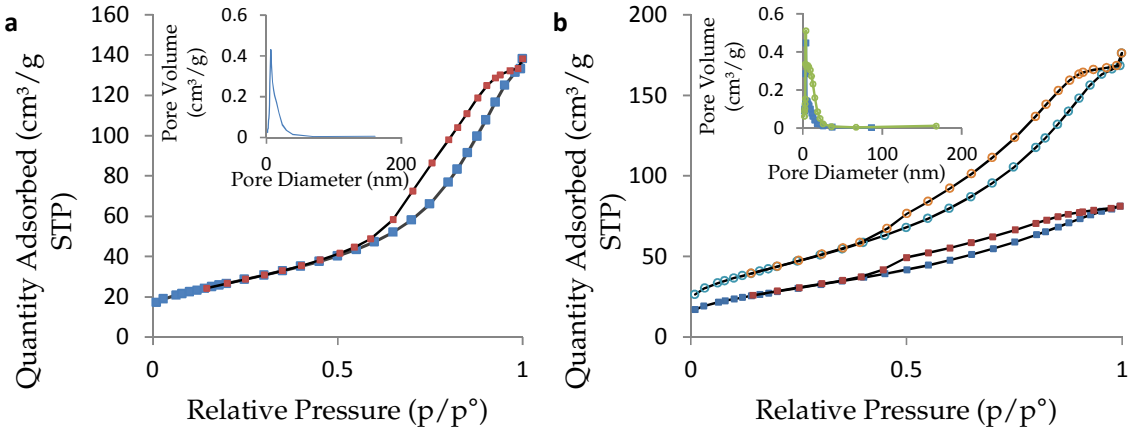

Figure 3.9. N_2 adsorption-desorption isotherms and BJH pore size distribution plot (inset) for Pluronic templated CZY at 1.0 molar ratio of (a) P123, (b) P65 (filled squares) and F127 (empty circles).

The N_2 adsorption-desorption curves show the hysteresis loop of typical type-IV isotherms for all three CZY materials synthesized with different Pluronic templates, indicating the presence of mesopores, in addition, the pore size distribution plots are unimodal. The results also indicate that the BET surface area for the different CZY materials increases as the Pluronic is changed from P123 to P65 to F127, with surface areas ranging from 96 to 159 m^2g^{-1} (Table 3.11) and the BJH average pore diameter decreases from 6.2 to 3.7 nm, respectively. These results show that F127 might be the best option as a template in terms of the BET surface area but the Pluronic P123 yields larger diameter pores on average. However, no clear relationship is observed between template content, chain length and surface area or pore diameter.

Table 3.11. Comparative chart of Pluronic template effects on CZY materials [Pluronic® P123 ($PEO_{20}PPO_{70}PEO_{20}$); Pluronic® P65 ($PEO_{20}PPO_{30}PEO_{20}$); Pluronic® F127 ($PEO_{106}PPO_{70}PEO_{106}$)]

Pluronic	Molar ratio	Weight % template**	BET surface Area (m^2/g)*	BJH pore diameter (nm)*
P123	1.0	46.0	96	6.2
P65	1.0	33.3	102	3.8
F127	1.0	64.9	159	3.7

* The error margin for the surface area is ±5 m^2/g and for the pore diameter, ±0.5 nm
**Weight percents are based on the weight of the nitrate salts and the template only.

The wide-angle XRD patterns for the calcined CZY materials synthesized with different Pluronic templates are shown in Figure 3.10. From these patterns, one can observe that the samples are well crystallized. The absence of twinned peaks suggests no phase segregation occurred and the distribution of the oxides is homogeneous. The line broadening in the pattern shows that nanocrystallites constitute the bulk of the crystalline portion of the sample and one can also observe that the use of different Pluronic templates during synthesis does not play a role in the resulting phase structure of the samples as all XRD patterns are basically the same, which was the identical conclusion reached in the previous section when BC template concentration was varied.

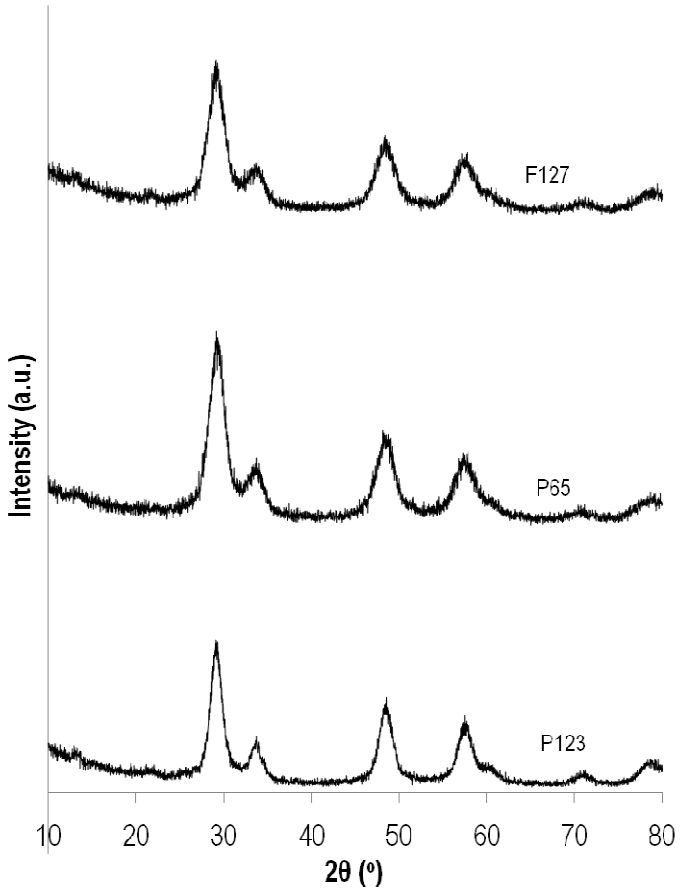

Figure 3.10. Wide-angle powder X-ray diffractogram for synthesized CZY mixed oxides at a molar ratio of 1.0 for different block copolymer templates.

Table 3.12 shows the primary crystal size as calculated by the Scherrer equation. The size of the crystallites was between 3.8 and 5.3 nm and decreased as the Pluronic template was varied from block copolymer P123 to P65 to F127 with no clear relation with template content or chain length. Small angle XRD patterns (not shown) did not reveal any long-range order in the mesostructures as deduced from the absence of low angle peaks in the different samples regardless of the different block copolymers used during synthesis.

Table 3.12. Comparative chart of crystallite dimensions for the different Pluronic templated CZY oxides at a molar ratio of 1.0 calculated using the Scherrer equation on the diffraction peaks.

Template	Weight % template*	Mean crystallite dimension (nm)
P123	46.0	5.3
P65	33.3	4.2
F127	64.9	3.8

*Weight percentages are based on the weight of the nitrate salts and the template only.

ICP-AES experiments to determine the elemental composition of the samples were carried out in order to determine if the presence of a different template during synthesis affected the proportions of oxides remaining after calcination. The expected composition on a molar basis is 45, 5, and 50 mol% of ZrO_2, Y_2O_3, and CeO_2, respectively. Table 3.13 shows that the oxides are well incorporated in the final sample since the oxide compositions are within the margin of error of the expected values.

Table 3.13. Elemental compositions for the different Pluronic templated CZY oxides after calcination.

Sample	ZrO_2 (mol %)[g]	$YO_{1.5}$ (mol %)[g]	CeO_2 (mol %)[g]
Theoretical/Predicted	45.00	5.00	50.00
P123 R 1.0	46.13	4.99	48.88
F127 R1.0	46.60	5.10	48.30
P65 R1.0	46.28	4.99	48.73

g. The error margin for the elemental composition is ±2.0 mol%

Figure 3.11 shows the TEM images of some of the calcined CZY samples. The micrographs exhibit mesoscale pores. However, there is no long-range order in the pore arrangement of the CZY oxides using Pluronics P65 and F127 as templates. The TEM

results confirm the XRD results. The change in Pluronic template does not seem to improve the 3-D arrangement of the crystallites.

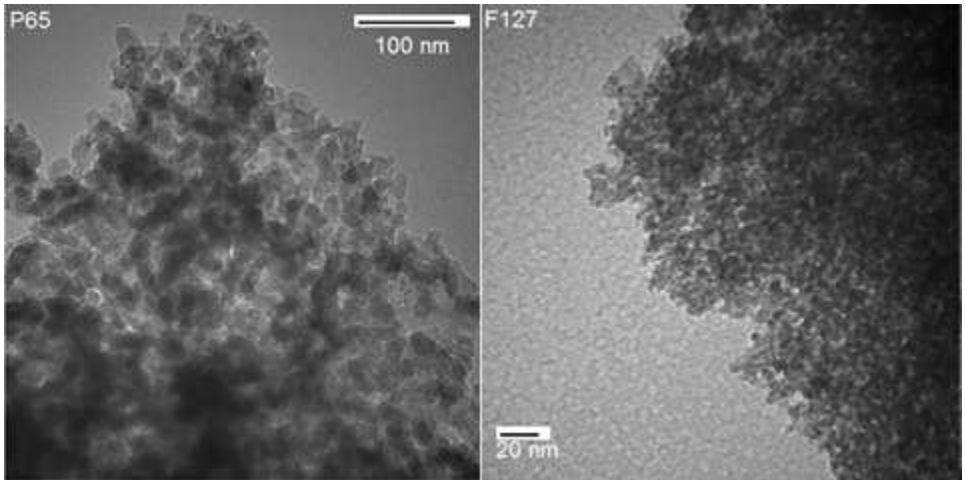

Figure 3.11. TEM images of calcined CZY samples at different Pluronic templates at 1.0 molar ratio.

The TEM data suggests that no self-assembly of micelles occurred during CZY synthesis as is commonly the case for silica based materials. Thus, the end result from the sol-gel synthesis, independent of the Pluronic polymer used as template, was a random arrangement of CZY oxide nanocrystals with mesopores resulting from the voids between the oxides particles that were generated by the randomly arranged Pluronic templates.

Previous work[37] has suggested that the hydrophobic oligomer of the Pluronics (PPO) is responsible for micellization, apparently due to diminishing hydrogen bonding between water and PPO. This might suggest that block copolymers with larger PPO chains (P123 and F127) would favor the formation of micelles that could self-order and contribute to the formation of ordered oxide structures druing the sol-gel CZY synthesis process. However, as pointed out before, the change in Pluronic template did not contribute to

more ordered structures in this case. In the same study, it was concluded that the effect of the different molecular weight of the samples was more pronounced than the effect of the length of the chains.

Since each Pluronic has a very different molecular weight, the molar ratios of Pluronic F127 and P65 were varied in order to be able to compare similar weight percent of Pluronic templates during the synthesis of the CZY oxide materials. The results for the BET surface area and BJH average pore size diameter for these materials are shown in Table 3.14.

Table 3.14. Comparative chart of composition effects of CZY materials synthesized with different Pluronics at similar template weight %.

Template	Molar ratio	Weight % template **	BET surface area (m^2/g)*	BJH pore diameter (nm)*
P123	1.0	46.0	96	6.2
P65	2.0	50.0	122	3.7,7.4
F127	0.5	48.1	121	9.1

* The error margin for the surface area is ±5 m^2/g and for the pore diameter, ±0.5 nm
**Weight percentages are based on the weight of the nitrate salts and the template only.

The BET surface area for P123 is significantly smaller than for the other BC templates. The average pore size does not have a clear trend. Further, the bimodal pore size distribution of the P65 sample has yet to be fully explained and understood but its smaller hydrophobic and hydrophilic chains as compared to P123 and F127 respectively might be a factor.

The changes in concentration for the Pluronic P65 and F127 were also studied. Tables 3.15 and 3.16 show the BET surface area and BJH average pore size for CZY supports made with Pluronic P65 template and F127 template at different molar ratios. Additional

isotherms and pore size distribution plots for these compositions are not shown since their shape is very similar of that shown in Figure 3.9.

Table 3.15. Comparative chart of P65 composition effects on CZY materials.

Molar ratio	Weight % template **	BET surface area (m^2/g)*	BJH pore diameter (nm)*
1	33.3	102	3.8
2	50.0	122	3.7, 7.4
3	60.0	139	12.5

* The error margin for the surface area is ±5 m^2/g and for the pore diameter, ±0.5 nm
**Weight percentages are based on the weight of the nitrate salts and the template only.

Table 3.16. Comparative chart of F127 composition effects on CZY materials.

Molar ratio	Weight % template **	BET surface area (m^2/g)*	BJH pore diameter (nm)*
0.5	48.1	121	9.1
1	64.9	159	3.7
2	78.7	159	14.9

* The error margin for the surface area is ±5 m^2/g and for the pore diameter, ±0.5 nm
**Weight percents are based on the weight of the nitrate salts and the template only.

From Table 3.15 it is possible to appreciate that the BET surface area for the different CZY materials increases as the concentration of P65 in the sol-gel increases, 102 to 139 m^2g^{-1}, and the BJH average pore diameter increases as well from 3.8 to 12.5 nm with a bimodal pore size distribution for the case of a molar ratio of 2.0 (i.e. higher template loadings). The presence of larger amounts of block copolymer during the synthesis causes an increase in the observed pore size. This can be attributed to higher levels of template incorporation into the as synthesized oxide, which upon calcination yields larger void volumes and higher surface areas per unit weight of oxide, which is the same result obtained from earlier discussed experiments where the P123 concentration was varied.

Similar results for pore volume are also observed with varying F127 sol-gel concentrations (Table 3.16), but for these studies, the average pore diameter did not exhibit a clear trend. This might be due to variations during the filtration and washing process not allowing the complete incorporation of the template in the final structure. However, no clear reason is attributable to this phenomenon.

Conclusions

Mesoporous CZY supports were synthesized from nitrate precursors using three different block copolymer templates via sol-gel synthesis techniques. The presence of different Pluronic templates during synthesis does not have a significan effect over the surface area and average pore size of the calcined oxide samples. For future work, the present finding lead us to believe that the type of Pluronic is not an important factor to consider when designing the synthesis procedure for these oxides.

Also, all Pluronic templated samples showed uniform crystalline structures and the various ceria, zirconia, and yttria oxides were well incorporated into the final structure. However, none of the mesostructures were well ordered, suggesting that neither the BC template type nor the length of the hydrophobic or hydrophilic chains of the polymer template have an effect on the formation of periodic pore structures within the final mesoporous CZY oxides. We can conclude that not the type of the BC, but the synthesis method and parameters can affect the morphology of the mesoporous CZY structure.

References

(1) Kresge, C. T.; Leonowicz, M. E.; Roth, W. J.; Vartuli, J. C.; Beck, J. S. *Nature* **1992**, *359*, 710-712.

(2) Li, X.; Ji, W.; Zhao, J.; Zhang, Z.; Au, C. *Journal of Catalysis* **2006**, *238*, 232-241.

(3) Nie, W.; Wang, X.; Ji, W.; Yan, Q.; Chen, Y.; Au, C. T. *Catalysis Letters* **2001**, *76*, 201-206.

(4) Melosh, N. A.; Lipic, P.; Bates, F. S.; Wudl, F.; Stucky, G. D.; Fredrickson, G. H.; Chmelka, B. F. *Macromolecules* **1999**, *32*, 4332-4342.

(5) Sun, M.; Hong, L.; Tan, G. M. *J. Phys. Chem. C* **2012**, *116*, 352-360.

(6) Semsarzadeh, M. A.; Azadeh, M. *Iran. J. Polym. Sci. Technol. (Persian Ed.)* **2012**, *24*, 445English, 446Persian-453Persian.

(7) Yang, Y.; Liu, J.; Bai, S.; Li, X.; Yang, Q. *Chem Asian J* **2013**, *8*, 582-7.

(8) Verboekend, D.; Chabaneix, A. M.; Thomas, K.; Gilson, J.; Perez-Ramirez, J. *CrystEngComm* **2011**, *13*, 3408-3416.

(9) Zhou, W.; Sun, F.; Pan, K.; Tian, G.; Jiang, B.; Ren, Z.; Tian, C.; Fu, H. *Adv. Funct. Mater.* **2011**, *21*, 1922-1930.

(10) Nguyen, T.; Simon, F.; Khelfallah, N. S.; Schmutz, M.; Mesini, P. J. *J. Mater. Chem.* **2010**, *20*, 3831-3833.

(11) Calvo, A.; Yameen, B.; Williams, F. J.; Soler-Illia, G. J. A. A.; Azzaroni, O. *J. Am. Chem. Soc.* **2009**, *131*, 10866-10868.

(12) Zalusky, A. S.; Olayo-Valles, R.; Taylor, C. J.; Hillmyer, M. A. *J. Am. Chem. Soc.* **2001**, *123*, 1519-1520.

(13) Anyaba, P. N. Novel techniques for the synthesis of three-way catalytic converter support materials, Clemson University, 2009.

(14) Soni, S. S.; Brotons, G.; Bellour, M.; Narayanan, T.; Gibaud, A. *J Phys Chem B* **2006**, *110*, 15157-15165.

(15) Gazit, O.; Khalfin, R.; Cohen, Y.; Tannenbaum, R. *J. Phys. Chem. C* **2009**, *113*, 576-583.

(16) Frauenrath, H. Block Copolymer Phases of Diblock, Triblock, and Miktoarm Star Copolymers. *http://lmom.epfl.ch/courses/class_supramolecular_24.pdf* (accessed 06/21, 2013).

(17) Brinker, C. J.; Lu, Y.; Sellinger, A.; Fan, H. *Adv Mater* **1999**, *11*, 579-585.

(18) Soler-Illia, G. J. d. A. A.; Crepaldi, E. L.; Grosso, D.; Sanchez, C. *Current Opinion in Colloid & Interface Science* **2003**, *8*, 109-126.

(19) Lelong, G.; Bhattacharyya, S.; Kline, S.; Cacciaguerra, T.; Gonzalez, M. A.; Saboungi, M. *J. Phys. Chem. C* **2008**, *112*, 10674-10680.

(20) Schuth, F. *Chem. Mater.* **2001**, *13*, 3184-3195.

(21) Soler-Illia, G.; Sanchez, C.; Lebeau, B.; Patarin, J. *Chem. Rev.* **2002**, *102*, 4093-4138.

(22) Wu, J.; Antonietti, M.; Gross, S.; Bauer, M.; Smarsly, B. M. *ChemPhysChem* **2008**, *9*, 748-757.

(23) Peng, J.; Li, X.; Kim, D. H.; Knoll, W. *Macromol. Rapid Commun.* **2007**, *28*, 2055-2061.

(24) Wang, H.; Patil, A. J.; Liu, K.; Petrov, S.; Mann, S.; Winnik, M. A.; Manners, I. *Adv. Mater. (Weinheim, Ger.)* **2009**, *21*, 1805-1808.

(25) Fang, H.; Wan, T.; Shi, W.; Zhang, M. *J. Non-Cryst. Solids* **2007**, *353*, 1657-1661.

(26) Du, Y.; Sun, Y.; Di, Y.; Zhao, L.; Liu, S.; Xiao, F. *J. Porous Mater.* **2006**, *13*, 163-171.

(27) Chen, H.; Gu, J.; Shi, J.; Liu, Z.; Gao, J.; Ruan, M.; Yan, D. *Adv. Mater. (Weinheim, Ger.)* **2005**, *17*, 2010-2014.

(28) Ma, B.; Ma, J.; Goh, G. K. L. *J. Mater. Sci.* **2008**, *43*, 4297-4302.

(29) Cheng, W.; Baudrin, E.; Dunn, B.; Zink, J. I. *J. Mater. Chem.* **2001**, *11*, 92-97.

(30) Feng, R.; Yang, X.; Ji, W.; Au, C. *Mater. Chem. Phys.* **2008**, *107*, 132-136.

(31) Feng, R.; Yang, X.; Ji, W.; Aua, C. *Materials Chemistry and Physics* **2008**, *107*, 132-136.

(32) Noronha, F. B.; Fendley, E. C.; Soares, R. R.; Alvarez, W. E.; Resasco, D. E. *Chemical Engineering Journal* **2001**, *82*, 21-31.

(33) Hirano, M.; Suda, A. *Journal of the American Ceramic Society* **2003**, *86*, 2209-2211.

(34) Atribak, I.; Bueno-Lopez, A.; Garcia-Garcia, A. *Journal of Catalysis* **2008**, *259*, 123-132.

(35) Schuth, F. *Angew. Chem. Int. Ed.* **2003**, *42*, 3604-3622.

(36) Hunter, R. J. In *Foundations of Colloid Science;* Oxford University Press: New York, 1987; Vol. 1, pp 565.

(37) Alexandridis, P.; Holzwarth, J.; Hatton, A. *Macromolecules* **1994**, *27*, 2414-2425.

CHAPTER FOUR

CERIA-ZIRCONIA-YTTRIA MESOSTRUCTURES VIA CLASSICAL SOL-GEL AND EVAPORATION INDUCED SELF-ASSEMBLY METHODS

Introduction

Mesoporous oxides exhibit unique properties that make them useful in a wide range of applications, including catalysis,[1-4] adsorption,[5, 6] biomolecular separation,[7, 8] and drug delivery[9, 10]. These properties are derived from their high surface area, uniform pore size distribution, large pore volume and thermal stability. Much of the early work on mesoporous materials focused on siliceous rich materials, starting with the successful synthesis of MCM-41 materials.[11] Whereas, more recent efforts have focused on expanding the molecular diversity of mesoporous materials, so as to include a variety of mesoporous transition metal oxide materials.[12-14] These latter efforts have exposed a key problem with applying the synthetic methodologies developed for siliceous materials to systems containing significant amounts of transition metal oxides. Namely, the hydrolysis and condensation reaction rates of most transition metal cation precursors, especially low-cost metal salts, are vastly different than siliceous material precursors, with the reaction rates for most transition metal oxide precursors being much faster. These faster reaction rates often lead to a loss of morphological control and the formation of condensed oxide structures. This results from the rate of metal precursor hydrolysis being too fast, providing insufficient time for reactive oxide intermediates to oligomerize and assemble around mesopore structure directing agents (templates).

Given the varied chemistry of many transition metal oxides, there are numerous applications for mesoporous oxide structures. Of particular interest are ceria, zirconia

and yttria oxides as they have been widely used for a number of catalytic and electronic applications. For example, ceria, which has unique oxygen storage and release properties, has found applications in areas such as solid oxide fuel cells, high temperature ceramics and catalysis, while zirconia based materials have applications as medicinal agent carriers, catalysts, fuel cell electrolytes, electro-optical materials, damage-resistant optical coatings and gate dielectrics.[15-24] Yttria has also been widely used in high temperature ceramic, catalysis and solid-state laser applications, in part because it enhances the mechanical stability of high temperature ceramics.[25] Additionally, combinations of these oxides have found widespread use. For example, yttria-stabilized zirconia (YSZ) has been widely used for thermal barrier, jewelry, and solid oxide fuel cell applications, whereas ceria-zirconia-yttria (CZY) mixed oxides are used as catalyst supports for applications including solid oxide fuel cells[26-29] and three-way catalysts (TWC) for automotive exhaust emission control.[30-32]

The development of three-way catalysts (TWCs) resulted from a need to simultaneously convert the hydrocarbons (HCs), carbon monoxide (CO) and nitrogen oxides (NO_x) present in automotive exhaust to less harmful gases, such as H_2O, CO_2 and N_2. In the late 1980s, conventional TWCs employed Rh and Pt as active noble metals and ceria as a catalyst support. The ceria support was essential for optimal catalyst performance as it was able to store oxygen under fuel-lean operating conditions and supply oxygen for converting HCs and CO under fuel-rich conditions, where gas phase concentrations of oxygen are insufficient to completely oxidize these pollutants. The broad use of ceria in automotive pollution control catalysts quickly lead to it becoming

the largest application of rare earth oxides.[33] Over the last two decades, however, the inclusion of ceria in automotive three-way catalysts (TWCs) has transitioned away from alumina-supported ceria to high surface area, thermally stable, preformed ceria rich powders.[34]

The use of ceria catalyst supports with enhanced thermal stability was driven by the so-called close coupled catalyst (CCC) for cold start engine emissions. These catalysts experience temperatures up to 1373 K, which required an extremely high thermal resistance.[33] The thermal stability of CeO_2 is a critical point in determining the promoting effects of CeO_2 since as soon as significant sintering of CeO_2 particles occurs, both oxygen storage capacity (OSC) and metal-support interactions appear inhibited. Jen et al.[34] showed that pure ceria has poor surface area stability compared to solid solutions of ceria and zirconia (CZ) , and retains little useful OSC after 1050 °C aging.

Zirconia promotes the formation of more structurally active ceria sites and imparts added thermal stability to supported ceria catalysts. CO oxidation studies [35] have shown that, following high-temperature calcination, CZ model catalysts show higher activities toward promotion of the ceria-mediated mechanism than ceria samples. Thus, it appears that zirconia helps to promote the OSC of ceria in an automotive emissions catalytic converter by promoting the formation and the stabilization of more active ceria sites than those present for bulk ceria. In summary, use of ZrO_2 resulted in effectively improving the thermal stability of CeO_2 as reported in patent literature. [36]

Still, problems with CZ homogeneity (zirconia higher than 20%) resulted in the addition of yttrium as a third cation showing improved homogeneous solid solutions over

the whole range from ceria 100% to 0% mol. The resulting CZY oxides were evaluated for OSC before and after thermal aging and showed great improvement compared to other ceria based oxides. Combinations like $Ce_{0.60}Zr_{0.30}Y_{0.10}$ oxide and $Ce_{0.40}Zr_{0.45}Y_{0.15}$ showed almost no decrease in OSC at 500°C after 800°, 900° and 1000°C thermal aging.[37]

Further evidence of performance improvement by the use of CZY supports was given by studies of Pd supported on CZY oxides[38] confirming the support excellent performance under fuel fluctuating conditions, pollutant conversions and vehicle emissions tests over ceria and CZ materials.

Moreover, an ordered mesoporous CZY structure presents advantages over a disordered one. Ordered mesoporous supports overcome size constrains of microporous materials facilitating the mass transport of bulky molecules. Their intrinsic high surface area allows a high concentration of active sites per mass of material. These active sites are also highly dispersed and spatially uniform. Compared to other support materials, ordered mesopores have the advantage of reduce sintering of catalysts by stabilizing metal particles since they cannot grow to sizes larger than the pore size unless they move to the external surface of the particle.[39] These characteristics provide CZY supports that do not only enhance the catalysis performance of the noble metals by their OSC but also improve their dispersion and longevity by increasing their surface area and reducing metal sintering.

The synthesis of mesoporous ceria, zirconia and yttria has been widely reported, but creating ordered oxide structures has presented numerous difficulties,[40-49] especially for

classical sol-gel synthesis approaches. Blin et al.[47] and Rezaei et al.[46] reported the sol-gel synthesis of mesoporous zirconia using zirconyl chloride and zirconyl nitrate, respectively, but both materials failed to exhibit the presence of an ordered array of mesopores. Similarly, Chen et al.[32, 50] and Yuan et al.[51] reported the synthesis of mesoporous zirconia by a classical sol-gel route using zirconium propoxide. Despite the resulting materials displaying a relatively homogeneous mesostructure, analysis via TEM showed no evidence of an ordered arrangement of pores. Following this path, Ciesla et al.[52] prepared highly ordered porous zirconium oxide-sulfate and zirconium oxo phosphate materials, yet they were unsuccessful at preparing ordered mesoporous zirconia. It is believed that the sulfate and phosphate groups were responsible for inhibiting crystallization, thus, enabling sufficient time for the amorphous zirconia oligomers to assemble into ordered hexagonal arrangements. Lyons et al.[40] reported the synthesis of ordered ceria using cerium acetate as the inorganic framework precursor. However, TEM images of the resulting material showed the presence of both ordered and disordered mesostructures within the same sample.

These synthesis challenges are magnified when the goal is to prepare mesoporous mixed oxides (e.g., ceria-zirconia, yttria-zirconia) with an ordered arrangements of pores.[28, 42, 53-62] Using typical sol-gel synthesis, Feng et al.[61] reported the synthesis of mesoporous ceria-zirconia-yttria and zirconia-yttria using metal nitrates as oxide precursors, instead of expensive alkoxides, and cetyltrimethylammonium bromide (CTAB) as the structure directing agent, but the resulting oxides showed no long range order. In a similar unsuccessful synthesis effort, Terribile et al.[62] used both cerium and

zirconyl chlorides as precursors and CTAB as the template. Later, Teng et al.[57] documented the synthesis of ceria-zirconia via the polyol method using zirconyl chloride and cerium nitrate as oxide precursors and poly(vinylpyrrolidone) in ethylene glycol as the template, but the procedure yielded only disordered mesoporous structures. Mesoporous ceria-zirconia was also obtained by Desphande and Niederberger[63] using nitrate precursor salts and a nanocasting approach with polymeric beads as the structure directing agent, but again, no ordered oxide structure was formed. In a more successful study, Zhao et al.[64] prepared three-dimensionally ordered macroporous (3-DOM) yttria-stabilized zirconia (YSZ) via an aqueous organic gel method, using the interstitial spaces between polystyrene spheres assembled on glass substrates as the structure directing agent. However, this study was never expanded to include the synthesis of ordered mesoporous materials. Likewise, prior work at Clemson has successfully shown that mesoporous CZY mixed oxides with good physical properties (e.g., high surface area, homogeneous oxide, crystalline uniformity, and thermal stability) can be prepared using metal nitrate precursors and a variety of templates (e.g., CTAB, porous activated carbons, amine functionalized dendrimers, etc.) by classical sol-gel synthesis methods. However, CZY materials exhibiting long range order remained elusive.[65] In summary, to-date the synthesis of ordered mesoporous ceria, zirconia or yttria using a classical sol-gel approach has not been reported.

More recently, studies abandoning traditional sol-gel methods have successfully shown that ordered mesoporous zirconia and related materials can be prepared using evaporation induced self-assembly (EISA).[66, 67] This process enables the rapid

production of patterned porous or nanocomposite materials in the form of films, fibers or powders. With these systems, self-assembly of oxide precursors is driven by the evaporation of metal precursor containing organic solvents and the absorption of a hydrolyzing agent (water) from the vapor phase. As the hydrolyzing agent (water) slowly enters the organic metal-rich phase, metal oxide oligomers form, diffuse, and assemble around template materials included in the starting organic phase mixture. Following a further loss of organic solvent and the addition of sufficient water, a final inorganic oxide phase is formed around the template, often yielding a thin film exhibiting a long-range mesoporous architecture. For example, Hung et al.[58, 59] reported the synthesis of ordered yttria-zirconia mesoporous structures using chloride precursors for zirconia and yttria along with evaporation induced self-assembly (EISA) synthesis at 40° C for 3 days controlling the relative humidity at 40%. Using a variant of this same method, Yuan et al.[53, 54] reported the successful synthesis of ordered zirconia based functional materials. Kim et al. [48] and Yang et al. [44] also reported the use of EISA methods and zirconyl chloride as the metal precursor to obtain ordered mesoporous zirconia. Additionally, Li et al.[56] synthesized ordered ceria-zirconia macrostructures using nitrate metal precursors and block copolymer and PMMA colloidal microspheres as templates in a procedure resembling EISA. EISA methods were also combined with a novel type of amphiphilic block copolymer template by Brezesinski et al.[42] to yield mesostructured thin films of ceria, zirconia and ceria-zirconia mixed oxides having highly crystalline pore walls and ordered arrays of mesopores. Despite these advances, EISA has to-date not been used to

synthesize a highly-ordered porous oxide containing a homogeneous mixture of ceria, zirconia, and yttria oxides.

From this brief review, it should become apparent that traditional sol-gel methods are not easily adapted to the synthesis of order mesoporous materials containing a mixture of ceria, zirconia, and yttria (CZY) oxides, but evaporation induced self-assembly (EISA) methods show great promise for preparing such materials. Therefore, this work carefully describes the kinetic, thermodynamic and transport phenomena driving the formation of CZY mixed oxide structures using both templated sol-gel and EISA methods. It also compares the local structure and composition of mesoporous CZY oxides prepared using both methods, with special attention given to the distinct oxide structures that lead to the observation of mesoporosity via nitrogen physisorption techniques yet exhibit very different pore morphologies. More broadly, this chapter seeks to inform about the limitations associated with forming ordered mesoporous oxide materials via self-assembly processes employing structure directing agents.

Experimental

Materials. Pluronic® P-123 (M_{av} = 5800, PEO_{20} $PPO_{70}PEO_{20}$) and Pluronic® F-127 (M_{av} =12,600, PEO_{106} $PPO_{70}PEO_{106}$) were obtained from BASF. Zirconyl nitrate hexahydrate ($ZrO(NO_3)_2 \cdot 6H_2O$, 99%), zirconyl chloride octohydrate ($ZrOCl_2 \cdot 8H_2O$, 98%) and yttrium nitrate hexahydrate ($Y(NO_3)_3 \cdot 6H_2O$, 99.9%) were purchased from Sigma-Aldrich. Cerium nitrate hexahydrate ($Ce(NO_3)_3 \cdot 6H_2O$, 99.5%) was obtained from Alfa Aesar, while ammonium hydroxide (NH_4OH), hydrogen peroxide (H_2O_2), ethanol

and 1-propanol were obtained from Fisher Scientific. All chemicals were used as received without further purification.

A. Synthesis of Mesoporous CZY via classical sol-gel. In a typical synthesis, 0.75 g of zirconyl nitrate, 0.14 g of yttrium nitrate and 1.56 g of cerium nitrate were dissolved in 80 ml of distilled water; 0.5 ml of hydrogen peroxide was incorporated to the solution to oxidize Ce(III) to Ce(IV). Separately, a specified amount of Pluronic P123 was dissolved in 40-200 ml of an aqueous ethanol solution (50 vol% ethanol). The quantity of P123 included in the sol-gel was varied from 0.2 to 20 g, so as to test for Pluronic concentration effects. The two solutions were added together with vigorous stirring, drops of ammonium hydroxide were added slowly with mixing until reaching a pH of 10 or greater to precipitate the metal oxides. The resulting solution was aged for 1 day at about 100 °C in a closed PFA Teflon vial. The precipitate was washed and filtered to eliminate any impurities remaining in the product, then dried at 100 °C for 1 day and calcined in air at 400 °C for 4 hours using a heating rate of 1 °C/min. A subset of samples was calcined at 600 °C using the same heating rate.

B. Synthesis of CZY via EISA. Triblock copolymer Pluronic F127 (0.9-1.1 g) was dissolved in 10 ml of ethanol at room temperature. To this solution was added zirconyl chloride (0.8 g), yttrium nitrate (0.1 g) and of cerium nitrate (1.2 g), and the solution was stirred until all salts were completely dissolved. The resulting solution was aged for 1 to 2 days in an open petri dish at 40 °C and 50 % relative humidity (RH) in a humidity controlled oven until a gel is formed as a result of solvent evaporation and hydrolysis. The remaining product is finally dried at 100 °C for 1 day and calcined in air at 400 °C

for 4 hours using a heating rate of 1 °C/min to avoid collapse of the mesoporous structure. A subset of samples was calcined at 600 °C using the same heating rate.

Sample containers during the evaporation process were varied to have different evaporative surface areas and solution levels to allow ethanol evaporation rates to differ as well as to vary the influx of the hydrolyzing agent (water) to the system. Appendix F shows pictures of the EISA experimental process set up.

Characterization.

Catalyst structure was determined by several techniques including electron microscopy, x-ray diffraction and nitrogen physisorption methods. The bulk elemental composition of catalyst samples was determined using a Horiba JobinYvon ULTIMA 2 inductively couple plasma atomic emission spectrometer (ICP-AES). To dissolve the samples, 0.1 g of calcined CZY oxides were mixed in a PFA vessel with 0.5 g of ammonium sulfate ($(NH_4)_2SO_4$), 10 ml of concentrated sulfuric acid (H_2SO_4) and 30 ml of distilled water. The sample dissolution was carried out in a CEM Mars 5 Microwave Accelerated Reaction System with microwave power range between 0 to 100% with options of 300, 600 and 1200 W. The microwave digestion protocol consisted of 5 heating stages, where the samples were heated to progressively lower digestion temperatures of 230, 200, 180, 130 and 120 °C over the course of five hours, with each sample maintained for 1 hour at each of the specified temperatures. All microwave heating stages were performed at 600 W and 100% power. Thermogravimetric analysis (TGA) and differential scanning calorimetry (DSC) of as-synthesized (i.e., dried but not calcined) CZY samples were carried out using a SDT Q600 Simultaneous DSC/TGA

analyzer, and the results used to evaluate the thermal stability and optimal calcination temperature for the samples.

Nitrogen adsorption and desorption isotherms at 77 K were measured using a Micromeritics ASAP 2020 system after the samples were outgassed at 473 K overnight. The sorption data were analyzed using the Barret-Joyner-Halenda (BJH) model to obtain the pore size distribution and with the Brunauer-Emmet-Teller (BET) model for surface area. Phase characterization was performed by powder X-ray diffraction (PXRD) using a Scintag XDS Model 2000 diffractometer and a Rigaku Ultima IV X-ray diffractometer with Cu Kα radiation (λ = 1.5406 Å) and Ni filter, operated at 30 kV-20 mA and 40 kV-44 mA, respectively. Small–angle X-ray diffraction (SAXD) patterns were obtained with the Rigaku Ultima IV X-ray diffractometer and used to show the presence of ordered mesopores in the samples.

The transmission electron microscopy (TEM) studies were carried out on a Hitachi H9500 TEM, a Hitachi H7600 TEM and on a Hitachi HD 2000 STEM at 300, 120 and 200 kV, respectively, to determine the morphology and pore sizes for the samples.

Results

Characterization of Materials

Mesoporous CZY samples were obtained via classical sol-gel techniques as well as evaporation induced self-assembly processes. Commercial block copolymers and inexpensive salts were chosen as starting materials, so as to evaluate synthesis techniques that are more commercially viable. The mixture of ceria, zirconia and yttria used during

material synthesis is representative of the composition of three-way catalyst supports that are commonly used for automotive exhaust emissions control applications.

Elemental composition studies using ICP-AES were carried out in order to determine if the proportions of oxides included during synthesis were unchanged after all synthesis and calcination processes. This is important because prior studies have shown that catalytic converter performance can be significantly enhanced using specific ratios of ceria, zirconia, and yttria oxides as catalyst supports.[68-70] The results are shown in Table 4.1. These and other composition data indicate that all three metals are well incorporated into the final oxide structures in the proportions used during their respective synthesis.

Table 4.1. Elemental composition of representative CZY synthesis mixtures and calcined products.

Sample	**ZrO_2 (mol%)***	**$YO_{1.5}$ (mol%)***	**CeO_2 (mol%)***
Starting Sol Gel Mixture	35.30	5.88	58.82
Post-Calcination Classical Sol-gel Sample	36.85	5.86	57.30
Starting EISA Mixture	45.00	5.00	50.00
Post-Calcination EISA Sample	43.25	5.55	51.24

* Elemental composition error is ± 0.5 mol%.

From earlier studies, it is well known that the overly aggressive calcination of organically templated CZY oxides can lead to the precipitous collapse of their pore structure[65]. This collapse can be induced by high temperature (>600 °C) calcination processes as well as the local generation of hot spots via the rapid oxidation of occluded organics (template). The former can be mitigated by limiting the upper temperature to which the sample is exposed, while the latter is avoided by reducing the calcination

heating rate to an appropriate level. To identify the minimum temperature that can be used to completely remove the organic structure directing agent via calcination in air, thermogravimetric (TGA) studies, see Fig. 4.1, were conducted on non-calcined samples synthesized by both sol-gel and EISA techniques. For the classical sol-gel synthesized sample, the amount of organic template incorporated during synthesis is much less than in the case of EISA samples even though the amount of template used for sol-gel synthesis was twice the quantity used for EISA synthesis. This can be explained by the fact that sol-gel samples go through washing and filtration steps before drying and EISA samples do not. For materials synthesized by both methods, oxidation of the organic template begins at approximately 190 °C and is completed at around 350 °C, which confirms that 400 °C is a reasonable calcination temperature for these materials.

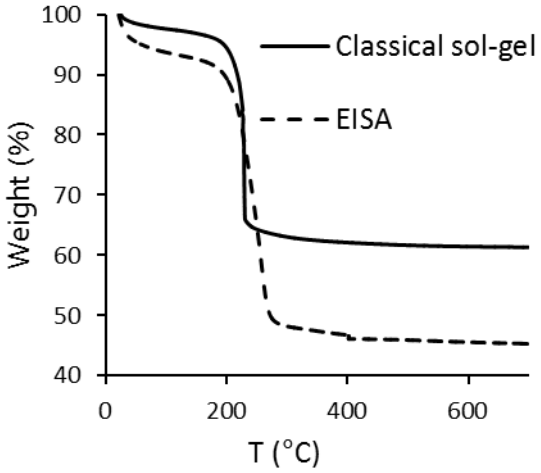

Figure 4.1. Thermogravimetric analysis of CZY samples synthesized using sol-gel and EISA methods (in air at a heating rate of 1 °C/min).

Differential scanning calorimetry (DSC) was used to identify heating rates and temperatures that might lead to the local generation of hot spots that are capable of

collapsing the mesoporous CZY oxide pore structure. It should also be recognized that the upper allowable heating rate is a function of the organic loading of the starting CZY material, with higher loadings demanding lower calcination heating rates. The DSC and TGA curves of the classical sol-gel synthesized CZY materials at different template concentrations are shown in supporting information. Two different calcination protocols were compared in order to decide if the heating rate had any effect on the final calcined structure. Heating rates of 1 and 20 °C/min were tested but the latter showed incomplete template removal at 400 °C. Moreover, TEM images showed samples calcined at 20 °C/min had structurally collapsed. Thus, calcination heating rates of 1 °C/min were always used.

The nitrogen adsorption/desorption isotherms and the Barret-Joyner-Halenda (BJH) pore size distribution for classical sol-gel and EISA synthesized CZY oxides are shown in Figure 4.2. Both samples exhibit the same isotherm and pore size distribution shapes. The hysteresis loops shown in the plots resemble that of a type IV isotherm, indicating the presence of mesopores. The pore size distribution (inset) is unimodal for both materials with an average pore size of 6.2 ± 0.5 nm and 4 ± 0.5 nm for classical sol-gel and EISA samples, respectively. Likewise, the BET surface area is similar for both materials, with the classical sol-gel and EISA materials having calculated surface areas of 96 ± 5 m^2/g and 105 ± 5 m^2/g, respectively. These results demonstrate that samples synthesized by both techniques have high surface areas, large pore volumes and narrow pore size distributions.

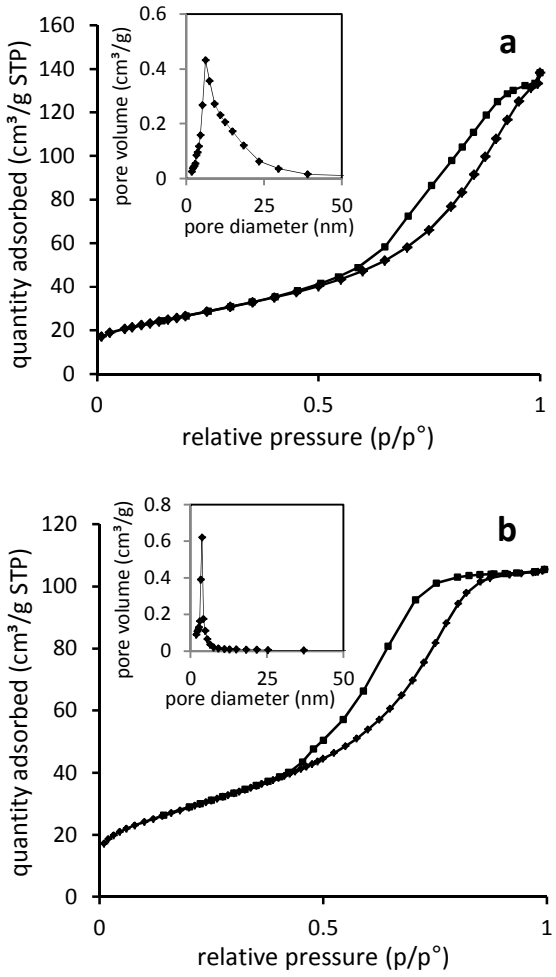

Figure 4.2. N_2 adsorption-desorption isotherms and BJH pore size distribution (inset) for (a) classical sol-gel and (b) EISA synthesized CZY materials.

It was observed that the BET surface area for the CZY materials synthesized using sol-gel technique A increased with P123 composition. The original molar ratios were $10CeO_2$:$6ZrO_2$:$1YO_{1.5}$:1P123 and were varied from a P123 molar ratio of 0.1 to a ratio of 10. For materials prepared using this range of P123 concentrations, the BET surface area of samples increased from 92 to 165 m^2/g, respectively. Likewise, the average BJH pore diameter of samples increased from 5.2 to 17.9 nm. Thus, the presence of larger amounts of block copolymer in the synthesis sol-gel leads to increases in the observed pore size of

calcined samples, indicating that the P123 template is incorporated in the as-synthesized CZY solid in proportion to its concentration in solution.

Powder X-ray diffraction (PXD) was used to ascertain the presence of ordered pores as well as the type(s) and size(s) of crystalline domains within calcined CZY samples. Example wide-angle powder x-ray diffractograms for calcined CZY materials prepared using classical sol-gel and EISA syntheses are shown in Figure 3. The wide-angle XRD patterns for all materials were similar showing well-resolved broad peaks similar to those observed with a reference ceria material, indicating that the crystalline domains within the samples exhibit the same cubic structure as ceria[71].

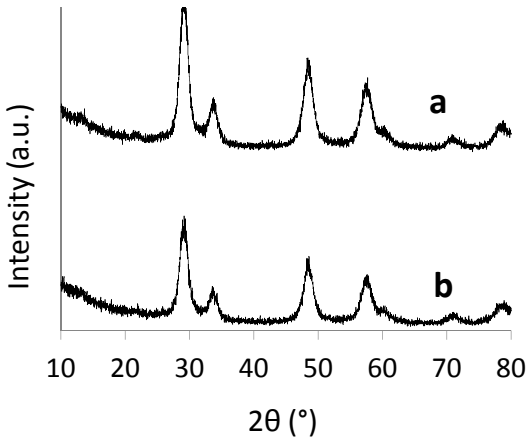

Figure 4.3 Wide-angle powder X-ray diffractogram of representative CZY mixed oxides prepared via classical sol-gel (b) and EISA (a) methods.

The line broadening in the XRD patterns indicates that the powders consist of nanocrystalline oxide domains. Additionally, the absence of split ends at the peaks suggests that no phase segregation occurred, which indicates that the final product is a homogeneous framework consisting of well dispersed crystalline domains that are cross-linked by oxides that are likely of similar composition. The size of the observed

crystalline domains was between 4.3 and 5.6 nm as calculated by the Scherrer equation, using the diffraction peak centered near a 2θ angle of 29°.

The concentration of P123 in the initial sol-gel did not appear to play a role in the type of oxide phase formed in classical sol-gel synthesized samples, as the PXD patterns are similar for all P123 concentrations tested. However, the size of the oxide crystallites tends to decrease as the concentration of the template was increased. This result agrees quite well with the trends observed in the BET surface area analysis, where higher surface area and pore volume suggest that smaller crystallites are forming on the periphery of the larger P123 aggregates during synthesis via classical sol-gel methods.

The small angle XRD patterns for samples synthesized by techniques A and B are shown in Figure 4.4. The XRD pattern for samples prepared by the classical sol-gel (A) technique did not reveal any low angle peaks between 1° and 2°, whereas the EISA synthesized samples showed a clear peak at 1.1°. The presence of reflections at small angles suggests that the EISA synthesized sample may consist of a highly regular or ordered mesostructure throughout the material. Confirmation of such a structure was achieved used TEM analysis. This is the first result that shows significant differences between samples prepared by the differing sol-gel methods and is related to the ordering of the mesopores. Using Bragg's law, the low angle XRD peak in the EISA samples corresponds to a mesopore diameter of 8 nm.

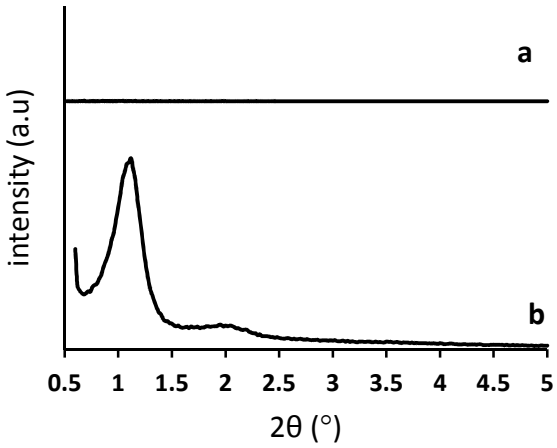

Figure 4.4. Comparison of small-angle powder X-ray patterns for synthesized CZY mixed oxides by (a) classical sol-gel and (b) EISA techniques.

In order to better understand the types of mesostructures present in the classical sol-gel and EISA derived samples, TEM images were collected for representative samples and are shown in Figure 4.5. Numerous highly ordered pores with average pore size of 8 nm were observed for EISA synthesized samples calcined at 400 °C (Fig. 4.5b) versus an agglomeration of nanosized particles exhibiting no order for the oxides synthesized by the classical reaction-limited sol-gel technique and calcined both at 400 °C and 600 °C (Fig. 4.5a).

High-resolution TEM (HRTEM) shows that the walls of the EISA derived samples are highly crystalline with a lattice spacing of 0.298 nm (see Fig. 4.5c). HRTEM of the classical sol-gel synthesized samples also exhibited regions of high crystallinity, though those regions were more spherical in nature. Additionally, HRTEM analysis of EISA samples showed that the ordered framework was lost if the materials was calcined at higher temperatures (600 °C, Fig.4.5d). While mesopores are clearly observed for all

samples, only the samples synthesized via the EISA method have well-ordered mesopores, as predicted by low angle PXD.

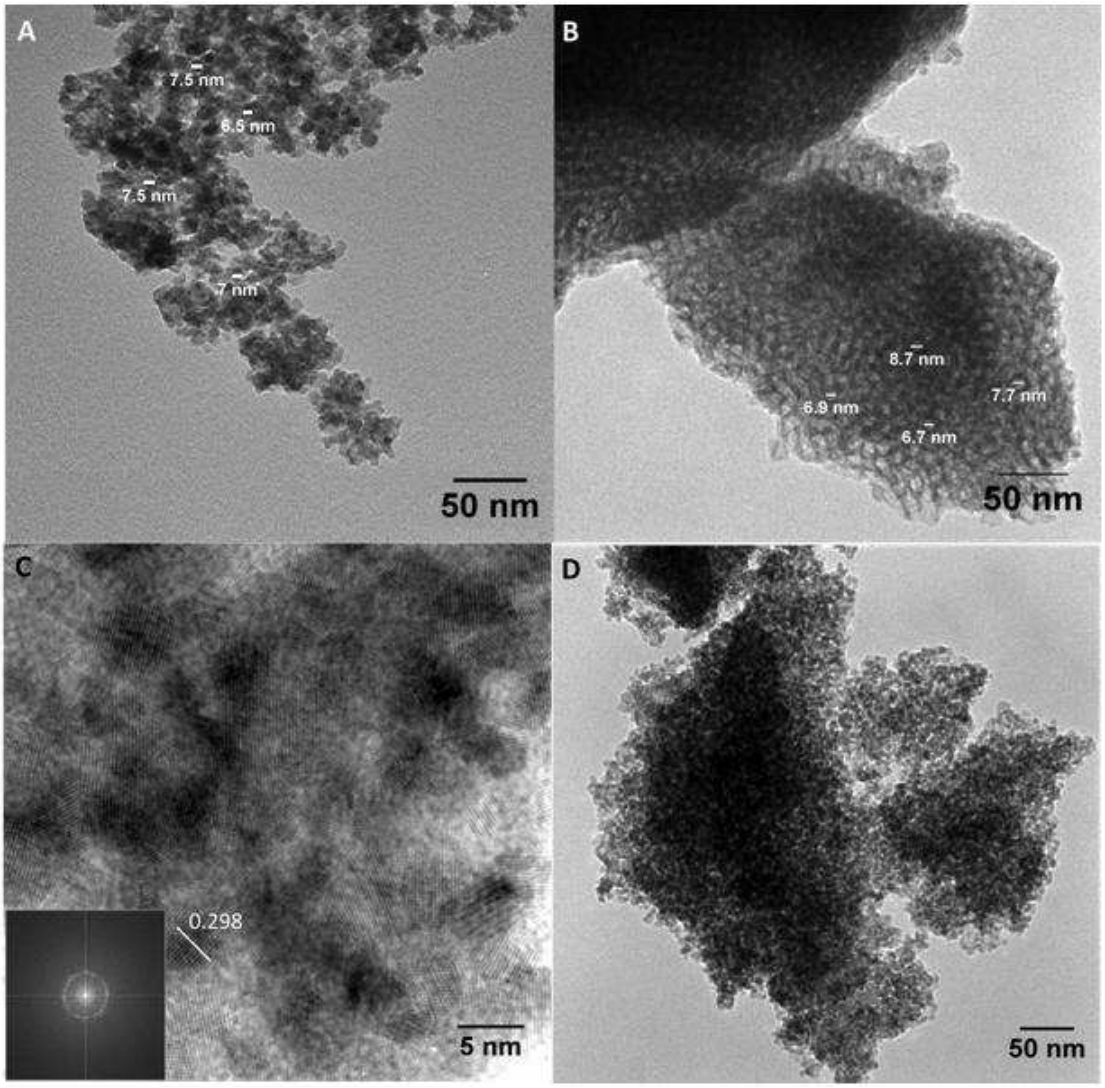

Figure 4.5. TEM images of mesoporous CZY mixed oxides by (a) reaction-limited classical sol-gel and (b) EISA methods; (c) HRTEM of EISA synthesized CZY (FFT diffractogram inset) and (d) EISA derived CZY material after calcining at 600°C.

Synthesis-structure relationships for the EISA method

Given that the EISA synthesis method is a diffusion-limited process (as opposed to the reaction-limited scheme observed with classical sol-gel methods), it is important to

understand how experimental variables may influence the diffusion phenomena that directly impact final catalyst structure. For these studies, different sample containers were used during the evaporation process with the purpose of having different evaporative surface areas and solution levels so as to allow ethanol evaporation rates to differ as well as to vary the influx of the hydrolyzing agent (water) to the system. Certainly, the geometry and size of the evaporative container made an impact on the results. TEM images for zirconia samples synthesized by EISA methods employing reaction vessels of varying geometry are shown in Figure 4.6.

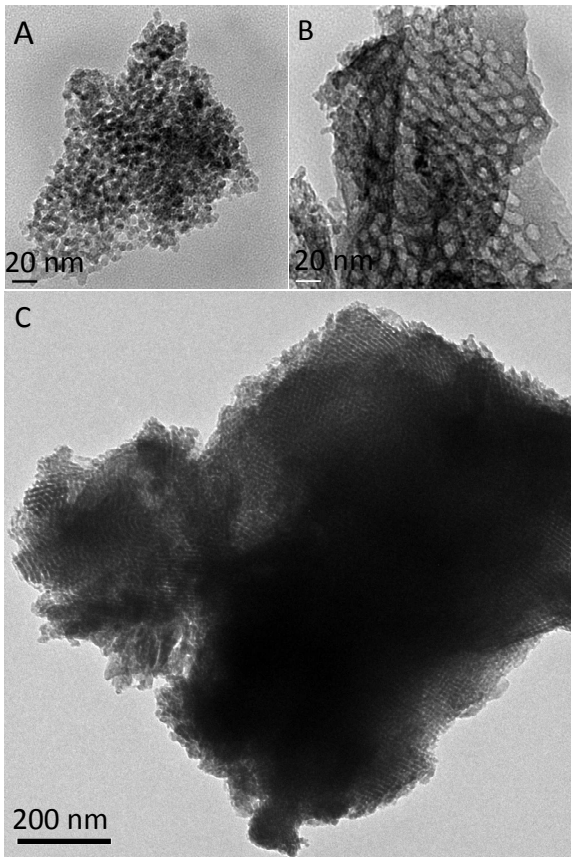

Figure 4.6 TEM of calcined zirconia samples synthesized using EISA and evaporated in cylindrical vessels of different dimensions: (a) 50ml capacity with a starting liquid level of 25 ml (d= 4cm, h= 5 cm); (b) 15 ml capacity with starting level of 3 ml (d= 1.5 cm, h= 9 cm) and (c) 100 ml capacity with a starting liquid level of 1 ml (d = 9 cm, h = 1.6 cm).

Samples evaporated in the 50 ml dish filled at half capacity (Fig. 6a) did not show any order. This can be explained by the large surface area of the container, which increased the evaporation rate, and the relatively high liquid depth that promoted large concentration gradients through the sample. An important observation made during the gelling process for samples in this size vessel was the appearance of a hard, oxide-rich layer (or crust) on top of the evaporating solution. This crust consists of precipitated oxides, which form a network that prevents the homogeneous evaporation of solvents from the container, thereby, limiting the formation of ordered materials in the remainder of the solution. It is possible that some of these samples did contain a small amount of ordered mesoporous material, but no such material was observed by either low angle PXD or HRTEM.

CZY oxide materials with ordered arrangements of mesopores were observed in samples prepared in the test tube (6b) and Petri dish (6c). Samples evaporated in the test tubes had a long aging stage since the small diameter of the container slowed the evaporation of ethanol, often a week was required to completely evaporate all the alcohol. However, they showed non-homogeneous results, the sample contained both ordered and disordered arrangements of CZY oxides. This is a result of the large concentration gradient through the sample, which varied over time. At the start of the EISA process, the test tubes were fuller and the evaporation process was faster, but as the solution level dropped the rate of ethanol evaporation and water infusion also decreased, reducing the concentration of hydrolyzing species in the reactive sol-gel solution.

On the other hand, thin samples prepared in Petri dishes proved to be more homogeneous, yielding very ordered structures, so long as the relative humidity and temperature were kept very steady at 40 °C and 50% RH, and the air flow across the surface of the samples was low. For this purpose, samples were kept inside a specially designed box, residing in a well-mixed convection oven, which allowed air to flow slowly across the sample in one direction, keeping the sol-gel evaporation rates at a low level (see Appendix F). If air was allowed to flow at high speed over the samples, the evaporation process was accelerated resulting in disordered structures. The rapid evaporation of solvent caused by rapid air flow provides insufficient time for the polymerizing oxide structures to diffuse and self-assemble around the existing micelles; thus, larger bulk oxide particles are formed.

The ratio of precursors to template is another factor to consider in the synthesis of these materials. It has to be finely tuned so as to ensure that the optimal number of appropriately-sized micelles are formed during the synthesis process. The optimal template concentration is impacted by the choice of solvent, the chemical nature and solubility of the templating agent, and the localized concentration of salts and hydrolyzing agents. With the aim of tuning this quantity, different Pluronic concentrations were tested for the classical sol-gel process. However, TEM images did not indicate a significant change in morphology between these samples. Similar studies have been previously done for the for the EISA process; therefore, the optimal template concentrations identified in those studies was used for all EISA samples.[53]

Discussion

Based on my experimental observations and the known chemical behavior of the reagents that are used to prepare CZY materials, I present in Figure 4.7 a graphical representation of the mechanistic pathways taken by classical sol-gel and EISA synthesis methods for CZY and related oxide materials. It is important to note that the chemical behavior depicted in Fig. 4.7 is derived from fast reacting metal salt precursors; thus, slower reacting silica based reagents will not show the same tendency.

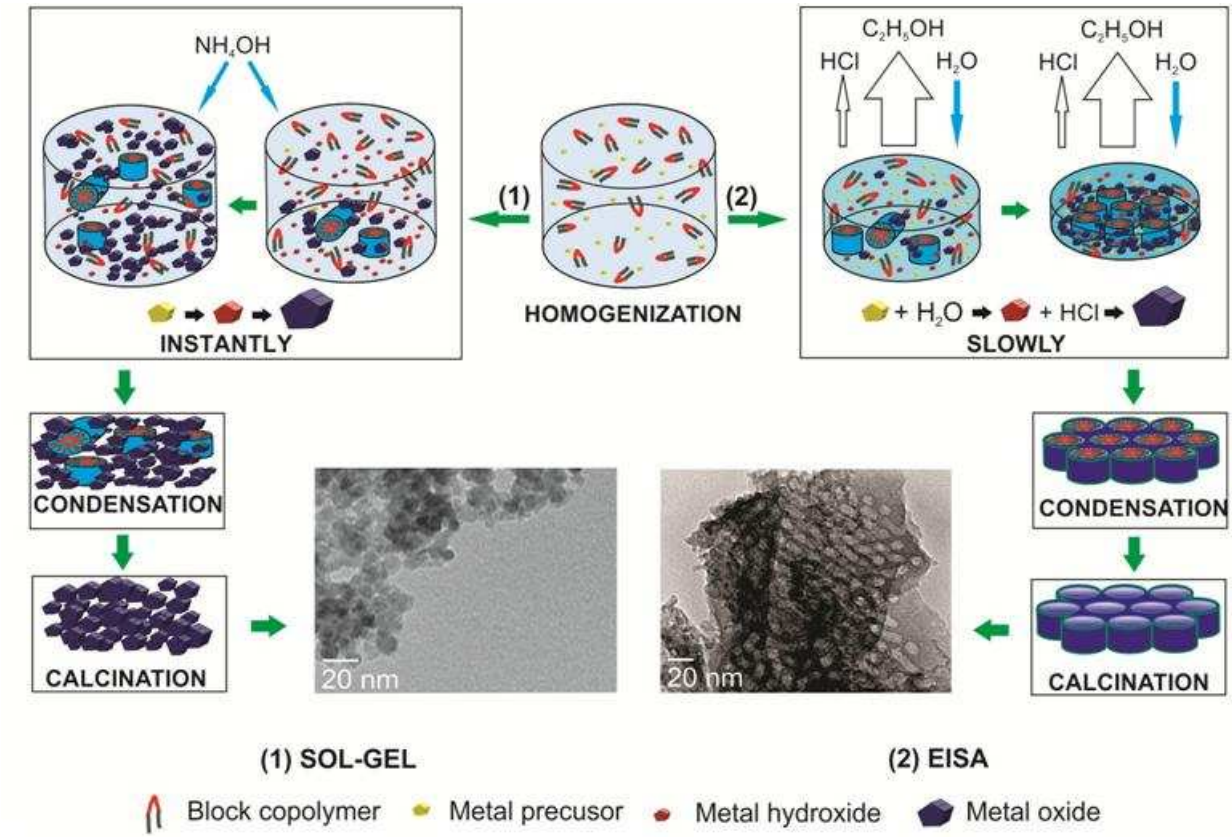

Figure 4.7. Synthesis of mesoporous CZY oxides by (1) classical sol-gel and (2) EISA techniques. In the classical sol-gel synthesis, the precursors are in a closed system and rapidly undergo hydrolysis and condensation without allowing sufficient time for the ordering of oxide oligomers around self-organized micellar structures. On the contrary, the EISA method employs an open system in which the reaction is limited by the rate at which water diffuses from the atmosphere into the reaction solution. By significantly

slowing the rate of reaction, the micelle structure is allowed sufficient time to self-assemble and oxide precursors allowed to diffuse and assemble around this framework before becoming locked in place by the formation of cross-linking or network forming oxide bonds.

The classical sol-gel (pathway 1) method involves all materials being mixed in an ethanolic solution (50% vol.) at the start of the process and the mixture contained in a closed vessel. The use of water in the sol-gel solution immediately transforms the CZY precursor salts into highly reactive hydroxides. The hydrated metal salts associate with water generating hydroxy ligated metals species and the respective acid (HCl or HNO_3):

$$[M–OH_2]^{z+} \rightarrow [M–OH] + H^+ \text{ (Hydrolysis)}$$

During this acidification process, template micelles are beginning to form and some condensation is occurring as the hydroxides come in contact with one another. This process is further accelerated by the addition of ammonium hydroxide, resulting in the immediate generation of the oxides via condensation reactions:

$$M–OH + M–OH \rightarrow M–OH–M–OH \rightarrow M–O–M + H_2O$$

With this classical sol-gel synthesis approach, it is the rate of metal hydroxy(oxide) condensation that defines the final product morphology. Other reaction parameters like temperature, water concentration, and the type of reaction vessel do not have a major effect on the structure of the final material produced, making this process a *reaction-limited process*. The lack of periodicity in the arrangements (Fig 4.5a) is caused by the short time (minutes) in which the hydrolysis-condensation reactions occur, which provide insufficient time for 1) the micelles to self-assemble into secondary structures and 2) the oxide oligomer precursors to diffuse and self-assemble around the micellar array. The specific micelle formation rate constants for block copolymers are scarce, especially

since each experimental condition affects these rate constants greatly and even reported values for the same block copolymer often differ significantly. I do not provide them as for the best of my knowledge they have not been reported before for this specific system.

Once the basic hydrolyzing agent (ammonium hydroxide) is added to the sol-gel and mixed throughout the solution, the base catalyzed condensation reactions occur rapidly resulting in the immediate precipitation of agglomerated oxide particle that do not exhibit long range order or the presence of an ordered pore structure. Due to the absence of oxide precursor ordering, the classical sol-gel synthesis method yield random arrangements of CZY oxides nanoparticles with mesopores resulting from the voids generated by the removal of the Pluronic template from between the loosely connected oxide nanoparticles. It is unclear at this point as to the full extent to which the presence of the template controls or influences the size of the oxide nanoparticles formed, but initial findings by our group using HRTEM suggest that higher template loadings lead to the formation of oxides consisting of agglomerations of smaller oxide nanoparticles (i.e., higher template concentrations yield agglomerates of smaller oxide nanoparticles).

The classical sol-gel process generates particles and pores of the right size with large surface area, good oxide incorporation, crystalline uniformity and thermal stability as the results have shown but does not yield ordered mesostructures. In order to generate an ordered oxide structure, one must limit or control the rate of metal hydrolysis so as to allows time for the structure directing agent (SDA) to self-organize and also permits the simultaneous condensation-polymerization process of the metal oxides to generate a

robust ordered oxide network around the template. In this sense, a slow controlled reaction/assembly process is necessary to create the material desired.

In contrast, evaporation induced self-assembly is an open system synthesis. The starting solution, salts dissolved in alcohol, contains only water from the hydrated salts. The water necessary for hydroxide formation and condensation is gradually available as it diffuses into the reaction medium from the atmosphere. As a result, precursors are slowly converting into hydroxides by reacting with water coming from the humidity of the environment (set at 50%).This hydrolysis of zirconium oxide chloride and cerium and yttrium nitrates provides an acidic environment and slows the oxide formation allowing sufficient time for the self-arrangement of SDAs into micellar arrays. As the block copolymers become micelles, these micelles start to form secondary structures; the hydrolysis process continues and condensation occurs as hydroxides react with each other forming metal oxides. Furthermore, these metal oxides will also associate with each other allowing oxide polymerization. Again, the acidic environment generated by the hydrolysis reaction slows down the cross-linking rate of the doped metal species making their condensation-polymerization process occur at the same time. These oxides will organize around the micelle arrangement as a result of the interactions between them. Also the acidic environment is kept through the process and no base is added to accelerate reactions as in classical sol-gel which makes this process of self-arrangement happens slowly over the course of 24 to 48 hours in the EISA method, compared to minutes in the case of classical sol-gel. This self-assembly process is responsible for the final highly ordered mesostructure obtained by EISA and shown in figure 4.5b.

For this method the use of chloride precursors is highly important. This can be explained by taking a look at the reaction process:

$$[M^{+}– Cl^{-}]+ H_2O \rightarrow [M–OH] + HCl\ (\uparrow)$$

The hydrolysis process for the metal chloride generates HCl that tends to evaporate. The acidity of the solution changes and the equilibrium is forced ahead. At the same time, water enters the system and more HCl is formed slowing the reaction rates again and the process is repeated.

$$[M^{+}– NO_3^{-}]+ H_2O \rightarrow [M–OH] + HNO_3\ (\ell)$$

Nitric acid on the other hand is not volatile and tends to stay in solution. More time is required to get the same extent of reaction as HCl which makes it less effective for the reaction process extending gelation time. It has been reported that for these oxides at least one chloride precursor is necessary to obtain an ordered arrangement of pores whereas using only nitrates as precursors will not generate ordered arrangements[53].

The diffusion rates of water and ethanol into and out of solution during this procedure are extremely important as they control the speed of the hydroxide formation reaction and ultimately control the material's morphology. Although water is directly responsible for hydrolysis reactions, fast evaporation of ethanol accelerates the aging process, possibly preventing the self-assembly of the SDAs.

Another issue is the homogeneity of the system as a fast evaporation rate induces a large concentration gradient in the sample whereas a slow one will favor a more homogeneous solution. The concentration gradient through the sample is promoted by the evaporation at the solution-air interface due to which the transformation to the

supramolecular arrangement first appears at the interface[74]. Large concentration gradients (CG) are likely to generate multiphase systems since the reagents do not have the same chemical composition at both interfaces. In such a case, the top part of the film tends to be ethanol deficient condensing prematurely and possibly trapping an intermediate phase as a result of this poor mobility. This is explained by a too high local rigidity and less time to permit rearrangement for fast systems. As a result, higher degree of orientation is favored for lower evaporation rates. In my experience, there are numerous cases were I find systems with ordered and disordered structures within the same sample resulting from such a scenario (Fig. 4.6b).

This means EISA is actually a *diffusion-limited* process; hydrolysis and condensation reactions do not occur immediately but are constrained by the diffusion of water into the initial solution and the evaporation of ethanol from it which depends on temperature, relative humidity (RH) and numerous other factors.

Near the end of the evaporation process, the micelle structure has been formed and oxides have polymerized around it in a robust network. Temperature and relative humidity are main factors that come into play at this stage as well, affecting the formation of ordered structures (for this case, typical conditions for EISA of 40 °C and 50% RH were adopted). Besides its importance as a water source for the hydrolysis reactions during the synthesis process, humidity is especially important since it has been demonstrated[66] that the control of the final mesostructure is possible by allowing water to reenter and depart the film (swelling and contracting of the hydrophilic network) during the modulable steady state. The concept of a modulable steady state was introduced by

Cagnol et al.[66] and corresponds to the end of the drying line (all solvent has been evaporated). At this point, too low or too high humidity can lead to disordered structures. Finally, as the micellar structure has been formed and the oxide network has strengthened around it, the last step is template removal. The block copolymer structure is calcined at low heating rates (1 °C/min) to a maximum of 400 °C, since it has been shown that going to higher temperatures (600 °C ; Fig 4.5d) or heating rates (20° C/min; not shown) results in structure collapse. After calcination an ordered porous oxide network is obtained.

Conclusions

This chapter shows that a slow controlled reaction/assembly process is necessary to create ordered CZY mesostructures since reducing the reaction rate allows time for the SDA to self-organize and also permits the simultaneous condensation-polymerization process of the metal oxides to generate a robust ordered oxide network.

Classical sol-gel and EISA techniques generated materials with very good properties but the creation of an ordered structure proved to be difficult. For classical sol-gel the reaction rate defined the final product morphology since the short time at which the reactions occur do not allow enough time for the micelles self-assembly into secondary structures. In contrast, evaporation induced self-assembly is a diffusion-limited process where hydrolysis and condensation reactions do not occur immediately but are constrained by the diffusion of water into the initial solution and the evaporation of ethanol from it which depends on temperature, relative humidity and numerous other factors. The acidic environment generated by the hydrolysis reaction slows down the cross-linking rate of the metal species making their condensation-polymerization process

occur at the same time as micelles self-assembly into supramolecular structures to provide the final ordered framework.

Another issue to take into consideration for EISA was the control of the diffusion rates of water and ethanol. Although water is directly responsible for hydrolysis reactions, fast evaporation of ethanol accelerates the aging process possibly preventing the self-assembly of the SDAs and also might create non-homogeneous multiphase systems where ordered and disordered structures appear in the same sample.

Acknowledgements. This study was supported by Toyota Motor Engineering & Manufacturing North America, Inc. The authors would like to acknowledge Haijun Qian for his help with TEM imaging of CZY samples.

References

(1) Bhaumik, A.; Tatsumi, T. *J. Catal.* **2000**, *189*, 31-39.

(2) Aprile, C.; Abad, A.; Garcia, H.; Corma, A. J. *J. Mater. Chem.* **2005**, *15*, 4408-4413.

(3) Fujiwara, M.; Terashima, S.; Endo, Y.; Shiokawa, K.; Ohue, H. *Chem. Comm.* **2006**, 4635-4637.

(4) Chandra, D.; Laha, S. C.; Bhaumik, A. *Appl. Catal. , A: Gen.* **2008**, *342*, 29-34.

(5) Yoshitake, H.; Yokoi, T.; Tatsumi, T. *Chem. Mater.* **2003**, *15*, 1713-1721.

(6) Gierszal, K. P.; Jaroniec, M. *J. Phys. Chem. C* **2007**, *111*, 9742-9748.

(7) Sathe, T. R.; Agrawal, A.; Nie, S. *Anal. Chem.* **2006**, *78*, 5627-5632.

(8) Fan, R.; Huh, S.; Yan, R.; Arnold, J.; Yang, P. *Nat. Mater.* **2008**, *7*, 303-307.

(9) Vallet-Regı, M. *Chem. Eur. J.* **2006**, *12*, 5634-5643.

(10) Yang, P.; Quan, Z.; Li, C.; Lian, H.; Huang, S.; Lin J. *Microporous Mesoporous Mater.* **2008**, *116*, 524-531.

(11) Beck, J. S.; Vartuli, J. C.; Roth, W. J.; Leonowicz, M. E.; Kresge, C. T.; Schmitt, K. D.; Chu, C. T. W.; Olson, D. H.; Sheppard, E. W.; McCullen, S. B.; Higgins, J. B.; Schlenker, J. L. *J Amer Chem Soc* **1992**, *114*, 10834-10843.

(12) Schuth, F. *Chem. Mater.* **2001**, *13*, 3184-3195.

(13) Schuth, F. *Angew. Chem. Int. Ed.* **2003**, *42*, 3604-3622.

(14) He, X.; Antonelli, D. *Angew. Chem. Int. Ed.* **2002**, *41*, 214-229.

(15) Jaenicke, S.; Chuah, G.; Raju, V.; Nie, V. *Cat Surv Asia* **2008**, 153-169.

(16) Yuan, Q.; Li, L.; Lu, S.; Duan, H.; Li, Z.; Zhu, Y.; Yan, C. *J Phys. Chem. C* **2009**, *113*, 4117-4124.

(17) Badwall, S. P. S. *Appl. Phys. A* **1990**, *50*, 449-462.

(18) Garvie, R. C.; Hannik, R. H.; Pascoe, R. T. *Nature* **1975**, *258*, 703-704.

(19) Murase, Y.; Kato, E. *J. Am. Ceram. Soc.* **1982**, *66*, 196-200.

(20) Phillips, J. M. *J. Appl. Phys.* **1996**, *79*, 1829-1849.

(21) Leon, C.; Lucia, M.L.; Santamaria, J. *Phys. Rev. B* **1997**, *55*, 882-887.

(22) Mansour, N.; Mansour, K.; Stryland, E. W. E.; Soileau, M. J. *J. Appl. Phys.* **1990**, *67* 1475-1477.

(23) Wilk, G. D.; Wallace, R. M.; Anthony, J. M. *J. Appl. Phys.* **2001**, *89*, 5243-5276.

(24) Affanasev, V. V.; Houssa, M.; Stesmans, A.; Heyns, M. M. *Appl. Phys. Lett.* **2001**, *78*, 3073.

(25) Micheli, A. L.; Dungan, D. F.; Mantese, J. V. *J Am Ceram Soc* **1992**, *75*, 709-711.

(26) Mamak, M.; Coombs, N.; Ozin, G. *J. Am. Chem. Soc.* **2000**, *122*, 8932-8939.

(27) Mamak, M.; Coombs, N.; Ozin, G. *Adv Mater* **2000**, *12*, 198-202.

(28) Chen, F.; Liu, M. *J. Mater. Chem.* **2000**, *10*, 2603-2605.

(29) Wang, Y.; Yin, L.; Palchik, Y.; Hacohen, Y.; Kotypin, A.; Gedaken, A. *Langmuir* **2001**, *17*, 4131-4133.

(30) He, H.; Dai, H.; Ng, K.; Wong, W.; Au, T. *J. Catal.* **2002**, *206*, 1-13.

(31) Ho, C.; Yu, Y.; Wang, X.; Lai, S. Y.; Qui, Y. F. *J. Mater. Chem.* **2005**, *15*, 2193-2201.

(32) Chen, L. F.; Gonzalez, J. A.; Wang, L. E.; Norena, A.; Toledo, S.; Castillo, M.; Moran-Pineda, M. *Appl. Surf. Sci* **2005**, *243*, 319-328.

(33) Kašpar, J.; Fornasiero, P.; Graziani, M. *Catalysis Today* **1999**, *50*, 285-298.

(34) Jen, H. -.; Graham, G. W.; Chun, W.; McCabe, R. W.; Cuif, J. -.; Deutsch, S. E.; Touret, O. *Catalysis Today* **1999**, *50*, 309-328.

(35) Putna, E. S.; Bunluesin, T.; Fan, X. L.; Gorte, R. J.; Vohs, J. M.; Lakis, R. E.; Egami, T. *Catalysis Today* **1999**, *50*, 343-352.

(36) Ohata, T.; Tsuchitani, K.; Kitaguchi, S. European Patent Patent EP0337809, 1989.

(37) Tanaka, H.; Yamamoto, M. *SAE Technical Papers* **1996**, 960794.

(38) Yamamoto, M.; Tanaka, H. *SAE Technical Papers* **1998**, *1353*, 1.

(39) Taguchi, A.; Schüth, F. *Microporous and Mesoporous Materials* **2005**, *77*, 1-45.

(40) Lyons, D. M.; Ryan, K. M.; Morris, M. A. *J. Mater. Chem.* **2002**, *12*, 1207-1212.

(41) Brezesinski, T.; Smarsly, B.; Groenewolt, M.; Antonietti, M.; Grosso, D.; Boissière, C.; Sanchez, C. *N e w J . C h e m .* **2005**, *Volume 156*, 243-248.

(42) Brezesinski, T.; Antonietti, M.; Groenewolt, M.; Pinna, N.; Smarsly, B. *New J. Chem.* **2005**, *29*, 237-242.

(43) Li, X.; Chen, F.; Lu, X.; Ni, C.; Chen, Z. *Journal of rare earths* **2009**, *27*, 943-947.

(44) Yang, P.; Zhao, D.; Margolese, D. I.; Chmelka, B. F.; Stucky, G. *Chem. Mater.* **1999**, *11*, 2813-2826.

(45) Larsen, G.; Lotero, E.; Nabity, M.; Petkovic, L.; Shobe, D. *Journal of Catalysis* **1996**, *164*, 246-248.

(46) Rezaei, M.; Alavi, S.; Sahebdelfar, S.; Xinmei, L.; Yan, Z. *J Mater Sci* **2007**, *42*, 7086-7092.

(47) Blin, J. L.; Flamant, R.; Su, B. L. *International Journal of Inorganic Materials* **2001**, *3*, 959-959-972.

(48) Kim, A.; Bruinsma, P.; Chen, Y.; Wang, L.; Liu, J. *Chem. Commun.* **1997**, 161-162.

(49) Ni, C.; Li, X.; Chen, Z.; Li, H. H.; Jia, X.; Shah, I.; Xiao, J. Q. *Microporous and Mesoporous Materials* **2008**, *115*, 247-252.

(50) Chen, H.; Yan, J.; Ye, Z.; Zhang, L.; Gao, J.; Shi, J.; Yan, D. *J Mater Sci* **2009**, *44*, 6531-6531-6537.

(51) Yuan, Z.; Vantomme, A.; Léonard, A.; Su, B. *Chem. Commun.* **2003**, , 1558-1559.

(52) Ciesla, U.; Froba, M.; Stucky, G.; Schuth, F. *Chemistry of Materials* **1999**, *11*, 227-234.

(53) Yuan, Q.; Li, L.; Lu, S.; Duan, H.; Li, Z.; Zhu, Y.; Yan, C. *The Journal of Physical Chemistry C* **2009**, *113*, 4117-4124.

(54) Yuan, Q.; Liu, Q.; Song, W.; Feng, W.; Pu, W.; Sun, L.; Zhang, W.; Yan, C. *J. Am. Chem. Soc.* **2007**, *129*, 6698-6699.

(55) Deshpande, A. S.; Pinna, N.; Beato, P.; Antonietti, M.; Niederberger, M. *Chemistry of Materials* **2004**, *16*, 2599-2604.

(56) Li, H.; Zhang, L.; Dai, H.; He, H. *Inorg. Chem.* **2009**, *48*, 4421-4434.

(57) Teng, M.; Luo, L.; Yang, X. *Microporous and Mesoporous Materials* **2009**, *119*, 158-164.

(58) Hung, M.; Fung, K.; Hung, D.; Hon, M. *Journal of the European Ceramic Society* **2008**, *28*, 1161-1161-1167.

(59) Hung, M.; Hung, D.; Fung, K.; Hon, M. *Materials Letters* **2008**, *62*, 1147-1147-1150.

(60) Hung, M.; Hung, D.; Fung, K.; Hon, M. *Journal of the European Ceramic Society* **2006**, *26*, 2627-2632.

(61) Feng, R.; Yang, X.; Ji, W.; Aua, C. *Materials Chemistry and Physics* **2008**, *107*, 132-132-136.

(62) Terribile, D.; Trovarellia, A.; Llorcab, J.; Leitenburga, C.; Dolcetti, G. *Catalysis Today* **1998**, *43*, 79-88.

(63) Deshpande, A.; Niederberger, M. *Microporous and Mesoporous Materials* **2007**, *101*, 413-418.

(64) Zhao, J. P.; Li, Y.; Xin, W. H.; Li, X. *Journal of Solid State Chemistry* **2008**, *181*, 239-244.

(65) Anyaba, P. N. Novel techniques for the synthesis of three-way catalytic converter support materials, Clemson University, 2009.

(66) Grosso, D.; Cagnol, F.; Soler-Illia, G. J. d. A. A.; Crepaldi, E. L.; Amenitsch, H.; Brunet-Bruneau, A.; Bourgeois, A.; Sanchez, C. *Adv. Functional Mater.* **2004**, *14*, 309-322.

(67) Brinker, C. J.; Lu, Y.; Sellinger, A.; Fan, H. *Adv Mater* **1999**, *11*, 579-585.

(68) Noronha, F. B.; Fendley, E. C.; Soares, R. R.; Alvarez, W. E.; Resasco, D. E. *Chemical Engineering Journal* **2001**, *82*, 21-31.

(69) Hirano, M.; Suda, A. *Journal of the American Ceramic Society* **2003**, *86*, 2209-2211.

(70) Atribak, I.; Bueno-Lopez, A.; Garcia-Garcia, A. *Journal of Catalysis* **2008**, *259*, 123-132.

(71) Zhang, F.; Chan, S.; Spanier, J. E.; Apak, E.; Jin, Q.; Robinson, R. D.; Herman, I. P. *Appl. Phys. Lett.* **2002**, *80*, 127-129.

(72) Huo, Q.; Margolese, D. I.; Ciesla, U.; Demuth, D. G.; Feng, P.; Gier, T. E.; Sieger, P.; Firouzi, A.; Chmelka, B. F. *Chem. Mater.* **1994**, *6*, 1176-1191.

(73) Yang, X.; Zhou, L.; Chen, C.; Xu, J. *Mater. Chem. Phys.* **2010**, *120*, 42-45.

(74) Gibaud, A.; Grosso, D.; Smarsly, B.; Baptiste, A.; Bardeau, J. F.; Babonneau, F.; Doshi, D.; Chen, Z.; Brinker, C. J.; Sanchez, C. *J. Phys. Chem. B* **2003**, , 6114-6118.

CHAPTER FIVE

SIMULATION OF SOLVENT/WATER DIFFUSION FOR THE CONTROLLED SYNTHESIS OF ORDERED MESOPOROUS ZIRCONIA AND CERIA-ZIRCONIA-YTTRIA MESOSTRUCTURES VIA EISA

Abstract

The present study reports on the relationship between the appearance of ordered structures and the diffusion rates of solvent and water during the synthesis of ordered mesostructured zirconia and CZY materials via evaporation induced self-assembly (EISA) using Pluronic triblock copolymer F127 as the structure directing agent (SDA). This chapter has two main parts: an experimental sections, which describe efforts to ascertain the mass transfer behavior of the CZY based EISA synthesis gel under varying reaction conditions; and a simulation section, where the experimental behavior of the EISA synthesis gel was modeled using a simplified model of the system.

To better understand how ordered mesoporous CZY materials are formed by the EISA technique, a simplified water-ethanol evaporation model was developed to mimic some of the key mass transport phenomena. This model treats the cylindrical system as a moving boundary mass transport problem, as the EISA gel is in open vessel undergoing evaporation and absorption. Previous reported syntheses of ordered zirconia based materials[19, 25] failed to examine how the rate of diffusion of ethanol and water during aging affects the ability of these systems to form an ordered product. Other simulations for aerosol EISA systems[41, 42] have dealt with the ethanol-water behavior by modeling droplets undergoing evaporation. Though the essential EISA phenomena are identical for

spherical droplets and a cylindrical system (with a single axial surface open for transport), the asymmetrical nature of the cylindrical system can significantly impact the degree of uniformity of the resulting oxide materials. The extent of sample non-uniformity is of great significance to large scale catalyst synthesis schemes that employ moving particle conveyors to age, react, and calcine CZY materials that may be prepared by EISA techniques.

Introduction

Controlling the rate of metal oxide condensation is essential to the creation of ordered mesoporous oxides via sol-gel type processes. With evaporation induced self-assembly (EISA), the rate of oxide condensation is controlled by the rate of addition of the hydrolyzing agent (water – via absorption) and the rate at which the sol-gel solvent is evaporated. A better understanding of these aspects is needed to design zirconia and ceria-zirconia-yttria (CZY) materials with the desired morphology in a reproducible manner. This chapter focuses on the evaporation or aging process in the synthesis of zirconia and CZY mesoporous oxides via EISA as this phenomenon is a key aspect in the creation of ordered mesostructures as shown in Chapter 4. The following section will describe the EISA technique and the primary variables that influence the outcome of a given mesoporous oxide synthesis so that the importance of this study is better understood.

Evaporation induced self-assembly

"Self-assembly is the spontaneous organization of materials through non-covalent interactions with no external intervention".[1] The evaporation induced self-assembly (EISA) process starts with a homogeneous solution of precursors and template in a volatile solvent and sometimes water. The template choice is typically asymmetric molecules that are pre-programmed to organize into well-defined supramolecular assemblies (e.g., amphiphilic surfactant molecules or polymers composed of hydrophobic and hydrophilic parts).

The initial solution is exposed to a well-controlled set of conditions so that evaporation of the solvent can take place and the assembly of the oxide structures can begin. As evaporation takes place, the solution reaches its “critical micelle concentration” (cmc). At this point, micelles start to form larger secondary structures. Evaporation continues until all of the solvent is evaporated at the conditions for the experiment. When the solvent is nearly all evaporated, the system conditions are such that the metal oxide precursors are still somewhat mobile and the system is said to be at a “modulable steady-state”. This is very important in EISA as the secondary structures (e.g., mesoporous structures) formed earlier become locked in place via the increased formation of rigid oxide structures. This process is illustrated in Figure 5.1.

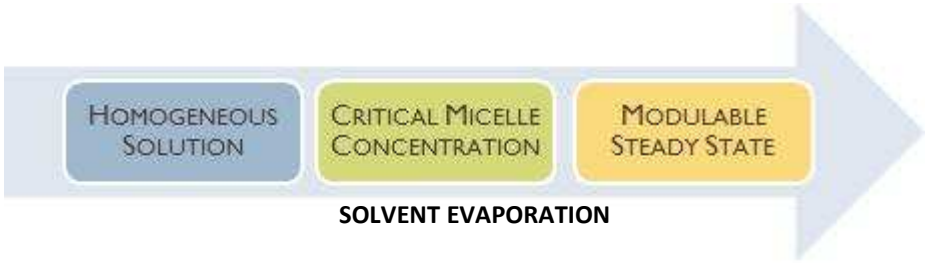

Figure 5.1. Evaporation process during EISA synthesis.

EISA is a relatively simple synthesis technique, comparable to other techniques for mesoporous materials. It has yielded more uniform mesoporous materials for siliceous and non-siliceous systems compared with traditional sol-gel approaches as seen in Chapter 4. The systems investigated in this study of the EISA synthesis method include zirconia, ceria-zirconia and yttria-zirconia.

Inorganic precursors have been used to synthesize all three ceria, zirconia and yttria mesoporous oxides[2-11] and their combinations[3, 5, 12-21]. Some relatively recent studies have

successfully shown the creation of ordered materials. [12, 13, 17, 18, 22-24] However, designing the self-assembly of zirconium oxide or CZY nanoparticles with controllable pore structure using surfactant templating pathways is still a challenge.[25]

Considerations for the creation of ordered mesostructures via EISA

The focus of this work is on the effects of synthesis conditions on the morphology of zirconia and CZY samples prepared via the evaporation induced self-assembly method. For this technique, the nature of the final oxide structure is influenced by three factors: the metal oxide precursor to template ratio, the chemical nature of the inorganic precursor and the relative humidity (RH).[26] For this study, all three of these factors were studied in detail, with some of the initial parameters being adopted from the literature (e.g. 40 °C and 50% RH).

Furthermore, soft templates, such as triblock copolymers or surfactants, which form the self-aggregated superstructures in solution phase, play a strategic role in directing the formation of organized porous structures.[25] In the EISA method, the evaporation of the solvent promotes progressive increases in the concentration of non-volatile species, which in turn causes surfactant micelle formation and their self-assembly with inorganic moieties (precursors) present in the synthesis solution. For a given solution, the evaporation rate of solvent (often ethanol) and absorption rate of the metal precursor hydrolyzing agent (water) are functions of the sol film thickness, external RH, vapor pressure of ethanol, temperature and the diffusivity of volatile species (viscosity).[27]

Another consideration is the surface of the evaporating solution. Evaporation at the film-air interface results in a concentration gradient through the film. Due to this gradient

the transformation to the supramolecular arrangement first appears at the interface. A phase transition can be hindered due to a high local viscosity.[27] This is a common occurrence, especially in thick samples (>0.01mm high) such as the ones studied in this chapter.

This chapter provides insight into the diffusion processes of solvent, water, and hydrochloric acid as well as the reactions that drive the synthesis of mesostructured zirconia and CZY via evaporation induced self-assembly (EISA) for larger batch systems (as compared to thin film systems). A simplified evaporation model has been developed, treating the evaporation process as a moving boundary mass transport problem so as to understand the phenomena causing the formation of oxide mesostructures. As previously mentioned, prior reported syntheses of ordered zirconia based materials[12, 18] failed to examine how the rate of diffusion of ethanol and water during aging affects the ability of these systems to form an ordered product. Other simulations for ethanol-water systems[28, 29] have dealt with aerosol EISA by modeling droplets undergoing solvent evaporation. The results of this simulation provide interesting insight into the evaporation process and the interdependencies of the synthesis parameters and how they impact final oxide material properties.

Experimental

Materials

Pluronic® F-127, zirconyl chloride octohydrate ($ZrOCl_2 \cdot 8H_2O$) and yttrium nitrate hexahydrate ($Y(NO_3)_3 \cdot 6H_2O$) were purchased from Sigma-Aldrich. Cerium nitrate

hexahydrate ($Ce(NO_3)_3 \cdot 6H_2O$) and ethanol were obtained from Fisher and Alfa Aesar, respectively. All chemicals were used as received without further purification.

Synthesis

Mesoporous zirconium oxide

The synthesis procedure for zirconia mesostructures is the same as that shown by Yuan et al.[12] and is not listed here for brevity.

Mesoporous CZY mixed oxides

In a typical synthesis, the structure directing agent, Pluronic F127, is added to 10 ml of ethanol at room temperature. After at least 4 hours of vigorous stirring, a homogeneous solution is obtained. Then, 0.5 g of zirconyl chloride, 0.066 g of yttrium nitrate and 0.749 g of cerium nitrate are added to the ethanol solution and the mixture stirred until all salts are completely dissolved. The resulting solution is aged for 2 to 6 days at about 40 °C and 50% RH in a Cincinnati Sub-Zero MicroClimate® humidity controlled oven until a gel is formed as a result of solvent evaporation. The remaining product is dried at 100 °C for 1 day and then calcined at 400 °C for 4 hours using a heating rate of 1 °C/min to avoid any collapse of the mesostructure. The synthesis procedure is illustrated in Figure 5.2 and typical sol compositions for the synthesis of CZY materials via EISA are shown in Table 5.1.

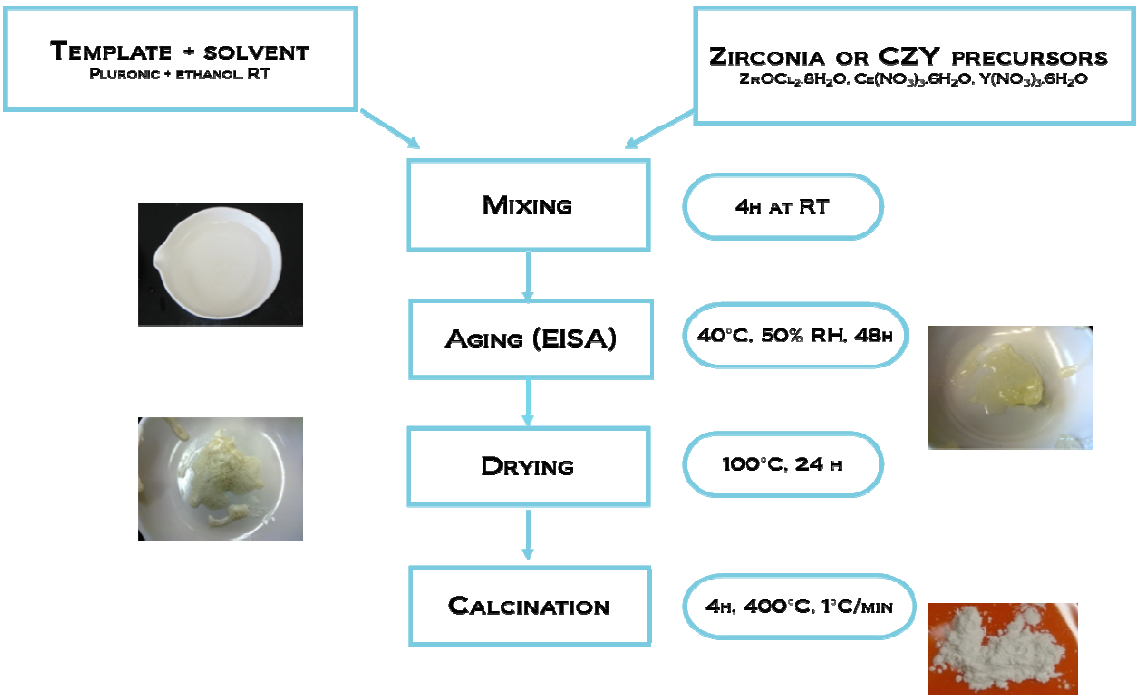

Figure 5.2. Synthesis procedure for CZY supports using evaporation induced self-assembly.

All samples were prepared using the same procedure above, but the types of containers during the evaporation process were varied to have different evaporative surface areas and solution levels to allow ethanol evaporation rates to differ as well as to vary the influx of the hydrolyzing agent (water) to the system. The impact of these changes was evaluated by different characterization techniques of the resulting samples.

Table 5.1. Typical composition of P123 templated CZY mixed oxides using a molar ratio of 0.1 for the block copolymer.

	Oxide Molar Ratio	**Scaled Salt Wt (g)**
$ZrOCl_2.8H_2O$ (ZrO_2)	9	0.5
$Y(NO_3)_3.6H_2O$ ($Y_1O_{1.5}$)	1	0.066
$Ce(NO_3)_3.6H_2O$ (CeO_2)	10	0.749
F127		1.086
Ethanol		10 ml

Characterization

The samples were characterized using nitrogen physisorption (BET model for surface area and BJH model for pore size distribution), small-angle X-ray diffraction (SAXRD), transmission electron microscopy (TEM), differential scanning calorimetry (DSC) and thermogravimetric analysis (TGA). All conditions for analysis using these techniques are explained in the characterization section of previous chapters.

Simulation

EISA evaporation model

The following set of equations helps to define a simplified synthesis model, which can quantitatively describe the evaporation induced self-assembly method that was used to synthesize ordered zirconia and ceria-zirconia-yttria mesostructures. The model described herein focuses solely on the mass transfer aspects of absorption and evaporation because these processes have the greatest impact on the formation of ordered mesoporous structures that are prepared via the EISA method. As the models developed in this chapter are preliminary (and should be expanded in future studies), the effects of metal species concentrations on solution behavior (salting out effects) and the loss of water due to reactions with the metal precursors are only marginally addressed – i.e., the system is initially modeled as a pure ethanol-water system. Even with these simplifications, considerable insight can be gained about the optimal vessel design for the formation of ordered mesoporous materials.

For this study, the EISA process is carried out in cylindrical containers. Thus, key mass transport phenomena are defined using cylindrical coordinates as shown in Figure 5.3. All nomenclature for this chapter is presented in Appendix G. Species A refers to water and B to ethanol.

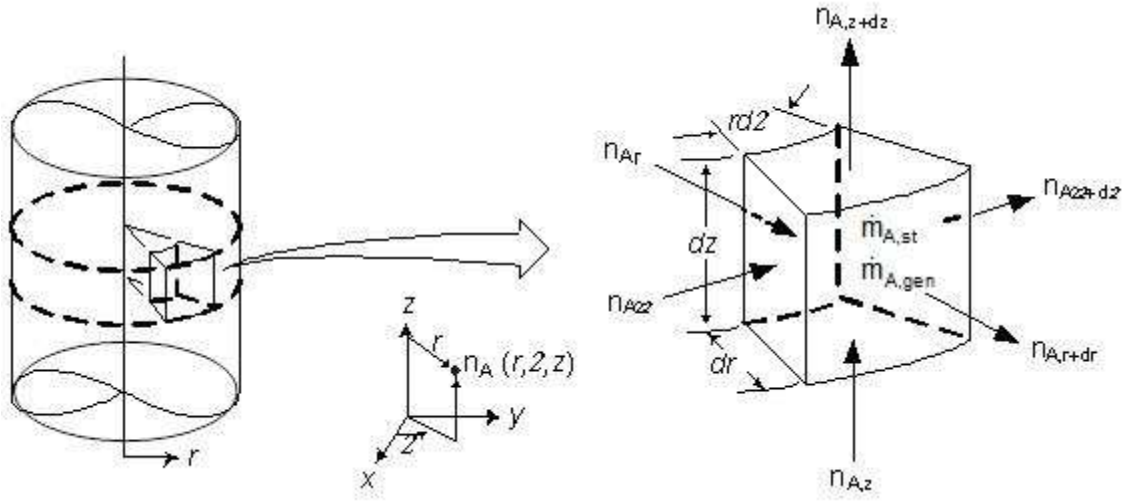

Figure 5.3. Diagram of cylindrical coordinates used for the model in this section.

Water diffusion into the solution (species A, liquid phase)

Component Molar Shell Balance for a Cylindrical System:

$$-\frac{\partial N_A}{\partial r}-\frac{1}{r}\frac{\partial N_A}{\partial \varphi}-\frac{\partial N_A}{\partial z}+\ddot{M}_{A,gen}=\frac{\partial C_{A,l}}{\partial t}$$

Assuming that water absorption into the solution is unidirectional in the z axis (i.e., an open top cylindrical vessel filled with the ethanol solution):

$$\frac{\partial N_A}{\partial r}=\frac{\partial N_A}{\partial \varphi}=0$$

$$\therefore \quad -\frac{\partial N_A}{\partial z}+\ddot{M}_{A,gen}=\frac{\partial C_{A,l}}{\partial t}$$

The diffusion of species *A* (water) through the gas into the liquid phase is a unimolecular, unidirectional diffusion process, which contains stagnant ethanol (species B), which can be described the relationship:

$N_A = J_A^* + x_A\left(N_A + N_B\right)$, where $N_B = 0$ since ethanol does not diffuse back into the liquid phase significantly.

Rearranging variables, $N_A\left(1 - x_A\right) = J_A^*$

Substitution of Fick's law into the flux equation above yields:

$$N_A = \frac{J_A^*}{\left(1 - x_A\right)} = \frac{-\rho_m \mathcal{D}_{AB,l}}{\left(1 - x_A\right)} \frac{\partial x_A}{\partial z}$$

Further substitution of the diffusion flux equation into the general flux equation derived earlier yields:

$$\frac{\partial}{\partial z}\left(\frac{\rho_m \mathcal{D}_{AB,l}}{\left(1 - x_A\right)} \frac{\partial x_A}{\partial z} \right) + \ddot{M}_{A,gen} = \frac{\partial C_{A,l}}{\partial t}$$

At this point, one can assume that since the water is present only at low concentrations then $\left(1 - x_A\right) \approx 1$. Thus, the above equation simplifies to:

$$\frac{\partial}{\partial z}\left(\rho_m \mathcal{D}_{AB,l} \frac{\partial x_A}{\partial z} \right) + \ddot{M}_{A,gen} = \frac{\partial C_{A,l}}{\partial t}$$

The mass generation term can be expressed as:

$$\ddot{M}_{A,gen} = r_A = -\sum_{i=1}^{i=n} k_i C_A C_{metal_i} + \sum_{j=n+1}^{j=nf} k_j C^2_{metaloxide_{j-n}}$$

This is a result of the homogeneous/heterogeneous reaction at the surface:

$[M–OH_2]^{z+} \rightarrow [M–OH]^{(z-1)+} + H^+ \rightarrow [M=O]^{(z-2)+} + 2H^+$ (hydrolysis)

$M–OH + M–OH \rightarrow M–OH–M–OH \rightarrow M–O–M + H_2O$ (condensation)

where M represents the metal ion.

<u>Note</u>*: The term expressed here is just an approximation of the actual generation term.*

In order to solve this differential equation, I must define the **boundary conditions** at the upper and lower boundaries of the system (see Figure 5.4).

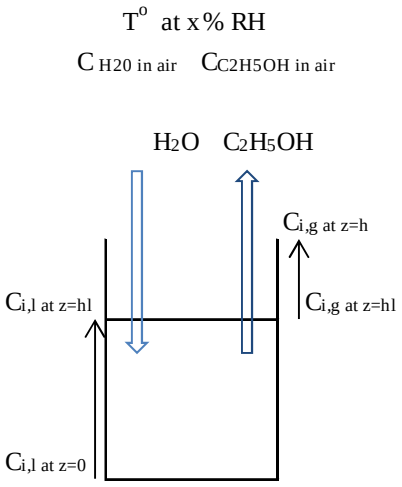

h: Height of vessel
hl: Height of solution in the vessel
Ci & h are a function of time

Figure 5.4. Representation of vessel containing evaporating solution.

At t = 0: $x_{A,hl,0} = 0$ $x_{A,0,0} = 0$

Because the extent of hydration of the metal precursors varies, this term will vary somewhat and depends on the system being modeled, zirconia only or CZY. However, it is likely to be very small.

At t > 0: $x_{A,hl,t} = \frac{y_A \varphi_A P}{\gamma_A P_A^{sat}}$ and $N_{A,0,t} = 0$

Water diffusion from the top of the vessel to the solution surface (species A, vapor phase)

$$-\frac{\partial N_A}{\partial r} - \frac{1}{r}\frac{\partial N_A}{\partial \varphi} - \frac{\partial N_A}{\partial z} + \ddot{M}_{A,gen} = \frac{\partial C_{A,v}}{\partial t}$$

Assuming water entering the system is unidirectional in the z axis:

$$\frac{\partial N_A}{\partial r} = \frac{\partial N_A}{\partial \varphi} = \ddot{M}_{A,gen} = 0$$

$$\therefore \quad -\frac{\partial N_A}{\partial z} = \frac{\partial C_{A,v}}{\partial t}$$

The diffusion of water is a unimolecular, unidirectional diffusion process, which can be described by the relationship:

$N_A = J_A^* + y_A\left(N_A + N_B\right)$, where $N_B\, y_A = 0$.

Rearranging variables, $N_A\left(1 - y_A\right) = J_A^*$

Substitution of Fick's law into the flux equation above yields:

$$N_A = \frac{J_A^*}{\left(1 - y_A\right)} = \frac{-\rho_m \mathcal{D}_{AB,v}}{\left(1 - y_A\right)} \frac{\partial y_A}{\partial z}$$

Further substitution of the diffusional flux equation into the general flux equation derived earlier yields:

$$\frac{\partial}{\partial z}\left(\frac{\rho_m \mathcal{D}_{AB,v}}{\left(1 - y_A\right)} \frac{\partial y_A}{\partial z} \right) = \frac{\partial C_{A,v}}{\partial t}$$

The boundary conditions at the top of the vessel (z = h) and the liquid surface (z = hl) are:

$y_{A,h} = y_{A,o}$ and $y_{A,hl} = \frac{x_A \gamma_A P_A^{sat}}{\varphi_A P}$

$y_{A,o}$ will be determined using the relative humidity (RH) value for the experiment.

Ethanol evaporation from the solution (species B, vapor phase)

$$-\frac{\partial N_B}{\partial r}-\frac{1}{r}\frac{\partial N_B}{\partial \varphi}-\frac{\partial N_B}{\partial z}+\ddot{M}_{B,gen}=\frac{\partial C_{B,v}}{\partial t}$$

Assuming ethanol leaving the system is unidirectional in the z axis:

$$\frac{\partial N_B}{\partial r}=\frac{\partial N_B}{\partial \varphi}=\ddot{M}_{B,gen}=0$$

$$\therefore \quad -\frac{\partial N_B}{\partial z}=\frac{\partial C_{B,v}}{\partial t}$$

The diffusion of species *B* (ethanol) from the liquid phase is a unimolecular, unidirectional diffusion process, which can be described by the relationship:

$N_B = J_B^* + y_B\left(N_A + N_B\right)$, where $N_A\, y_B = 0$.

Rearranging variables, $N_B\left(1-y_B\right)=J_B^*$

Substitution of Fick's law into the flux equation above yields:

$$N_B=\frac{J_B^*}{\left(1-y_B\right)}=\frac{-\rho_m \mathcal{D}_{AB,v}}{\left(1-y_B\right)}\frac{\partial y_B}{\partial z}$$

Further substitution of the diffusion flux equation into the general flux equation derived earlier yields:

$$\frac{\partial}{\partial z}\left(\frac{\rho_m \mathcal{D}_{AB,v}}{\left(1-y_B\right)}\frac{\partial y_B}{\partial z}\right)=\frac{\partial C_{B,v}}{\partial t}$$

The boundary conditions at the top of the vessel (z = h) and the liquid surface (z = hl) are:

$y_{B,h}=0$ and $y_{B,hl}=\frac{x_B\gamma_B P_B^{sat}}{\varphi_B P}$

These two boundary conditions are expected to be the same at $t = 0$ and $t > 0$ since ethanol vapor is continually leaving the gas-phase through the vent.

Other model considerations

All activity coefficients describing the equilibrium between vapor and liquid phases will be expressed using the non-random two-liquid (NRTL) model, which is based on a local mole fraction concept developed by Renon and Prausnitz[30]. The density of the ethanol–water solution is calculated as a function of temperature and the ethanol weight fraction. The Vignes[31] relation is used to determine the binary diffusion coefficients in the liquid phase at finite concentrations, also, the correlation developed by Chapman and Enskog[32] is used to estimate diffusion coefficients for gas phase systems at moderate temperatures and pressures. These detailed models and equations are shown in Appendix H.

The mass transport equations described above are somewhat simplified, as several thermodynamic phenomena (salt effects on volatility, etc.) are ignored. Heat transport equations and boundary conditions are not shown here but are necessary to solve the system of transport equations and are considered in the model. Moreover, to simulate the system and apply the above equations, some considerations are necessary.

First, since it is an evaporation process the level and concentration of components in the system changes over time. To consider this, *time-dependent moving boundaries* are necessary. Second, it is important to take into account that *all physical properties are interconnected and change with both time and location*. Third, *chemical reactions* are taking place so component transformations must be modeled. Finally, the quick

appearance of a *network of oxides in the surface* due to surface water availability can cause the appearance of ordered-disordered mesopores systems. However, the impact of these latter phenomena on variations in diffusion properties was not included in the model.

The system of transport equations was solved using COMSOL Multiphysics® modeling and simulation software using a moving boundary finite difference method. The system was divided into a large number of control elements (grids, infinitesimal in size) that include surrounding air as shown in Figure 5.5.

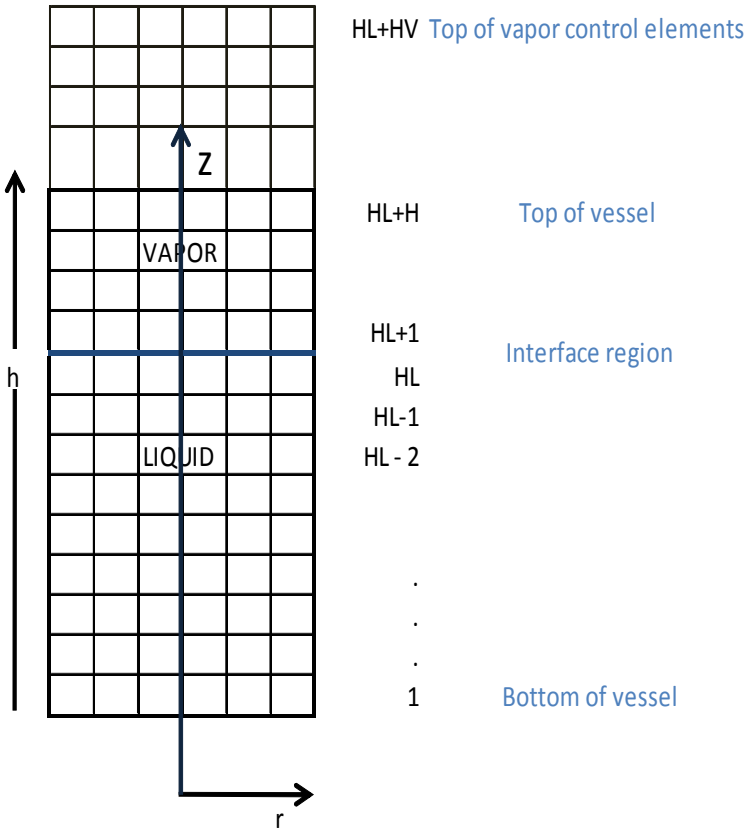

Figure 5.5. Control elements or grids of infinitesimal size used to solve the evaporation model.

Experimental Results and Discussion

Given that the EISA synthesis method is a diffusion-limited process (as explained in Chapter 4), it is important to understand how experimental variables may influence the diffusion phenomena that directly impact final catalyst structure. For these studies, different cylindrical containers were used during the evaporation process with the purpose of having different evaporative surface areas and solution levels so as to allow ethanol evaporation rates to differ as well as to vary the influx of the hydrolyzing agent (water) to the system. Certainly, the geometry and size of the evaporative container made an impact on the results.

One of the most important steps for the synthesis of mesoporous materials with ordered networks is the formation of micelle structures around which the oxides will be deposited during precipitation. Previous efforts by our research group have suggested that the ordering of the mesopores has been affected by fast oxide precipitation hindering micelle formation, which results in the formation of disordered structures. Thus for the EISA process, increasing evaporation times by decreasing the surface area exposed to the environment during the synthesis of these mesostructures can raise the possibility of creating ordered oxide mesostructures by allowing sufficient time for the formation of consolidated micellar structures.

Zirconia Observations and Experimental Results

Table 5.2 summarizes the characterization results for mesoporous zirconia synthesized using three types of cylindrical containers for the EISA process with different diameters (8 cm, 5 cm & 1.5 cm). Besides the evaporative surface area changes,

containers were filled at different levels (highest level shown here is the full level of the respective vessel) so water diffusion into the system also varies. Pictures before, during and at the end of the evaporation process for the vessels in the table below are shown in Appendix I.

Table 5.2. Characterization Results for Zirconia Samples Synthesized Using EISA in Three Different Types of Containers.

Sample	**Time starts gelling* (h)**	**BET S.A** (m^2/g)**	**BJH pore size** (nm)**	**SAXD peaks (1)**	**TEM (1)**	**(2)**
10 ml dish	1	71	5.4	0.4; 1	N.O	O.
25 ml dish	2	72	6.2	0.2; 0.4	N.O	O.
50 ml dish	2	59	6.0	0.5	N.O	N.O
10 m cru.	2	48	4.5	0.5, 0.7	N.O	O. / N. O.
25 ml cru.	2.5	33	3.5	0.2, 0.3	N.O	N. O.
50 ml cru.	2.5	38	4.0	0.2,0.3	N.O	O. / N. O.
3 ml tube	48-72	16	3.8, 40	0.2, 0.4	O	N. O.
6 ml tube	> 120	36	3.5, 17.5	0.2,0.4	N.O	N. O.
9 ml tube	> 120	41	3.7, 18.1	0.2,0.4	N.O	N. O.
12 ml tube	> 120	38	3.8, 18.5	0.4	N.O	N. O.
15 ml tube	> 120	25	3.6, 17.8	0.2, 0.4	N.O	N. O.

- N.O.: Not Ordered O.: Ordered cru.: crucible Container type is color coded.
- (1) refers to the first sample prepared (2) is an exact sample reproduction under the same conditions.
- All characterization data corresponds to sample (1)
- Diameter evap. dish = 8 cm, diameter crucible= 5 cm, diameter tube=1.5 cm.
- The volume listed before the name of the container refers to the initial liquid level in the vessel.
- Gelling under fixed RH at 50% and Temperature 40 °C for a period of 48 hours.
- All samples were dried after a 48 h waiting period.
- The error margin for the surface area is ±5 m^2/g and for the pore diameter, ±0.5 nm

Not surprisingly the containers with the smaller surface area took the longest to gel during evaporation. The test tubes solution evaporated very slowly compared to other samples.

The BET surface area and BJH pore diameter for the different zirconia samples varied for each sample synthesized in a different container. The BET surface area decreases for samples synthesized in containers with a smaller evaporative surface area but there is no particular trend for samples synthesized within the same type of container for different levels of starting solution. In general, the surface area and pore size for the samples synthesized using larger diameter vessels is larger than for the ones synthesized in other containers. It appears to be beneficial to have a larger evaporative surface area that decreases the gelling time and lets the hydrolyzing agent easily diffuse to the solution to obtain a higher BET surface area.

The TEM images of some of the calcined samples are shown in Figure 5.6. The existence of mesopores is clearly observed but the mesopores are ordered only for the test tube filled at the lowest level at the beginning. All other samples look like an agglomeration of nanosized particles with no particular order like the sample on the left differing from the morphology of the MCM-41 and SBA-15 type family of materials.

By repeating the same experiment, it was found that structures were not reproducible and ordered arrangements were found for samples synthesized in the larger diameter vessels. This might indicate that samples were either not reproducible between experiments or consisted of ordered and disordered pore arrangements within themselves. Small angle XRD patterns showed peaks in the low angle region which suggest the

presence of ordered pores. However those peaks correspond to a larger size pore than the ones I are interested in seeing. SAXD did not reveal any low angle peaks between 1° and 2° for any of the materials indicating the lack of long range ordered mesostructures in the different samples corroborating TEM results. For the case of the sample that appeared ordered this might indicate that it had ordered and disordered areas within itself.

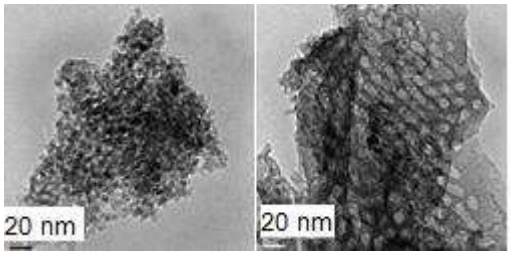

Figure 5.6 TEM of calcined zirconia samples synthesized using EISA. Left: sample evaporated in a dish (d=8cm) with starting level of 25 ml. Right: sample evaporated in a test tube (d=1.5 cm) with the lowest starting level (3ml).

The existence of systems with ordered and disordered structures within the same sample might be explained by the existence of a large concentration gradient during synthesis induced by a fast evaporation rate. The rate of evaporation is very important since a fast evaporation rate induces a large concentration gradient (CG), whereas a slow evaporation rate will favor a more homogeneous solution. The concentration gradient through the sample is promoted by evaporation at the solution-air interface, which explains why the presence of phase separated oxide type structures first appears at the interface[27].

Large concentration gradients (CG) are likely to generate multiphase systems because the reagents do not have the same chemical composition at both interfaces. In such a case, the top part of the film tends to be ethanol deficient, causing premature oxide

condensation and possibly trapping an intermediate phase as a result of this poor mobility. This is explained by the local rigidity of the oxide structure being too high and for fast systems, a decreased time for oxide precursor rearrangement.[27] As a result, a higher degree of orientation is favored for lower evaporation rates.

For systems that resulted in only disordered CZY mesostructures, it is unlikely that an ordered assembly process occurred during the synthesis process, yielding random arrangements of bonded oxide nanoparticles with mesopores resulting from the voids generated by the removal of Pluronic template from between the oxides particles. The lack of structure periodicity in the CZY oxides likely results from the rapid condensation of the oxides, which occurred at a rate to fast for the template micelles to self-assemble into ordered (honeycomb type) tertiary structures.

In order to evaluate the evaporation rates of the synthesized samples, weight loss and/or volume loss for the samples was recorded over time during the EISA aging step. These results are shown in Figure 5.7.

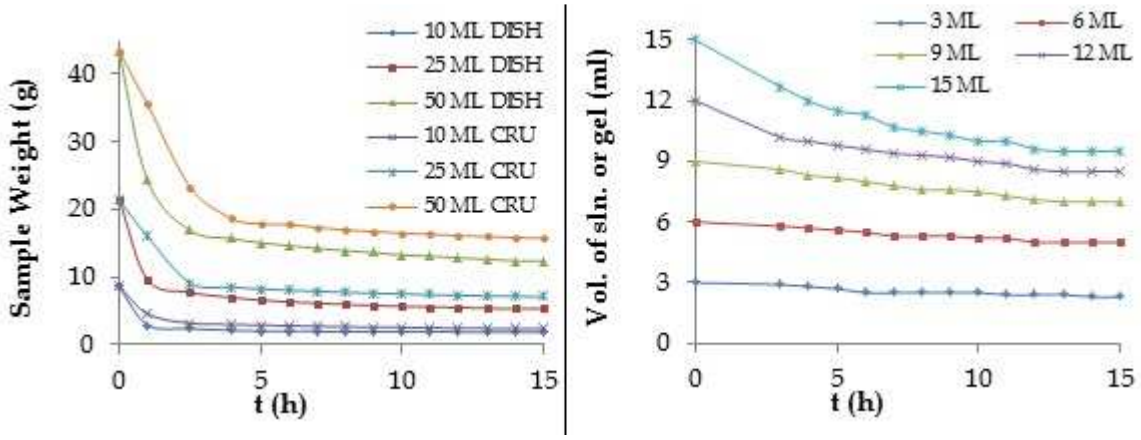

Figure 5.7. Zirconia solution evaporation rates expressed in sample weight over time for the larger diameter cylindrical vessels (left) and in volume over time for the smaller diameter vessels or tubes (right).

From the data shown in Figure 5.7, it is observed that the liquid from samples synthesized in the larger diameter cylindrical vessels was fully evaporated in the first 3 h of the 48 h aging period, much faster than the samples in the smaller diameter test tubes. In general, the rate of fluid loss from the tube was much more uniform over time.. In light of the last assessment, one might have expected that the samples synthesized in the smaller diameter vessels, with subsequently slower rates of evaporation, would have an ordered arrangement of mesopores, as the greater time was available for the micelles to self-assemble. However, only one of these samples ever showed (Via PXD analysis) some extended ordering of pores.

One of the likely reasons that CZY samples prepared in small diameter test tubes did not show ordered mesostructures was the fact that calcination and characterization was done to all samples after evaporating for 48 hours, which did not give enough time for all the samples to gel (only the one that was ordered gelled completely). This means that the oxides had not precipitated yet and were forced to do so during the drying/calcination step. Additionally, homogeneity is another factor that comes into play. For the vessels with the smallest diameter, large concentration gradients were predicted; thus, increasing the probability of multiphase systems (ordered/disordered pore structures).

Another important observation made during the gelling process is the appearance of a hard oxide rich layer (or crust) on top of the evaporating solution as shown in Figure 5.8. This crust is basically precipitated oxides forming a network that prevents the homogeneous evaporation of solvents from the container, thereby limiting the formation of ordered materials in the remainder of the solution. This fast precipitation of CZY

oxides at the liquid-air interface is not surprising, as the oxide precursor solution surface is predictably enriched in the hydrolyzing agents (water), which promotes oxide forming hydrolysis reactions at the solution surface. This crust might also be responsible for the lack of ordered mesopores in some CZY samples.

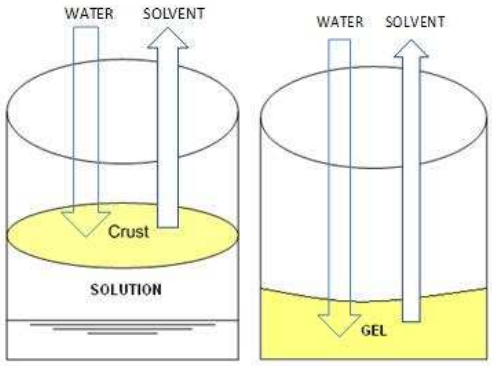

Figure 5.8**.** A CZY precursor solution evaporating in a vessel with (left) an oxide network crust appearing on the top of the solution as a result of ethanol (solvent) evaporation being slow relative to water absorption; whereas, more equal rates of water absorption and solvent evaporation lead to the formation of an ordered oxide precursor gel (right).

In addition, temperature and relative humidity are two of the main factors that affect the formation of ordered structures. The effects of humidity can be better understood by analyzing Figure 5.9. The plot shows how relative humidity alters the modulable steady state period (oxide growth period). The concept of a modulable steady state was introduced by Cagnol et al.[33] and corresponds to the end of the drying line (all solvent has been evaporated). Previous studies for systems similar to ours have found that a 50% RH is the most appropriate balance of conditions to obtain ordered mesostructures.[12, 17]

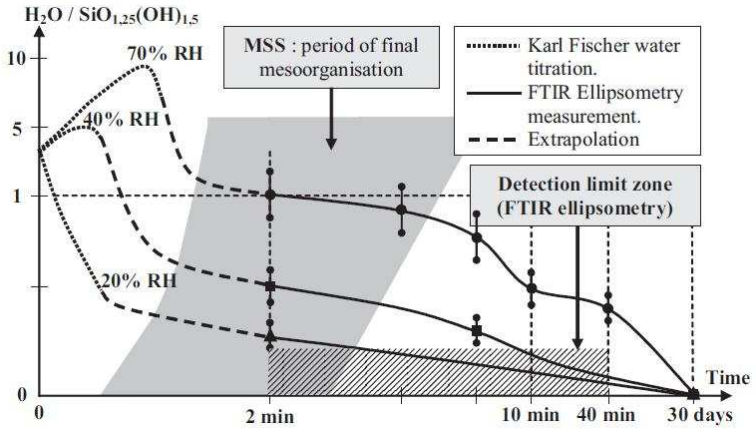

Figure 5.9. Evolution of water content in the film (estimated from Karl Fisher titration from 0 to 1 min, and measured by FTIR ellipsometry after 2 min) over time from the deposition (0s) to 1 month after deposition at three different RH. Reprinted with permission from ref[26]. Copyright © John Wiley & Sons, Inc.

As illustrated in Figure 5.10 (taken from[26]), water is not only essential for hydrolysis reactions during the synthesis process, it has been demonstrated[30] that control of the final mesostructure is possible by allowing water to reenter and depart the film (swelling and contracting of the hydrophilic network) during the modulable steady state phase of the synthesis process, which is the final structuration period for the sample. At this point, too low or too high a humidity level can lead to disordered structures. In this case, the existence of an oxide crust layer can hinder these essential water transport processes and prevent a homogeneous structuration process.

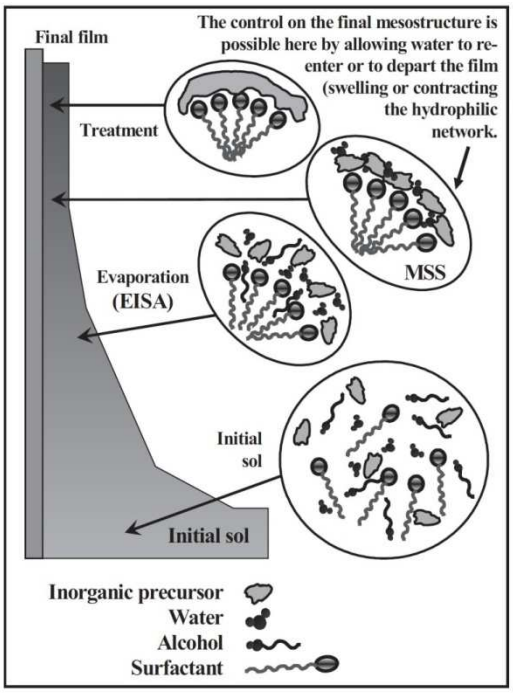

Figure 5.10. Mesostructured thin-film formation by dip-coating. Step 1: the isotropic initial sol where the condensation is optimally slowed down. Step 2: the evaporation proceeds and micelles start to form above the CMC. Step 3: the evaporation is complete; the film equilibrates with its environment (MSS) and the final mesostructure is selected by adjusting the RH before further inorganic condensation. Step 4: the inorganic network is condensed; the hybrid mesostructure is stabilized. Reprinted with permission from ref[26]. Copyright © John Wiley & Sons, Inc.

As a result of these observations, it was necessary to come up with a synthesis apparatus that will promote homogeneity during synthesis and low evaporation rates. This experimental set up and its advantages will be discussed below.

CZY Experimental Results

CZY oxide synthesis using test tubes were conducted due to the issues already seen with large evaporation area vessels for zirconia samples. Special attention was paid to the gelling process including concentration gradients and the hard oxide rich layer appearance during EISA. Table 5.3 summarizes the characterization results for ceria-

zirconia-yttria samples synthesized using test tubes (d = 1.5 cm) filled at different levels (highest level shown here is the full level of the respective vessel) during the EISA process so that water diffusion into the system would vary as a function of the path length between the vessel top and liquid surface.

Table 5.3. Physical properties of CZY samples synthesized using the EISA technique with tubes of very fluid level.

Starting volume (cm^3)	**22 (h=7cm)**	**15.7 (h=5 cm)**	**9.4 (h=3cm)**	**3.1 (h=1cm)**
Time gelling starts (h)	12 to 24[a]	12 to 24[a]	12 to 24	4 to 5
Small XRD peaks	0.18, 0.28	0.18, 0.28	0.18, 0.36	0.56,0.86
BET (m^2/g) surface area[b]	105	104	95	92
BJH (nm) pore size[b]	3.8	3.5	3.5	3.4
TEM (1)	Ordered	Not ordered	Not ordered	Not ordered
TEM (2)	Not ordered	Not ordered	Not ordered	Not ordered

a. Liquid bottom underneath hard film on surface
b. The error margin for the surface area is ±5 m^2/g and ±0.5 nm for the pore diameter
(1) refers to the first sample prepared, (2) is an exact sample reproduction under the same conditions.

For the case of CZY samples, it was observed that gelling started between 12 and 24 hours for all tubes. BET surface areas and BJH pore sizes were similar for all samples regardless of their starting level. However the only sample that appeared to be ordered was the one that contained more fluid initially.

Samples evaporated in the test tubes required a longer aging time as seen in Figure 5.11. This longer aging time was required because of reduced diffusion rates to/from the vessel, which were the caused by the smaller diameter of the container. Often a week was required to completely evaporate all the alcohol solvent. Further, they showed non-homogeneous/inconsistent results – many samples contained both ordered and disordered

arrangements of CZY oxides. This is a result of the large concentration gradient through the sample, which varied over time. At the start of the EISA process, the test tubes were fuller and the evaporation process was faster, but as the solution level dropped, the rate of ethanol evaporation and water infusion also decreased, reducing the concentration of hydrolyzing species in the reactive sol-gel solution.

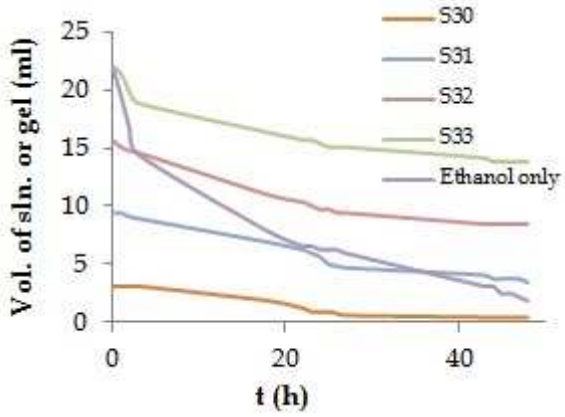

1

Figure 5.11. CZY solution evaporation rates expressed in volume over time for the small diameter vessels.

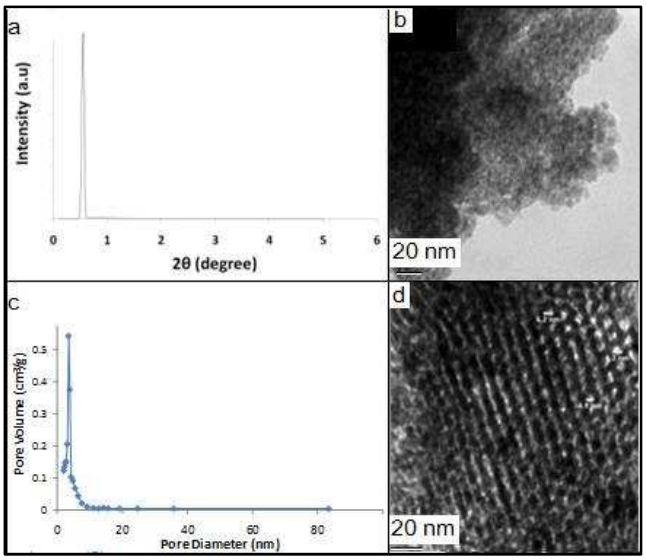

Figure 5.12. CZY synthesized via EISA. (a) Small XRD diffractogram of sample h=1, TEM images of sample (b) h=3 and (d) h=7. (c) BJH pore size distribution of h=5

These results for CZY oxides show that although evaporation rates were decreased, homogeneity is still a large problem; it impedes a controlled evaporation process and hinders the creation of ordered structures. Next section shows a solution for these issues.

Homogeneous ordered zirconia & CZY Samples

Previous experiments described in the sections above have shown some of the issues that prevent the creation of homogeneous ordered mesostructures. Figure 5.13 (from Chapter 4) will help explain the evaporation and diffusion processes seen experimentally and precedes the discussion of how homogeneous ordered mesostructures are created. The EISA process involves an open system. The starting solution consists of metal precursors (salts or neutral metal complexes) dissolved in alcohol and only contains trace amounts of water from the hydrated salts. The water necessary for hydroxide formation and condensation is gradually available as it diffuses into the reaction medium from the

atmosphere. As a result, metal precursors are slowly converted into hydroxides and later oxides by reacting with water coming into the solution from the humidity of the heated environment (set at 50% RH). The overall reaction for metal hydrolysis is:

$[M–OH_2]^{z+}$ (metal precursors in alcohol/water) → $[M–OH]^{(z-1)+}$ (metal hydroxide) + H^+ (acid)

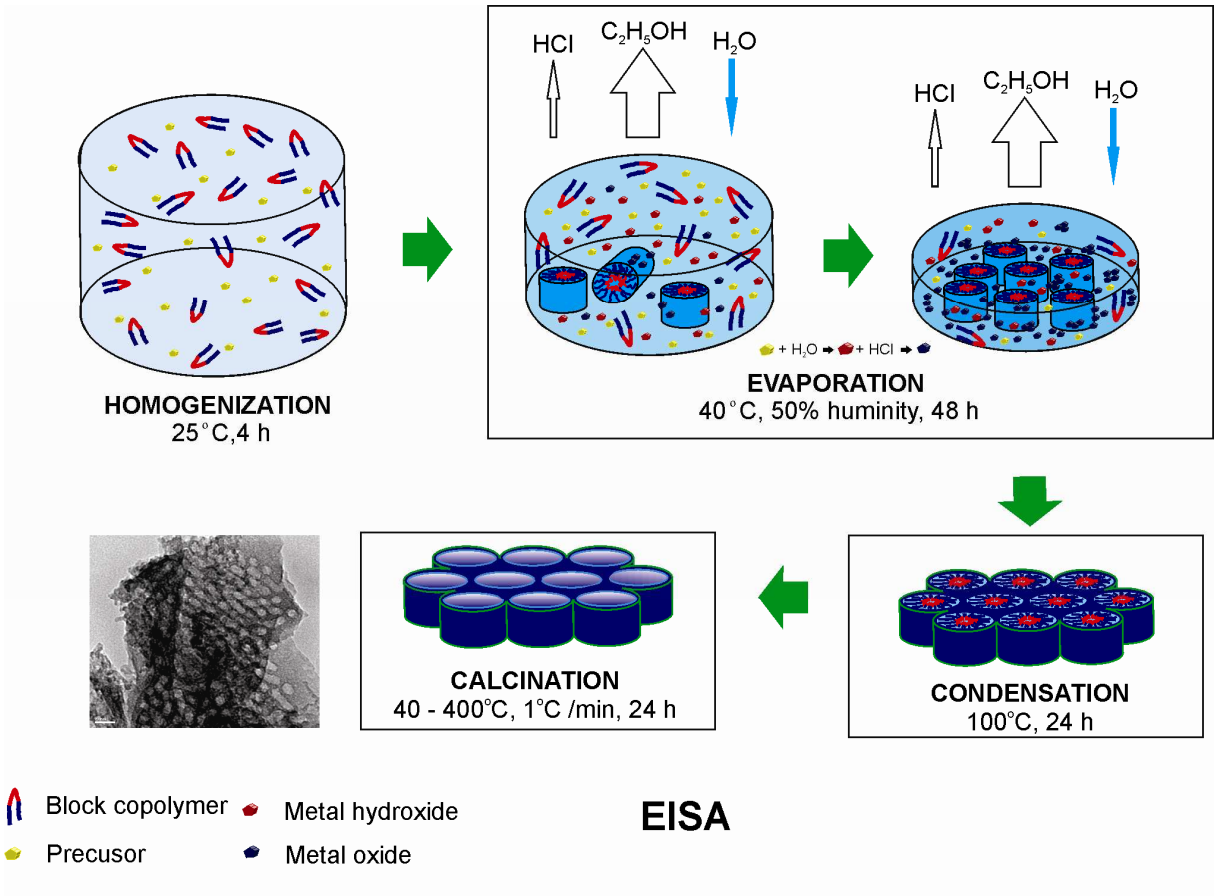

Figure 5.13. Evaporation induced self-assembly synthesis of mesoporous CZY oxides. The evaporation process is especially important as the interchanges between the environment and the sample determine the morphology of the resulting sample.

This process provides an acidic environment that slows the oxide formation allowing sufficient time for the self-arrangement of SDAs into micellar arrays. As the block copolymers become micelles, these micelles start to form other secondary and tertiary

structures; the hydrolysis process continues and condensation occurs as hydroxides react with each other forming metal oxides as shown in the reaction below.

M–OH + **M–OH** (metal hydroxides) → M–OH–M–OH → **M–O–M** (metal oxide) + H_2O

Both evaporation and self-assembly processes happen simultaneously. Also, depending on the initial template concentration, the evaporation of solvent can help the template reach a critical concentration where micelles begin to form. Ethanol evaporation and water incorporation control the speed of the hydroxide formation reaction and ultimately control the material's morphology. As ethanol evaporates, micelles start to form secondary structures and water diffusing from the environment starts the hydrolysis process forming metal hydroxides. These metal hydroxides will form metal oxides as they associate with each other allowing oxide polymerization.

Although water is directly responsible for hydrolysis reactions, fast evaporation of ethanol accelerates the aging process, possibly preventing the self-assembly of the SDAs. If solvent evaporation is too fast, micelles cannot self-assemble before the condensation process has occurred, creating disordered arrangement of oxide pores. Also, as mentioned previously, water should ideally diffuse homogeneously into the solution and not only the surface layer of the solution, as surface reactions can create a barrier of oxides that hinder the evaporation of the solution at the bottom of the vessel. Hydrochloric acid also evaporates changing the pH of the solution and influencing the rate of reaction as an acidic environment favors a slower reaction process. Specifically, dissolved HCl slows the cross-linking rate of the doped metal species making their condensation-

polymerization process occur at the same time. Thus, these oxides will organize around the micelle arrangement as a result of the interactions between them.

All of the experimental conditions must be carefully controlled, which makes it more difficult to exactly reproduce a specific synthesis condition. This is one of the challenges to solve, as it was observed that the reproduction of zirconia and CZY samples has been difficult to achieve, despite the relative humidity and temperature being held at specified conditions via a humidity-controlled oven. Other conditions like air flow over the sample are important and strongly influence solvent evaporation rates.

Ordered mesoporous CZY structures were synthesized but product uniformity within a given sample and from batch to batch were recurring problems. Thus, it is important to reduce concentration gradients (CGs) and reduce evaporation rates. In order to reduce CGs, a glass cylindrical vessel (petri dish) with large evaporative area and small starting solution height (d = 9 cm, h = 1.6 cm) were found to be optimal for uniform materials synthesis. They had 100 ml capacity and a starting liquid volume of 1 ml. These vessels reduced CGs and prevented the appearance of precipitated oxides barriers in the solution surface as the starting solutions were thinner and evaporation was more homogeneous. However, since the evaporative surface was larger, evaporation rates were larger as well. To compensate for the increase in evaporative surface area, the air flow over the samples was reduced significantly, which helped to reduce overall evaporation rates.

For this purpose, samples were kept inside a specially designed box, residing in the well-mixed convection oven, which allowed air to flow slowly across the sample in one direction, keeping the evaporation rates at a low level. If air was allowed to flow at high

speed over the samples, the evaporation process was too rapid, resulting in disordered structures. The rapid evaporation of solvent caused by rapid air flow provides insufficient time for the polymerizing oxide structures to diffuse and self-assemble around the existing micelles; thus, larger bulk oxide particles are formed. This special box and other EISA experimental features for thin cylindrical vessels are shown in Figure 5.14. Further details are shown in Appendix F.

Figure 5.14. Box designed to decrease air flow (upper left); samples inside box in convection humidity-controlled oven (upper right); thin petri dishes with solution during EISA (bottom left) and sample at the end of evaporation process (bottom right).

Analysis of the CZY products prepared using a range of conditions, showed that thin samples prepared in cylindrical containers (petri dishes) routinely yielded the uniform samples displaying highly-ordered mesoporous CZY structures. The optimal relative humidity and temperature were found to be 40 °C and 50% RH, and the air flow across the surface of the samples was minimized. TEM images of the obtained mesoporous zirconia and CZY structures are shown in Figure 5.15.

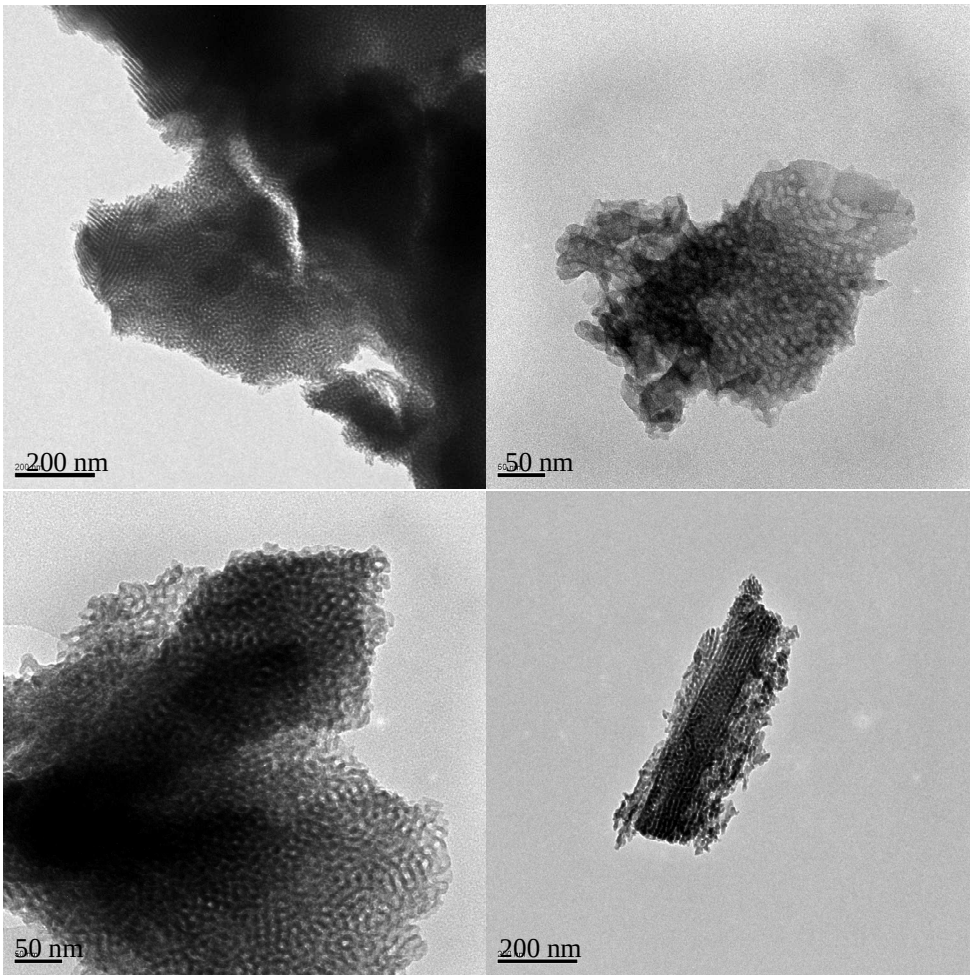

Figure 5.15. TEM images of zirconia and CZY (bottom right) samples synthesized via EISA using thin cylindrical vessels and a special designed box during synthesis.

Simulation Results

Simulations of the EISA synthesis process were done using COMSOL multiphysics modeling and simulation software using a moving boundary finite difference method and the equations modeled in the sections above. Figure 5.16 shows the concentration of water diffusing into the surface of the evaporating liquid. The simulated container is 1 cm tall, and it can be seen that there is rapid increase in water concentration at the beginning of the experiments. These concentration gradients are still pronounced after 5000 seconds, but at this point in time water has finally reached the bottom of the vessel. It is also shown that the height of the solution changes as a function of time. Note that the liquid-vapor interface is located at the position where the water concentration approaches a value of 1 mol/m^3. These models help predict the rates of ethanol loss for different synthesis vessel geometries and gas flow conditions. Further, the predicted concentration profiles for water in the metal-alcohol mixture during the EISA process provide a clear explanation of why syntheses attempted in vessels with significant fluid height yielded non-homogeneous products – i.e., CZY product homogeneity is directed related to the homogeneity of the synthesis solution and deep solutions are less homogeneous.

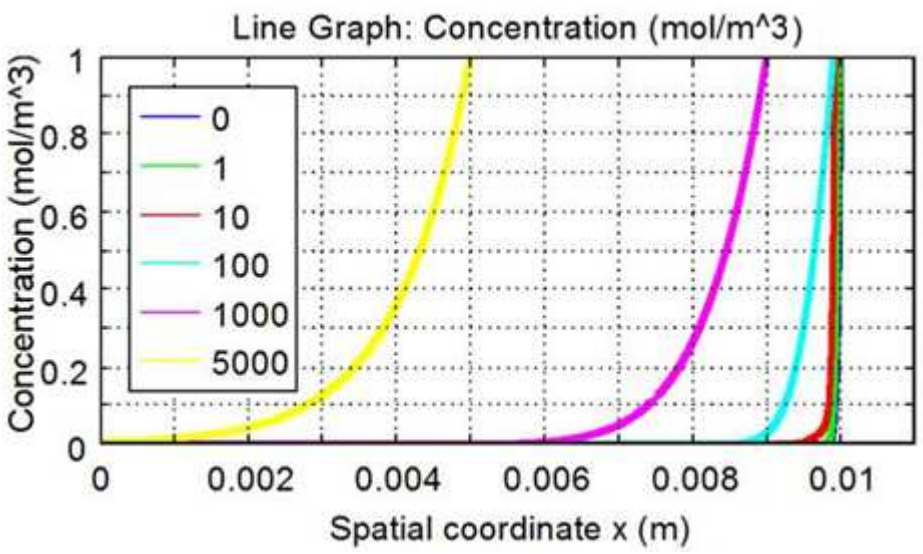

Figure 5.16. Concentration of compound A (water) diffusing into the surface of an evaporating liquid as function of distance from the air-liquid interface (x) at times ranging from 0 to 5000 sec (legend). Profiles terminate at the upper surface of the liquid.

Since water availability allows the hydrolysis reaction, higher concentrations at the surface can generate the already discussed hard oxide layer at the top of the solution. This decreases sample homogeneity and greatly affects the controlled evaporation process. It can be concluded from these simulations, that water CG are prominent, even for solution depths of just 1cm tall (what I had considered to be thin samples). Thus, future efforts should examine the use of even more shallow solution heights.

Figure 5.17 shows the concentration profiles for metal hydroxides as a function of time formed from water diffusing into the evaporating solution using a simple first order reaction. The phenomenon perceived in the last plot is seen again as hydroxides concentrations being very inhomogeneous in the EISA synthesis solution.

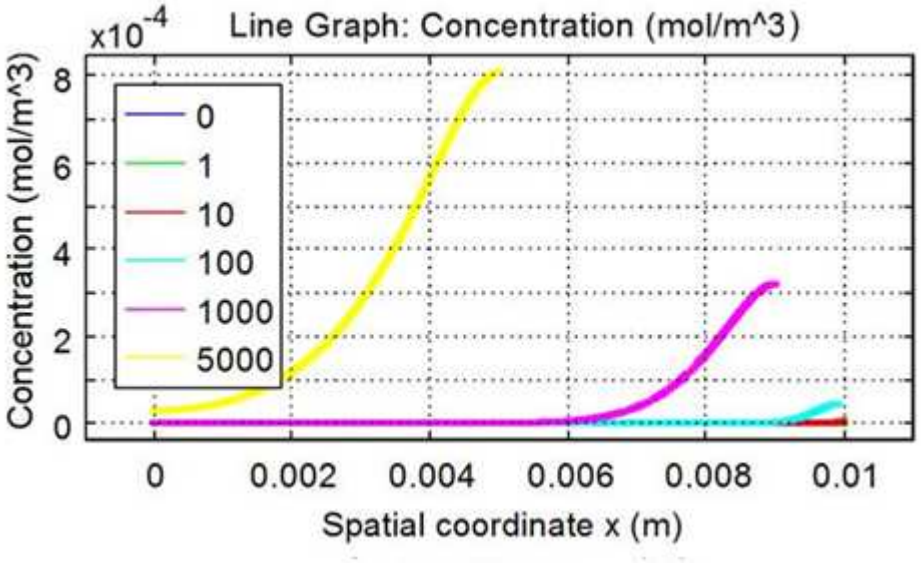

Figure 5.17. Concentration profiles of compound B (metal hydroxides) as a function of time formed from compound A (water) by a first-order reaction.

Additional potential useful results from these simulations are temperature and concentration profiles, CG behavior at varying conditions, precipitation behavior (oxide appearance) that can provide an extraordinary insight into how conditions couple together to control final particle morphology and structure. To improve the predictive nature of these modeling efforts, more detailed kinetic information is required for the water-metal complex reactions as a function of pH (recall that the HCl concentration in the solution changes over time and is known to affect metal hydroxide condensation rates).

Conclusions

Mesoporous ordered zirconia and CZY supports were synthesized from inorganic salts using a block copolymer template via EISA. As observed in previous chapters, water and ethanol diffusion rates during the aging process have a strong influence on the

final morphology of samples playing a key role in the formation of mesoporous structures.

Enhancements to pore ordering in oxide materials prepared by EISA were achieved by decreasing the surface area for evaporation as a fast evaporation rate induces a large concentration gradient (CG), whereas a slow evaporation rate favors a more homogeneous solution. However, the results for these systems showed that multiple phases were present, with ordered and disordered mesopores being appearing in significant fractions of the sample. This resulted from a hard oxide layer formed in tall containers that hindered the evaporation of the solution at the bottom of the vessel. It was later shown that it was better to reduce the evaporation rate by limiting the air flow (air velocity) over the sample with a special designed box and maintain a large evaporative area so samples were as thin as possible and as a result more uniform. These experiments provided insight into the critical parameters that enable the reproducible formation of ordered mesopore structures via the EISA method.

The transport model developed for the EISA synthesis process describes the effect of water concentration during the process, the evolution of composition, the time of evaporation, and other parameters in the system that influence the formation of ordered mesoporous structures. Additionally, it can potentially be used to predict composition, precipitation and temperature profiles under varying aging conditions, which are difficult to experimentally determine. This is very relevant as the code can ultimately help develop new protocols for mesoporous material synthesis.

References

(1) Brinker, C. J.; Lu, Y.; Sellinger, A.; Fan, H. *Adv Mater* 1999, *11*, 579-585.

(2) Lyons, D. M.; Ryan, K. M.; Morris, M. A. *J. Mater. Chem.* 2002, *12*, 1207-1212.

(3) Brezesinski, T.; Antonietti, M.; Groenewolt, M.; Pinna, N.; Smarsly, B. *New J. Chem.* 2005, *29*, 237-242.

(4) Brezesinski, T.; Smarsly, B.; Groenewolt, M.; Antonietti, M.; Grosso, D.; Boissière, C.; Sanchez, C. *N e w J . C h e m .* 2005, *Volume 156*, 243-248.

(5) Li, C.; Gu, X.; Wang, Y.; Wang, Y.; Wang, Y.; Liu, X.; Lu, G. *Journal of rare earths* 2009, *27*, 211-215.

(6) Yang, P.; Zhao, D.; Margolese, D. I.; Chmelka, B. F.; Stucky, G. *Chem. Mater.* 1999, *11*, 2813-2826.

(7) Larsen, G.; Lotero, E.; Nabity, M.; Petkovic, L.; Shobe, D. *Journal of Catalysis* 1996, *164*, 246-248.

(8) Rezaei, M.; Alavi, S.; Sahebdelfar, S.; Xinmei, L.; Yan, Z. *J Mater Sci* 2007, *42*, 7086-7092.

(9) Blin, J. L.; Flamant, R.; Su, B. L. *International Journal of Inorganic Materials* 2001, *3*, 959-972.

(10) Kim, A.; Bruinsma, P.; Chen, Y.; Wang, L.; Liu, J. *Chem. Commun.* 1997, , 161-161-162.

(11) Ni, C.; Li, X.; Chen, Z.; Li, H. H.; Jia, X.; Shah, I.; Xiao, J. Q. *Microporous and Mesoporous Materials* 2008, *115*, 247-252.

(12) Yuan, Q.; Li, L.; Lu, S.; Duan, H.; Li, Z.; Zhu, Y.; Yan, C. *The Journal of Physical Chemistry C* 2009, *113*, 4117-4124.

(13) Yuan, Q.; Liu, Q.; Song, W.; Feng, W.; Pu, W.; Sun, L.; Zhang, W.; Yan, C. *J. Am. Chem. Soc.* 2007, *129*, 6698-6699.

(14) Chen, F.; Liu, M. *J. Mater. Chem.* 2000, *10*, 2603-2605.

(15) Deshpande, A. S.; Pinna, N.; Beato, P.; Antonietti, M.; Niederberger, M. *Chemistry of Materials* 2004, *16*, 2599-2604.

(16) Teng, M.; Luo, L.; Yang, X. *Microporous and Mesoporous Materials* 2009, *119*, 158-164.

(17) Hung, M.; Fung, K.; Hung, D.; Hon, M. *Journal of the European Ceramic Society* 2008, *28*, 1161-1167.

(18) Hung, M.; Hung, D.; Fung, K.; Hon, M. *Materials Letters* 2008, *62*, 1147-1150.

(19) Hung, M.; Hung, D.; Fung, K.; Hon, M. *Journal of the European Ceramic Society* 2006, *26*, 2627-2632.

(20) Feng, R.; Yang, X.; Ji, W.; Aua, C. *Materials Chemistry and Physics* 2008, *107*, 132-136.

(21) Terribile, D.; Trovarellia, A.; Llorcab, J.; Leitenburga, C.; Dolcetti, G. *Catalysis Today* 1998, *43*, 79-88.

(22) Du, Y.; Sun, Y.; Di, Y.; Zhao, L.; Liu, S.; Xiao, F. *J. Porous Mater.* 2006, *13*, 163-171.

(23) Crepaldi, E. L.; Soler-Illia, G. J.; Bouchara, A.; Grosso, D.; Durand, D.; Sanchez, C. *Angew. Chem. Int. Ed.* 2003, *42*, 347-351.

(24) Ciesla, U.; Froba, M.; Stucky, G.; Schuth, F. *Chemistry of Materials* 1999, *11*, 227-234.

(25) Das, S. K.; Bhunia, M. K.; Sinha, A. K.; Bhaumik, A. *The Journal of Physical Chemistry C* 2009, *113*, 8918-8923.

(26) Grosso, D.; Cagnol, F.; Soler-Illia, G. ?. ?. ?.; Crepaldi, E. ?.; Amenitsch, H.; Brunet-Bruneau, A.; Bourgeois, A.; Sanchez, C. *Advanced Functional Materials* 2004, *14*, 309-322.

(27) Gibaud, A.; Grosso, D.; Smarsly, B.; Baptiste, A.; Bardeau, J. F.; Babonneau, F.; Doshi, D.; Chen, Z.; Brinker, C. J.; Sanchez, C. *J. Phys. Chem. B* 2003, , 6114-6118.

(28) Jiang, X.; Brinker, C. J. *J. Am. Chem. Soc.* 2006, *128*, 4512-4513.

(29) Homer, C. J.; Jiang, X.; Ward, T. L.; Brinker, C. J.; Reid, J. P. *Phys. Chem. Chem. Phys.* 2009, *11*, 7780-7791.

(30) Renon, H.; Prausnitz, J. *AIChE J.* 1968, *14*, 135-144.

(31) Vignes, A. *Ind. Eng. Chem. Fund.* 1967, *6*, 614-616.

(32) Chapman, S.; Cowling, T. G. In *The Mathematical Theory of Non-uniform Gases: An Account of the Kinetic Theory of Viscosity, Thermal Conduction and Diffusion in Gases;* Cambridge University Press: 1970.

(33) Grosso, D.; Cagnol, F.; Soler-Illia, G. J. d. A. A.; Crepaldi, E. L.; Amenitsch, H.; Brunet-Bruneau, A.; Bourgeois, A.; Sanchez, C. *Adv. Functional Mater*. 2004, *14*, 309-322.

CHAPTER SIX

DIFFUSIONAL PROPERTIES OF CERIA-ZIRCONIA-YTTRIA CATALYSTS SUPPORTS WITH DIFFERING MESOPOROSITY

Abstract

The diffusional properties of n-hexane in mesoporous ceria-zirconia-yttria (CZY) mixed oxides with differing pore size and morphologies are studied by the Zero Length Column (ZLC) method. The diffusion coefficients for n-hexane in mesoporous CZY and MCM-41 samples were calculated from desorption curves using a long-time range analysis method, and these values were verified using an intermediate time analysis of the desorption data. Results indicated that the diffusion rates for n-hexane were higher in CZY materials with linear, ordered arrangements of mesopores as compared to CZY systems of similar pore volume but having a disordered pore network.

Introduction

There are many reaction processes that use catalysts to enhance reaction rates, lower reaction temperatures, or improve product selectivity. Heterogeneous catalysis is presently the most common type of industrial reaction process and often involves the use of active metal species supported on a thermally stable supports, such as porous oxides or activated carbon. These catalysts supports help to disperse the active metals, limit catalyst losses, and in some cases are actively involved with the creation or stabilization of reaction intermediates. Depending on the pore structure of the catalyst support, overall reaction rates can be affected by the rates of mass transfer of species to and from the active catalytic species located within the catalyst pore structure. Generally catalysts are

considered to have certain simplified geometries, but in reality, the geometry of the pore structure is much more complicated. Thus, a partly empirical approach is required to study the mass transfer restrictions imposed by the pore structure of the catalyst. This is most easily achieved by measuring the diffusion rates of reactive species or their simulants in the support.

The various diffusion measuring techniques for porous solids may be classified as microscopic or macroscopic with respect to the relevant diffusion paths, and they can also be described as either equilibrium or non-equilibrium techniques.[1] The techniques for diffusion measurement referred to as macroscopic are the ones when the diffusion paths covered by the molecules during the experiments are typically much larger than the individual crystallites. For these cases, the diffusion through the entire crystals is studied. In contrast, measuring techniques that are able to monitor molecular displacements or the evolution of molecular concentration profiles over space scales smaller than the crystallite diameters are referred to as microscopic techniques. Among them, the pulsed field gradient (PFG) NMR technique has attained particular relevance, since with this technique a number of inconsistencies in the results reported in the literature with other techniques came to light.[1]

By the early 90's most researchers studying diffusion in porous materials came to the conclusion that only microscopically determined diffusivities were reliable and that macroscopic methods where not in agreement with these measurements, and reflected the kinetic limitations due to heat transfer, external film, bed effects and surface barriers.[2]

However, more recently experts believe that macroscopic measurements can be reliable if all considerations of the earlier difficulties are ensured.

Macroscopic techniques can be economically advantageous if done properly as they do not require complicated and expensive measuring devices or cumbersome procedures. The macroscopic diffusion behavior of gases in porous solids has been studied through the direct measurement of diffusion rates of molecules through a sample (steady state experiments) or from concentration measurements as a function of time at a given point (unsteady state experiments). Among these macroscopic approaches, the Zero-Length-Column (ZLC) method has proven to be very useful in measuring diffusivities in microporous and mesoporous materials because it minimizes the effects of axial dispersion, heat transfer and mass transfer resistance on the diffusion kinetics.

The ZLC technique was developed by Eic and Ruthven[3] in 1988 to directly measure transport diffusivities in porous adsorbent particles. The technique is relatively simple and consists of measuring the rate of desorption of a select gas moiety from a previously equilibrated sample. The sample is contained between two sintered discs in a very small quantity, which eliminates mass and heat transfer effects. The adsorbate concentration is very low and the carrier flow rate during desorption is high, which enables one to measure transport limited diffusion behavior instead of equilibrium. Over the last decade, this technique has been used to measure diffusion rates in microporous and macroporous systems for a wide variety of gases and even liquids. The relevant parameters are extracted using the long-time asymptote of the desorption curve[3] or with a short-time approximate method[4].

Among porous solid catalysts and catalysts supports, mesoporous materials have been extensively studied over the last two decades because of their applications in catalysis,[5-8] adsorption,[9, 10] biomolecular separation,[11, 12] and drug delivery[13, 14]. These materials have achieved such widespread attention because of their unique properties, which include high surface area, uniform pore size distribution, large pore volume and thermal stability.

Mesoporous ceria-zirconia-yttria (CZY) oxides are of particular importance due to the varied chemistry of these transition metal oxides. They have been widely used in a number of catalytic and electronic applications, the largest as catalyst supports for solid oxide fuel cells[15-18] and three-way catalysts (TWC) for automotive catalytic converters.[19-21]

Our group has prepared CZY oxides using multiple synthesis approaches,[22] which have yielded materials with somewhat similar properties but different pore sizes and morphologies. One of the biggest differences between the CZY materials prepared is the existence of a well-ordered arrangement of mesopores for some of the soft template synthesized oxides. It has been hypothesized that this ordered mesopore morphology has advantages when it comes to catalytic performance. For example, the larger pore size as compared to microporous supports readily facilitates the mass transport of bulky molecules, and the linear pore channels offer few interferences for the diffusion of molecules. Finally, the high surface areas exhibited by these materials, where a large fraction of the surface is readily accessible to reactive species, allow for there to be a uniform and highly dispersed distribution of active sites. Compared to other support materials, ordered mesopores have the advantage of reducing sintering of catalysts by

stabilizing metal particles since they cannot grow to sizes larger than the pore size unless they move to the external surface of the particle.[23] The well-organized pore topology is also ideal for diffusion and equilibrium studies as they avoid pore-networking effects on adsorption and transport.

To date, the most cost effective methods for preparing these mesoporous materials are via techniques that employ endo-templates (i.e., soft templates, such as surfactants, dendrimers, and block copolymers) and exo-templates (i.e., hard templates, such as porous carbons and resins). The soft templating techniques generally involve sol-gel or EISA methods, while the hard templates require no sol-gel chemistry to achieve the desired templating effect.

Limited studies have been published on the effect of CZY pore morphology on catalyst performance. Thus, this study examines diffusion effects related to CZY pore morphology using the Zero Length Column (ZLC) method. The CZY supports studied have been synthesized using a variety of templates: block copolymers, resins, activated carbon and dendrimers. The results obtained from this study provide insight into the diffusion phenomena occurring within the pores of the tested CZY catalyst samples and will aid in the identification of an optimal catalyst support material.

The ZLC technique: Mathematical Model Summary

A detailed description of the mathematical basis for calculating diffusion rates from desorption curves using the ZLC method are explained elsewhere [3, 24] and presented in Appendix D for completeness. The general analysis is based on four main assumptions,

as described by Qiao and Bathia[25], presented in Chapter 2 and detailed below again for convenience.

a. Gas hold up in the fluid phase is neglected.
b. The catalysts consists of uniform spherical particles, where adsorption equilibrium is attained at the particle surface and very low partial pressures of the sorbate ensure that Henry's law applies.
c. The flow rate of inert purge gas is high, eliminating bulk mass and heat transfer limitations.
d. The temperature in the system is uniform and constant.

The analytical ZLC solution[26] that describes desorption from of a porous 3-dimensional material with the above assumptions can be presented using the following set of equations:

$$\frac{c(t)}{c_o} = \sum_{n=1}^{\infty} \frac{2L}{\beta_n^2 + L(L-1)} . \exp(-\beta_n^2 \frac{D_{eff}}{R^2} t) \qquad \text{(6-i)}$$

$$0 = \beta_n \cdot \cot \beta_n + L - 1 \qquad \text{(6-ii)}$$

$$L = \frac{1}{3} \frac{F}{V_s} \cdot \frac{R^2}{K_H D_{eff}} \qquad \text{(6-iii)}$$

where c is the concentration of sorbate in the fluid phase, L a dimensionless parameter that introduces the flow rate to the set of equations and represents the ratio of the diffusional time constant and the washout time for the solid phase, D_{eff} is the effective diffusion constant, β_n are the positive roots of Equation b, R is the mean particle radius, t

is time, V_s is the solid volume, F is the fluid flow rate and K_H is the dimensionless Henry constant.

In the long-time region equation (a) is simplified to

$$\ln(\frac{c}{c_o}) \approx \ln\left[\frac{2L}{\beta_1^2 + L(L-1)}\right] - \beta_1^2 \frac{Dt}{R^2} \qquad \text{(6-iv)}$$

Under these conditions, I can determine L and D/R^2 from the intercept and slope, respectively, of the long-time asymptote of the semilogarithmic plot of $\frac{c}{c_0}$ versus t. This method is known as long-time (LT) analysis.

The experimental n-hexane desorption curves for all samples were analyzed so as to obtain the pore diffusivities by the LT analysis method. The results obtained by this mathematical method were verified using a separate analysis technique called the intermediate analysis method, which makes use of an earlier portion of the desorption curve. The details of this latter method are discussed in Appendix D. Further, diffusivities were measured for a mesoporous silica reference material (MCM-41) and those values compared to accepted literature values.

Experimental Section

Materials. All CZY mixed oxides used in this study were prepared using a range of organic templates: soft templates (block copolymers, dendrimers, surfactants) and hard templates (resins and activated carbon). All details about the synthesis of these materials are explained elsewhere[22] (see Chapter 3). Two synthesis techniques were used to prepare all tested samples: classical sol-gel and evaporation induced self-assembly (EISA)

methods. The synthesized CZY materials were all mesoporous, but the overall pore morphology varied with the type of synthesis technique and template used during synthesis.

High purity hexane (>95%; Alfa Aesar) and ultra-high-purity helium (>99.99%, Airgas) were used as the adsorptive agent and carrier gas, respectively.

Characterization. The structure of all CZY materials was characterized by several techniques, including nitrogen physisorption, powder x-ray diffraction and electron microscopy. Nitrogen adsorption and desorption isotherms at 77 K were measured using a Micromeritics ASAP 2020 system after the samples were outgassed at 473 K overnight. The sorption data were analyzed using the Barret-Joyner-Halenda (BJH) model to obtain the pore size distribution and with the Brunauer-Emmet-Teller (BET) model for surface area.

Transmission electron microscopy (TEM) studies were carried out on a Hitachi H9500 TEM, a Hitachi H7600 TEM and on a Hitachi HD 2000 STEM at 300, 120 and 200 kV, respectively, to determine the morphology and pore sizes for all samples. Small-angle X-ray diffraction (SAXD) patterns were obtained with the RigakuUltima IV X-ray diffractometer with Cu Kα radiation (λ = 1.5406 Å) and Ni filter, operated at 40 kV and 44 mA. This data, in conjunction with TEM images, was used to identify the presence of ordered mesopores in the samples.

Finally, particle size distributions were determined for all samples by using standard sieves. The sample (powder) was separated by size and particles between 37 and 45μm were used for all different diffusion experiments.

The ZLC technique: Experimental Set Up. The general components of ZLC systems have been extensively described elsewhere,[27] and generally consist of a short cell or sample chamber, where the adsorbent material is placed, a carrier gas/adsorbate delivery system, and an analytical device (often a gas chromatograph or mass spectrometer) for measuring gas concentrations. The adsorbent is equilibrated with an inert carrier gas containing a low concentration of an adsorbate gas. After the adsorbate is equilibrated with the sample, it is desorbed into a high flow carrier gas. The desorption curve for the adsorbate can later be analyzed to calculate the diffusivity for the adsorbate moving through the porous.

The experimental apparatus constructed by our group is depicted in Figure 6.1. It features a permeation cell (KIN-TEK Laboratories, Inc.), instead of the usual bubbler used for ZLC experiments, which contains a liquid hydrocarbon (adsorbate). The carrier gas flows through the permeation cell at a fixed flow rate, which ensures that a constant amount of adsorbate is added to the carrier gas. The ability to accurately control the dose rate of adsorbent is important for getting reproducible results. The 1/16 in. gas lines are heat traced to avoid condensation or adsorption of the adsorbate gas on the tube walls, these heating loops also help to preheat the gas before it enters the furnace that contains the zero-length cell. Inside the furnace the gas feed line is coiled several times to ensure that the adsorbate/carrier gas is heated to the desired temperature before passing through the ZLC cell containing the porous material. After going through the adsorbent material, the concentration of the adsorbate in the exit gas stream is recorded with a mass spectrometer (Balzers Prisma QME 2000, quadrupole mass spectrometer, MS), which is

connected directly after the cell through a short capillary line (slip stream) that is also heat traced. Most of the gas exiting the ZLC is evacuated through the vent. A heated four-way valve is used to switch between the adsorbate gas and the pure carrier gas streams and their flow rate is controlled by separate mass flow controllers (MFC). The mass flow controllers are frequently calibrated using a bubble flow meter. System pressure is carefully controlled in both the carrier and adsorbate lines to ensure they are maintained at near identical values to avoid a jump in the flow after switching the gas flows through the ZLC.

The particular design of this apparatus has been carefully planned so it is feasible to do isotopic labeling experiments as well using the steady state isotopic transient kinetic analysis[28] (SSITKA) technique.

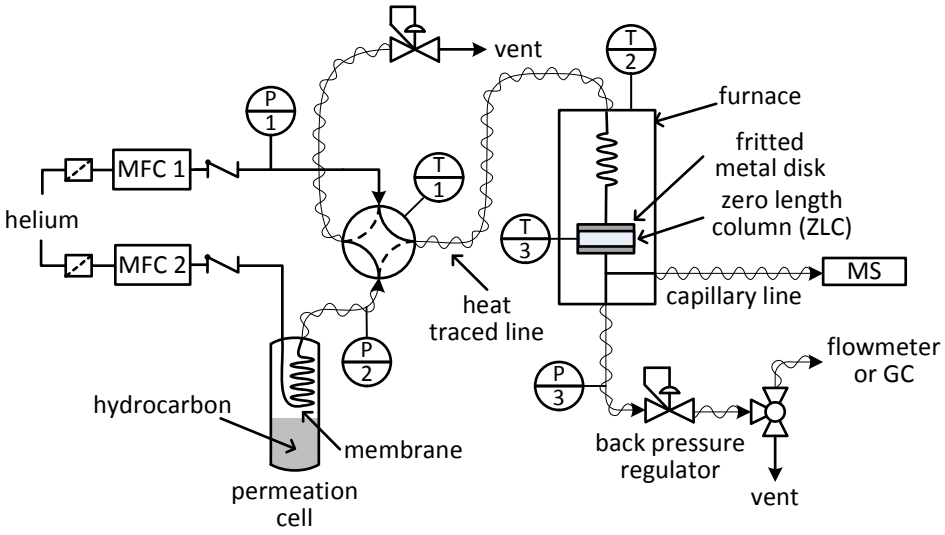

Figure 6.1. Simplified schematic diagram of ZLC apparatus. The Zero-Length Column contains a very small quantity of adsorbent material between two sintered disks.

Diffusion Measurements. A small sample (2-2.5mg) of CZY materials were placed between two sintered disks in a 1/8 in. stainless steel Swagelok union, which was placed inside the ZLC system furnace and equilibrated with an inert carrier (helium UHP, Airgas) stream containing a very small concentration of an adsorbent, in this case hexane (95%+, Alfa Aesar). After equilibrium is reached, the flow is switched to a pure He carrier stream, and the effluent concentration of the adsorbent component is monitored using an MS detector for greater accuracy. Before analysis, each sample was purged with pure helium for 12 hrs at 250 °C. At the start of each diffusion experiment the sample was exposed to a helium/hexane gas mixture until the concentration of hexane in the gas did not change. The mixed flow was then continued for an additional hour. Desorption of n-hexane from CZY mixed oxides was performed at pure carrier gas flow rates of 80,120 and 160 ml/min at 60 °C. Five different CZY adsorbent materials were studied, all five mixed oxides had equivalent proportions of ceria, zirconia and yttria and were synthesized via sol-gel or EISA techniques using a range of templates that included block copolymers, dendrimers, surfactants, activated carbons and organic resins.

The diffusional time constant R^2/D is determined by matching the experimental response curve to the theoretical curve derived from the appropriate solution to the Fickian diffusion equation.

Results and Discussion

The ceria-zirconia-yttria materials used for these experiments all contain a significant quantity of mesopores but differ either in surface area, pore size or mesopores arrangement. All oxides had an average crystallite diameter of 41μm. Because one of the

main purposes of this work is to understand how the diffusional properties of CZY mixed oxides vary with morphology, the key physical characteristics of these materials were measured and are shown below.

Physical Properties of CZY mixed oxides. All synthesized CZY materials are comprised of approximately 50% ceria, 45% zirconia, and 5% yttria (mol%), as determined by ICP-AES, in the form of a homogeneous mixed oxide. The nitrogen adsorption/desorption isotherms and Barret-Joyner-Halenda (BJH) pore size distribution data for sol-gel and EISA synthesized CZY oxides are shown in Figure 6.2. The BET surface area, average BJH pore size and other CZY characteristics are summarized in Table 6.1.

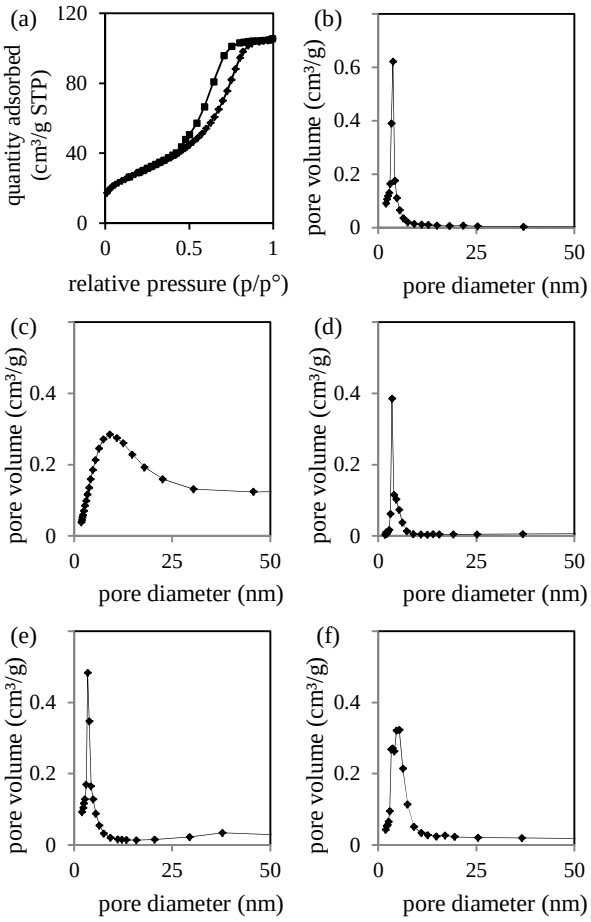

Figure 6.2. Nitrogen adsorption-desorption isotherm (a) and BJH pore size distribution (b) for a block copolymer template CZY material synthesized via EISA; (b)-(f) show the BJH pore size distribution for CZY materials prepared using sol-gel techniques using block copolymer, activated carbon, dendrimer, resin or surfactant templates, respectively.

Figure 6.2a presents the physisorption isotherm for the EISA synthesized CZY mixed oxides. The plot shows the typical hysteresis loop characteristic of mesoporous materials. This suggests that indeed the materials obtained are mesoporous. All prepared mesoporous CZY oxides exhibit physisorption isotherms similar to that shown in Figure 6.2a.

The BJH pore size distributions (see Figures 6.2b-f) are largely unimodal for all CZY materials independent of synthesis techniques or templating agent. Despite these

similarities, the materials do display some variations in average pore size, as reported in Table 6.1. For example, the EISA block-copolymer templated CZY (Figure 6.2b) sample has a significantly sharper distribution, where most of the pore volume (>60%) corresponds to pores with a diameter of approximately 4 nm. Whereas, only 35% to 45% of the pores in all other CZY oxides have a similar pore size. From the peak widths at half-height for the unimodal pore volume distributions for all CZY samples, it is observed that the EISA templated CZY oxides have a more uniform pore structure as compared to CZY materials prepared by other methods. Further, the activated carbon and surfactant templated CZY oxides have a less uniform pore structure with broader pore size distributions. Finally, the resin templated CZY materials are the only samples with a second smaller quantity of pores having a much larger pore diameter (40 to 60 nm).

As it is impossible to accurately predict exact pore morphologies from nitrogen physisorption data, other characterization techniques are required to fully define the pore structure of these oxides. Thus, high-resolution TEM analysis of CZY materials, as shown in Figure 6.3, was used quantify the pore size, structure regularity, and morphology of these catalysts supports.

Review of the TEM images shows that four of the samples are disordered, while one exhibited highly ordered mesopores. The material with ordered mesopores corresponds to the block copolymer templated CZY that was synthesized via EISA techniques. This observation is consistent with the BET surface area and BJH pore size distributions described previously.

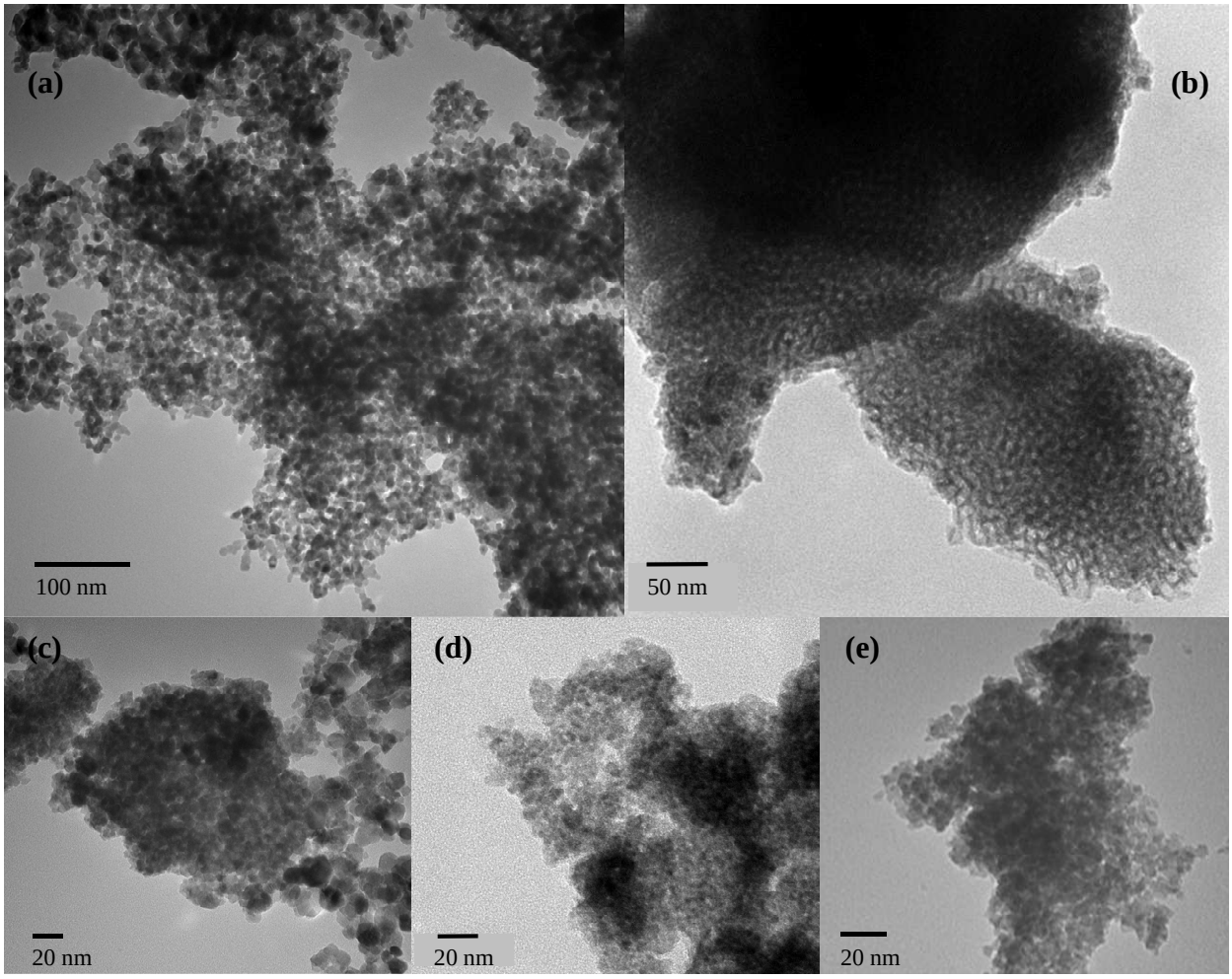

Figure 6.3. TEM images of mesoporous CZY materials synthesized using (a) activated carbon hard template (b) block copolymer template and EISA technique (c) dendrimer and sol-gel technique (d) resin hard template (e) surfactant template and sol-gel technique.

The TEM observations are further confirmed by the small angle x-ray diffraction patterns shown in Figure 6.4. The EISA synthesized CZY was the only sample that showed a low angle x-ray diffraction peak consistent with the presence of ordered mesopores, whereas all other samples did show any low-angle diffraction peaks, which was similar thre behavior observed with surfactant templated CZY samples prepared using sol-gel techniques (see Figure 6.4b).

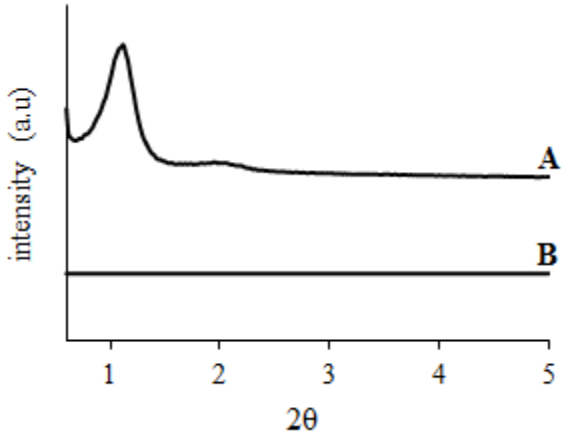

Figure 6.4. Comparison of small-angle powder X-ray patterns for porous CZY oxides synthesized using (a) block copolymer templates and the EISA technique and (b) surfactant templates and sol-gel technique.

Diffusional Properties of CZY oxides. The rate of hexane desorption from CZY oxides with differing mesoporosity at 60 °C are shown in Figure 6.5 for purge gas flow rates of 80, 120 and 160 ml/min. The relatively high purge gas flow rates were chosen so as reduce mass transfer limitation external to the catalyst particles and to assure that kinetic (or transient) behavior, as opposed to equilibrium limitations, controlled the concentration of hexane in the exiting purge gas flow. From these hexane desorption curves it is possible to extract diffusion parameters for hexane within the CZY pores, with the added assumption that the diffusivities are measured under conditions of zero surface loading and low gas phase concentrations where Henry's law adequately describes the phase equilibria behavior of hexane.

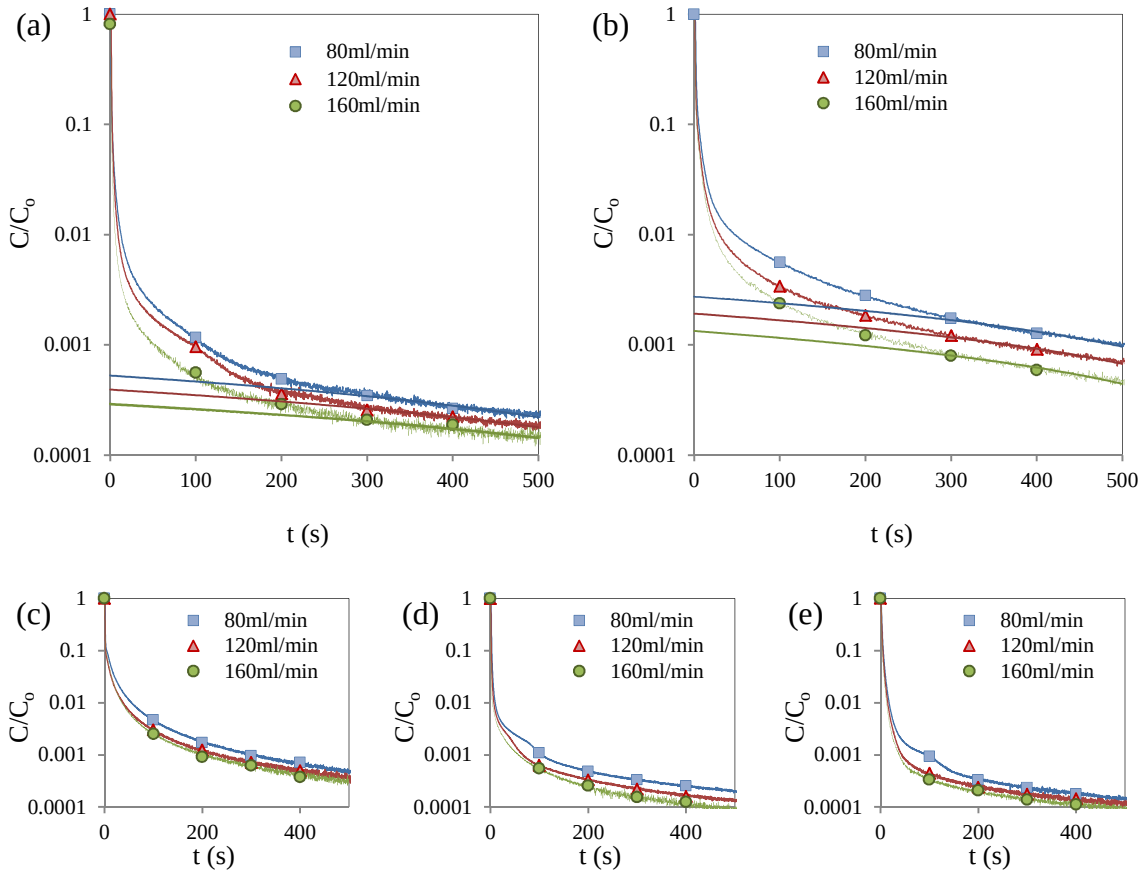

Figure 6.5 Effect of helium purge flow rate on the rate of desorption of hexane in CZY materials synthesized using (a) activated carbon templates, (b) block copolymer templates and the EISA technique, (c) dendrimer templates and the sol-gel technique, (d) resin template, and (e) surfactant templates and the sol-gel technique. Hexane desorption curves were measured at 60 °C. Symbols are shown for a select few data points on each desorption curve for illustration purposes, each desorption curve consists of approximately 2000 data points.

The desorption curves shown in Figure 6.5 display a slow exponential decay behavior which indicates a diffusion-controlled process as compared to the linear desorption behavior more indicative of equilibrium based processes. The rate at which the concentration of hexane decreases is directly related to the transport rate, and as expected, these results show that desorption rates decrease as the purge gas flow rate decreases. Slope and intercept values for linearized regions of the desorption curves can

be used to determine diffusivity parameters for the mesopores of CZY materials using the long-time ZLC mathematical model.[3, 29] The ZLC derived parameters and calculated diffusion coefficients (D) are shown in Table 6.1. Analysis of this data indicates that the desorption rates are purge flow rate dependent, but the resulting diffusion coefficients are insensitive to this purge rate, which is consistent with the ZLC model. The insensitivity of the calculated diffusivity values to purge flow rate clearly demonstrates that the transport (desorption) process is kinetically controlled with resistances dominated by intraparticle diffusion as opposed to interparticle diffusion processes whose mass transfer resistance would vary with purge gas flow rate.

Table 6.1. ZLC model parameters (F and L) and CZY diffusion coefficients (D) as a function of purge gas flow rate for n-hexane desorption at 60 °C from CZY materials synthesized using EISA and sol-gel techniques with a range of structure directing agents (templates).

CZY template	**F (cm^3/min)**	**L**	**Flow rate ratio**	**L ratio**	**D (cm^2/s)**	
					Individual	Average
block copolymer with EISA technique	80	528	1	1.00	6.96E-08	7.1E-08
	120	748	1.5	1.42	7.02E-08	
	160	1040	2	1.97	7.43E-08	
dendrimer with sol-gel technique	80	675	1	1.00	6.29E-09	5.8E-09
	120	1060	1.5	1.57	5.65E-09	
	160	1306	2	1.94	5.53E-09	
surfactant with sol-gel technique	80	4022	1	1.00	4.28E-09	4E-09
	120	5820	1.5	1.45	3.79E-09	
	160	6899	2	1.72	4.04E-09	
activated carbon	80	2907	1	1.00	3.83E-09	3.6E-09
	120	4082	1.5	1.40	3.41E-09	
	160	5076	2	1.75	3.61E-09	
resin	80	2875	1	1.00	6.86E-08	7.2E-08
	120	4196	1.5	1.46	7.08E-08	
	160	5654	2	1.97	7.65E-08	

The *L* value is another ZLC model parameter that can be used to indicate whether the process is kinetically or equilibrium controlled. When the *L* value is relatively high (>5), i.e., the removal rate of sorbate by the purge gas is faster than pore transport, then the process is kinetically controlled, whereas an *L* value below 0.5 is indicative of an equilibrium controlled process. For all experiments in this study, the calculated *L* value is very high, indicating pore diffusion-controlled behavior. Further, prior work by others[2-4,30-31] has shown the ZLC model is only valid when the *L* value is proportional to the purge gas flow rate, and for all studies described herein, the ratio of these values remained approximately constant; thus, validating the use of this technique to study diffusion in mesoporous CZY samples.

The diffusivity values obtained in this study appear to be similar to various results reported in the literature for similar gases in mesoporous materials. For example, Gobin[26] reported that the diffusivity of n-heptane in SBA-16 at 50 °C varied from $1x10^{-9}$ to $4x10^{-9}$ cm^2/s; similarly, Quiao and Bathia[30] obtained a diffusivity of $2.93x10^{-7}$ cm^2/s for hexane in MCM-41 at 50 °C. In the present study, the diffusivity values vary between $3.6x10^{-9}$ cm^2/s for the activated carbon templated CZY samples to $7.2x10^{-8}$ cm^2/s for resin templated CZY samples. The EISA synthesized and resin templated samples have significantly larger gas diffusivity values as compared to the other CZY materials. The larger diffusivity for the case of the EISA synthesized CZY is attributable to the ordered pore structure of the material. This ordered mesostructure facilitates the intraparticle transport of bulky molecules, improving diffusion properties significantly.

For the resin templated materials, the reason for enhanced gas transport is less obvious. Compared to the other disordered CZY mesoporous materials, the resin templated sample has a unique structure. Analysis of the resin CZY pore structure using TEM, provided little new information as the oxide connectivity resembled that of the other disordered CZY samples; however, analysis of the resin CZY pore structure using nitrogen physisorption identified an increase in the number of pores with diameters from 40 to 60 nm relative to the other disordered CZY materials. It is the presence of these larger pores that is believed to be the cause for enhanced gas diffusion rates in the resin CZY samples that contains a disordered arrangement of mesopores. To more clearly illustrate the differences between CZY mesoporous materials prepared using multiple templating and synthesis strategies, Table 6.2 shows the hexane diffusivity for the oxides as well as their surface area, average pore size and morphology.

Table 6.2. Physical Characteristics and Diffusivities of Prepared CZY Materials.

	Soft Template			Hard Template	
	Block Copolymer (EISA)	Dendrimer	Surfactant	Activated Carbon	Resin
BET surface area (m^2/g)	105	76	78	118	98
BJH avg. pore size (nm)	4	3.5	6.2	9	3.4; 60
Mesopore morphology	Ordered	Disordered	Disordered	Disordered	Disordered
Diffusivity (cm^2/s)	7.14E-08	5.83E-09	4.03E-09	3.62E-09	7.2E-08

For the soft templated samples, we see that both the surfactant and dendrimer templated CZYs, which were synthesized by the classical sol-gel approach, have approximately the same surface area and a disordered mesostructure but differ in average

pore size. Despite these pore size differences, the measured hexane diffusivities and TEM morphologies for these materials were nearly identical, which suggests that the primary resistance to hexane diffusion was the necked down regions between pseudo-spherical CZY oxide nanoparticles in these samples.

On the other hand, the hexane diffusivity measured for the EISA synthesized CZYs, which are templated using the block copolymer soft templates, differ by an order of magnitude from the values for less ordered materials. Specifically, the ordered arrangement of linear pores leads to an increase in oxide surface area and provides greater pore size uniformity, which ultimately leads to increased gas diffusivity via the elimination of the pore constrictions that are present in most of the other synthesized CZY samples. Though the structural characteristics ascertained by nitrogen physisorption experiments are often useful predictors of transport properties, the irregular pore structures of classical sol-gel templated CZY samples leads to these methods being of less use in the prediction of the gas transport properties, which play a central role in catalytic behavior. It is important to understand the parameters that affect diffusion since controlling it may suggest new materials with advanced performance. The higher the diffusivity, the faster reactants reach active reactions site located within the pores; thus, it is advantageous to find identify catalyst supports with the highest diffusivity.

For the hard templates, the resin templated CZY material exhibits unexpectedly high gas diffusivity, despite the CZY material templated by activated carbon having greater surface area, a larger average pore size, and similar mesoporosity. This anomaly can be explained by the BJH pore size distribution for the resin templated samples, which shows

that these samples have an increased number of large mesopores (diameters of 40 to 60 nm). Also, the pore size distribution is more uniform with 45% of the resin templated pores having a diameter of about 3.4 nm, as compared to the activated carbon CZY samples, where approximately 25% of pores have a diameter of about 9 nm. The activated carbon samples have a more random distribution of pores with the BJH pore size distribution showing a broader peak for pore size (see Figure 2c). This wider distribution also means that there are more small pores. The existence of these small pores introduces a diffusion limiting structural feature to the material, especially if these smaller pores are at the entrance of larger diameter structures. This latter situation is analogous to diffusion through the super-cage structure of zeolite Y, where small diameter pores provide access and limit the diffusion of species to the larger super-cages.

In general, it can be concluded that pore morphology has a greater impact on diffusivity in CZY materials than surface area or average pore size. Further, traditional physical characterization techniques, such as N_2 physisorption, only provide a partial picture of the pore structure in CZY materials and can be a poor predictor of species transport through the material. For the case of the carbon templated CZY sample, its surface area and average pore size are very high appearing to be a better material for catalytic applications but it is the material with the lowest hexane diffusivity. This behavior is attributable to its morphology, and compared to other CZY disordered mesostructures, it has the least uniform pore size distribution. The observed diffusion behavior suggests that access to the larger pores is limited by a bottleneck, such as a smaller diameter entrance pore.

Figure 6.6 illustrates the effect of pore morphology on gas diffusion rates; disordered structures can have pore connectivity issues like the existence of closed and blind pores. Also the pathways the gas follows can be complex which can diminish diffusivities incredibly. On the other hand, straight pore channels are the ideal case for fast gas transport, where no obstacles interfere with the free flow of gaseous species. An additional case is presented in Figure 6.7, where straight mesoporous channels are connected to other mesopores via translated pore opening, which leads to a pore constriction at the interface between the mesoporous channels.

Additionally, diffusion rates for large straight pore systems can be reduced if the pore channels change directions frequently. This latter case can happen for ordered CZY materials and might explain the variations found between literature values for similar mesoporous ordered structures.

The block copolymer templated CZY prepared using the EISA technique displayed the highest gas diffusivity. This well-ordered mesostructure has transport advantages as it improves pore connectivity and has a larger surface area as compared to other CZY materials. This accentuates the importance of using EISA methods to synthesize CZY materials with long-range ordered mesostructures, as compared to the disordered CZY mesoporous oxides prepared using more traditional sol-gel techniques. This is especially important as we look at an order of magnitude difference in the diffusion parameter, which for catalytic applications can mean a significant improvement in catalyst performance.

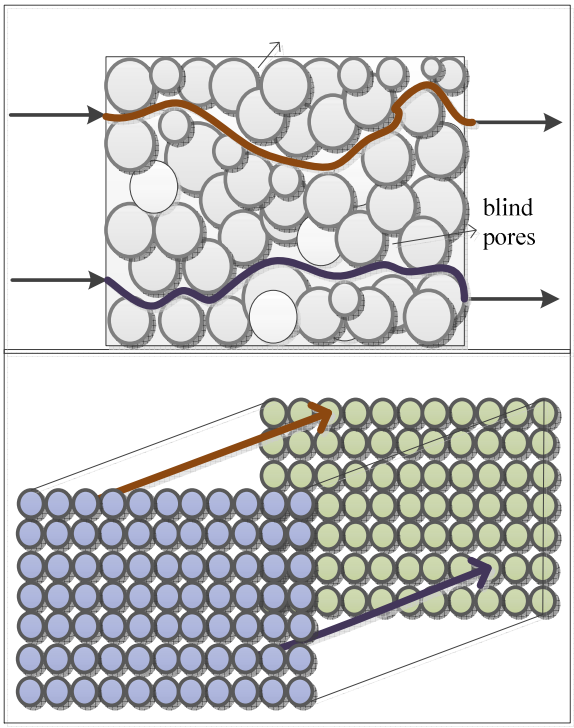

Figure 6.6. Representation of gas diffusion through CZY pore channels with disordered (top) and ordered (bottom) mesostructures.

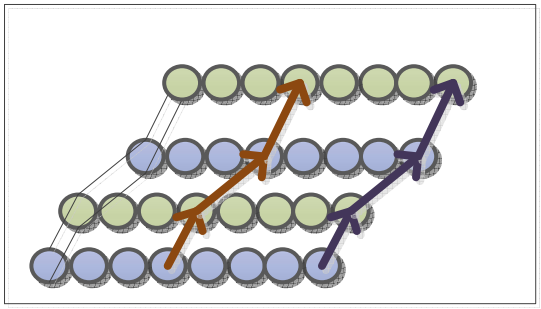

Figure 6.7. Representation of gas diffusion through CZY straight pore channels of different lengths.

Validation of Results

As explained in the results and discussion section, enough evidence is given of kinetic behavior and not equilibrium-controlled phenomena so as to trust the calculated diffusivities. The first clear evidence being the shape of the desorption curves since

instead of being straight lines passing through the origin in semi-logarithmic coordinates, they show significant curvature. Also, at high flow rates, the *L* values are proportional to purge gas flow rates as expected. Further confirmation of hexane desorption being under kinetic control is shown in Figure 6.8, where $\log(C/C_0)$ is plotted as a function of Ft as described by Brandani et al.[31] The time range of the kinetically controlled region was obtained from the plot which shows diverging curves at the long-time region. The calculated L values are also greater than five as sought.

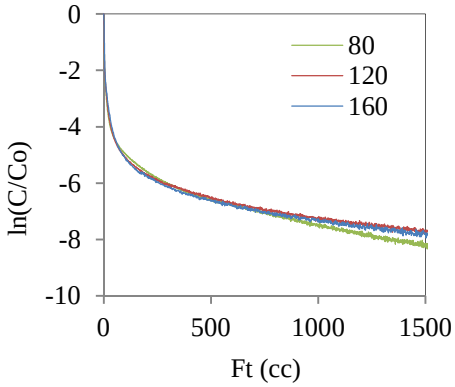

Figure 6.8. ZLC response curves plotted in the form ln(C/C0) vs. Ft for CZY mixed oxides synthesized using a block copolymer soft template and the EISA technique, showing kinetic diffusion control at varying purge gas flow rates at long times. Legend values are given in ml per min.

To further validate our experimental technique, we measured the diffusivity of hexane in MCM-41 (a well-studied mesoporous silica material) and compared our results to published values. About 2 mg of MCM-41 were placed between two sintered disks inside the oven. The sample was purged overnight at 250 °C using pure helium. Then helium with a very small concentration of the hexane adsorbent was flown through the system until the sample was equilibrated with the absorbent and measurements of desorption were taken at 60 °C. Figure 6.9 shows the desorption curves for these measurements.

The measured diffusivity values for MCM-41 samples are shown in Table 6.3 and are similar to results reported in the literature. For example, Gobin[26] reported that the diffusivity of n-heptane in SBA-16 (a mesoporous silica) at 50 °C ranged from $1x10^{-9}$ to $4x10^{-9}$ cm^2/s using the same long-time analysis method and ZLC technique used herein. For these studies, the *L* value from the ZLC analysis is very high, indicating diffusion-controlled behavior and as expected, the *L* value from the ZLC model is proportional to the purge gas flow rate.

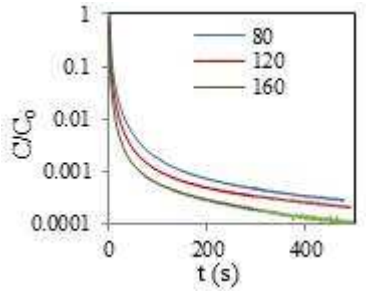

Figure 6.9. Effect of helium purge flow rate on the rate of hexane desorption in MCM-41. Desorption curves were measured at 60 °C. Each curve contains approximately 2000 data points.

Table 6.3. ZLC model parameters and gas diffusivity for n-hexane in MCM-41 materials as a function of purge flow rate. Desorption experiments were performed at 60 °C.

F (cm^3/min)	**L**	**Flow rate ratio**	**L ratio**	**D (cm^2/s)**	
				Individual	Average
80	2044	1	1	1.09E-09	1.1E-09
120	2872	1.5	1.41	1.03E-09	
160	4755	2	2.33	1.17E-09	

Qiao and Bathia[30] found a diffusivity of $2.93x10^{-7}$ cm^2/s at 50 °C and a D/R^2 of 0.21s for this system. However, measurements presented significant equilibrium limitations.

This study used a complete time range analysis. Other published values obtained by NMR[32] showed a diffusivity of $4x10^{-6}$ cm^2/s. As expressed by Brandani[2] the current general consensus is that all these measurements are in fact correct within their respective uncertainties and the results reflect the fact that the crystals have internal imperfections that dominate the macroscopic measurements. Different techniques can yield diffusivity values that differ up to three orders of magnitude from that of an ideal crystal.

It is concluded from these observations that for our MCM-41 system, using the same analysis technique, the literature values are very similar to the ones found here. The long-time analysis is also found to be accurate for our case as shown in the relative concentration versus Ft curves. It is hard to conclude if the values found throughout the study are in fact the accurate absolute diffusivity values. However, they are accurate for this technique and it is valid to use these values to compare diffusional properties between similar systems to have an idea of the diffusional advantages of a system versus another and find the best material for our catalyst applications. Further analysis of the desorption curves obtained for the experiments in this article can be found in Appendix J.

Conclusions

Multiple CZY samples with differing mesoporosity were prepared using a range of structure directing agents and synthesis techniques. The diffusion kinetics of n-hexane in these mesoporous CZY materials were measured at 60 °C using the ZLC method. The diffusion coefficients were derived by the long-time range analysis method and are in the range of $3.6x10^{-9}$ to $7.2x10^{-8}$ cm^2/s, with disordered oxides having generally lower

diffusion rates than oxides prepared using the EISA method. These diffusivity values were validated to be kinetic (non-equilibrium) measurements as they were independent of the purge gas flow rate. Further, the measured diffusivities were highly dependent on the morphology of the respective CZY mixed oxide.

The diffusion behavior of n-hexane in mesoporous CZY materials was found to be significantly impacted by the geometry and connectivity of the pores and more specifically, the presence of small diameter connection channels between mesoscale void spaces within the oxides. Interestingly, CZY physical characteristics such as surface area and average pore size had far less an impact on measured diffusion rates, suggesting that these values may not be good predictors of catalyst transport properties. The ZLC technique provides a straightforward method for calculating gas phase diffusion rates through mesoporous catalyst materials enabling a more accurate prediction of final catalyst performance when the catalysts are used under conditions where reactions are transport limited.

Acknowledgement. This study was supported in part by Toyota Motor Engineering & Manufacturing North America, Inc. The authors would like to acknowledge Haijun Qian for his help with the TEM imaging of CZY samples and Ha Nguyen for his work assembling the gas-phase diffusion apparatus.

References

(1) Kärger, J.; Vasenkov, S. *Microporous and Mesoporous Materials* **2005**, *85*, 195-206.

(2) Brandani, S. *Diffusion Fundamentals* **2007**, *6*, 4.1-4.10.

(3) Eic, M.; Ruthven, D. M. *Zeolites* **1988**, *8*, 40-45.

(4) Hufton, J. R.; Ruthven, D. M. *Ind Eng Chem Res* **1993**, *32*, 2379-2386.

(5) Bhaumik, A.; Tatsumi, T. *J. Catal.* **2000**, *189*, 31-39.

(6) Aprile, C.; Abad, A.; Garcia, H.; Corma, A. J. *J. Mater. Chem.* **2005**, *15*, 4408-4413.

(7) Fujiwara, M.; Terashima, S.; Endo, Y.; Shiokawa, K.; Ohue, H. *Chem. Comm.* **2006**, 4635-4637.

(8) Chandra, D.; Laha, S. C.; Bhaumik, A. *Appl. Catal. , A: Gen.* **2008**, *342*, 29-34.

(9) Yoshitake, H.; Yokoi, T.; Tatsumi, T. *Chem. Mater.* **2003**, *15*, 1713-1721.

(10) Gierszal, K. P.; Jaroniec, M. *J. Phys. Chem. C* **2007**, *111*, 9742-9748.

(11) Sathe, T. R.; Agrawal, A.; Nie, S. *Anal. Chem.* **2006**, *78*, 5627-5632.

(12) Fan, R.; Huh, S.; Yan, R.; Arnold, J.; Yang, P. *Nat. Mater.* **2008**, *7*, 303-307.

(13) Vallet-Regı, M. *Chem. Eur. J.* **2006**, *12*, 5634-5643.

(14) Yang, P.; Quan, Z.; Li, C.; Lian, H.; Huang, S.; Lin J. *Microporous Mesoporous Mater.* **2008**, *116*, 524-531.

(15) Mamak, M.; Coombs, N.; Ozin, G. *J. Am. Chem. Soc.* **2000**, *122*, 8932-8939.

(16) Mamak, M.; Coombs, N.; Ozin, G. *Adv Mater* **2000**, *12*, 198-202.

(17) Chen, F.; Liu, M. *J. Mater. Chem.* **2000**, *10*, 2603-2605.

(18) Wang, Y.; Yin, L.; Palchik, Y.; Hacohen, Y.; Kotypin, A.; Gedaken, A. *Langmuir* **2001**, *17*, 4131-4133.

(19) He, H.; Dai, H.; Ng, K.; Wong, W.; Au, T. *J. Catal.* **2002**, *206*, 1-13.

(20) Ho, C.; Yu, Y.; Wang, X.; Lai, S. Y.; Qui, Y. F. *J. Mater. Chem.* **2005**, *15*, 2193-2201.

(21) Chen, L. F.; Gonzalez, J. A.; Wang, L. E.; Norena, A.; Toledo, S.; Castillo, M.; Moran-Pineda, M. *Appl. Surf. Sci* **2005**, *243*, 319-328.

(22) Anyaba, P. N. Novel techniques for the synthesis of three-way catalytic converter support materials, Clemson University, 2009.

(23) Taguchi, A.; Schüth, F. *Microporous and Mesoporous Materials* **2005**, *77*, 1-45.

(24) Hufton, J. R.; Ruthven, D. M. *Ind Eng Chem Res* **1993**, *32*, 2379-2386.

(25) Qiao, S. Z.; Bhatia, S. K. *Microporous and Mesoporous Materials* **2005**, *86*, 112-123.

(26) Gobin, O. SBA 16 Materials: synthesis, diffusion and sorption properties. Laval University, Quebec, Canada, 2006.

(27) Ruthven, D.; Brandani, S. *Recent Advances in Gas Separation by Microporous Ceramic Membranes* **2000**, *6*, 187-212.

(28) Shannon, S. L.; Goodwin, J. G. *Chem. Rev.* **1995**, *95*, 677-695.

(29) Ruthven, D. M.; Stapleton, P. *Chemical Engineering Science* **1993**, *48*, 89-98.

(30) Qiao, S. Z.; Bhatia, S. K. *Ind Eng Chem Res* **2005**, *44*, 6477-6484.

(31) Brandani, S.; Jama, M. A.; Ruthven, D. M. *Chemical Engineering Science* **2000**, *55*, 1205-1212.

(32) Adem, Z.; Guenneau, F.; Springuel-Huet, M.; Gon, A.; Iapichella, J.; Cacciaguerra, T.; Galarneau, A. *J. Phys. Chem. C* **2012**, *116*, 13749-13759.

CHAPTER SEVEN

CONCLUSIONS

The present work succeeded in developing novel mesoporous ceria-zirconia-yttria (CZY) catalyst supports to further enhance the efficiency and longevity of automotive catalytic converters. The created CZY supports will likely maintain the dispersion and enhance the activity of three-way catalysts used in automobile emissions control, minimizing the quantities of noble metals needed to achieve the required level of performance and thereby reducing costs for the automobile industry.

In order to achieve the research objectives, I focused on advanced synthesis strategies that yielded improvements to the morphology and physical properties of CZY mixed oxides as well as the use of advanced characterization techniques that are capable of evaluating the diffusional enhancements gained by the formation of novel mesoporous structures.

The first part of this dissertation discussed the synthesis and characterization of mesoporous CZY oxides that were prepared via classical sol-gel methods using block copolymers (BC) as templates and inorganic nitrate salts as metal oxide precursors. The resulting oxide materials showed high surface area, large pore volume, uniform pore size distribution, and uniform oxide incorporation among other improved characteristics. A range of PEO-PPO-PEO block copolymer templates and sol-gel concentrations were studied.

Studies were undertaken to address the hypothesis that the concentration of block copolymer (Pluronic P123) template species in the CZY sol-gel synthesis media would

significantly impact the morphology of the resulting CZY oxide materials obtained from those syntheses. In agreement with my hypothesis, favorable increases were observed in the surface area and average pore size with increases in sol-gel template concentration. This confirmed it is possible to tune the pore diameter of CZY mesostructures by changing the (template):(precursors) ratio in the initial sol-gel synthesis media. However, despite all of the CZY oxides showing uniform crystalline structures, none of the sol-gel synthesized mesostructures were well ordered, suggesting that template concentration did not impact the periodicity of pores formed in the final oxide structures.

The proportions of CZY oxides for the different materials were remained consistent throughout synthesis and calcination processes, with the exception of materials prepared with extremely high block copolymer concentrations. It was also shown that using a low heating rate and maintaining appropriate template concentrations limits the probability of collapse of the structure due to the formation of hot spots during the calcination process that is used to remove the organic templates from the oxide materials. Specifically, differential scanning calorimetry (DSC) analyses showed that exotherms were observed during template oxidations processes and that these exotherms increased in intensity as the heating rate and block copolymer content increased.

Additional studies examined the effects of block/oligomer chain length on the sol-gel templating ability of select block copolymer templates. Pluronic P65 and Pluronic F127 were chosen as alternatives to P123. The other block copolymers considered had the same poly(ethylene oxide)-poly(propylene oxide)-poly(ethylene oxide) (PEO-PPO-PEO) structure but featured shorter hydrophobic chains and larger hydrophilic chains,

respectively. Significantly different molecular weight is also shown among the three. However, the presence of different Pluronic templates during synthesis did not significantly impact the resulting surface area and average pore size of the calcined oxide samples. Also, all of the tested Pluronic templated samples showed uniform crystalline structures and the oxides were well incorporated into the final structure. Finally, none of the mesostructures were well ordered, suggesting that within the limits of a classical sol-gel synthesis process, the BC template type or length of the hydrophobic or hydrophilic blocks of the polymer template does not influence the formation of periodic oxide structures.

Classical sol-gel syntheses generated materials with catalytically useful properties but the creation of a ordered structures proved elucive. For classical sol-gel methods, the metal precursor hydrolysis rate defined the final product morphology. Because the CZY precursor reaction rates are very rapid, there is insufficient time for the rapidly growing metal oxyhydroxide oligomers to become associated with the micellar block copolymer templates. It is also questionable whether the template molecules have sufficient time to fully organize into micellar secondary structures before the entire oxide forming reaction process has been completed. Thus, the CZY condensation reactions leading to the formation of rigid oxide frameworks are *reaction-limited*, with the formation of polyoxyhydroxides occuring rapidly as a result of the availability of water and hydrolyzing agents in the initial sol-gel solution. All of these phenomena lead to the formation of disordered CZY mesostructures.

Since ordered mesostructures are hypothesized to be advantageous for reducing noble metal sintering and enhancing reactant and product diffusion rates through the material, later efforts focused on the development of reproducible methods for synthesizing ordered CZY mesostructures. The somewhat elusive ordered mesostructures were achieved by the evaporation induced self-assembly (EISA) method using block copolymers as structure directing agents (templates). The ordered mesoporous CZY oxides synthesized by EISA also had all of the advantageous properties previously observed with materials synthesized by classical sol-gel methods.

The evaporation induced self-assembly process for preparing CZY mesostructures was found to be *diffusion-limited*, where the rate of oxide forming reactions is limited by: 1) the slow diffusion of water into the initial ethanolic-metal salt solution and 2) the slow evaporation of ethanol from the alcohol rich solution. These limiting phenomena are heavily dependent on the reaction temperature, the relative humidity of the air above the ethanolic solution, the rate of removal of HCl gas from the vapor phase, as well as other factors. The acidic environment generated by the hydrolysis reaction slows the cross-linking rate of the metal oxide species, and the slow loss of ethanol by evaporation enables the polymer template to self-organize and permits the simultaneous condensation-polymerization of metal oxide/hydroxide species to generate a robust oxide network around the periphery of the ordered polymer templates. Thus, for the templated synthesis of mesoporous CZY materials, it is the rate of metal oxide condensation that determines the nature of the resulting oxide structure.

Although water is directly responsible for hydrolysis reactions, the fast evaporation of ethanol accelerates the aging process by preventing the self-assembly of the SDAs and also might create disordered or non-homogeneous multiphase mesoporous systems. I studied these effects in depth by both experimental and simulation approaches, and both approaches indicated that the diffusion rates of water and ethanol during the EISA aging process were the driving forces that controlled the ordering of mesopores within the oxide products.

A positive impact on morphology was observed by decreasing the surface area for ethanol evaporation during the EISA aging step, since a fast evaporation rate induces a large concentration gradient, whereas a slow one favors a more homogeneous solution. However, these experiments also showed that for deeper solutions (i.e., high height to diameter ratio systems) it was more likely that a multiphase system would emerge from the starting ethanolic solution, with the top layer consisting of a hard oxide layer that was exposed to higher water levels and a lower liquid layer that saw low water levels because it was difficult for the water to diffuse through the upper oxide layer. This layered system consisted of oxide mesopores products that were both ordered and disordered.

It was later shown that it was better to reduce the evaporation rate by keeping the air flow controlled and maintain a large evaporative area so samples were as thin as possible and as a result more uniform. These experiments provided keen insights into the critical parameters that must be controlled if an EISA process is to be able to reproducibly produce ordered mesoporous oxide structures.

It was also shown that a slow *controlled* reaction/assembly process is necessary to create ordered CZY mesostructures. To approach a more controlled process and be able to design and develop new protocols for mesoporous material synthesis, the experimental behavior was modeled using a simplified version of the system treating evaporation as a moving boundary mass transport problem

The transport based EISA models described the effects of water concentration during the process, the evolution of composition, rates of solvent evaporation, hydroxide formation and other parameters in the system that control whether or not ordered structures are formed. Additionally, the model could potentially be used to predict composition, precipitation and temperature profiles under varying aging conditions which are difficult to experimentally determine.

The second part of this work focused on the diffusional properties of CZY materials synthesized by sol-gel and EISA techniques and prepared using either endo-templates (block copolymers, surfactants, and dendrimers) or exo-templates (resins and activated carbon). The diffusion of gases inside the pores of CZY samples having different pore geometries and sizes leads to an understanding of the advantages of some catalyst supports over others. These experiments focused on the measurement of n-hexane diffusion rates through the pores of CZY oxides, with hopes of identifying a specific pore morphology and/or size that was optimal for the conversion of gaseous exhaust pollutants.

The zero-length column (ZLC) method was used to measure the intracrystalline diffusivities of n-hexane at 60 °C in mesoporous CZY materials. This technique was

proven to be very useful for gas diffusion studies in mesoporous materials. The impact of morphology on the diffusion behavior of n-hexane in CZY materials was verified, showing diffusional advantages for ordered mesoporous CZY oxides. It was concluded that the transport properties of these materials are highly dependent of the geometry of the void space and *pore connectivity*. Further, the effects of pore morphology were found to be far more relevant to diffusional properties than other physical characteristics, such as surface area or average pore size.

In summary, I developed novel mesoporous ceria-zirconia-yttria (CZY) catalyst supports with improved characteristics like high surface area, large pore volume, uniform pore size distribution and uniform oxide incorporation by both sol-gel and EISA synthesis approaches. Furthermore, I created CZY supports with and ordered arrangement of mesopores by the EISA method, which were proven to have advantageous diffusional properties as measured by the ZLC method. These catalyst supports, having optimal pore morphologies, further enhance the efficiency and longevity of automotive catalytic converters.

CHAPTER EIGHT

RECOMMENDATIONS

The main objective of this study was to create novel mesoporous ceria-zirconia-yttria (CZY) materials with improved physical and diffusional characteristics that increased their efficiency and enhanced their performance as catalyst supports for three-way catalysts. This has been accomplished by the synthetic control of CZY mesoporous materials morphology and the characterization of their physical and diffusional properties. Thus, further studies aimed simply at new synthesis strategies for CZY materials are probably not required.

There is however considerable scope for further application of the evaporation induced self-assembly (EISA) technique both to explore the structural relationships when varying synthesis parameters and to create more efficient ways to develop these CZY materials for industrial applications. For example, the development of CZY oxides with ordered mesostructures by aerosol-assisted EISA for nanofabrication in series.

One obvious development would be to extend transport simulations of the EISA aging process to include missing parameters not available during the current study (e.g. experimental reaction rates for metal precursor hydrolysis). This effort could also include experimental studies examining the rates of hydrolysis of metal oxide precursors in alcohol and mixed alcohol-water solutions. In principle, the models developed during this study could be used and any new kinetic information substituted for the estimates currently used in the model.

With respect to diffusional studies, the ZLC experimental system was built and modified as experience was gained. If further work is to be continued it would be desirable do some upgrades. For example, to run most of the lines and the ZLC cell for the system inside a gas chromatography oven to improve temperature accuracy. Also some volumetric flow controllers could be traded for higher flow rate rated controllers and smaller pore diameter sintered disks could be used for the zero-length column cell to avoid problems with very fine powders clogging the lines during measurements.

In order to shed more light on the effects of pore geometry on the diffusional properties of CZY materials, new ZLC studies could be planned using other gases closer to the ones this support material encounters in operating conditions and at working temperatures.

Evaluation of the catalytic performance for reactions used in emission abatement control as applied to three–way catalytic converters of the different mesoporous CZY materials that have been synthesized would be interesting as well, specifically, catalytic activity or light-off temperature of all the reactant species (CO, C_xH_y, and NO_x) that participate in the redox reactions and loss of surface area during thermal aging for each CZY sample. These two tests address the critical aspects of ongoing efforts focused on reducing noble metal loadings on three way catalysts and extending their active life.

Additionally, experimental or/and simulation work for simultaneous diffusion and reaction inside CZY pores with or without the actual catalyst could be carried out. The diffusion studies developed so far did not include any reaction behavior. This could be extremely beneficial in order to better assess the advantages of CZY catalyst supports

with different morphologies. Simulations can be used to predict optimized pore structure and size, accounting for both diffusion and reaction phenomena.

Finally, a large portion of work that I consider very important but did not have the opportunity to undertake is the use of isotope labeling to measure diffusion rates. Steady-state isotopic-transient kinetic analysis (SSITKA) is a very useful technique for the kinetic study of heterogeneous catalytic reactions. A variant of this technique can also be used to obtain diffusion rates inside CZY oxide mesopores. Actual SSITKA experiments could also be used to study precious metal loaded CZY catalysts – obtaining detailed reaction rate information for the complete reaction mechanism. These results could reveal new characteristics and details of the process, enabling the further improvement of catalytic converter catalysts.

APPENDICES

Appendix A

Synthesis Conditions- Literature Review

Table A-1: Detailed conditions literature review of mesoporous materials. All temperatures (T) given in °C & time (t) in hours.

Type of material	Precursors	Template	Other agents	Solvent	Hlz. agent	Method	ag. T	ag. t	RH%	dry T	dry t	calc. T	calc. t	Low angle peak	Ordered TEM	Ref
TiO_2	Ti isopropoxide	Akylphosphate Surf.	ACAC													[1]
Mes. YZ	Zr ethoxide; Y acetate	CTAB	N_2 atm	$C_2H_6O_2$; alcohol	Sodium hydroxide	Precipitation	80	24 to 120	N.A	N.A		600	4	Yes	YN	[2, 3]
Mes. CZ	Zr propoxide; $(NH_4)_2Ce)NO_3)_6$	P123 or CTAB	N.A	Propanol	Ammonia	EISA	40	12	NM	100		500	4	Yes	No	[4]
Mes. Zr	Zr propoxide	P123; Brij56	N.A	Water	N.A	Precipitation	130	12	N.A	Extraction		500	6	Yes	YN	[5]
Mes. Zr	Zr propoxide	CTAB	$(NH4)_2SO_4$	Water	Retarding (HCl)	Precipitation	100	48	N.A	NM		500	5	Yes	Yes	[6]
Mes. Zr	Zr propoxide	CTAB	N.A	Water	N.A	Precipitation	60	48	N.A	60		Soxhlet extraction		Yes	No	[7]
Mes. Zr	Zr propoxide	F127 or P123	N.A	Water	N.A	Precipitation	120	24	N.A	NM		500	4	Not shown	No	[8]
Mes. Zr	Zr propoxide	Amphiphilic compounds	N_2 atm	Propanol	Water	Precipitation	80	96	N.A	RT		400	6	Yes	YN	[9]
Mes. Zr	Zr propoxide	P_{12} and S_{12} surf.	N_2 atm	Not specified	Retarding (HCl)	Precipitation	40	12	N.A	140		500	12	Yes	No	[10]
Mes. Zr	Zr propoxide	P_{12} and S_{12} surf.	Not used	Not specified	N.A	Precipitation	90-120	12	N.A	140		500	12	Yes	No	[11].

Table A-1 cont.

Type of material	Precursors	Template	Other agents	Solvent	Hlz. agent	Method	ag. T	ag. t	RH%	dry T	dry t	calc. T	calc. t	Low angle peak	Ordered TEM	Ref
Mes. Zr	Zr propoxide	P_{12} and S_{12} surf.	N.A	Not specified	N.A	Precipitation	90-120	12	N.A	140		500	12	Yes	No	12
Zr Particles	Zr propoxide, ethoxide and butoxide	Not used	N_2 atm	Alcohol	Water	Precipitation	60	4	N.A	N.A		N.A		Not shown	No	13
YSZ	Zr and Y isopropoxides	Not used	N_2 atm	Benzene	Water	Precipitation	80	0.5	N.A	100		500	1	No	No	14
Nanosized metal oxides	Metal alkoxide (Ti methoxide or propoxide)	OMC	Special reactor	Not specified	Water vapor	Gas phase hydrolysis	70	Not specified	N.A	110	48	800	2	Not shown	No	15
Mes. YSZ membranes	Zr propoxide; Y nitrate	Porous a-alumina disks	ACAC; N_2 atm	Propanol	Water	EISA (dip coating)	RT	48	70	RT	48	300; 650	2;3	Not shown	Not shown	16
YSZ fibers	Zr propoxide sln; Y acetate	Not used	N.A	Propanol	Water	Fiber drawing/ Dry spinning	Not used		N.A	NM		Not mentioned		No	No	17
Mes. Zr, CZ and YSZ	Zirconyl chloride; Ce nitrate; Y nitrate	F127	N.A	Ethanol	N.A	EISA	40	48	50	100	24	400	4	Yes	Yes	18
Mes. Ceria	Ce acetate	Hexadecyl amine	N.A	Ethanol	N.A	Precipitation	60	48	Atm cond.	150	6	300	4	Yes	Yes	19
YSZ	Zirconyl and Y chlorides	P103	N.A	Ethanol	N.A	EISA	40	72	100	100		500 to 800	2	Yes	No	20
Mes. Ce, Zr and CZ	Ce and Zr chlorides	KLE	N.A	Ethanol; THF	N.A	EISA (dip coating)			10 to 20	300	1	600	1	Yes	Yes	21, 22

Table A-1 cont.

Type of material	Precursors	Template	Other agents	Solvent	Hlz. agent	Method	ag. T	ag. t	RH%	dry T	dry t	calc. T	calc. t	Low angle peak	Ordered TEM	Ref
Ce-Sn mixed oxides (macromol. Mes. foam)	Ce nitrate; Sn chloride	F127	N.A	Ethanol	N.A	EISA	40	48	50	60;100	48; 24	400	3	Not shown	Yes	23
Mes. Ce	Ce nitrate	CTAB	N.A	Ethanol; Water	Retarding (Citric acid)	EISA	40	120	NM	NM		300 to 600	5	Not shown	No	24
Mes. CZ beads	Zirconyl chloride; $NH_4)_2Ce)NO_3)_6$	Amberlite polystyrene beads	N.A	Water	Ammonia	EISA	60	48	NM	90 to 100	24	500	8	Not shown	No	25
Mes. Zr-based materials	Zirconyl chloride; Ce and Y nitrates	F127	N.A	Ethanol	N.A	EISA	40	48	50	100	24	400	4	Yes	Yes	26
CZ Solid sln.	Ce and Zr nitrates	F127 and PMMA spheres	N.A	Ethanol	N.A	Precipitation/ EISA	RT	48	< 40			300; 550	3;6	Yes	YN	4, 27
Mes. $Ce_{1-x}Zr_xO_2$	Zirconyl chloride; ammonium cerium nitrates	Not used	Poly(vinylpyrrolidone)	Ethylene glycol	N.A	Precipitation (Polyol)	190	7	N.A	NM		400	4	Yes	No	28
Mes. metal oxides (Zr)	Inorganic chloride	Block copolymers	N.A	Ethanol	N.A	EISA	40	24	Atm cond.	NM		300 to 600	4	Not shown	Yes	29
Mes. Zr	Zirconyl chloride	Sodium lauryl sulfate	ACAC	Water; Ethanol	Ammonia	Precipitation	110	6	N.A	130	0.5	575		No	No	30
Mes.YSZ	Zr and Y chlorides	F127	N.A	Water; Ethanol	N.A	EISA	40	72	40	NM		500 to 600	4	Yes	Yes	31

Table A-1 cont.

Type of material	Precursors	Template	Other agents	Solvent	Hlz. agent	Method	ag. T	ag. t	RH%	dry T	dry t	calc. T	calc. t	Low angle peak	Ordered TEM	Ref
Mes.YSZ	Zr and Y chlorides	F127	N.A	Ethanol; Water	N.A	EISA	40	72	NM	NM		500	2	Yes	Yes	[32]
Mes. CZY	Zirconyl, Ce and Y nitrates	CTAB	N.A	Water	Sodium hydroxide	Precipitation	100	48	N.A	80	12	550	8	Yes	No	[33]
Mes. Zr	Zirconyl nitrate	P123	N.A	Water	Ethylene diamine	Precipitation	20-80	6 to 24	N.A	110	24	600	4	Not shown	No	[34]
Mes. $Ce_{1-x}Zr_xO_2$	Zirconyl chloride; Ce nitrate	P123	N.A	Ethanol	N.A	EISA	40	48	50	100	24	400	4	Yes	Yes	[35]
Mes. Zr	Zirconyl chloride	CTAB	N.A	Water	Sodium hydroxide	Precipitation	100	24	N.A	NM		Extraction	30	Not shown	No	[36]
CZ	Zirconyl and Ce chlorides	CTAB	N.A	Water	Ammonia	Precipitation	90	120	N.A	60	24	450 to 900	2	No	No	[37]
Mes. Zr	Zirconyl chloride	Cocamido propylbetaine	N.A	Water	N.A	Precipitation	70	96	N.A	NM		350		No	No	[38]
Mes. Ce	Ce acetate	P123 or F127	N.A	Ethanol	N.A	EISA	60	72	NM	NM		400	5	Not shown	Yes	[39]
Mes.YSZ	Zirconyl and Y nitrates	CTAB	N.A	Water	Urea	Precipitation	80	6	N.A	60	12	600	4	Not shown	No	[40]
Mes. Zr	Zirconyl chloride	Brij-58	N.A	Ethanol	N.A	EISA (dip coating)	RT	0.08-0.4 cm/s	10-80%	60	12	150-500	2	Not shown	Y	[41]

ABBREVIATIONS USED	
Hlz	Hydrolizing
ag.	Aging
RH	Relative humidity
calc.	calcination
YSZ	Yttria Stabilized Zirconia
Mes.	Mesoporous
Zr	Zirconium/Zirconia
Y	Yttrium
Ti	Titanium
sln	Solution
Ce	Cerium
CTAB	Cetyl trimethylammonium bromide
Surf.	Surfactants
P123	Block copolymer Pluronic P123
F127	Block copolymer Pluronic F127
OMC	Ordered Mesoporous Carbon
P103	Block copolymer Pluronic P103
KLE	Novel block copolymer
THF	Tetrahydrofuran
Atm. Cond.	Atmospheric conditions
Sat.	Saturated
RT	Room temperature
YN	Yes but minimal
CZ	Ceria-zirconia
NM	Not mentioned
N.A	Not applicable or not used

References

(1) Antonelli, D. M.; Ying, J. Y. *Angewandte Chemie International Edition in English* **1995**, *34*, 2014-2017.

(2) Mamak, M.; Coombs, N.; Ozin, G. *J. Am. Chem. Soc.* **2000**, *122*, 8932-8939.

(3) Mamak, M.; Coombs, N.; Ozin, G. *Adv Mater* **2000**, *12*, 198-202.

(4) Li, C.; Gu, X.; Wang, Y.; Wang, Y.; Wang, Y.; Liu, X.; Lu, G. *Journal of rare earths* **2009**, *27*, 211-215.

(5) Chen, L. F.; Gonzalez, J. A.; Wang, L. E.; Norena, A.; Toledo, S.; Castillo, M.; Moran-Pineda, M. *Appl. Surf. Sci* **2005**, *243*, 319-328.

(6) Ciesla, U.; Froba, M.; Stucky, G.; Schuth, F. *Chemistry of Materials* **1999**, *11*, 227-234.

(7) Yuan, Z.; Vantomme, A.; Léonard, A.; Su, B. *Chem. Commun.* **2003**, , 1558-1559.

(8) Chen, H.; Yan, J.; Ye, Z.; Zhang, L.; Gao, J.; Shi, J.; Yan, D. *J Mater Sci* **2009**, *44*, 6531-6531-6537.

(9) Wong, M.; Ying, J. *Chem. Mater.* **1998**, *10*, 2067-2077.

(10) Pacheco, G.; Zhao, E.; Garcia, A.; Sklyarovb, A.; Fripiat, J. J. *Chem. Commun.* **1998**, *8*, 219-226.

(11) Pacheco, G.; Zhao, E.; Garcia, A.; Sklyarovb, A.; Fripiat, J. J. *Chem. Commun.* **1997**, , 491-492.

(12) Pacheco, G.; Fripiat, J. J. *J. Phys. Chem. B* **2000**, *104*, 11906-11911.

(13) Widoniak, J.; Eiden-Assmann, S.; Maret, G. *European Journal of Inorganic Chemistry* **2005**, *2005*, 3149-3155.

(14) Igarashi, A.; Yamazaki, H. *J. Sol Gel Sci. Technol.* **1994**, *2*, 413-415.

(15) Gerlach, I.; Kawase, M.; Miura, K. *J Nanopart Res* **2009**, *11*, 2049-2059.

(16) Changrong, X.; Huaqiang, C.; Hong, W.; Pinghua, Y.; Meng, G.; Peng, D. *Journal of Membrane Science* **1999**, *162*, 181-188.

(17) Clauss, B.; Grüb, A.; Oppermann, W. *Adv Mater* **1996**, *8*, 142-146.

(18) Yuan, Q.; Li, L.; Lu, S.; Duan, H.; Li, Z.; Zhu, Y.; Yan, C. *The Journal of Physical Chemistry C* **2009**, *113*, 4117-4124.

(19) Lyons, D. M.; Ryan, K. M.; Morris, M. A. *J. Mater. Chem.* **2002**, *12*, 1207-1212.

(20) Chen, F.; Liu, M. *J. Mater. Chem.* **2000**, *10*, 2603-2605.

(21) Brezesinski, T.; Smarsly, B.; Groenewolt, M.; Antonietti, M.; Grosso, D.; Boissière, C.; Sanchez, C. *N e w J . C h e m* . **2005**, *Volume 156*, 243-248.

(22) Brezesinski, T.; Antonietti, M.; Groenewolt, M.; Pinna, N.; Smarsly, B. *New J. Chem.* **2005**, *29*, 237-242.

(23) Li, L.; Xu, J.; Yuan, Q.; Li, Z.; Song, W.; Yan, C. *Small* **2009**, *5*, 2730-2737.

(24) Li, X.; Chen, F.; Lu, X.; Ni, C.; Chen, Z. *Journal of rare earths* **2009**, *27*, 943-947.

(25) Deshpande, A.; Niederberger, M. *Microporous and Mesoporous Materials* **2007**, *101*, 413-418.

(26) Yuan, Q.; Li, L.; Lu, S.; Duan, H.; Li, Z.; Zhu, Y.; Yan, C. *J Phys. Chem. C* **2009**, *113*, 4117-4124.

(27) Li, H.; Zhang, L.; Dai, H.; He, H. *Inorg. Chem.* **2009**, *48*, 4421-4434.

(28) Teng, M.; Luo, L.; Yang, X. *Microporous and Mesoporous Materials* **2009**, *119*, 158-164.

(29) Yang, P.; Zhao, D.; Margolese, D. I.; Chmelka, B. F.; Stucky, G. *Chem. Mater.* **1999**, *11*, 2813-2826.

(30) Larsen, G.; Lotero, E.; Nabity, M.; Petkovic, L.; Shobe, D. *Journal of Catalysis* **1996**, *164*, 246-248.

(31) Hung, M.; Fung, K.; Hung, D.; Hon, M. *Journal of the European Ceramic Society* **2008**, *28*, 1161-1161-1167.

(32) Hung, M.; Hung, D.; Fung, K.; Hon, M. *Materials Letters* **2008**, *62*, 1147-1147-1150.

(33) Feng, R.; Yang, X.; Ji, W.; Aua, C. *Materials Chemistry and Physics* **2008**, *107*, 132-132-136.

(34) Rezaei, M.; Alavi, S.; Sahebdelfar, S.; Xinmei, L.; Yan, Z. *J Mater Sci* **2007**, *42*, 7086-7092.

(35) Yuan, Q.; Liu, Q.; Song, W.; Feng, W.; Pu, W.; Sun, L.; Zhang, W.; Yan, C. *J. Am. Chem. Soc.* **2007**, *129*, 6698-6699.

(36) Blin, J. L.; Flamant, R.; Su, B. L. *International Journal of Inorganic Materials* **2001**, *3*, 959-959-972.

(37) Terribile, D.; Trovarellia, A.; Llorcab, J.; Leitenburga, C.; Dolcetti, G. *Catalysis Today* **1998**, *43*, 79-88.

(38) Kim, A.; Bruinsma, P.; Chen, Y.; Wang, L.; Liu, J. *Chem. Commun.* **1997**, , 161-161-162.

(39) Ni, C.; Li, X.; Chen, Z.; Li, H. H.; Jia, X.; Shah, I.; Xiao, J. Q. *Microporous and Mesoporous Materials* **2008**, *115*, 247-252.

(40) Hung, M.; Hung, D.; Fung, K.; Hon, M. *Journal of the European Ceramic Society* **2006**, *26*, 2627-2632.

(41) Crepaldi, E.; Soller-Illia, G.; Grosso, D.; Abouey, P.; Sanchez, C. *Chem. Commun.* **2001**, , 1582-1583.

Appendix B

Literature Review for ZLC Technique

Table B-1: Detailed conditions literature review of the ZLC technique

Paper	System	Flow rates (ml/min)	Slope (s^{-1})	Intercept	D/R^2 (s^{-1})	L	D (cm^2/s)
Eic & Ruthven 1988	o-xylene &NaX zeolite crystals (50 microns)	30;100;140	4.4;8.9;10.4E-3	0.75;0.35;0.27	1.39E-03	1.5; 5.6; 7.5	
	o-xylene &NaX zeolite crystals (100 microns)	100;160	0.00175; 0.00236	0.92; 0.54; 0.37	3.30E-04	3.17; 5.16	
Eic & Ruthven 1988 (zeolites 1988)	n-butane in 13X zeolite	30;100;140	4.4;8.9;10.4E-3	0.75;0.35;0.27	1.39E-03	1.5; 5.6; 7.5	4E-7
	butane in NaX @ 80 °C (50 microns)					1 to 25	3.5E-7
	pentane in NaX @ 80 °C (50 microns)					6 to 10	2.35E-7
	heptane in NaX @115 °C (50 microns)					1.46	1.68E-7
Brandani & Ruthven 1996	Propane/NaX at 85 C-100µm-Tracer ZLC	11.8			8.40E-03	158	
	Propane/NaX at 85 C-100µm-Normal ZLC	14.2			4.80E-03	63	
Hufton& Ruthven 1993	n-butane/silicate27micron @ 75° C –ST	34			6.01E-03		2.22E-8
	n-butane/sil.43micron @ 75 °C	34			2.92E-02		3.41E-8
	n-butane/s.69micron @ 75 °C	34			6.67E-02		11.8E-8

Table B-1 cont.

Paper	System	Flow rates (ml/min)	Slope (s^{-1})	Intercept	D/R^2 (s^{-1})	L	D (cm^2/s)
Ruthven & Vidoni, 2012	Ethane in DDR	5.82			1.50E-03	15	
		17.52			1.50E-03	49	
		58.38			1.50E-03	150	
Micke et al 1994, 1995	Benzene on H-ZSM-5 crystals	141			1.95E-03	22.9	
		256			9.96E-04	58.3	
Qiao &Bathia 2005	n-decane in mesoporous MCM-41-(2R=20.86microns) @50 °C	60			9.54E-03	0.74	1.04E-08
		80			1.02E-02	0.98	1.11E-08
		100			1.03E-02	1.22	1.12E-08
		120			1.06E-02	1.46	1.15E-08
		140			1.11E-02	1.7	1.20E-08
Bradani 2000	Benzene and p-xylenein zeolite-25 Å	p-xylene -30	0.007	0.07	9.00E-04	8.42	
		50.5	0.0077	0.042		14.2	
		benzene-19	0.0089	0.0058	1.00E-03	21	
Zhu et al 2004	isobutane in silicate	273 °C			2.70E-04		
		303 °C			1.30E-03		
		338 °C			4.50E-03		

Table B-1 cont.

Paper	System	Flow rates (ml/min)	Slope (s^{-1})	Intercept	D/R^2 (s^{-1})	L	D (cm^2/s)
Brandani	Linear paraffins (hexane to tetradecane) in NaCaA zeolite	150 C (hexane)					1.64 E -9
Jiang and Eic	Ethane & Buthane in ZSM-5						
Hufton & Ruthven	Ethane & Buthane in ZSM-5						
Brandani	Propane-13X zeolite-						
Brandani	Propane and propylene in 5A and 13X						
Brandani & Ruthven	Benzene in NaX and CaX						
Ruthven	Benzene and the xylene isomers in silicalite/HZSM-5						
Eic	MCM-48 and H-USY samples						
	n-heptane in SBA-15						
	Toluene in SBA-15						
Brandani & Ruthven 2003	CO_2-C_2H_4 and CO_2-C_3H_8 on several cationic adsorbents				Separation factor		
	(NaLSX, NaX, CaX, and CaA)--Equilibrium						
Brandani & Ruthven 2003	CO_2-CaA, CO_2-NaLSX						
	Equilibrium						

Table B-1 cont.

Paper	System	Flow rates (ml/min)	Slope (s^{-1})	Intercept	D/R^2 (s^{-1})	L	D (cm^2/s)
Brandani 2002-thesis	CO_2-C_2H_4;C_3H_8;CH_4 in zeolite A-X&Silicate- Equilibrium						
Zaman et al 2005	1,3-diisopropylbenzene and 1,3,5-triisopropylbenzene				4E-4 to 8E-5	3 to 14	
	from 0.9-μm NaY-zeolite						
Ruthven 1988	C_4H_{10};C_5H_{12};C_7H_{16};$C_{10}H_{22}$;cyclo hexane in 5A zeolite				1to4 E-7 cm2/s	1 to 45	
	C_4H_{10};C_5H_{12};C_7H_{16};$C_{10}H_{22}$;cyclo hexane in NaX zeolite				0.0026to10 E-9cm2/s	9 to 606	
Gobin-Thesis 2006	n-heptane, cumene or mesitylene in SBA-16						
	n-heptane in SBA-16 (S-45-1)	100 at 50 °C			2.67E-04	50	1.07E-9
	n-heptane in SBA-16 (S-60-1 15μm)	100 at 50 °C			5.62E-04	87	1.27E-9
	n-heptane in SBA-16 (S-100-1 23μm)	100 at 50 °C			7.74E-04	96	4.1E-9
Wu 1982	hexane in silicate at 20° C						0.75E-11
	hexane in silicate at 100° C						4.2E-11
	hexane in silicate at 200° C						13.3E-11

Table B-1 cont.

Paper	System	Flow rates (ml/min)	Slope (s^{-1})	Intercept	D/R^2 (s^{-1})	L	D (cm^2/s)
Quiao & Bathia 2005	hexane, heptane, octane and decane in MCM-41 (2R=23.6microns; 3.79nm pore D)						
	hexane @50 °C (23.6 micron)	100			0.2108	1.06	2.93E-07
	heptane @50 °C	100			8.05E-02	1.12	1.12E-07
	octane @50 °C	100			2.50E-03	1.22	1.37E-08
	decane @50 °C	100			7.10E-03	1.24	3.00E-09
Menjoge 2010	Toluene in SBA-15 (45 microns)-TZLC	25 °C			9.40E-04		
	Toluene in SBA-15 (45 microns)-NMR	26 °C					6.50E-04
Huang et al. 2010	Heptane in SBA15 @30 °C				1.6 E -3	20	
Malekian 2007	n-heptane in ZMS-5	100 °C	2.01		1.61E-04		
	o-xylene in UL-ZSM5-100-6	50 °C	4.25		1.32E-04	12	
	o-xylene in Al-Meso-100	60 °C	4.99		1.09E-04	14	
Olson & co workers	Hexane in ZSM-5	313 K					4.00E-09
Nowak 2005	hexane in MCM-41 (R=1-2 micron)				1.48E-02		
Santhong 2008	hexane in MCM-41						5E-4 to 4.3E-6
Courivaud 2000	hexane in MCM-41 (6-7micron)						(1.61 to 5.81) E-5
Adem et al 2012	hexane in MCM-41 (50 micron)						4.10E-06

Appendix C

ZLC Experimental System

Figure C.1. ZLC process equipment.

Figure C.2. Flow rate, temperature and pressure controllers for the ZLC system.

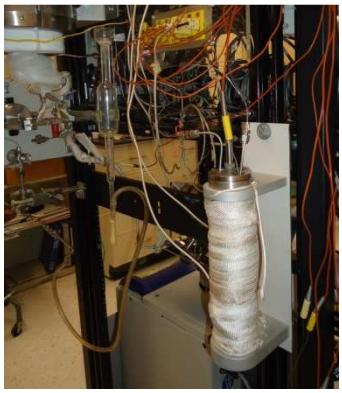

Figure C.3. Permeation cell connected to mass flow controllers and the ZLC system.

Figure C.4. ZLC cell inside the temperature controlled oven and connected to gas lines.

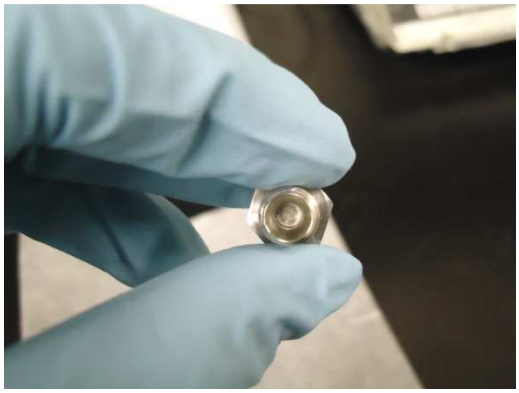

Figure C.5. ZLC cell with sintered metal discs inside

Appendix D

Derivation of ZLC model

The derivation of the mathematical ZLC model is shown as derived by Brandani and Ruthven[1] and as presented by Goblin[2].

The governing equations for the experimental section presented in chapter 5 are two: the fluid-phase and the solid-phase mass balance in radial coordinates, without negligence of the fluid-phase hold-up:

$$V_S \cdot \frac{d\bar{q}}{dt} + V_f \cdot \frac{dc}{dt} + F \cdot c(t) = 0 \tag{D.1}$$

$$\frac{\partial q}{\partial t} = D \cdot \left(\frac{\partial^2}{\partial r^2} + \frac{2}{r}\frac{\partial q}{\partial r}\right) \tag{D.2}$$

where $\bar{q}$ is the value of q averaged over the particle.

The initial conditions of the system are:

$$q(r,0) = q_0 = K_H c_0; \qquad c(0) = c_0 \tag{D.3}$$

and the boundary condition:

$$\left(\frac{\partial q}{\partial r}\right)_{r=0} = 0 \tag{D.4}$$

Equation D.1 can be considered as a boundary condition on the solid-phase mass balance:

$$\frac{4}{3}\pi R^3 \frac{d\bar{q}}{dt} = 4\pi R^2 D \left(\frac{\partial q}{\partial r}\right)_{r=R} \tag{D.5}$$

with equilibrium at the surface:

$$q(R,t) = K_H c(t) \tag{D.6}$$

The fluid-phase mass balance D.1 can be written as:

$$\frac{3}{R}DV_s\left(\frac{\partial q}{\partial r}\right)+\frac{V_f}{K_H}\frac{\partial q}{\partial t}+\frac{F}{K_H}\ q|_{r=R}=0 \tag{D.7}$$

Introducing the change of variable ($\zeta = rq$), equation D.2 reduces to:

$$\frac{\partial \zeta}{\partial t}=D\frac{\partial^2 \zeta}{\partial r^2} \tag{D.8}$$

Since $q(r,t)$ is always finite the boundary condition in equation D.4, can be rewritten as:

$$\zeta(0,\mathrm{t})=0 \tag{D.9}$$

Equation D.8 can be solved through separation of variables:

$$\zeta(\mathrm{r},\mathrm{t})=\mathrm{Q}(\mathrm{t})\cdot\mathrm{T}(\mathrm{t}) \tag{D.10}$$

$$Q\frac{dT}{dt}=DT\frac{d^2Q}{dr^2} \tag{D.11}$$

$$\frac{1}{DT}\frac{dT}{dt}=\frac{1}{Q}\frac{d^2Q}{dr^2}=-\lambda^2 \tag{D.12}$$

where λ is a constant, These differential equations are separable and give the following solution:

$$T=Cexp(-\lambda^2Dt);\quad Q=A\cdot sin(\lambda r)+B\cdot cos(\lambda r) \tag{D.13}$$

where λ must be real (ζ is always finite). Furthermore, from equation D.9 it is concluded that B must be zero. The general solution is given by:

$$q=\frac{a}{r}\sin(\lambda r)\cdot\exp(-D\lambda^2 t) \tag{D.14}$$

where a=AC

Substituting in the fluid-phase mass balance (D.7):

$$\frac{3}{R}DV_s\left(\frac{\lambda}{R}\cdot cos(\lambda R)-\frac{1}{R^2}\cdot sin(\lambda R)\right)-\frac{D\lambda^2V_f}{K_HR}sin(\lambda R)+\frac{F}{K_HR}\ sin(\lambda R)=0 \tag{D.15}$$

which give as the characteristic equation:

$$\beta_n cot\beta_n + L - 1 - \gamma\beta_n^2 = 0 \tag{D.16}$$

with

$$L = \frac{1}{3}\frac{F}{KV_s}\frac{R^2}{D}; \quad \gamma = \frac{V_f}{3K_H V_s} \quad \beta = \lambda R \tag{D.17}$$

The general solution is therefore given by:

$$q(r,t) = \sum \frac{a_n}{r} \sin\left(\beta_n \frac{r}{R}\right) \cdot \exp\left(-\beta_n^2 \frac{D}{R^2} t\right) \tag{D.18}$$

and for the initial solution:

$$q(r,0) = q_0 = \sum \frac{a_n}{r} \sin\left(\beta_n \frac{r}{R}\right) \tag{D.19}$$

To evaluate a_n, I have to consider the following integral:

$$\int_0^R \sin\left(\beta_n \frac{r}{R}\right) \sin\left(\beta_m \frac{r}{R}\right) dr \tag{D.20}$$

After integrating twice by parts and taking into account equation D.16 and D.19 I get for a_n (see Brandani & Ruthven[1]):

$$a_n = \frac{\int_0^R r q_0 \sin\left(\beta_n \frac{r}{R}\right) dr + \gamma R^2 q_0 \sin(\beta_n)}{\int_0^R \sin^2\left(\beta_n \frac{r}{R}\right) dr + \gamma R \sin^2(\beta_n)} \tag{D.21}$$

taking into account D.16:

$$\frac{a_n}{q_0} = \frac{2R}{\sin(\beta_n)} \cdot \frac{L}{\beta_n^2 + (1 - L + \gamma\beta_n^2)^2 + L - 1 + \gamma\beta_n^2} \tag{D.22}$$

The solution of the problem is therefore given by:

$$\frac{q(r,t)}{q_o} = \frac{R}{r} \sum \frac{2\mathrm{L}}{\beta_n^2 + (1 - L + \gamma\beta_n^2)^2 + L - 1 + \gamma\beta_n^2} \cdot \frac{\sin\left(\beta_n \frac{r}{R}\right)}{\sin(\beta_n)} \cdot \exp\left(-\beta_n^2 \frac{D}{R^2} t\right) \tag{D.23}$$

for r = R and under assumption of linearity of the system, I get the desorption curve:

$$\frac{c(t)}{c_o} = 2L \sum \frac{2\mathrm{L}}{\beta_n^2 + (1 - L + \gamma\beta_n^2)^2 + L - 1 + \gamma\beta_n^2} \cdot \exp\left(-\frac{{\beta_n}^2 Dt}{R^2}\right) \tag{D.24}$$

Under negligence of the fluid-phase hold-up ($\gamma = 0$), the solution reduces to:

$$\frac{c(t)}{c_o} = \sum \frac{2L}{\beta_n^2 + L(L-1)} \cdot \exp\left(-\frac{{\beta_n}^2 Dt}{R^2}\right) \tag{D.25}$$

which is the final form of the ZLC model as used in Chapter 5 of this thesis.s.

Appendix E

EDX Results for some of the CZY samples shown in Chapter 3 Section 1

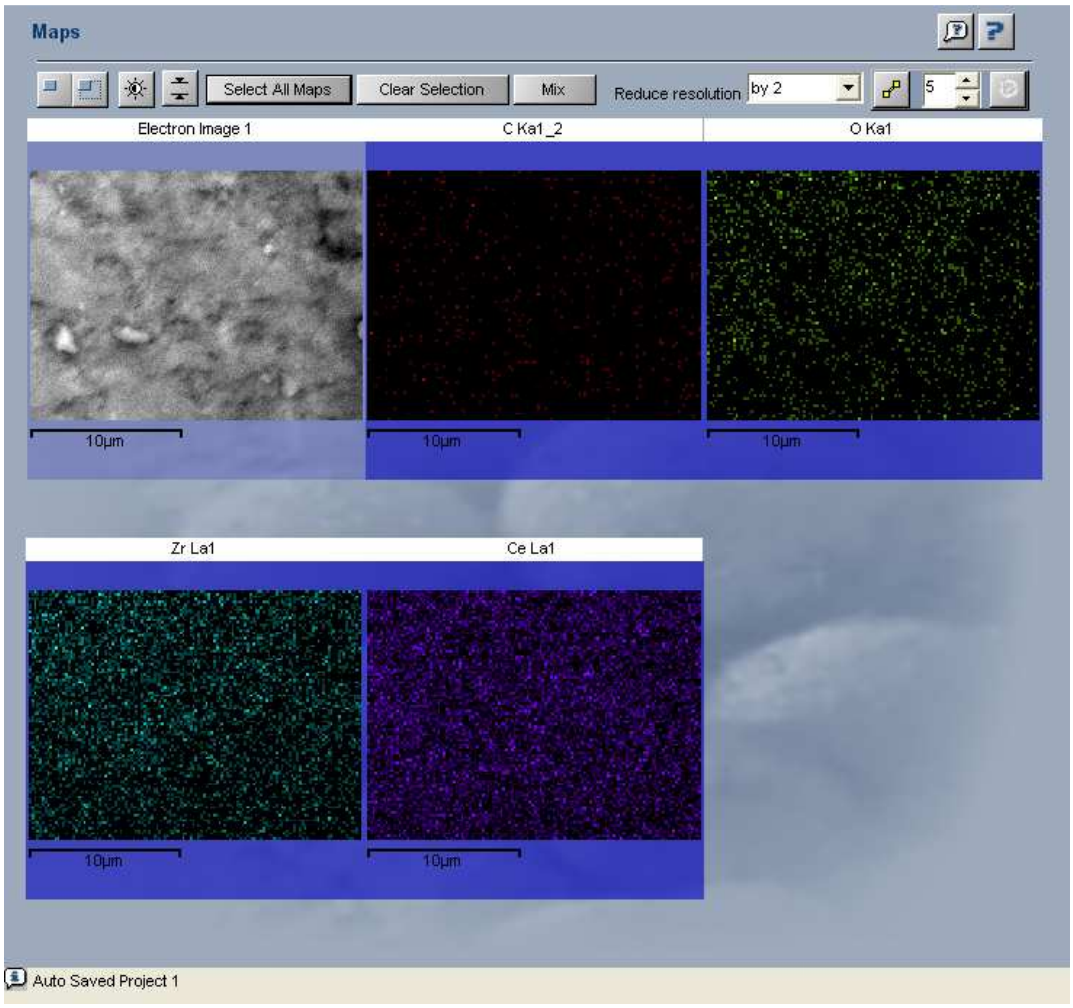

Figure E.1. EDX mapping for a sol-gel synthesized CZY sample with a ratio of 0.5 P123: 10 CeO_2: 9 ZrO_2: 1 $YO_{1.5}$

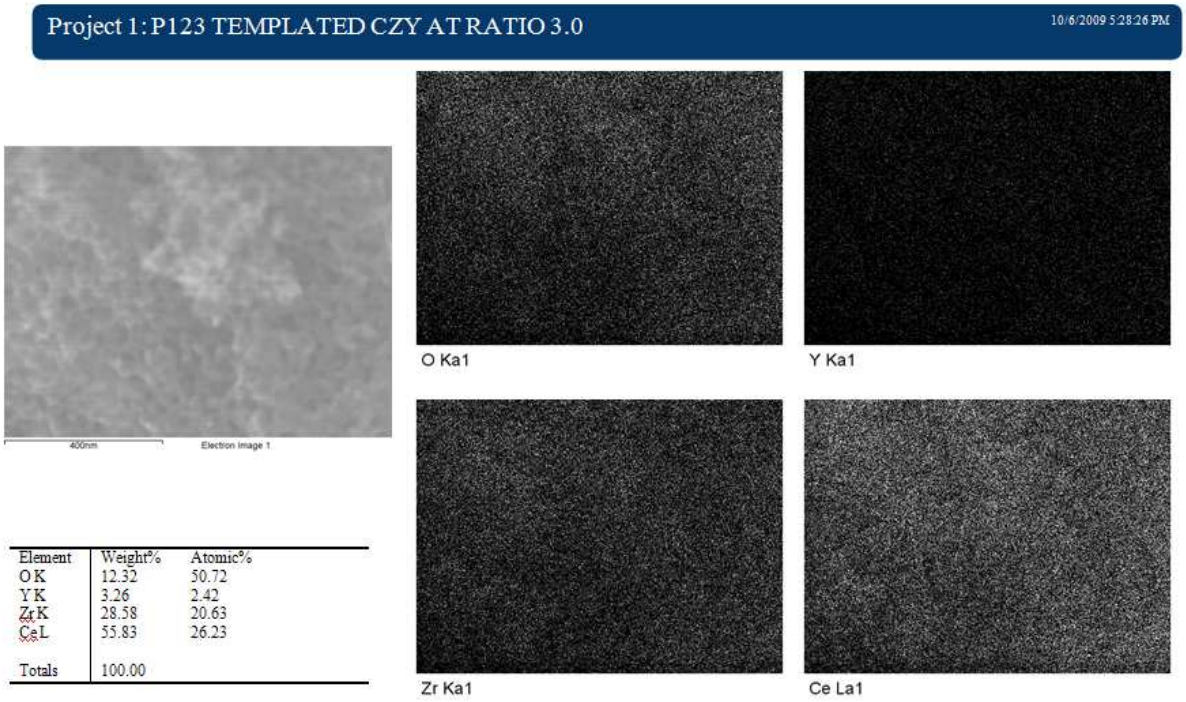

Element	Weight%	Atomic%
O K	12.32	50.72
Y K	3.26	2.42
Zr K	28.58	20.63
Ce L	55.83	26.23
Totals	100.00	

Figure E.2. EDX mapping for a sol-gel synthesized CZY sample with a ratio of 3 P123: 10 CeO_2: 9 ZrO_2: 1 $YO_{1.5}$

Appendix F

EISA Process Images

Figure F.1. Humidity and Temperature Controlled Oven.

Figure F.2. Settings used for CZY support synthesis.


Figure F.3. Sample by the end of the aging process. A gel is obtained.

Figure F.4. Regular oven used for drying samples.

Figure F.5. Settings used during drying step.

Figure F.6. Sample reaching the end of drying step.

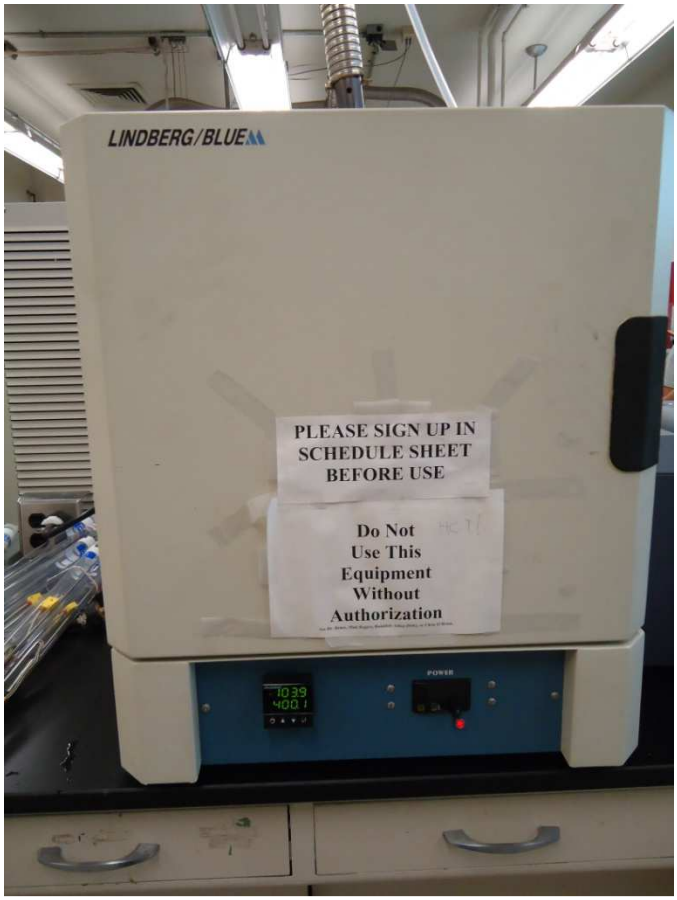

Figure F.7. Oven used during calcination of samples set to reach 400 °C.


Figure F.8. Box especially designed for EISA aging process (front view).

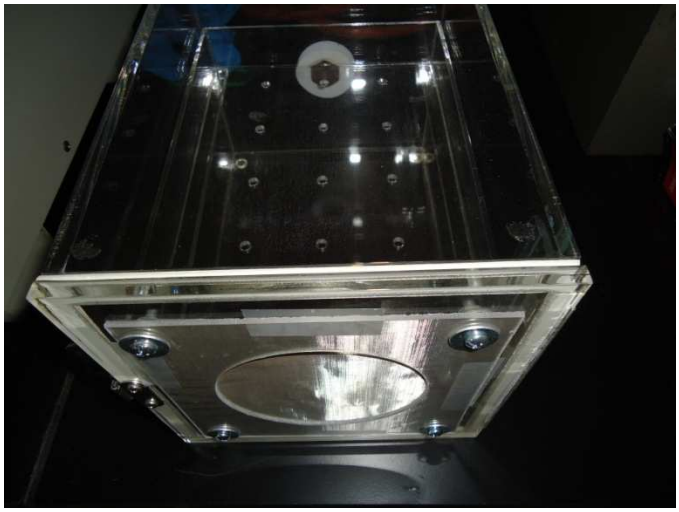

Figure F.9. Box especially designed for EISA aging process (upper view).

Figure F.10. Box especially designed for EISA aging process (side view). All samples were placed in the bottom part of the box and the hole in the left side of the box is a vent that lets hydrochloric acid leave the oven without corroding it.

Appendix G

Nomenclature for Chapter Five

$C_A = \rho_{m,A} = \rho_m x_A$ = concentration or molar density of species A (moles of A/m^3)

$C_T = \rho_m$ = total concentration or system molar density (mole/m^3)

D_{AB} = binary diffusion coefficient for system A-B (cm^2/s)

$\mathcal{D}^{\circ}_{AB}$ = binary diffusion coefficient for an infinitely dilute system of A in solvent B (cm^2/s)

$\overline{G}_j$ = partial molal Gibb's free energy ($kg \cdot m^2/s^2 \cdot$mole of j)

J_A = ordinary molar flux of A relative to the mass average velocity (mole/$m^2 \cdot s$)

$\dot{m}_{A,gen}$ = rate of generation of mass of A via chemical reaction in a control volume (kg/s)

$\dot{M}_A$ = molar flow rate of species A (mole/s) – also $\dot{M}_{A,in}$ and $\dot{M}_{A,out}$

$\dot{M}_{A,gen}$ = rate of generation of moles of A via chemical reaction in a control volume (mole/s)

m_A = mass of species A (kg)

M_A = moles of species A (mole)

$M_A = MW_A$ = molecular weight of species A (g/mole)

N_A = ordinary molar flux of A relative to stationary coordinates (mole/$m^2 \cdot s$)

N_{Kn} = Knudsen Number (dimensionless)

t = time (s)

P = pressure (atm)

P_A = partial pressure of species A (atm)

P_C = critical pressure (atm)

r = radius (m)

T = temperature (K)

T_C = critical temperature (K)

V = total vapor molar flow rate (mole/s) or system volume (m^3)

x = Cartesian coordinates (m)

x_A = mole fraction for component A, liquid phase (mole of A/moles total)

$x_i = \frac{C_i}{C_{Total}} = \frac{\rho_{m,i}}{\rho_m}$ local mole fraction of species *i* (x_i) is defined as

y = Cartesian coordinate (m)

y_A = mole fraction for component A, vapor phase (mole of A/moles total)

z = Cartesian coordinate or column height (m)

$\alpha_{T,A}$ = thermal diffusion factor or thermal diffusivity (m^2/s)

ε_A = Lennard-Jones force constant ($kg \cdot m^2 / s^2$)

ρ = system mass density (kg/m^3)

$\rho_m = C_T$ = system molar density ($mole/m^3$)

$\rho_m = C_{Total} = \sum_{i=1}^{n} C_i$ total molar density or total molar concentration for the mixture at a point

ρ_A = mass density of species A (kg of A/m^3)

σ_A = Lennard-Jones molecular diameter (Å)

ω_A = mass or weight fraction for component A (kg of A/kg total)

ϕ = phi angle for spherical coordinates (degrees)

$\hat{\phi}$ = unit vector for spherical coordinates (dimensionless)

λ_A = mean free path of gas molecule A (m)

μ_i = chemical potential ($\partial G/\partial n_i$)

$\Omega_{D,AB}$ = diffusion collision integral (dimensionless)

Appendix H

Equations for Unknown Parameters for Chapter Five

From the work of Homer et. al. 2009[1] that simulated an evaporating ethanol-water droplet using the non-random two-liquid (NRTL) model, which is based on a local mole fraction concept developed by Renon and Prausnitz. The ***activity coefficients*** are expressed as:

$$\ln \gamma_B = x_A{}^2[\tau_{AB}(\frac{G_{AB}}{x_B + x_A G_{AB}})^2 + \frac{\tau_{BA} G_{BA}}{(x_A + x_B G_{BA})^2}]$$

$$\ln \gamma_A = x_B{}^2[\tau_{BA}(\frac{G_{BA}}{x_A + x_B G_{BA}})^2 + \frac{\tau_{AB} G_{AB}}{(x_B + x_A G_{AB})^2}]$$

Where X_A and X_B are mole fractions of water and ethanol, respectively, and

$$\tau_{BA} = \frac{g_{BA} - g_{AA}}{RT}$$
$$\tau_{AB} = \frac{g_{AB} - g_{BB}}{RT}$$

$$\ln G_{AB} = -\alpha_{BA}\tau_{AB}$$
$$\ln G_{BA} = -\alpha_{BA}\tau_{BA}$$

Thus, there are three temperature-dependent binary parameters ($g_{BA} - g_{AA}$, $g_{AB} - g_{BB}$ and α_{BA}) which must be parameterized to fully define the activity coefficients. Homer et. al.[1] used the following equations:

$$\frac{g_{BA} - g_{AA}}{R} = -0.68681T + 261.77$$
$$\frac{g_{AB} - g_{BB}}{R} = -8.0894x10^{-5}T^4 + 0.10998T^3 - 56.011T^2 + 1.2667x10^4 T - 1.0729x10^6$$

and α can be derived from the NRTL equation as

$$\alpha = 1 - 2x_B x_A [\frac{\tau_{AB} G_{AB}^{\ 2}}{(x_B + x_A G_{AB})^3} + \frac{\tau_{BA} G_{BA}^{\ 2}}{(x_A + x_B G_{BA})^3}]$$

The ***density of the ethanol–water solution*** is calculated as a function of temperature and ethanol weight fraction, w,

$$\rho = A_0 (T - 273.15)^2 + A_1 (T - 273.15) + A_2$$

Where,

$$A_0 = -5.9820x10^{-7} w^2 + 8.8495x10^{-5} w - 3.7194x10^{-3}$$

$$A_1 = 1.2845x10^{-4} w^2 + 2.0625x10^{-2} w - 4.4985x10^{-2}$$

$$A_2 = -1.05171x10^{-2} w^2 + 0.88651w - 999.748$$

The Vignes relation is used to determine the binary ***diffusion coefficients in the liquid phase*** at finite concentrations,

$$\mathcal{D}_{AB,l} = \left(\mathcal{D}^{\circ}_{AB}\right)^{x_B} \left(\mathcal{D}^{\circ}_{BA}\right)^{x_A} \alpha$$

Where D^0_{AB} and D^0_{BA} are the infinite diffusion coefficients ($m^2\ s^{-1}$) described by the equations,

$$\mathcal{D}^{\circ}_{AB} = 1x10^{-9} \exp(\frac{-2271.9}{T} + 7.7897)$$

$$\mathcal{D}^{\circ}_{BA} = 1x10^{-9} \exp(\frac{-2261.5}{T} + 7.7695)$$

Diffusion coefficients for gases

The correlation developed by Chapman and Enskog [Chapman and Cowling, 1970] is routinely used to estimate diffusion coefficients for gas phase systems at moderate temperatures and pressures. It is normally accurate to within ±8 %.

$$\mathcal{D}_{AB,v} = \frac{1.8583 \cdot 10^{-7} \cdot T^{3/2}}{P \sigma_{AB}^2 \Omega_{D,AB}} \left(\frac{1}{\mathcal{M}_A} + \frac{1}{\mathcal{M}_B} \right)^{1/2}$$

where D_{AB} has units of cm^2/s, T is in Kelvin and P in atm.

The collision diameter for the mixture (σ_{AB}) is calculated from pure component molecular diameters using the equation:

$$\sigma_{AB} = 0.5 \cdot (\sigma_A + \sigma_B) = \text{ Collision diameter (in Å)}$$

Where:

Lennard-Jones parameters can be estimated using the correlations below:

$$\sigma_A = 2.44 \cdot \left(\frac{T_{C,A}}{P_{C,A}} \right)^{1/3}$$

where T_c and P_c are the critical properties of the molecule in units of K and atm, respectively.

The collision integral can be accurately calculated using the relation of Neufield, et al. [1972]:

$$\Omega_{D,AB} = \frac{A}{(T^*)^B} + \frac{C}{\exp(D \cdot T^*)} + \frac{E}{\exp(F \cdot T^*)} + \frac{G}{\exp(H \cdot T^*)}$$

$T^* = k_B T/\varepsilon_{AB}$	C = 0.19300	F = 1.52996
A = 1.06036	D = 0.47635	G = 1.76474
B = 0.15610	E = 1.03587	H= 3.89411

The term T* can be found using the equation below, which uses standard combination rules for the required Lennard-Jones force constant parameters.

$$T^* = \frac{k_B T}{\varepsilon_{AB}} = \frac{T}{\left(\frac{\varepsilon_A}{k_B} \cdot \frac{\varepsilon_B}{k_B}\right)^{1/2}}$$

where k_B is Boltzmann's constant, T is the system temperature in degrees K, and $\varepsilon_{AB} = (\varepsilon_A \cdot \varepsilon_B)^{1/2}$.

$$\frac{\varepsilon_A}{k_B} = 0.77 \cdot T_{C,A}$$

$$\frac{\varepsilon_A}{k_B} = 1.15 \cdot T_{Boil,A}$$, where $T_{Boil,A}$ is the normal boiling temperature in K.

Using the Chapman-Enskog equation as a guide, one can easily calculate diffusivity values at a different temperature or pressure if the quantity is known at one set of conditions:

$$\mathcal{D}_{AB,T2,P2} = \mathcal{D}_{AB,T1,P1}\left(\frac{P_1}{P_2}\right)\left(\frac{T_2}{T_1}\right)^{3/2}\left(\frac{\Omega_{D,AB,T1}}{\Omega_{D,AB,T2}}\right)$$

Where temperature is in degrees K and pressure is in any consistent set of units.

Table H-1. Binary Diffusivities, Gases

System Components		Temperature T (K)	Pressure P (atm)	Mole Fraction x_A (unitless)	Diffusivity D_{AB} (cm^2/s)	Reference
A	B					
air	ethanol	273	1	dilute	0.102	[2]
air	water	289.1	1	dilute	0.282	[2]
air	water	298.2	1	dilute	0.260	[2]
air	water	312.6	1	dilute	0.277	[2]
air	water	333.2	1	dilute	0.305	[2]

Table H-2. Binary Diffusivities, Liquids

System Components		Temperature T (K)	Mole Fraction x_A (unitless)	Diffusivity D_{AB} (10^{-5}, cm^2/s)	Reference
A	B				
air	water	298	dilute	2.00	[3]
ethanol	water	298	0.05	1.13	[4]
ethanol	water	298	0.275	0.41	[4]
ethanol	water	298	0.50	0.90	[4]
ethanol	water	298	0.70	1.40	[4]
ethanol	water	298	0.95	2.20	[4]
chlorine	water	298	dilute	1.25	[3]
hydrogen chloride	water	298	dilute	3.10	[2]
water	ethanol	298	dilute	1.24	[5]

References for Data in this Appendix:

(1) Homer, C. J.; Jiang, X.; Ward, T. L.; Brinker, C. J.; Reid, J. P. *Phys. Chem. Chem. Phys.* 2009, *11*.

(2) *International Critical Tables;* Vol. 5, pp 63.

(3) Cussler, E. L. In *Diffusion, Mass Transfer in Fluid Systems; Diffusion, Mass Transfer in Fluid Systems*; Cambridge: 1976.

(4) Johnson, P. *Chem. Rev.* 1956, *56*, 387.

(5) Reid, R.; Prausnitz, J.; Sherwood, T. In *The properties of gases and liquids;* 1977.

Appendix I

Zirconia Synthesis Aging Process

The purpose of the experiment is to observe the effects of diffusion of water to the system and rates of evaporation of ethanol from the system. Water reentering the samples can have a great impact on how the materials self assemble. Also, diffusion of water in tubes with lower levels is more difficult. Details for these are explained in Chapter 6. This appendix features pictures of the experiments and details of the process.

50 ml evap. dishes. Diameter1=8cm
Diameter2=5.5cm Height= 2cm.
Starting points: 50 ml, 25 ml, 10 ml

Figure I-1. Evaporation of initial solution in ceramic dishes.

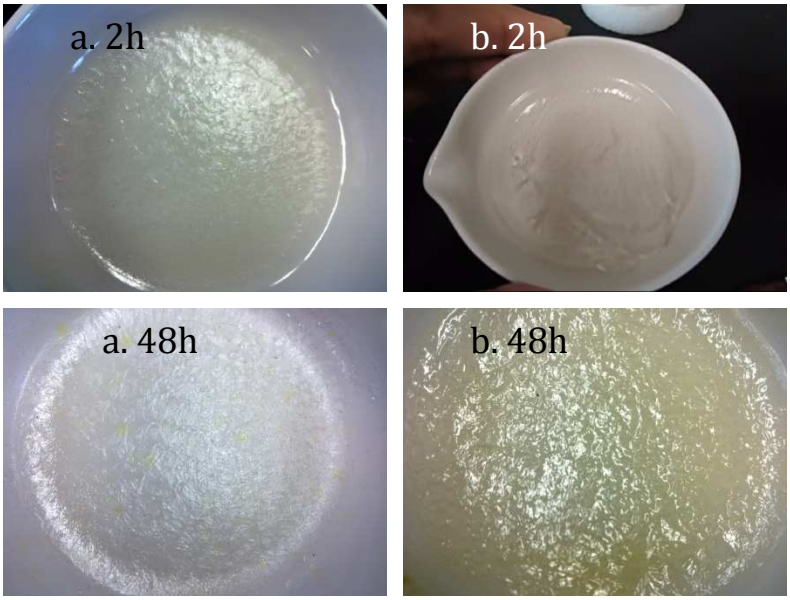

Figure I-2. Evaporation Dishes (a) 10 ml (b) 50 ml starting level at different aging times.

50 ml crucibles. Diameter1=5cm Diameter2=2.5cm
Height= 4.5cm.
Starting points: 50 ml, 25 ml, 10 ml

Figure I-3. Evaporation of initial solution in crucibles.

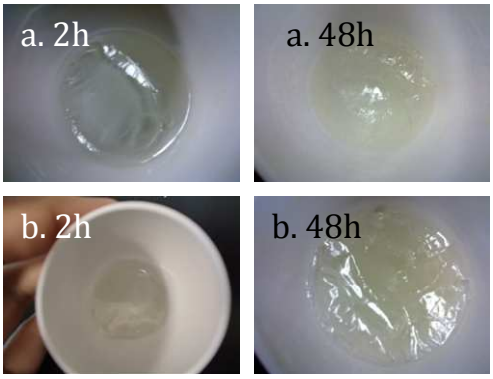

Figure I-4. Crucibles (a) 25 ml (b) 50 ml starting level.

15 ml graduated tubes. Diameter=1.5cm
Height= 11.8cm. Starting points: 15ml, 12 ml, 9 ml, 6 ml, 3 ml.

Figure I-5. Evaporation of initial solution in graduated tubes.

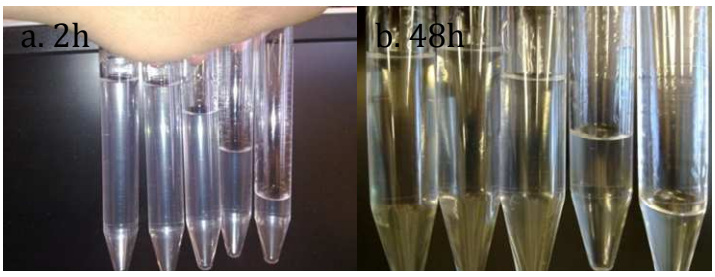

Figure I-6. Tubes at 15 ml, 12 ml, 9 ml, 6 ml, 3 ml starting level at (a) 2 and (b) 48 h aging.

Sample	Time starts gelling* (h)	BET S.A** (m^2/g)	BJH pore size** (nm)	Small XRD peaks AUG	TEM AUG (2) OCT	
10 ml dish	1	71	5.4	0.4; 1	N.O	O.
25 ml dish	2	72	6.2	0.2; 0.4	N.O	O.
50 ml dish	2	59	6.0	0.5	N.O	N.O
10 m cru.	2	48	4.5	0.5, 0.7	N.O	O. / N. O.
25 ml cru.	2.5	33	3.5	0.2, 0.3	N.O	N. O.
50 ml cru.	2.5	38	4.0	0.2,0.3	N.O	O. / N. O.
3 ml tube	48-72	16	3.8, 40	0.2, 0.4	O	N. O.
6 ml tube	> 120	36	3.5, 17.5	0.2,0.4	N.O	N. O.
9 ml tube	> 120	41	3.7, 18.1	0.2,0.4	N.O	N. O.
12 ml tube	> 120	38	3.8, 18.5	0.4	N.O	N. O.
15 ml tube	> 120	25	3.6, 17.8	0.2, 0.4	N.O	N. O.

- N.O: Not Ordered O: Ordered cru.: crucible
- Diameter evap. dish = 8 cm. Diameter crucible= 5 cm Diameter tube=1.5 cm
- Gelling under fixed RH at 50% and Temperature 40 C. Under a 48 hour observation period
- All samples were dried after a 48 h waiting period
- * The error margin for the surface area is ±5 m^2/g and for the pore diameter, ±0.5 nm

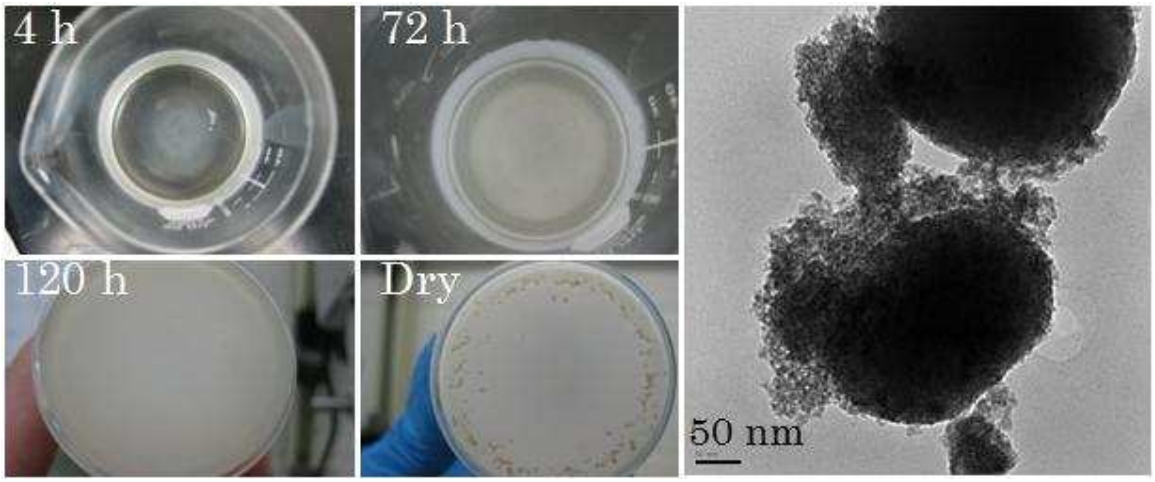

Figure I-8. Aging process during the synthesis of zirconia mesoporous oxides via EISA. The solution to gel process is homogeneous. However the synthesis conditions are not optimal yielding a disordered mesostructure.

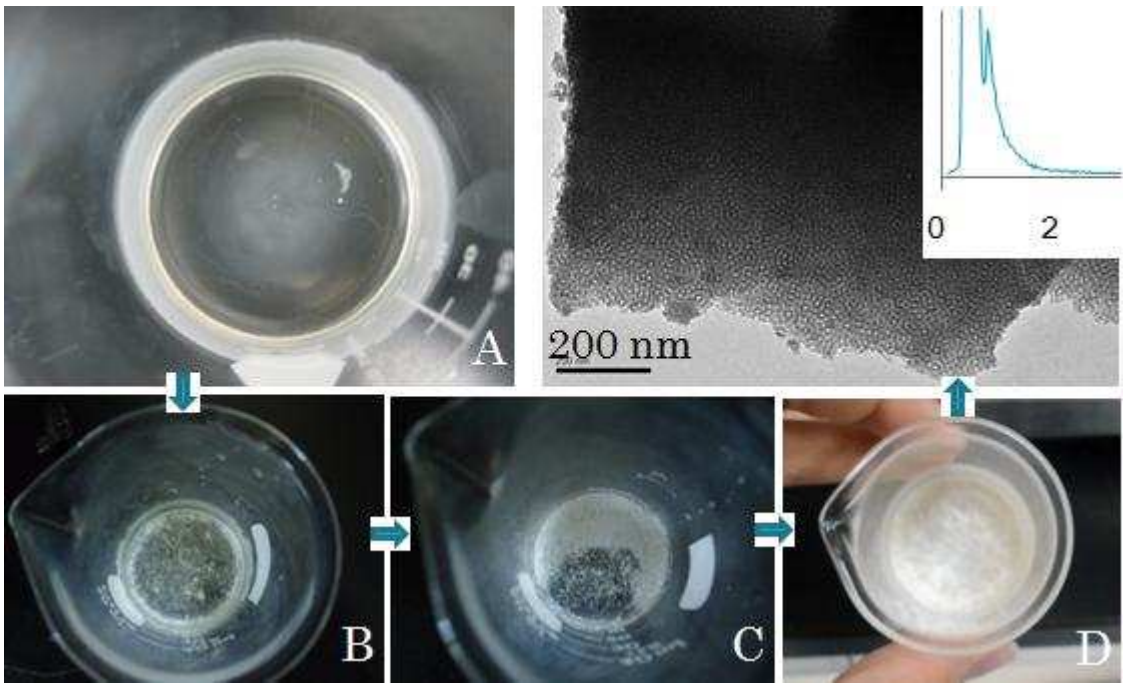

Figure I-9. Precipitation process during mesoporous zirconia synthesis via EISA. Although the process did not happen homogenously, the surface was not covered by an oxide network allowing the evaporation of the sample. The resulting structure is very ordered and has a small angle peak as well meaning the structure has a long-range ordered mesostructure.

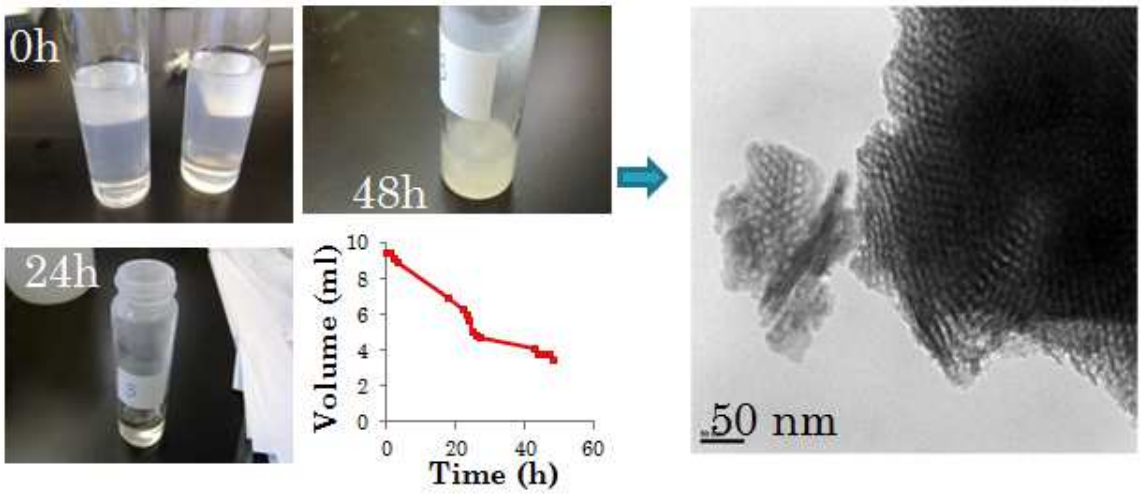

Figure I-10. Improved aging process. Since the evaporation area is smaller, the evaporation rate is more uniform and a uniform ordered mesoporous zirconia structure is obtained.

CZY SYNTHESIS- AGING PROCESS

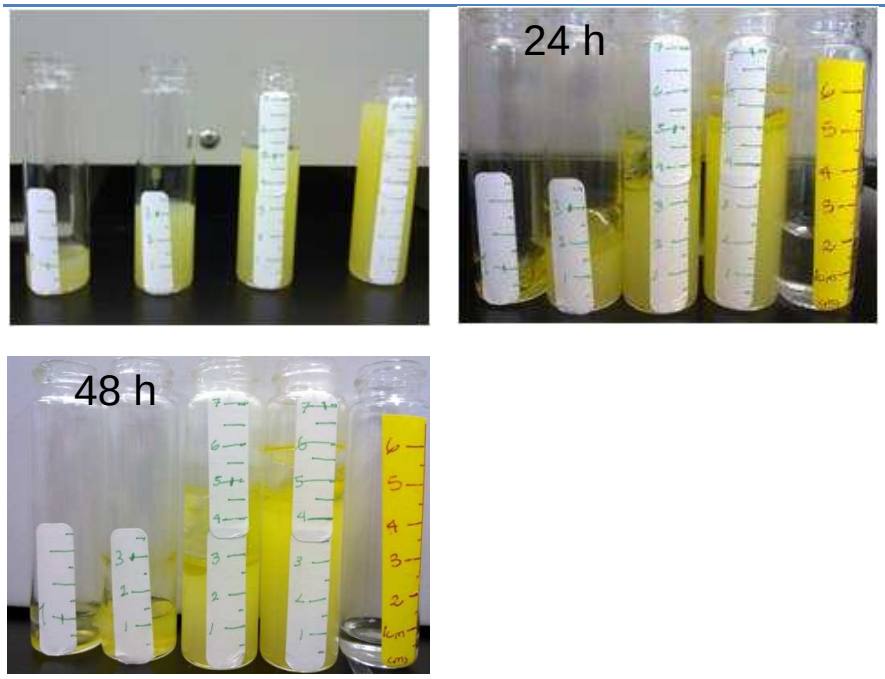

Figure I-11. Aging in 25 ml vial (d=1.5 cm; h= 8cm). Starting points: h =1, 3, 5, 7 cm. Condensation on the surface generates crust that slows evaporation.

Starting volume (cm^3)	**22 (h=7cm)**	**15.7 (h=5 cm)**	**9.4 (h=3cm)**	**3.1 (h=1cm)**
Time gelling starts (h)	12 to 24[a]	12 to 24[a]	12 to 24	4 to 5
Small XRD peaks	0.18, 0.28	0.18, 0.28	0.18, 0.36	0.56,0.86
BET (m^2/g) surface area *	105	104	95	92
BJH (nm) pore size *	3.8	3.5	3.5	3.4
TEM AUGUST (2)	Ordered	Not ordered	Not ordered	Not ordered
TEM OCTOBER	Not ordered	Not ordered	Not ordered	Not ordered

* The error margin for the surface area is ±5 m^2/g and for the pore diameter, ±0.5 nm
a. Liquid bottom underneath hard film on surface. Surface area =3.14 cm^2

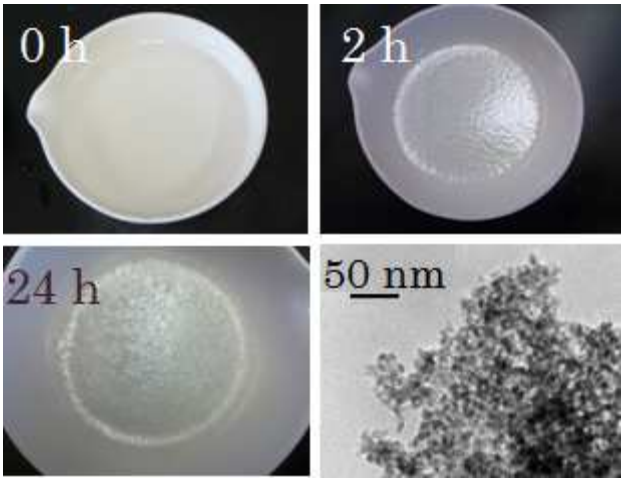

Figure I-12. Aging process during the synthesis of CZY mesoporous oxides via EISA. The solution does not homogeneously become a gel. A crust of oxides appears in the surface slowing the evaporation of solvent under the surface yielding a disordered mesostructure.

Appendix J

MCM-41 Analysis

Validation & Blank Response Correction

For the MCM-41 analysis, the kinetic behavior was confirmed by a C/Co versus Ft semi-logarithmic plot as shown in Figure J-1 below and indicated by the diverging curves at the long-time range.

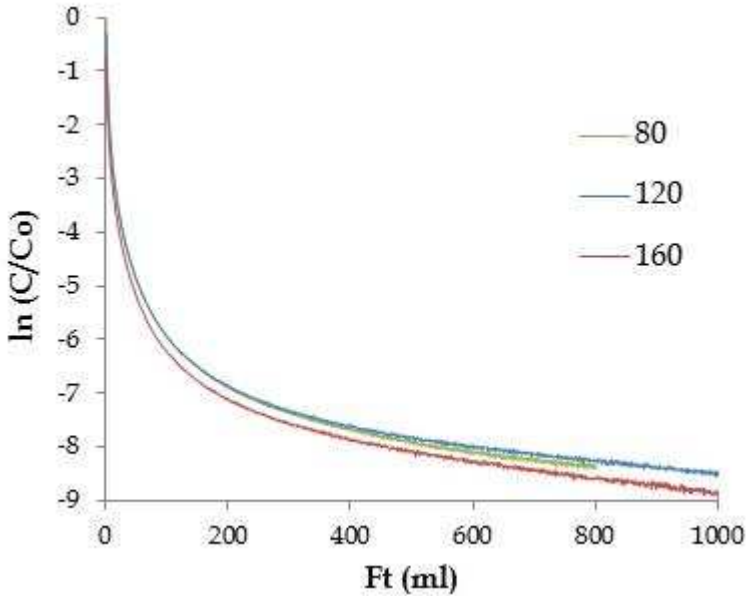

Figure J-1. ZLC response curves plotted in the form $\ln(C/C_0)$ vs. Ft for MCM-41 showing kinetic control at chosen flow rates at long times.

Since the blank used for the measurements is closer to the real curves than other articles have reported I tried to do corrections of the measurements by subtracting the blanks. The raw and the corrected desorption curves are shown in Figure J-2 and Figure J-3.

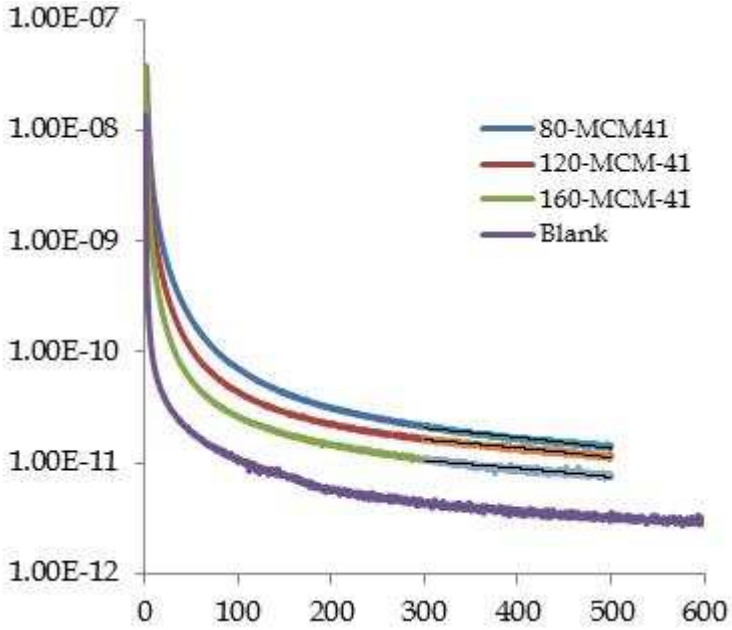

Figure J-2. Raw desorption curves for hexane in MCM-41 and a blank measurement. Desorption curves were measured at 60°C. Each curve has approximately 2000 data points.

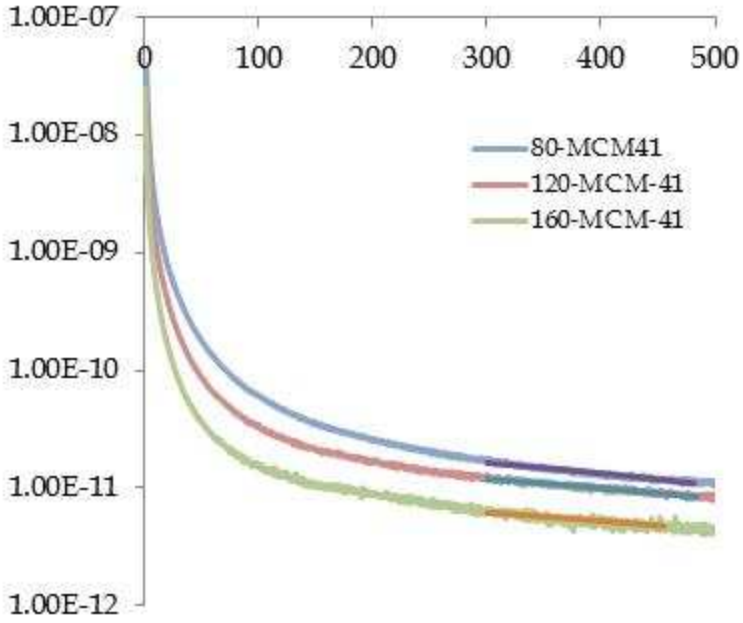

Figure J-3. Corrected desorption curves of hexane in MCM-41 (raw values minus blank).

However, upon normalizing the desorption curves, the trends are changed some as shown in Figure J-4. The behavior might be due to the long-time (LT) region values being so small that the corrections have a very high effect on them. As explained by Hufton et al.[1], it is very difficult to baseline the curves before further calculations are made and that is the reason if the measurements in the LT region are done incorrectly, the procedure can significantly alter the slope of the LT tail and therefore the apparent value of the diffusion coefficients.

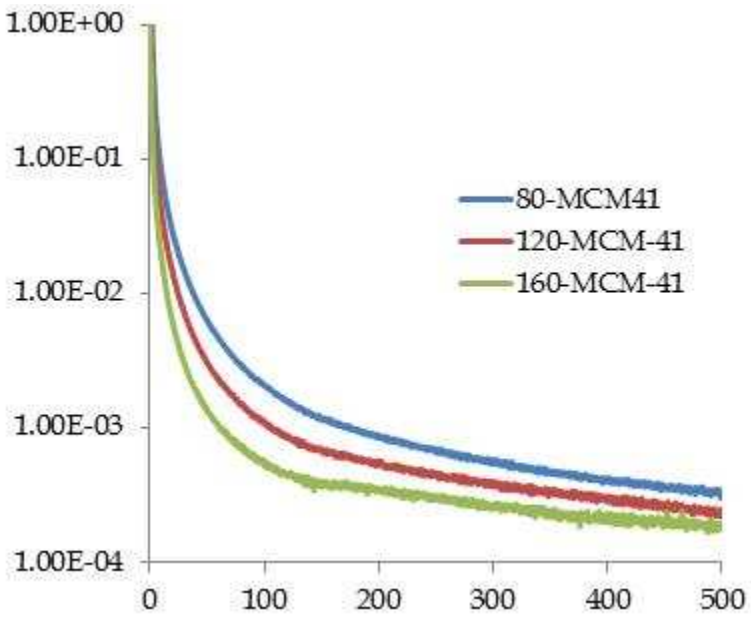

Figure J-4. Normalized desorption curves for hexane in MCM-41 corrected for blank measurements.

Table J-1 shows the values obtained from the curves shown above. The trends are off, as shown by the L value losing its proportionality with respect to the flow rate. However the diffusivity values are very similar to the ones found for the non-corrected desorption curves shown in Chapter 6. It only changes from $1.1x10^{-9}$ to $1.02x10^{-9}$ cm^2/s. I believe that since the values used in the chapter were normalized before doing the measurements,

no extra corrections were needed. Also the experimental set-up is such that the blank is designed not to have a big effect in the curves since the dead volume in the system is as small as possible.

Table J-1. Variation of parameters with purge flow rate for n-hexane in MCM-41 materials. Desorption experiments were performed at 60 C

Flow rate (ml/min)	L	D/R^2	Flow rate ratio	L ratio	D (cm^2/s)
80	1545	2.85E-04	1	1	1.17E-09
120	2412	2.72E-04	1.5	1.56	1.12E-09
160	4850	1.86E-04	2	3.14	7.64E-10
Average					1.02E-09

The values for 80 and 120 do not change much from the corrected values and I can learn that the closer the data set is to the blank, the more error shown in the diffusivity values when corrections are done. Also the correction does not affect the D values in any perceptive way but changes the L values making the technique applied invalid.

Intermediate time analysis

The LT-method robustness and reliability has been confirmed in many previous experimental studies.[2-6] However, when the sorbate is both weekly adsorbed and fast diffusing, it is not always possible to determine the long time asymptote with sufficient accuracy. In that situation, an alternative approach based on the "intermediate time" approximation of the ZLC response is useful.[7] In the short-time region (after a time directed by the blank response and before the long time asymptote is reached) for sufficiently high values of L:

$$\frac{c}{c_0} \approx \frac{1}{L}\left[\sqrt{\frac{R^2}{\pi D t}} - 1\right]$$

In this regime a plot of ($^{c}/_{c_0}$) versus $\frac{1}{\sqrt{t}}$ should yield a straight line with an intercept of $\sqrt{^{\pi D}/_{R^2}}$ on the $\frac{1}{\sqrt{t}}$ axis allowing the direct determination of $^{D}/_{R^2}$; and an intercept of $-\frac{1}{L}$ on the $^{c}/_{c_0}$ axis allowing the determination of L and the Henry constant. According to Brandani et al.[5] this solution is valid for the concentration range $^{c}/_{c_0} < 0.2$ and L >20. This approximation is usually used as a way to confirm solutions obtained by other techniques and has previously been used in numerous articles[5, 7-11]

Figure J-5 shows representative experimental response curves plotted in this way. The corresponding diffusivities are shown in Table J-2. The values found correspond to the ones found with the long-time asymptotic method. These diffusivities are invariant with purge flow rate and confirm the reliability of my results.

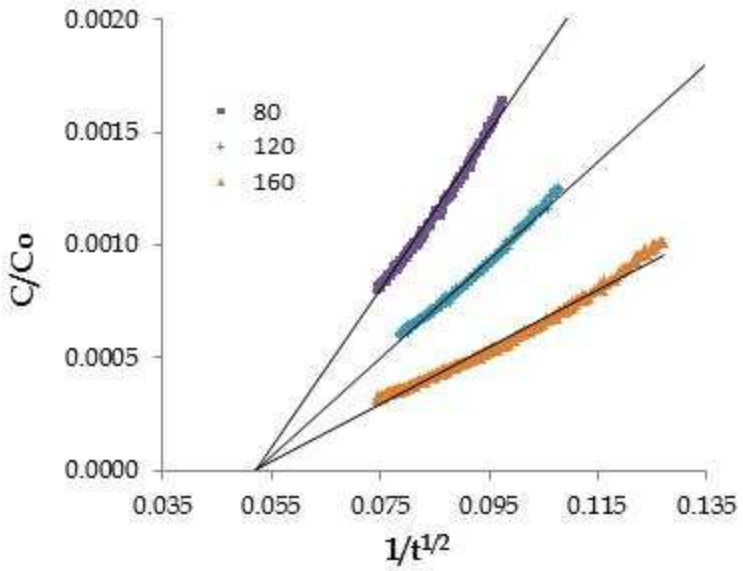

Figure J-5. ZLC response curve for intermediate time analysis for MCM-41 at 60 °C.

Table J-2. Variation of parameters with purge flow rate for n-hexane in MCM-41 materials using the intermediate time analysis. Desorption experiments were performed at 60 °C

Flow rate (ml/min)	**L**	**D/R^2**	**Flow rate ratio**	**L ratio**	**D (cm^2/s)**
80	549	2.74E-04	1	1	1.12E-09
120	883	2.74E-04	1.5	1.6095406	1.12E-09
160	1531	2.70E-04	2	2.7901991	1.11E-09

Since these values are based on short-time data, some error is expected as a result of dead volume effects due to the set-up of my system and the short time baseline. From these observations I concluded that the long-time asymptote analysis is more reliable for my system.

As the technique is valid when L>20 and $^{c}/_{c_0} < 0.2$ in the short time region and before the LT asymptote is reached, I found that different intermediate analysis approximations in this region for hexane in MCM-41 yield D values between

$2.5x10^{-10}$ and $9.5x10^{-9}$ $cm^2/_s$,which is within the range of diffusivity values found for the long-time solution.

References

(1) Hufton, J. R.; Ruthven, D. M. *Ind Eng Chem Res* **1993**, *32*, 2379-2386.

(2) Ruthven, D. M.; Brandani, S.; Eic, M. In *Measurement of Diffusion in Microporous Solids by Macroscopic Methods;* Molecular Sieves; Springer: Berlin, 2008; Vol. 7, pp 45-84.

(3) Ruthven, D.; Brandani, S. *Recent Advances in Gas Separation by Microporous Ceramic Membranes* **2000**, *6*, 187-.

(4) Karger, J.; Ruthven, D. M. In *Diffusion in Zeolites and other Microporous Solids;* John Wiley: New York, 1992; pp 328-333.

(5) Brandani, S.; Ruthven, D. *Adsorption* **1996**, *2*, 133-143.

(6) Eic, M.; Ruthven, D. M. *Zeolites* **1988**, *8*, 40-45.

(7) Vidoni, A. Adsorption and diffusion of light hydrocarbons in DDR zeolite, The University of Maine, Maine, 2011.

(8) Cavalcante Jr., C. L.; Brandani, S.; Ruthven, D. M. *Zeolites* **1997**, *18*, 282-285.

(9) Cavalcante Jr., C. L.; Eić, M.; Ruthven, D. M.; Occelli, M. L. *Zeolites* **1995**, *15*, 293-307.

(10) Malekian, A.; Vinh-Thang, H.; Huang, Q.; EiÄ‡, M.; Kaliaguine, S. *Ind Eng Chem Res* **2007**, *46*, 5067-5073.

(11) Huang, Q.; Eic, M.; Xiao, H.; Kaliaguine, S. *Adsorption* **2010**, *16*, 531-539.

Appendix K

Permission to Reproduce Figures

JOHN WILEY AND SONS LICENSE
TERMS AND CONDITIONS
Jun 24, 2013

This is a License Agreement between Alma I Cordova Morales ("You") and John Wiley and Sons ("John Wiley and Sons") provided by Copyright Clearance Center ("CCC"). The license consists of your order details, the terms and conditions provided by John Wiley and Sons, and the payment terms and conditions.

License Number	3152130713809
License date	May 18, 2013
Licensed content publisher	John Wiley and Sons
Licensed content publication	Angewandte Chemie International Edition
Licensed content title	Endo- and Exotemplating to Create High-Surface-Area Inorganic Materials
Licensed copyright line	Copyright © 2003 WILEY-VCH Verlag GmbH & Co. KGaA, Weinheim
Licensed content author	Ferdi Schüth
Licensed content date	Aug 7, 2003
Start page	3604
End page	3622
Type of use	Dissertation/Thesis
Requestor type	University/Academic
Format	Electronic
Portion	Figure/table
Number of figures/tables	1
Original Wiley figure/table number(s)	Figure 1
Will you be translating?	No
Total	0.00 USD
Terms and Conditions	

TERMS AND CONDITIONS

remain the exclusive property of John Wiley & Sons Inc or one of its related companies (WILEY) or their respective licensors, and your interest therein is only that of having possession of and the right to reproduce the Materials pursuant to Section 2 herein during the continuance of this Agreement. You agree that you own no right, title or interest in or to the Materials or any of the intellectual property rights therein. You shall have no rights hereunder other than the license as provided for above in Section 2. No right, license or interest to any trademark, trade name, service mark or other branding ("Marks") of WILEY or its licensors is granted hereunder, and you agree that you shall not assert any such right, license or interest with respect thereto.

5. NEITHER WILEY NOR ITS LICENSORS MAKES ANY WARRANTY OR REPRESENTATION OF ANY KIND TO YOU OR ANY THIRD PARTY, EXPRESS, IMPLIED OR STATUTORY, WITH RESPECT TO THE MATERIALS OR THE ACCURACY OF ANY INFORMATION CONTAINED IN THE MATERIALS, INCLUDING, WITHOUT LIMITATION, ANY IMPLIED WARRANTY OF MERCHANTABILITY, ACCURACY, SATISFACTORY QUALITY, FITNESS FOR A PARTICULAR PURPOSE, USABILITY, INTEGRATION OR NON-INFRINGEMENT AND ALL SUCH WARRANTIES ARE HEREBY EXCLUDED BY WILEY AND ITS LICENSORS AND WAIVED BY YOU.

6. WILEY shall have the right to terminate this Agreement immediately upon breach of this Agreement by you.

7. You shall indemnify, defend and hold harmless WILEY, its Licensors and their respective directors, officers, agents and employees, from and against any actual or threatened claims, demands, causes of action or proceedings arising from any breach of this Agreement by you.

8. IN NO EVENT SHALL WILEY OR ITS LICENSORS BE LIABLE TO YOU OR ANY OTHER PARTY OR ANY OTHER PERSON OR ENTITY FOR ANY SPECIAL, CONSEQUENTIAL, INCIDENTAL, INDIRECT, EXEMPLARY OR PUNITIVE DAMAGES, HOWEVER CAUSED, ARISING OUT OF OR IN CONNECTION WITH THE DOWNLOADING, PROVISIONING, VIEWING OR USE OF THE MATERIALS REGARDLESS OF THE FORM OF ACTION, WHETHER FOR BREACH OF CONTRACT, BREACH OF WARRANTY, TORT, NEGLIGENCE, INFRINGEMENT OR OTHERWISE (INCLUDING, WITHOUT LIMITATION, DAMAGES BASED ON LOSS OF PROFITS, DATA, FILES, USE, BUSINESS OPPORTUNITY OR CLAIMS OF THIRD PARTIES), AND WHETHER OR NOT THE PARTY HAS BEEN ADVISED OF THE POSSIBILITY OF SUCH DAMAGES. THIS LIMITATION SHALL APPLY NOTWITHSTANDING ANY FAILURE OF ESSENTIAL PURPOSE OF ANY LIMITED REMEDY PROVIDED HEREIN.

9. Should any provision of this Agreement be held by a court of competent jurisdiction to be illegal, invalid, or unenforceable, that provision shall be deemed amended to

achieve as nearly as possible the same economic effect as the original provision, and the legality, validity and enforceability of the remaining provisions of this Agreement shall not be affected or impaired thereby.

10. The failure of either party to enforce any term or condition of this Agreement shall not constitute a waiver of either party's right to enforce each and every term and condition of this Agreement. No breach under this agreement shall be deemed waived or excused by either party unless such waiver or consent is in writing signed by the party granting such waiver or consent. The waiver by or consent of a party to a breach of any provision of this Agreement shall not operate or be construed as a waiver of or consent to any other or subsequent breach by such other party.

11. This Agreement may not be assigned (including by operation of law or otherwise) by you without WILEY's prior written consent.

12. Any fee required for this permission shall be non-refundable after thirty (30) days from receipt

13. These terms and conditions together with CCC's Billing and Payment terms and conditions (which are incorporated herein) form the entire agreement between you and WILEY concerning this licensing transaction and (in the absence of fraud) supersedes all prior agreements and representations of the parties, oral or written. This Agreement may not be amended except in writing signed by both parties. This Agreement shall be binding upon and inure to the benefit of the parties' successors, legal representatives, and authorized assigns.

14. In the event of any conflict between your obligations established by these terms and conditions and those established by CCC's Billing and Payment terms and conditions, these terms and conditions shall prevail.

15. WILEY expressly reserves all rights not specifically granted in the combination of (i) the license details provided by you and accepted in the course of this licensing transaction, (ii) these terms and conditions and (iii) CCC's Billing and Payment terms and conditions.

16. This Agreement will be void if the Type of Use, Format, Circulation, or Requestor Type was misrepresented during the licensing process.

17. This Agreement shall be governed by and construed in accordance with the laws of the State of New York, USA, without regards to such state's conflict of law rules. Any legal action, suit or proceeding arising out of or relating to these Terms and Conditions or the breach thereof shall be instituted in a court of competent jurisdiction in New York County in the State of New York in the United States of America and each party hereby

consents and submits to the personal jurisdiction of such court, waives any objection to venue in such court and consents to service of process by registered or certified mail, return receipt requested, at the last known address of such party.

Wiley Open Access Terms and Conditions

Wiley publishes Open Access articles in both its Wiley Open Access Journals program [http://www.wileyopenaccess.com/view/index.html] and as Online Open articles in its subscription journals. The majority of Wiley Open Access Journals have adopted the Creative Commons Attribution License (CC BY) which permits the unrestricted use, distribution, reproduction, adaptation and commercial exploitation of the article in any medium. No permission is required to use the article in this way provided that the article is properly cited and other license terms are observed. A small number of Wiley Open Access journals have retained the Creative Commons Attribution Non Commercial License (CC BY-NC), which permits use, distribution and reproduction in any medium, provided the original work is properly cited and is not used for commercial purposes.

Online Open articles - Authors selecting Online Open are, unless particular exceptions apply, offered a choice of Creative Commons licenses. They may therefore select from the CC BY, the CC BY-NC and the Attribution-NoDerivatives (CC BY-NC-ND). The CC BY-NC-ND is more restrictive than the CC BY-NC as it does not permit adaptations or modifications without rights holder consent.

Wiley Open Access articles are protected by copyright and are posted to repositories and websites in accordance with the terms of the applicable Creative Commons license referenced on the article. At the time of deposit, Wiley Open Access articles include all changes made during peer review, copyediting, and publishing. Repositories and websites that host the article are responsible for incorporating any publisher-supplied amendments or retractions issued subsequently.
Wiley Open Access articles are also available without charge on Wiley's publishing platform, **Wiley Online Library** or any successor sites.

Conditions applicable to all Wiley Open Access articles:

- The authors' moral rights must not be compromised. These rights include the right of "paternity" (also known as "attribution" - the right for the author to be identified as such) and "integrity" (the right for the author not to have the work altered in such a way that the author's reputation or integrity may be damaged).

- Where content in the article is identified as belonging to a third party, it is the obligation of the user to ensure that any reuse complies with the copyright policies of the owner of that content.

- If article content is copied, downloaded or otherwise reused for research and

other purposes as permitted, a link to the appropriate bibliographic citation (authors, journal, article title, volume, issue, page numbers, DOI and the link to the definitive published version on Wiley Online Library) should be maintained. Copyright notices and disclaimers must not be deleted.

- Creative Commons licenses are copyright licenses and do not confer any other rights, including but not limited to trademark or patent rights.

- Any translations, for which a prior translation agreement with Wiley has not been agreed, must prominently display the statement: "This is an unofficial translation of an article that appeared in a Wiley publication. The publisher has not endorsed this translation."

Other Terms and Conditions:

BY CLICKING ON THE "I AGREE..." BOX, YOU ACKNOWLEDGE THAT YOU HAVE READ AND FULLY UNDERSTAND EACH OF THE SECTIONS OF AND PROVISIONS SET FORTH IN THIS AGREEMENT AND THAT YOU ARE IN AGREEMENT WITH AND ARE WILLING TO ACCEPT ALL OF YOUR OBLIGATIONS AS SET FORTH IN THIS AGREEMENT.

ELSEVIER LICENSE
TERMS AND CONDITIONS
Jun 24, 2013

This is a License Agreement between Alma I Cordova Morales ("You") and Elsevier ("Elsevier") provided by Copyright Clearance Center ("CCC"). The license consists of your order details, the terms and conditions provided by Elsevier, and the payment terms and conditions.

All payments must be made in full to CCC. For payment instructions, please see information listed at the bottom of this form.

Supplier	Elsevier Limited The Boulevard,Langford Lane Kidlington,Oxford,OX5 1GB,UK
Registered Company Number	1982084
Customer name	Alma I Cordova Morales
Customer address	108 Earle Halll CLEMSON, SC 29634
License number	3155980600433
License date	May 25, 2013
Licensed content publisher	Elsevier
Licensed content publication	Current Opinion in Colloid & Interface Science
Licensed content title	Block copolymer-templated mesoporous oxides
Licensed content author	Galo J.de A.A. Soler-Illia,Eduardo L. Crepaldi,David Grosso,Clément Sanchez
Licensed content date	March 2003
Licensed content volume number	8
Licensed content issue number	1
Number of pages	18
Start Page	109
End Page	126
Type of Use	reuse in a thesis/dissertation
Portion	figures/tables/illustrations
Number of figures/tables/illustrations	2
Format	both print and electronic
Are you the author of this Elsevier article?	No

Will you be translating?	No
Order reference number	None
Title of your thesis/dissertation	Synthesis, Characterization and Diffusion Properties of CZY Mesostructures
Expected completion date	Aug 2013
Estimated size (number of pages)	200
Elsevier VAT number	GB 494 6272 12
Permissions price	0.00 USD
VAT/Local Sales Tax	0.00 USD / 0.00 GBP
Total	0.00 USD
Terms and Conditions	

JOHN WILEY AND SONS LICENSE
TERMS AND CONDITIONS
Jun 24, 2013

This is a License Agreement between Alma I Cordova Morales ("You") and John Wiley and Sons ("John Wiley and Sons") provided by Copyright Clearance Center ("CCC"). The license consists of your order details, the terms and conditions provided by John Wiley and Sons, and the payment terms and conditions.

License Number	3157691137368
License date	May 28, 2013
Licensed content publisher	John Wiley and Sons
Licensed content publication	Advanced Functional Materials
Licensed content title	Fundamentals of Mesostructuring Through Evaporation-Induced Self-Assembly
Licensed copyright line	Copyright © 2004 WILEY-VCH Verlag GmbH & Co. KGaA, Weinheim
Licensed content author	D. Grosso,F. Cagnol,G.A.A. Soler-Illia,E.L. Crepaldi,H. Amenitsch,A. Brunet-Bruneau,A. Bourgeois,C. Sanchez
Licensed content date	Apr 19, 2004
Start page	309
End page	322
Type of use	Dissertation/Thesis
Requestor type	University/Academic
Format	Print and electronic
Portion	Figure/table
Number of figures/tables	2
Original Wiley figure/table number(s)	Figure 1 Figure 5
Will you be translating?	No
Total	0.00 USD
Terms and Conditions	

TERMS AND CONDITIONS

This copyrighted material is owned by or exclusively licensed to John Wiley & Sons, Inc. or one of its group companies (each a "Wiley Company") or a society for whom a

Wiley Company has exclusive publishing rights in relation to a particular journal (collectively "WILEY"). By clicking "accept" in connection with completing this licensing transaction, you agree that the following terms and conditions apply to this transaction (along with the billing and payment terms and conditions established by the Copyright Clearance Center Inc., ("CCC's Billing and Payment terms and conditions"), at the time that you opened your RightsLink account (these are available at any time at http://myaccount.copyright.com).

Terms and Conditions

1. The materials you have requested permission to reproduce (the "Materials") are protected by copyright.

2.You are hereby granted a personal, non-exclusive, non-sublicensable, non-transferable, worldwide, limited license to reproduce the Materials for the purpose specified in the licensing process. This license is for a one-time use only with a maximum distribution equal to the number that you identified in the licensing process. Any form of republication granted by this license must be completed within two years of the date of the grant of this license (although copies prepared before may be distributed thereafter). The Materials shall not be used in any other manner or for any other purpose. Permission is granted subject to an appropriate acknowledgement given to the author, title of the material/book/journal and the publisher. You shall also duplicate the copyright notice that appears in the Wiley publication in your use of the Material. Permission is also granted on the understanding that nowhere in the text is a previously published source acknowledged for all or part of this Material. Any third party material is expressly excluded from this permission.

3. With respect to the Materials, all rights are reserved. Except as expressly granted by the terms of the license, no part of the Materials may be copied, modified, adapted (except for minor reformatting required by the new Publication), translated, reproduced, transferred or distributed, in any form or by any means, and no derivative works may be made based on the Materials without the prior permission of the respective copyright owner. You may not alter, remove or suppress in any manner any copyright, trademark or other notices displayed by the Materials. You may not license, rent, sell, loan, lease, pledge, offer as security, transfer or assign the Materials, or any of the rights granted to you hereunder to any other person.

4. The Materials and all of the intellectual property rights therein shall at all times remain the exclusive property of John Wiley & Sons Inc or one of its related companies (WILEY) or their respective licensors, and your interest therein is only that of having possession of and the right to reproduce the Materials pursuant to Section 2 herein during the continuance of this Agreement. You agree that you own no right, title or interest in or to the Materials or any of the intellectual property rights therein. You shall have no rights hereunder other than the license as provided for above in Section 2. No

right, license or interest to any trademark, trade name, service mark or other branding ("Marks") of WILEY or its licensors is granted hereunder, and you agree that you shall not assert any such right, license or interest with respect thereto.

5. NEITHER WILEY NOR ITS LICENSORS MAKES ANY WARRANTY OR REPRESENTATION OF ANY KIND TO YOU OR ANY THIRD PARTY, EXPRESS, IMPLIED OR STATUTORY, WITH RESPECT TO THE MATERIALS OR THE ACCURACY OF ANY INFORMATION CONTAINED IN THE MATERIALS, INCLUDING, WITHOUT LIMITATION, ANY IMPLIED WARRANTY OF MERCHANTABILITY, ACCURACY, SATISFACTORY QUALITY, FITNESS FOR A PARTICULAR PURPOSE, USABILITY, INTEGRATION OR NON-INFRINGEMENT AND ALL SUCH WARRANTIES ARE HEREBY EXCLUDED BY WILEY AND ITS LICENSORS AND WAIVED BY YOU.

6. WILEY shall have the right to terminate this Agreement immediately upon breach of this Agreement by you.

7. You shall indemnify, defend and hold harmless WILEY, its Licensors and their respective directors, officers, agents and employees, from and against any actual or threatened claims, demands, causes of action or proceedings arising from any breach of this Agreement by you.

8. IN NO EVENT SHALL WILEY OR ITS LICENSORS BE LIABLE TO YOU OR ANY OTHER PARTY OR ANY OTHER PERSON OR ENTITY FOR ANY SPECIAL, CONSEQUENTIAL, INCIDENTAL, INDIRECT, EXEMPLARY OR PUNITIVE DAMAGES, HOWEVER CAUSED, ARISING OUT OF OR IN CONNECTION WITH THE DOWNLOADING, PROVISIONING, VIEWING OR USE OF THE MATERIALS REGARDLESS OF THE FORM OF ACTION, WHETHER FOR BREACH OF CONTRACT, BREACH OF WARRANTY, TORT, NEGLIGENCE, INFRINGEMENT OR OTHERWISE (INCLUDING, WITHOUT LIMITATION, DAMAGES BASED ON LOSS OF PROFITS, DATA, FILES, USE, BUSINESS OPPORTUNITY OR CLAIMS OF THIRD PARTIES), AND WHETHER OR NOT THE PARTY HAS BEEN ADVISED OF THE POSSIBILITY OF SUCH DAMAGES. THIS LIMITATION SHALL APPLY NOTWITHSTANDING ANY FAILURE OF ESSENTIAL PURPOSE OF ANY LIMITED REMEDY PROVIDED HEREIN.

9. Should any provision of this Agreement be held by a court of competent jurisdiction to be illegal, invalid, or unenforceable, that provision shall be deemed amended to achieve as nearly as possible the same economic effect as the original provision, and the legality, validity and enforceability of the remaining provisions of this Agreement shall not be affected or impaired thereby.

10. The failure of either party to enforce any term or condition of this Agreement shall

not constitute a waiver of either party's right to enforce each and every term and condition of this Agreement. No breach under this agreement shall be deemed waived or excused by either party unless such waiver or consent is in writing signed by the party granting such waiver or consent. The waiver by or consent of a party to a breach of any provision of this Agreement shall not operate or be construed as a waiver of or consent to any other or subsequent breach by such other party.

11. This Agreement may not be assigned (including by operation of law or otherwise) by you without WILEY's prior written consent.

12. Any fee required for this permission shall be non-refundable after thirty (30) days from receipt

13. These terms and conditions together with CCC's Billing and Payment terms and conditions (which are incorporated herein) form the entire agreement between you and WILEY concerning this licensing transaction and (in the absence of fraud) supersedes all prior agreements and representations of the parties, oral or written. This Agreement may not be amended except in writing signed by both parties. This Agreement shall be binding upon and inure to the benefit of the parties' successors, legal representatives, and authorized assigns.

14. In the event of any conflict between your obligations established by these terms and conditions and those established by CCC's Billing and Payment terms and conditions, these terms and conditions shall prevail.

15. WILEY expressly reserves all rights not specifically granted in the combination of (i) the license details provided by you and accepted in the course of this licensing transaction, (ii) these terms and conditions and (iii) CCC's Billing and Payment terms and conditions.

16. This Agreement will be void if the Type of Use, Format, Circulation, or Requestor Type was misrepresented during the licensing process.

17. This Agreement shall be governed by and construed in accordance with the laws of the State of New York, USA, without regards to such state's conflict of law rules. Any legal action, suit or proceeding arising out of or relating to these Terms and Conditions or the breach thereof shall be instituted in a court of competent jurisdiction in New York County in the State of New York in the United States of America and each party hereby consents and submits to the personal jurisdiction of such court, waives any objection to venue in such court and consents to service of process by registered or certified mail, return receipt requested, at the last known address of such party.

Wiley Open Access Terms and Conditions

Wiley publishes Open Access articles in both its Wiley Open Access Journals program [http://www.wileyopenaccess.com/view/index.html] and as Online Open articles in its subscription journals. The majority of Wiley Open Access Journals have adopted the Creative Commons Attribution License (CC BY) which permits the unrestricted use, distribution, reproduction, adaptation and commercial exploitation of the article in any medium. No permission is required to use the article in this way provided that the article is properly cited and other license terms are observed. A small number of Wiley Open Access journals have retained the Creative Commons Attribution Non Commercial License (CC BY-NC), which permits use, distribution and reproduction in any medium, provided the original work is properly cited and is not used for commercial purposes.

Online Open articles - Authors selecting Online Open are, unless particular exceptions apply, offered a choice of Creative Commons licenses. They may therefore select from the CC BY, the CC BY-NC and the Attribution-NoDerivatives (CC BY-NC-ND). The CC BY-NC-ND is more restrictive than the CC BY-NC as it does not permit adaptations or modifications without rights holder consent.

Wiley Open Access articles are protected by copyright and are posted to repositories and websites in accordance with the terms of the applicable Creative Commons license referenced on the article. At the time of deposit, Wiley Open Access articles include all changes made during peer review, copyediting, and publishing. Repositories and websites that host the article are responsible for incorporating any publisher-supplied amendments or retractions issued subsequently.
Wiley Open Access articles are also available without charge on Wiley's publishing platform, **Wiley Online Library** or any successor sites.

Other Terms and Conditions:

BY CLICKING ON THE "I AGREE..." BOX, YOU ACKNOWLEDGE THAT YOU HAVE READ AND FULLY UNDERSTAND EACH OF THE SECTIONS OF AND PROVISIONS SET FORTH IN THIS AGREEMENT AND THAT YOU ARE IN AGREEMENT WITH AND ARE WILLING TO ACCEPT ALL OF YOUR OBLIGATIONS AS SET FORTH IN THIS AGREEMENT.

From: Frauenrath Holger

Dear Alma,

sorry for the late reply. I can sure give you permission for publishing the figure as you find it in my class material. Please, let me know in case you need the actual figure (instead of the slide) in any particular graphics format.

Having said this, I just remade the figure myself "similar" to the actual graphics (of extremely poor quality) found in the original research papers by Bates et al. (the references I give on the slides). It is conceptually correct, but not in terms of the exact shape of the curves etc.

Best regards

Holger

Prof. Holger Frauenrath
Ecole Polytechnique Federale de Lausanne (EPFL)
Institute of Materials (IMX)
Laboratory of Macromolecular and Organic Materials (LMOM)

Mail address:
EPFL- STI - IMX - LMOM
Building MXG 037
Station 12
1015 Lausanne
Switzerland

Phone: (+41) 21 693 7399
Secr: (+41) 21 693 7395
Fax: (+41) 21 693 5270
Email: holger.frauenrath@epfl.ch
Web: http://lmom.epfl.ch/

Original e-mail:

June 21, 2013

Dear Dr. Frauenrath,

I am completing a doctoral dissertation at Clemson University entitled "Synthesis, Characterization and Diffusion Studies of Ceria-Zirconia-Yttria Mesostructures" I would like your permission to reprint in my dissertation a figure from the following:

From: http://lmom.epfl.ch/index.php?page=advancedpolymers

Teaching material from “Advanced Polymer Science”, section 2.4, third slide (page 156).

The figure is referenced from 3 papers but as I have checked them none has the figure depicted but only information related to it. So I think is probably your own figure.

The figure to be reproduced is: Theoretical AB Diblock Copolymer Phase Diagram (2nd Figure)

The requested permission extends to any future revisions and editions of my dissertation, and to the prospective publication of my dissertation by Clemson University. These rights will in no way restrict republication of the material in any other form by you or by others authorized by you. Your signing of this letter will also confirm that you own the copyright to the above-described material. Full credit to the original source will be given.

If you do not control the rights to this material, please supply the name and address of the person to whom requests should be directed.

If these arrangements meet with your approval, please sign the attached letter where indicated and return it to me via fax, e-mail or regular mail. Thank you very much.

VITA

Alma Iris Cordova Morales was born in San Salvador, El Salvador. She received her Bachelor of Science degree in Chemical Engineering from Universidad Centroamericana Jose Simeon Canas with the highest GPA of her class in 2008. She was awarded the "2008 Best Chemical Engineering Student" by the Salvadoran Association of Chemical Engineers. She also received the "Fantel Scholarship for National Education to the Academic Excellence" from 2003 to 2008. During her time in college, she was a mentor at the "Young Talents Program" in El Salvador where she taught children 6 to 14 years old different college-level classes that included trigonometry, introduction to discrete mathematics, geometry, among others. She also worked as a laboratory instructor for Physical Chemistry I and II courses at Universidad Centroamericana. After graduation she worked at Unilever of Central America as an administrative operator in their detergents plant where she supervised the operation of the packing area and reported daily production for that division.

In 2008 she began her doctoral studies in Chemical Engineering at Clemson University. During her time in Clemson, she was awarded the Philanthropic Educational Organization scholarship for two consecutive years. Her research in *Novel Ceria-Zirconia-Yttria Mesostructures: Synthesis, Characterization, Diffusional Studies and the Effects of Morphology on their Properties* was conducted under the guidance of Dr. David Bruce.